Site U1329[1]

Expedition 311 Scientists[2]

Chapter contents

[1] Expedition 311 Scientists, 2006. Site U1329. *In* Riedel, M., Collett, T.S., Malone, M.J., and the Expedition 311 Scientists. *Proc. IODP,* 311: Washington, DC (Integrated Ocean Drilling Program Management International, Inc.). doi:10.2204/iodp.proc.311.107.2006
[2] **Expedition 311 Scientists' addresses.**

Background and objectives

Site U1329 (proposed Site CAS-05D; Collett et al., 2005) is at the easternmost end of the southwest-northeast-trending, margin-perpendicular transect of sites drilled during Integrated Ocean Drilling Program (IODP) Expedition 311 and is located closest to shore (65 km) at a water depth of 946 m. Newly acquired bathymetry data showed that this site is located in an area characterized by multiple canyons of various sizes where water depth decreases rapidly from 500 to 1300 m over a distance of only 7.5 km with an average slope of 6° (Figs. **F3** and **F4** in the "Expedition 311 summary" chapter). The canyons appear to form scours that funnel sediment into the deeper basin. At the foot of the steep slope at a water depth of ~1300 m, the seafloor flattens abruptly into a plateau and some of the canyons continue across the plateau and die out in the slightly deeper midslope basin. Some of the slope canyons also appear to be connected to a sediment transport system further upslope as seen in Figure **F4** in the "Expedition 311 summary" chapter. Shallow sedimentation at Site U1329 is therefore expected to be dominated by turbidite sequences but could also show signs of more recent erosion.

A map of all the site survey seismic data acquired in preparation for this expedition in the area of Site U1329 is shown in Figure **F1.** High-resolution 3.5 kHz seismic data do not indicate the presence of the typical Holocene transparent layer described at the other site locations along the transect (Fig. **F2**). Seismic data do not generally reveal an obvious bottom-simulating reflector (BSR) at this site. The BSR is not detectable on multichannel seismic (MCS) Line 89-08 (Fig. **F3**); however, a faint BSR-like reflection can be identified along MCS Line PGC9902_ODP-1, but it is difficult to determine the polarity of this reflector (Fig. **F4**). In the perpendicular direction relative to the previous two lines, a better image of the BSR can be seen on Line PGC0408_CAS05_line03-04 (Fig. **F5**). Along this line, a clear reflector with polarity opposite to the seafloor is identified at a depth of 154 ms two-way traveltime (TWT). Using the vertical seismic profile (VSP) data from Ocean Drilling Program (ODP) Leg 146 Site 889, an average interval velocity of 1636 m/s was determined for the sediments between the seafloor and the BSR. This average velocity was determined to match observed BSR depths in MCS data with the depth of the BSR in the VSP data. Using this average velocity, the BSR at Site U1329 is ~126 meters below seafloor (mbsf). Using different velocity pro-

doi:10.2204/iodp.proc.311.107.2006

files representing higher velocities (i.e., more gas hydrate) or lower velocities (i.e., less gas hydrate) at depth yielded an error of about ±2.5 m in the BSR depth estimate.

MCS Line 89-08 (low-frequency content <50 Hz) is characterized by strong reflectivity in the sediments below 140 ms TWT (~115 mbsf using the average velocity of 1636 m/s). The frequencies of seismic reflections beneath this depth appear much lower than above, which may indicate the presence of free gas. The top of this high-amplitude, low-frequency horizon forms an erosional unconformity that deepens towards the northeast along MCS Line 89-08. Seismic reflectors above this unconformity are mainly seafloor parallel and form onlaps, whereas underneath the unconformity no clear orientation can be identified.

Objectives

The objectives of coring and logging this site are tied to completing the transect of scientific drill sites across the northern Cascadia margin. This site is the shallowest and most landward location at the eastward limit of gas hydrate occurrence on this margin. The depth to the BSR rapidly becomes shallower at this site and is only at half the depth compared to Site U1327.

At this eastern end-member site of gas hydrate evolution in the accretionary prism, the objectives include

- Studying the distribution of gas hydrate;
- Defining the nature of the BSR;
- Developing baseline geochemical and microbiological profiles; and
- Obtaining data needed to ground-truth remotely acquired imaging techniques, such as seismic or controlled-source electromagnetic surveys.

The operational plan to achieve these objectives was based on a general three-hole concept, which included

- A logging-while-drilling/measurement-while-drilling (LWD/MWD) hole;
- A continuously cored hole to characterize geochemical and microbiological baselines and proxies for gas hydrate;
- An additional "tools" hole for specialized pressure coring systems, including the IODP Pressure Core Sampler (PCS) and the HYACINTH Fugro Pressure Corer (FPC) and HYACE Rotary Corer (HRC) systems combined with selected spot-coring using the conventional extended core barrel (XCB) system; and
- A wireline logging program in the tools hole using the triple combination (triple combo) and Formation MicroScanner (FMS)-sonic tool strings.

Maximum allowable depth for the LWD/MWD logging hole at this site is 270 mbsf. Anticipated total depth for the continuously cored hole is 220 mbsf, with the BSR at 126 mbsf. Wireline logging and tools holes are planned to a total depth of 270 mbsf.

Operations

Hole U1329A

We transited 8.7 h from Site U1328 in dynamic positioning (DP) mode to Site U1329 (proposed Site CAS-05D; Collett et al., 2005) while we downloaded the LWD/MWD data collected at the three previous sites. Hole U1329A was spudded at 1830 h on 25 September 2005, at an estimated water depth of 959.1 meters below sea level (mbsl; 970 meters below rig floor [mbrf]) (see mudline core estimate in **"Hole U1329C"**). LWD/MWD drilling progressed without incident and within the prescribed protocol guidelines (see **"Downhole logging"** in the "Methods" chapter). A total depth (TD) of 220 mbsf was reached at 0800 h on 26 September. After displacing the hole with 10.5 pounds per gallon (ppg) mud, the last of the tools and the bit arrived on deck at 1330 h, officially ending operations in Hole U1329A. We offset 15 m to the north to start coring operations in Hole U1329B (Fig. **F6**).

Hole U1329B

On the morning of 26 September 2005, we learned that the LWD tool and personnel transfer boat had to return to Coos Bay, Oregon, twice: once to drop off a sick passenger and again because of engine problems. Ultimately, the engine problems were not serious, the transfer boat was quickly repaired, and it left Coos Bay at 1025 h. The exchange boat arrived at 1630 h on 27 September. Tool offloading and personnel transfer were completed, and the boat departed at 2125 h for Aberdeen, Washington. While waiting for the boat and during transfer operations, the drill string was tripped to near the seafloor. Hole U1329B was spudded, with the first core arriving on deck at 2105 h with 10.02 m of recovery, therefore not recovering the mudline. Recovery of the mudline core is important for high-resolution, shallow geochemical and microbiological studies. We terminated Hole U1329B to start a new hole so that we could obtain a mudline core.

Hole U1329C

The bit was raised 5 m higher than for the Hole U1329B spud position, and without offsetting, Hole

U1329C was spudded with core on the deck at 2150 h on 27 September 2005. Core 311-U1329C-1H recovered 8.19 m, providing an estimated seafloor depth of 946.4 mbsl (957.4 mbrf, which indicated that the seafloor depth had been overestimated by >6 m in Holes U1329A and U1392B (Table T1). Coring with the advanced piston corer (APC) system continued to 140.2 mbsf (106% recovery), where we switched to the XCB coring system and advanced the hole to 188.5 mbsf (82% recovery) (Table T1). Five APC temperature measurements were made with the advanced piston corer temperature (APCT) or third-generation advanced piston corer temperature (APC3) tools (Table T1). In addition, the APC3 housing was run without internal electronics to test water tightness for Core 311-U1329C-2H. Two PCS cores (311-U1329C-7P and 14P) were collected at 55.6 and 114.6 mbsf, respectively. Core 311-U1329C-14P was recovered without pressure. The third PCS core deployment (Core 311-U1329C-23P) returned to the rig floor at 0210 h on 29 September without the cutting shoe, which was left in the hole. Attempts to drill past it were unsuccessful. Coring in Hole U1329C was terminated at 189.5 mbsf; ~30 m shy of the target depth.

Swell from a nearby low pressure system (>5 m heave) made conditions too rough to attempt wireline logging or recover quality piston cores from a new hole; therefore, we decided to wait on the weather to improve before resuming operations. After displacing the hole with 10.5 ppg mud, the drill pipe was pulled to 81.5 mbsf at 0630 h on 29 September. After receiving the forecast for continued poor conditions throughout that day, we decided to pull out of Hole U1329C and drill a dedicated logging hole when better conditions would permit. This scenario had the added benefit of penetration to total depth and a better chance for good hole conditions for logging.

Hole U1329D

After pulling out of Hole U1329C, we offset 15 m south of Hole U1329A and spudded Hole U1329D at 1115 h on 29 September 2005. At 1955 h, after drilling Hole U1329D to 165.6 mbsf, increased ship heave (>6 m) forced us to suspend operations again. By 2130 h, improved conditions allowed us to resume drilling. After relatively slow drilling (~5 m/h) in the lower ~35 m, we took a single XCB core (311-U1329D-1X; 1.03 m of recovery) at the bottom of Hole U1329D, which was completed to a TD of 210.5 mbsf at 1015 h on 30 September. After reaching TD in Hole U1329D, we switched to the wireline logging program. The first tool string deployed was the standard triple combo, which reached a depth of 209 mbsf. The hole was logged without incident. The second logging run consisted of two passes of the FMS-sonic tool string. On the first run, the FMS-sonic tool string reached a depth of 209 mbsf, but on the second run the FMS-sonic tool string could only reach a depth of 171 mbsf. The caliper log showed that parts of the hole were severely enlarged. After the wireline tools were recovered, the hole was displaced with 10.5 ppg mud, and the pipe was pulled out of the hole, ending operations in Hole U1329D at 0020 h, 1 October.

Hole U1329E

After offsetting 15 m to the north of Hole U1329C in DP mode, Hole U1329E was spudded at 0235 h on 1 October 2005. Core 311-U1329E-1H recovered 5.05 m, which indicated a seafloor depth of 945.5 mbsl (956.5 mbrf). The hole was advanced with the APC system to 33.5 mbsf, where the PCS was deployed, and Core 311-U1329E-5P was recovered without pressure. After washing down to 54.5 mbsf, Core 311-U1329E-6H was taken to obtain a temperature measurement with the APCT tool. The Davis-Villinger Temperature Probe (DVTP) was deployed immediately after Core 311-U1329E-6H to provide a calibration point with the APCT. The rest of the hole was devoted to pressure coring runs with intervening washed intervals (Table T1). The PCS was deployed two more times at 73.5 and 125.0 mbsf (Cores 311-U1329E-7P and 10P, respectively), which were successfully recovered under pressure. The FPC was deployed at 104.0 mbsf but did not return under pressure. Finally, the HRC was deployed at 114.5 mbsf and retrieved a full core under pressure. After displacing the hole with 10.5 ppg mud, the bottom-hole assembly (BHA) was pulled clear of the seafloor at 2232 h on 1 October, ending operations in Hole U1329E. The drill string was tripped to the rig floor in preparation for the short 9.2 nmi transit to Site U1327.

Lithostratigraphy

Site U1329 is the easternmost and shallowest (~946 mbsl) site of the transect drilled during Expedition 311. Four of the five holes (Holes U1329B–U1329E) at this site were cored. Hole U1329B was cored to 9.5 mbsf, Hole U1329C was cored to 189.5 mbsf (187.5 m recovered), Hole U1329D was cored from 201 to 210.5 mbsf (9.5 m recovered), and Hole U1329E was cored to 34.5 mbsf and then from 54.5 to 126 mbsf (total recovery of 48.0 m). Recovery was generally good (Hole U1329B = 105.5%, Hole U1329C = 99.3%, Hole U1329D = 10.8%, and Hole U1329E = 78.6%).

We divide the 187.5 m thick sedimentary section recovered at Site U1329 into three lithostratigraphic units (Fig. F7) based on visual inspection of the recovered cores and analysis of smear slides. Other parameters, such as mineralogy data from X-ray diffraction (XRD) analyses, helped to better define the entire stratigraphic section. Results were also compared and correlated with two-dimensional seismic data, downhole LWD/MWD data, physical property measurements, and color reflectance spectrophotometry from the archive multisensor track.

Lithostratigraphic units

Lithostratigraphic Unit I

Intervals: Sections 311-U1329B-1H-1 through 1H-CC; 311-U1329C-1H-1 through 5H-1; and 311-U1329E-1H-1 through 4H-CC

Depths: Hole U1329B: 0.00–10.01 mbsf; Hole U1329C: 0.00–37.18 mbsf; and Hole U1329E: 0.00–33.31 mbsf

Age: Holocene?–Pleistocene

Unit I is composed of dark greenish gray (5GY 4/1) and dark gray (N4) clay and silty clay (Fig. F8) sometimes showing parallel lamination. The clay and silty clay are locally interbedded with silt, clayey silt, and sand layers and lenses. The major nonbiogenic components of Unit I are quartz, feldspar, clay minerals, opaque minerals, accessory minerals (mainly amphibole), and some glauconite. Rare sulfide mottling, appearing as dark gray (N4) stains, occurs in all cores from Unit I. Sulfide concretions were observed in all cores and are especially frequent in Core 311-U1329C-2H. Bioturbation is rare to abundant in Cores 311-U1329C-1H, 3H, and 4H.

The biogenic components have mostly very low concentrations in the major lithology (Fig. F7). In the minor lithology of Hole U1329B, as much as 60% diatoms was estimated by smear slide analysis. Some rare bivalve shell fragments are present in Cores 311-U1329-3H and 4H, and one gastropod is present in Section 311-U1329-2H-6. A 5 cm long piece of wood is present in Section 311-U1329E-1H-2 (Fig. F8).

Unlithified authigenic carbonate cements (Fig. F9A) and partly lithified carbonates (Fig. F9B), as well as lithified carbonates (Fig. F9C) are abundant in intervals 311-U1329C-4H-3, 90–142 cm; 311-U1329E-4H-5, 46–122 cm; and 4H-6, 30–90 cm. XRD analyses confirmed a dolomitic composition for all these intervals (Fig. F10). The occurrence of dolomites in Holes U1329C and U1329E at about the same depth suggests that dolomite precipitation is proceeding in a widespread "layer." Ca and Mg concentrations (see **"Interstitial water geochemistry"**) seem to confirm ongoing dolomite precipitation at this level. Some dispersed, millimeter-scale carbonate concretions are present in Section 311-U1329C-2H-1.

The Unit I/II boundary is marked by the first occurrence of diatom ooze in Section 311-U1329C-5H-1 at 58 cm, which can clearly be seen as a distinct change in color.

Lithostratigraphic Unit II

Intervals: Sections 311-U1329C-5H-1 through 16H-CC and 311-U1329E-5P-1 through 10P-1

Depths: Hole U1329C: 37.18–135.60 mbsf and Hole U1329E: 33.31–125.95 mbsf

Age: Pleistocene (>0.3–2.0 Ma)

Unit II is composed of dark greenish gray (5GY 4/1) and dark olive-gray (5Y 3/2) clay, silty clay (Fig. F11), silty clay with diatoms (Fig. F12), and diatom ooze (Fig. F11) locally interbedded with silt, clayey silt, sand, and foraminifer ooze layers and lenses. Often the diatom-rich sections display a more brownish color (dark olive-gray; 5Y 3/2), whereas the sections barren in diatoms are more grayish (Fig. F11). The major nonbiogenic components of this unit are quartz, feldspar, clay minerals, opaque minerals, accessory minerals (mainly amphibole), some glauconite, and volcanic glass. Rare sulfide mottling occurs throughout Unit II. Sulfide concretions were especially abundant in Cores 311-U1329C-10H and 11H. Rare to moderate bioturbation occurs in this unit.

The composition of the biogenic components is characteristic of Unit II, in particular the high content of diatoms forming diatom ooze (Fig. F13) with a biogenic opal content of ~78%, as estimated from smear slides. The biogenic carbonate fraction is low, on average 2%–8%. In the minor lithologies, the biogenic content is even higher, with as much as 87% biogenic opal and as much as 60% biogenic carbonate. Bivalve shell fragments are very abundant in Unit II, especially from Core 311-U1329C-10H to the bottom of the unit. A piece of wood is present in Section 311-U1329C-12H-1.

Unlithified, partly lithified, and lithified carbonates are dispersed throughout Unit II in Cores 311-U1329C-5H, 8H, 10H, 12H, and 16H. The composition varies from low-Mg calcite (2 mol% $MgCO_3$) to high-Mg calcite (6 and 13 mol% $MgCO_3$), which was confirmed by XRD analyses.

The Unit II/III boundary is marked by the occurrence of conglomerate (Fig. F14) (intervals 311-U1329C-16H-6, 120–150 cm, and 16H-7, 0–69 cm). This conglomerate is composed of partly lithified and lithified rounded clasts supported by a silty clay matrix. Various-colored clasts are observed (Fig. F14), such as light greenish gray, dark greenish gray, light dark

gray, and dark gray. The size of individual clasts is ~2–4 mm.

Lithostratigraphic Unit III

Intervals: Sections 311-U1329C-17H-1 through 23P-1 and 311-U1329D-1X-1
Depths: Hole U1329C: 135.60–189.50 mbsf and Hole U1329D: 201–202.03 mbsf
Age: late Miocene (>6.7 Ma)

Unit III is mainly composed of dark greenish gray (5GY 4/1), dark olive-gray (5Y 3/2), and dark gray (N4) clay (Fig. **F15**) and silty clay (Fig. **F16**). Coarser grained, interbedded silt and sand layers are very rare and occur only in Cores 311-U1329C-17H and 21X. The major nonbiogenic components of Unit III are quartz, feldspar, clay minerals, opaque minerals, accessory minerals (mainly amphibole), some glauconite, and volcanic glass. Almost no sulfide mottling or sulfide concretions are present. Moderate bioturbation is present only in Core 311-U1329C-18X.

Most smear slide samples were barren of biogenic components. Only Sample 311-U1329C-20X-1, 77 cm, in the major lithology contains ~10% diatoms. Some rare bivalve shell fragments are present in Cores 311-U1329C-17H, 18X, and 22X, and a wood fragment is present in Section 21X-2.

Unlithified carbonate cements, partly lithified carbonates, and lithified carbonates are abundant in Unit III in Cores 311-U1329C-18H through 23X. The composition is variable and shows no zonation with depth. Dolomite, siderite (Fig. **F17**), low-Mg calcite, and high-Mg calcite (Fig. **F16**) are present and were identified by XRD (Fig. **F18**).

A minor component in Unit III is glauconite, which is present in Sections 311-U1329C-18X-2, 18X-3, 22X-1, and 22X-2. Smear slide Sample 311-U1329C-18X-2, 126 cm, contains ~97% glauconite grains that have a diameter of ~100 µm (Fig. **F19**). Another minor component is very small volcanic ash lenses (<1 cm) composed of >90% volcanic glass shards (intervals 311-U1329C-18X-3, 1–2 cm; 18X-4, 50 cm; 19X-3, 6–68 cm; 19X-5, 95 cm; and 19X-6, 5–23 cm).

The bottom of Unit III consists of an accumulation (Core 311-U1329C-23P) of a wide variety of different clasts as large as 4 cm in diameter (sandstone/quartzite with a pyrite vein, different carbonate rocks, cemented bioturbation burrows, and different mud clasts of varying color). This conglomerate-type deposit is pronounced in the pressure core gamma ray log (see **"Pressure coring"**) and probably corresponds to the depth of increasing density and electrical resistivity in the LWD data of Hole U1329A (see **"Downhole logging"**) and the wireline logging data of Hole U1329D (see **"Downhole logging"**). A change in consolidation of the sediments is also visible through drilling biscuits that are present at the bottom of Unit III, starting with Core 311-U1329C-21X. The conglomerate probably marks a lithostratigraphic boundary, but because there was only one core recovered (Core 311-U1329D-1X) deeper in the section, it is difficult to describe this lithostratigraphic unit underneath the conglomerate. Core 311-U1329D-1X is composed of silty clay without any biogenic components.

Environment of deposition

Drilling at Site U1329, the shallowest site drilled during Expedition 311 on the continental slope off Vancouver Island, recovered a sequence dominated by slope sedimentary processes (see **"Background and objectives"**).

Lithostratigraphic Unit III is characterized by fine-grained (clay to silty clay) detrital sediments with only a few coarser interlayers from turbiditic deposits. The input of detrital sediments from turbidites is supported by the presence of nonmarine diatoms in the interval 180.5–186.39 mbsf (see **"Biostratigraphy"**). At the lowermost part of lithostratigraphic Unit III (188.5–189.5 mbsf) a conglomerate deposit, which was found in pressure Core 311-U1329C-23P, indicates a major event, possibly a debris flow. The total thickness of this deposit is unknown. The overall sedimentation rate of lithostratigraphic Unit III, which has a large uncertainty because of difficulties with the age constraints (see **"Biostratigraphy"**), indicates slow sedimentation of ~0.8–2.8 cm/k.y. The presence of abundant unlithified carbonate cements and lithified carbonates suggests that diagenetic processes were and are still active. The upper boundary of this unit corresponds to an upper Miocene/Pleistocene unconformity.

Lithostratigraphic Unit II is characterized by a high abundance of biogenic silica (mainly diatoms), which also corresponds to higher sedimentation rates. Although there are some uncertainties in the age constraints (see **"Biostratigraphy"**), the sedimentation rate seems to increase within lithostratigraphic Unit II from ~4 to 10 cm/k.y. The conglomerate at the base of the unit (134.80–135.79 mbsf) follows an important stratigraphic hiatus (no sediments preserved from 2 to 6.7 Ma) and probably illustrates uplift and erosion of Pliocene sediments. Assuming similar sedimentation rates in the Pliocene as in adjacent sediments, a sediment column of ~188 m thickness may have been eroded. The great abundance of diatoms along with resting spores of *Chaetoceros* within lithostratigraphic Unit II suggest blooming in a shallow-water shelf environment and

coastal upwelling (see "Biostratigraphy"). The presence of some dispersed unlithified carbonate cements and lithified carbonates suggests that diagenetic processes are active.

Lithostratigraphic Unit I is characterized by fine-grained detrital sediments (clay and silty clay) locally interbedded with coarse-grained sediments. The elevated sedimentation rates from the top of lithostratigraphic Unit II continue, but the absence of diatoms indicates a major change in the environmental conditions. The presence of dolomite at a depth of 31.00–31.52 mbsf in Hole U1329C and 30.46–32.40 mbsf in Hole U1329E indicates a local diagenetic process.

Biostratigraphy

Biostratigraphy determined for Site U1329 was based on an examination of all core catcher samples and several additional core samples from Hole U1329C (Table T2). Hole U1329C contains the most complete stratigraphic sequence: a 187.5 m thick upper Miocene sequence and its overlying Quaternary sedimentary section. No Pliocene sequence was recognized at this site.

Diatoms

Diatoms are rare and poorly preserved in the interval from the seafloor to ~27 mbsf, where diatom assemblages are dominated by marine diatoms *Thalassionema nitzschioides* and *Thalassiosira* spp. and the nonmarine diatom *Aulacoseira granulata* s.l. Diatoms are most abundant from ~37 to ~135 mbsf, where they range from mostly common to very abundant and moderately preserved. Diatoms in this interval are dominated by *Neodenticula seminae, Stephanopyxis dimorpha*, *Stephanopyxis* spp., *T. nitzschioides,* and *Thalassiosira* spp. and mostly associated with very abundant resting spores of *Chaetoceros*. Overall, the very abundant occurrence of diatoms along with numerous resting spores in this interval suggest they may be a product of coastal upwelling in a shelf area, which would require them to be transported by turbidites to this site. Diatoms such as *Actinocyclus oculatus, Proboscia curvirostris,* and *Thalassiosira jouseae* are rare but were recognized only in this interval. The interval from ~137 to ~177 mbsf is characterized by the lack of some of the diatoms recognized in the upper intervals, such as *A. oculatus*, *N. seminae, P. curvirostris,* and *T. jouseae* and are mostly dominated by *T. nitzschioides*. Some diatom assemblages in this interval contain diatoms such as *Neodenticula kamtschatica, Thalassionema schraderi,* and *Thalassiosira antiqua,* which are not contained in the upper intervals. Diatoms between ~179 and ~186 mbsf are generally very rare and poorly preserved and are dominated by the nonmarine diatom *Aulacoseira granulata* s.l.

The interval between the seafloor and Sample 311-U1329C-2H-CC (0.10–18.30 mbsf) contains *N. seminae* but lacks *P. curvirostris* and was assigned to North Pacific Diatom (NPD) Zone 12 (*N. seminae* Zone). The last occurrence (LO) of *P. curvirostris* was recognized in Sample 311-U1329C-4H-CC (37.18 mbsf), marking the NPD Zone 12/11 boundary (*P. curvirostris* Zone). The LO of *A. oculatus* was found in Sample 311-U1329C-4H-CC (37.18 mbsf). The interval between these two LOs (37.18–95.69 mbsf) was assigned to NPD Zone 11 (*P. curvirostris* Zone). The interval between Samples 311-U1329C-12H-CC (105.32 mbsf) and 16H-CC (135.98 mbsf) contains both *P. curvirostris* and *A. oculatus* but lacks *Neodenticula koizumii* and was assigned to NPD Zone 10 (*A. oculatus* Zone). The interval between Samples 311-U1329C-17H-1, 10–12 cm (135.70 mbsf), and 20X-3, 10–12 cm (161.20 mbsf), is characterized by rare occurrences of *N. kamtschatica*, *Rouxia californica,* and *T. antiqua* and the lack of *N. koizumii* and was assigned to NPD Subzone 7A (*R. californica* Zone). The LO and the first occurrence (FO) of *T. schraderi* were recognized in Samples 311-U1329C-20X-5, 10–12 cm (165.20 mbsf), and 21X-CC (176.98 mbsf), respectively. The interval between the LO and the FO of *T. schraderi* was assigned to NPD Subzone 6B (*T. schraderi* Zone). The interval between Samples 311-U1329C-22X-2, 10–12 cm (180.50 mbsf), and 22X-6, 10–12 cm (186.39 mbsf), might be assigned to NPD Subzone 6A (*Denticulopsis katayamae* Zone), but the lack of zonal diagnostic diatoms and the predominance of nonmarine diatoms makes it difficult to make a definite zonal assignment.

The upper three diatom zones in Hole U1329C are Holocene–Pleistocene in age, and the lower two (or possibly three) zones are late Miocene in age, respectively. The Pliocene is missing in this hole as a result of a hiatus at ~137 mbsf, where sediments ranging in age from 2.0 Ma (the base of NPD Zone 10) to 6.7 Ma (the top of NPD Subzone 7A) are missing. This hiatus between Pleistocene and Miocene sediments corresponds to the boundary between lithostratigraphic Units II and III (see "Lithostratigraphy").

Interstitial water geochemistry

A total of 52 interstitial water (IW) whole-round samples, 10–30 cm long, were collected at Site U1329. Forty samples were collected from Hole U1329C, with a sampling frequency of four per core in the second core, three in the first and third cores, two per core to a depth of 140 mbsf, and one per

core for the remaining cores. One sample was collected from pressure Core 311-U1329C-7P, retrieved from a depth of 55.6 mbsf. Sulfate analysis indicates that this sample was contaminated during coring and, therefore, was only analyzed for Cl concentration. The Cl concentration value corrected for seawater contamination is reported in Table T3. In Hole U1329D, only one whole-round sample was obtained from a depth of 201.7 mbsf. Hole U1329E was dedicated to high-resolution microbiological and geochemical sampling, from which a total of 11 samples were recovered, covering the interval from the seafloor through the sulfate/methane interface (SMI). Whole-round samples were taken adjacent to core sections sampled for microbiological studies, and headspace (HS) samples were taken adjacent to each whole-round IW sample. The sampling resolution was one sample per section in the first two cores. Two additional samples were collected in Core 311-U1329E-3H, but only one of them was processed because whole-round Sample 311-U1329E-1H, 135–150 cm, was highly disturbed and unsuitable for IW extraction. The IW data for Site U1329 are listed in Table T3 and illustrated in Figures F20, F21, and F22. The microbially mediated reactions and nonbiogenic, inorganic, and fluid-rock reactions that modified the IW chemistry at this site are discussed below.

Salinity and chlorinity

Salinity decreases from 33.8 to 30.3 at 44 mbsf. Below this depth, salinity values stabilize between 30.5 and 30.0 to 176.5 mbsf (Fig. F20). The last sample collected from Hole U1329C shows a sharp drop in salinity to 28. This depth corresponds to a marked change in resistivity and density in the LWD data (see "Downhole logging"). To confirm this low salinity value, further coring was attempted to sample the sediments corresponding to the anomalous LWD-inferred section. Unfortunately, only a 36 cm long sample was retrieved in the single XCB core collected from this hole because of drilling difficulties. We took a whole-round sample at 201.7 mbsf, which yielded a salinity value of 22, confirming the presence of highly freshened fluid below 176 mbsf. The anomalous composition of this fluid is also apparent in the concentration of major and minor elements (Table T3). Analyses of hydrocarbons collected from this zone also revealed anomalously low C_1/C_2 ratios in void gas and pressure core samples, indicative of a partial contribution from a thermogenic hydrocarbon source (see "Organic geochemistry").

The overall freshening trend is also observed in the chlorinity data. It is important to note, however, that the salinity versus depth profile does not mimic the dissolved Cl concentration profile. Chlorinity decreases from 547 mM at 1.5 mbsf to 480 mM at 183.6 mbsf and reaches a value of 380 mM in Sample 311-U1329D-1X-1, 52–88 cm, at 201.7 mbsf. Superimposed on the freshening trend with depth, there is a distinct, low-chloride anomaly in the pore fluids recovered from 111 to 135 mbsf, relative to a constant chloride concentration of 519 ± 1 mM that extends from 98 to 139 mbsf. The minimum value in dissolved chloride lies at ~125 mbsf, coincident with the depth of the BSR. If we assume that this anomaly was produced by in situ dissociation of disseminated gas hydrate, the calculated pore volume occupancy by gas hydrate is <2% based on 60% porosity (see "Physical properties"). However, because no direct visual or infrared (IR) evidence for methane hydrate presence at this depth interval was obtained, this Cl minimum may represent a paleohydrate dissociation zone. Assuming a sediment diffusion coefficient of 5×10^{-6} cm²/s, this low-Cl anomaly would dissipate in ~15,000 y.

The lower than seafloor chlorinity at the sediment/seawater interface probably reflects the modern bottom water value at this site, and the slight decrease in chlorinity in the uppermost ~20 m may reflect diffusion of low-Cl interglacial water into the sediment. From ~140 mbsf to TD, Cl concentration decreases more steeply, suggesting communication with a deep-seated, fresher fluid. At this depth interval, in addition to Cl, the concentrations of Na and K (Fig. F20) and Ca and Mg (Fig. F22) also decrease with depth, and each has a greater concentration gradient than above ~140 mbsf, supporting the suggestion of communication with a deeper sourced, fresher fluid. The discontinuity in the concentration profiles at this depth coincides with the lithostratigraphic Unit II/III boundary (see "Lithostratigraphy"). The conglomerate at the base of Unit II seems to act as a semipermeable diffusional barrier.

Biogeochemical processes

The concentration versus depth profiles indicate that the IW chemistry has been extensively modified from seawater by both microbially mediated reactions and by abiological, inorganic fluid-rock reactions. The microbially mediated reactions, such as bacterial sulfate reduction followed by carbonate reduction or methane oxidation and associated authigenic carbonate formation, are particularly intense in the uppermost ~15 m of the sediment section, as reflected in the concentration profiles of sulfate, alkalinity, ammonium, and phosphate (Fig. F21).

In Hole U1329E, sulfate concentrations decrease almost linearly from 22 mM at 1.5 mbsf to 0.2 mM at 9.4 mbsf at a rate of 2.8 mM/m and reach zero concentration between 9 and 10 mbsf. The decrease in

sulfate concentration is coupled with a sharp increase in alkalinity, suggesting that sulfate is consumed by microbially mediated sulfate reduction processes. The depth of sulfate depletion is concomitant with increasing methane concentration (Fig. F28), consistent with the anaerobic methane oxidation at the SMI.

Although utmost care was taken during cleaning of the samples prior to squeezing, occasional contamination by drilling fluid could not be avoided. For example, in Sample 311-U1329D-1X-1, 52–88 cm, where the sediment was highly disturbed, a dissolved sulfate concentration of 4.7 mM was measured, which reflects drilling fluid contamination. Reported sulfate concentrations below 0.4 mM are most likely an instrumental precision problem of the ion chromatograph.

Note that there is a clear offset in the uppermost 9 m between the sulfate profiles of Holes U1329C and U1329E (Fig. F21). It was initially thought that this was caused by double penetration of the APC at the onset of coring operations during high heave conditions. However, because none of the other concentration data show this offset, this discrepancy is most likely caused by unreliable ion chromatograph sulfate data. Nevertheless, we use the data from Hole U1329E and place the SMI at 9.5 mbsf pending postcruise revision of the sulfate data for Holes U1329C and U1329E (Fig. F23).

Anaerobic oxidation of organic matter is a continuous electron generating process. First, dissolved sulfate is exhausted by bacterial sulfate reduction; the next available electron acceptor is CO_2 (Claypool and Kaplan, 1974). At the depth where sulfate is exhausted, the alkalinity profile shows a reversal caused by the onset of CO_2 reduction by microbial methanogenesis. The net CO_2 produced by organic matter remineralization can be calculated by summing the CO_2 removed by authigenic carbonate precipitation and the CO_2 removed by methane production to the measured alkalinity.

Within the sulfate reduction and alkalinity generation zone, calcium and magnesium profiles show a rapid decrease with depth that reflects authigenic carbonate formation. In the uppermost 28 m, calcite and/or Mg-calcite formation preferentially consumes calcium, leading to the observed increase in Mg/Ca ratios to a value of 16, about three times that of seawater (Fig. F22; Table T3). At such high Mg/Ca ratios, high alkalinity values, and low sulfate values, dolomitization is the favored authigenic carbonate reaction. Indeed, from ~10 to ~70 mbsf, the decrease in alkalinity is coincident with a low-Ca and -Mg concentration zone, which includes the minima in calcium, magnesium, and Mg/Ca at ~30 mbsf, suggesting dolomitization reactions at this depth. The above reactions most likely were responsible for the formation of the dolomite concretions recovered in the core (see "Lithostratigraphy").

From ~60 mbsf through the BSR depth, Ca concentrations steadily increase, suggesting communication with a fluid at greater depth. Accordingly, the Mg concentrations should have decreased with depth, but, as seen in Figure F22, they are instead almost constant and even increase slightly with depth from 30 to ~55 mbsf. This is caused by Mg expulsion from clay-mineral ion exchange sites by ammonium, which reaches concentrations up to 7.7 mM at 108 mbsf (Fig. F21). Below the BSR and the zone of maximum ammonium concentrations, Ca increases at a steeper gradient and Mg decreases with depth.

Organic geochemistry

The shipboard organic geochemistry program for Site U1329 included analysis of the composition of volatile hydrocarbons (C_1–C_5) and nonhydrocarbon gases (i.e., O_2 and N_2) from HS gas samples, void gas samples, and gas samples recovered during PCS degassing experiments. Sediment from IW squeeze cakes was analyzed for inorganic carbon (IC; also expressed as weight percent $CaCO_3$), total carbon (TC), and total nitrogen (TN). Total organic carbon (TOC) was calculated as the difference between the TC and IC. A total of 55 HS gas samples (Holes U1329C and U1329E) and 51 samples for solid-state analysis (Holes U1329C and U1329E) were collected from the cut end of core sections facing the IW samples so that the gas and IW data could be integrated. The sampling plan (see "Interstitial water geochemistry") was designed to maximize resolution in shallow sediments near the SMI. We collected 39 HS gas and sediment samples from Hole U1329C, which was sampled to a depth of 186.7 mbsf. The additional 16 HS gas samples were obtained from Hole U1329E, which was sampled at high resolution from the surface to a depth of 30 mbsf to capture the SMI. A total of 29 void gas samples were collected from Hole U1329C from depths where gas expansion features in the sediment were first observed (26.6 mbsf) to a TD of 186.2 mbsf. Two gas samples were collected during degassing experiments of PCS cores recovered at 56 and 190 mbsf (see "Pressure coring"). Hole U1329D, which yielded one whole-round sample for IW analysis, was extensively washed with drilling fluid and was therefore deemed unsuitable for HS analysis.

The primary objectives of the organic geochemistry sampling program at this site were to

- Determine the origin (microbial versus thermogenic) of gases recovered by HS gas, void gas, and PCS degassing techniques;
- Investigate the fate of methane near the SMI; and
- Quantify the carbon and nitrogen contents in the sediments.

Hydrocarbons

Hydrocarbon measurements from Holes U1329C and U1329E HS gas samples are listed in Table **T4.** Results are reported in parts per million by volume (ppmv) of methane, ethane, ethylene, and propane in the air headspace of a 25.41 ± 0.18 mL serum vial and as the millimolar concentration of dissolved methane in the IW (see **"Organic geochemistry"** in the "Methods" chapter). The data are normalized to 3 mL sediment volumes. In Hole U1329E, methane and ethane results are plotted in Figure **F24** relative to depth. Methane content increased rapidly from just above background levels (2–37 ppmv) at 1.5–6.5 mbsf to ~16,413 ppmv at 23.5 mbsf. Below the elevated surface values and above the seismically inferred BSR (126 mbsf), HS methane ranged from ~5000 to 8000 ppmv. Below the BSR, the HS methane values decreased to a minimum value of ~1600 ppmv at 180.4 mbsf. An air sample collected from the catwalk area during Site U1329 operations had a concentration of 2.1 ppmv methane, which is slightly elevated relative to atmospheric methane concentrations (~1.7 ppmv). Because the HS vials contained atmospheric air prior to sampling, this contribution should be considered in future isotopic analysis of the HS methane. The data reported in Table **T4** are uncorrected for the atmospheric contribution.

Quantitative sampling of methane by the HS method is limited by the low solubility of methane in solution. Methane exsolution from IW caused by depressurization occurs during core recovery; an effect that may be exacerbated in deeper samples with low porosity. Low-porosity samples are compacted, which makes sampling difficult, and have a greater fraction of their sediment surface exposed to air during collection. Consequently, the apparent decrease in HS methane concentrations with depth may be a sampling artifact that does not necessarily represent in situ conditions. The concentrations reported are, therefore, minimal estimates.

Trace amounts of HS ethane were present below 12.6 mbsf (1.2 ppmv) in Hole U1329C and below 16.0 mbsf in U1329E. In Hole U1329C, HS ethane increased slightly to a mid-depth maximum of 3.6 ppmv at 108.1 mbsf. Trace levels of ethylene (≤0.8 ppmv) were also observed in this interval. Below the projected depth of the BSR (126 mbsf), the concentration of HS ethane, in general, decreased and was scattered between 0 and 4.1 ppmv until the base of the hole (186.7 mbsf), where the highest HS ethane concentration at Site U1329 was observed. Propane was only observed at the base of Hole U1329C at a concentration of 19.9 ppmv.

The composition of gas from voids in the core liner is shown in Table **T5** and concentrations of methane and ethane plotted relative to depth in Figure **F25.** The void gas was, on average, >90% methane with minimal air contamination (indicated by the concentrations of nitrogen and oxygen). Void gas samples reflect the composition of gas in the subsurface, but not the amount. The subsurface gas content is probably proportional to the general abundance and internal pressure of core voids, but it is difficult to quantify. Trace levels of *n*-butane (0.3–1.5 ppmv) and *i*-pentane (0.2–0.3 ppmv) were observed from 59.7 to 125.2 mbsf. With increasing depth to 180.8 mbsf and below the boundary that roughly coincides with the lithostratigraphic Unit II/III boundary (see **"Lithostratigraphy"**), propane and *i*-butane were first observed and the concentrations of *n*-butane and *i*-pentane increased. The sample collected at the base of the hole (Section 311-U1329C-22X-5; 186.2 mbsf) contained the highest concentrations of C_2–C_5 hydrocarbons. The complementary IW sample from this depth had the lowest salinity and dissolved chloride concentration of all samples from this site (see **"Interstitial water geochemistry"**).

Gas composition expressed as the C_1/C_2 ratios of HS gas is plotted relative to depth with the void gas and PCS data in Figure **F26.** The C_1/C_2 ratios from the HS gas samples are consistently lower than those from the void gas samples at equivalent depths. A possible explanation for the difference is that the in situ dissolved gases are preferentially enriched with ethane, but it is also possible that the difference may be caused by preferential exsolution of C_1 relative to C_2 during the formation of the gas cracks. The observation of methane enrichment in the void gas and ethane enrichment in the HS gas, which is produced from extraction of dissolved gases from solution that may have already lost some of its methane, is consistent with preferential exsolution of methane. PCS gas samples had a C_1/C_2 composition similar to the void gas data. Further research is required to conclusively understand the relationship of the offset between the C_1/C_2 ratios of the gas components. Hydrogen sulfide was absent in all void gas samples.

The routine monitoring of C_1/C_2 ratios in HS and void gas samples and its relationship to temperature was developed as a safety guideline by the Joint Oceanographic Institutions for Deep Earth Sampling

Pollution Prevention and Safety Panel during ODP. The C_1/C_2 ratios of HS and void gas samples are plotted relative to sediment temperature in Figure F27. The sediment temperature was estimated assuming the calculated geothermal gradient of 76.4°C/km (see "Physical properties"). C_1/C_2 ratios are described as either "normal" or "anomalous" depending upon where they plot relative to the slightly diagonal line. All values measured at Site U1329 were within the acceptable "normal" limits for safe drilling (Pimmel and Claypool, 2001).

The HS and void gas C_1/C_2 ratios show downhole transitions related to the lithology and, possibly, the BSR. The HS gas C_1/C_2 ratios are high in the surface sediments (15.6 mbsf, the shallowest depth of ethane occurrence) and decreased gradually throughout and slightly beyond lithostratigraphic Units I and II (see "Lithostratigraphy"). The high HS gas C_1/C_2 ratios in the surface sediments (from ~6,000 to 12,500) may be explained by production of methane in the shallow sediments (dilution of C_2) or as a sampling artifact. High-porosity sediments have a lower surface to volume ratio and, therefore, may retain more dissolved methane before they are sampled. Lower C_1/C_2 ratios (from ~1900 to 3300) above the estimated depth of the BSR (125 mbsf) reflect an increased contribution from ethane (Fig. F24), which was either produced in situ by low-temperature diagenetic reactions or by migration from a thermogenic source. The increase in the C_1/C_2 ratios below the BSR is the result of a decrease in C_2 (Figs. F25, F26). With increasing depth in lithostratigraphic Unit III, the C_1/C_2 values decreased to a minimum value of 422 at the base of Hole U1329C, which indicates a contribution from a deep thermogenic hydrocarbon source.

The void and PCS gas data followed a pattern similar to the downhole pattern of the HS gas data. The highest C_1/C_2 values (from ~15,900 to 18,100) were observed near the depth where void gas first appeared (~18,100 at 29.7 mbsf) and slightly below the BSR (~20,275 at 139.2 mbsf). With increasing depth within lithostratigraphic Unit II (see "Lithostratigraphy"), the C_1/C_2 ratios decreased to the estimated depth of the BSR. This decrease may be attributed to the dissociation of gas hydrate (because gas hydrate preferentially concentrates C_2 relative to methane [Sloan, 1998]), low-temperature diagenetic production of ethane, or an increased thermogenic gas contribution (Pimmel and Claypool, 2001). PCS gas C_1/C_2 data from 55.8 and 73.5 mbsf compared favorably with the void gas data from similar depths, although at 73.5 mbsf the PCS C_1/C_2 ratio is slightly higher.

The lowest void gas C_1/C_2 ratio from Site U1329 was measured at the base of Hole U1329C (~3900 at 186.2 mbsf). Gas collected during the degassing of PCS Core 311-U1329C-23P extended the observation of decreasing C_1/C_2 ratios with depth in lithostratigraphic Unit III to 188.5 mbsf (Table T6). The C_1/C_2 ratio of the PCS gas was 475, which was substantially lower than the void gas sample collected 2.3 m above the top of the PCS core depth. Also, the concentrations of C_2–C_5 hydrocarbon gases in the PCS sample were an order of magnitude greater than those of the void gas sample, and CO_2 was considerably higher (8,270 versus 22,247 ppmv). Salinity and chloride concentrations (22 and 380 mM, respectively) from 201.7 mbsf in Hole U1329D were also lower than values from the bottom portion of Hole U1329C (28 and 480 mM, respectively; 183.6 mbsf) (see "Interstitial water geochemistry"). The freshening of the IW was interpreted to be the result of migration of fluids from a deeper, fresh fluid source (see "Interstitial water geochemistry"). The similar pattern of rapid change in the void gas composition suggests a similar deep source for the hydrocarbon gas and CO_2. Determining the source of the dissolved hydrocarbons and associated fluids is a subject for further investigation.

Biogeochemical processes

The sulfate concentration profiles established the base of the sulfate reducing zone at 9.4 mbsf (see "Interstitial water geochemistry"). The IW sulfate data are plotted with the dissolved methane concentrations in Figure F28 to illustrate the relationship between the reduction of sulfate and the anaerobic oxidation of methane (AOM). The concentrations of sulfate and methane at the SMI were both 0.2 mM. At sediment depths above (7.9 mbsf) and below (11.0 mbsf) the SMI, the concentration of methane or sulfate were near or below the limit of analytical detection and are presumed to be insufficient for supporting the AOM. Delineating the processes occurring within this biogeochemically active region can only be achieved with high-resolution sampling and postcruise stable carbon isotope analysis of the various carbon phases.

Sediment carbon and nitrogen composition

The sediment IC, $CaCO_3$, TC, TOC, and TN concentrations and C/N ratios from Hole U1329C are listed in Table T7 and plotted relative to depth in Figure F29. IC was relatively low with 48 of 51 samples containing <1 wt% IC and an average IC of 0.48 wt%. The variability reflects primary changes in biogenic and authigenic carbonate. The samples that contained elevated carbonate were concentrated near the depth of the AOM-generated alkalinity peak at 17.8 mbsf (see "Interstitial water geochemistry")

and from 69.9 to 74.4 mbsf. TOC ranged from 0.1 to 1.7 wt% (average = 0.8 wt%) and TN ranged from 0.03 to 0.17 wt% (average = 0.08 wt%) (Table T7; Fig. F28). Lithostratigraphic Unit I (see "Lithostratigraphy") had the lowest TOC (average = 0.52 wt%) and TN (average = 0.06 wt%) values, although it is notable that a distinct peak in TOC (1.14 wt%) and TN (0.12 wt%) concentrations occurred near the SMI, a region where methane is converted to microbial biomass. Maximum TOC and TN concentrations occurred at 119.4 to 123.9 mbsf, which is near the projected depth of the BSR. Beyond the high concentrations observed near the projected BSR, TOC and TN contents displayed no apparent trend with depth in lithostratigraphic Units II and III (TOC = 0.93 wt% and TN = 0.10 wt%). Based on the C/N ratios, which averaged ~10.0 and showed no apparent trend with depth, organic matter in the sediment has a predominately marine origin with some terrestrial influence.

Microbiology

Site U1329 is located on the northeastern end of a transect of sites across the northern Cascadia accretionary prism. The goals of the microbiological sampling program and study were to identify the subsurface spatial distribution of optimal microbial activity and growth of methanogens and to elucidate how methanogenesis contributes to the formation of gas hydrate at the northern Cascadia margin. Within this subsurface zone of optimal microbial activity, measurements of methane production rate and organic compounds used for methane production should correlate with the biomass determined from direct cell counts and microbial community analysis. It is also a goal of this effort to cultivate and characterize the anaerobic methane oxidizing community in sediments where bacterial sulfate reduction and methane oxidation are coupled and high concentrations of gas hydrate exists. This expedition gives the opportunity to explore piezophilic, aerobic (heterotrophs), and anaerobic (sulfate reducers) microorganisms. Most of the shipboard effort was devoted to developing and implementing a sampling program to meet the goals of the program and to begin the cultivation of the high pressure–adapted microorganisms. However, most of the analyses needed to achieve these goals will be performed postcruise.

Microbiological sampling

Site U1329 was the first site sampled for microbiology during Expedition 311, and the samples taken and methods used reflect our learning process. Sampling from the mudline (Core 311-U1329C-1H-1, 0–10 cm) and the deepest core (Core 22X-4, 95–105 cm) in Hole U1329C targeted microorganisms for aerobic and anaerobic high-pressure culturing. Sampling in the upper sediment layers of Holes U1329D and U1329E targeted the SMI, where microbial consumption of methane peaks. Anaerobic oxidation of methane using sulfate as the electron acceptor has been the focus of several recent studies (Boetius et al., 2000; Orphan et al., 2002; Michaelis et al., 2002; Zhang et al., 2002) and is a major focus for the microbiology program of Expedition 311. Hole U1329C was first completed as a continuous, deep hole and, once the sulfate and methane data had been examined, the SMI was targeted for intensive, coupled microbiological and geochemical sampling in both Holes U1329D and U1329E (see "Interstitial water geochemistry" and "Organic geochemistry").

Methanogenesis can exist in most anaerobic environments, but it becomes the major process when other electron donors such as nitrate, Fe(III), and sulfate are depleted. We sampled regularly downhole to below the depth of the BSR to quantify methanogenesis in these sediments. In postcruise experiments, we will examine the correlation among the rates of methanogenesis, direct cell counts, phylogenetic analysis, geochemical analyses of methane gas concentrations, and IW chemistry. Samples were prepared for shore-based experiments in which sediments will be heated to in situ temperatures for measuring total methane production and estimating organic compounds utilized in methanogenesis.

The emphasis in sample processing was to work as quickly as possible without compromising microbiological integrity of the samples by maintaining samples at or below in situ formation temperatures and minimizing exposure to oxygen. Cores were kept at 4°C and left undisturbed in core liners until processed. The processing of samples from Hole U1329C was conducted in the Hold Deck reefer on the *JOIDES Resolution*.

Contamination tests

Perfluorocarbon tracers

Samples for perfluorocarbon tracer (PFT) and microsphere analyses were taken from the whole-round cores in the reefer. Each of the analyzed cores had ~5 cm^3 subsamples taken from outer and inner layers for gas chromatograph analysis as described in "Microbiology" in the "Methods" chapter. Samples were analyzed as described and the raw data are presented in Table T8. We found that the reefer contained high PFT levels (0.15 ng PFT/mL air). This might lead to false positive PFT concentrations for samples processed in the reefer.

Fluorescent microspheres

Comparison of paired samples collected from the edges and centers of cores by fluorescent microsphere penetration are summarized in Table T7. Microscopic analysis of the outer portions of cores showed detectable numbers of microspheres of 10^4 spheres/g of sediment, whereas microspheres were below the detection limit of 100 spheres/g in samples taken from core interiors.

Shipboard analysis

Samples were taken from the top (Sample 311-U1329C-1H-1, 0–10 cm) and bottom (Sample 22X-4, 95–105 cm; 184.35 mbsf) of Hole U1329C for inoculation of enrichment cultures targeting high pressure–adapted heterotrophic and sulfate-reducing microorganisms. Samples were maintained at low temperature, and dilution series were inoculated to culture for microorganisms at 55.1 MPa and 4°C. Only the sulfate reducers required preparation in the anaerobic chamber and were fed formate, acetate, or lactate as a carbon source. Because interpretation of the SMI at Site U1329 was unclear, methanogenic enrichments were postponed until the next site (U1327).

Physical properties

Site U1329 is the most landward site in the Expedition 311 transect across the accretionary margin. Seismic data suggest the presence of slope basin sediments that lap onto older, uplifted accretionary complex material. Seismic indicators of gas hydrate are present but more subdued than at all of the other sites. Physical properties were measured in cores recovered from Holes U1329B, U1329C, U1329D, and U1329E. Hole U1329B missed the mudline and contained only one core. Hole U1329C extended to 180 mbsf. The maximum depth of sampling was extended to 210 mbsf in Hole U1329D. Hole U1329E was dedicated to special tools. Figure F30 presents an overview of the physical property data obtained at this site. All cores from this site were systematically scanned as soon as they arrived on the catwalk to detect IR anomalies indicative of gas hydrate dissociation during core recovery.

Compared to other sites, Site U1329 is notable for the very low magnetic susceptibility of the sediments in all but the uppermost ~10 m. This very restricted zone of relatively high magnetic susceptibility was valuable for correlating the shallow cores collected from different holes. It also differs from the other sites in that no gas hydrate IR thermal anomalies were observed and because density and porosity are nearly constant over most of the depth range sampled.

Infrared images

All cores were scanned on the catwalk following the track-mounted IR camera procedures described in "Physical properties" in the "Methods" chapter. Portable Document Format images of the scans of all cores are available in the "Site U1329 core descriptions." Only minor cold anomalies were detected in the cores from this site (Fig. F31), consistent with evidence for only minor amounts of gas hydrate based on LWD resistivity measurements (see "Downhole logging") and chlorinity analyses (see "Interstitial water geochemistry"). Figure F32A shows the downhole temperature plot for Hole U1329C. A detailed plot from 38 to 45 mbsf shows the most distinct anomaly at ~41 mbsf. The ΔT for this anomaly is small at ~0.8°C. The overall downhole temperature trend is broadly consistent with increasing in situ temperature with depth and with the XCB cores typically exhibiting cooler temperatures than APC cores. Subtle cooling caused by small amounts of disseminated gas hydrate cannot be ruled out and will be assessed postcruise.

IR images of the cut ends of selected sections were acquired with a handheld IR camera. Figure F33 shows a typical IR image of a section end from Hole U1329C, with a plot of the associated cross-core temperature profile. The IR images of section ends were also checked for unusually cold centers that might indicate the dissociation of gas hydrate. No such features were observed.

IR images were typically made of the cut ends of sections identified for microbiological sampling and provided a measurement of the temperature profile through the cores just prior to removing them to the microbiology sampling area, which was maintained at 4°C. These images provide constraints on the maximum temperature to which the microbiology samples were exposed. For example, the core imaged in Figure F33 originated at a depth of 44.10 mbsf and a temperature of 6.5°C (see "In situ temperature profile"). The temperature had warmed to 10.1°C at the center of the core and ~12°C at the edges by the time the core reached the catwalk. These temperature estimates are based on an IR emissivity of ~0.89 for wet sediment and are corrected for ambient temperature at the time the IR images were collected.

Sediment density and porosity

Gamma ray attenuation (GRA) densities were measured on the multisensor track (MST), and bulk density, grain density, and porosity were calculated from

the measured wet and dry weights and dry volume of the sediments (moisture and density [MAD] measurements; Table T9). Both estimates of density were compared to in situ densities measured by the LWD/MWD tools (Fig. F30). These three different estimates of density were very similar, with a few notable exceptions. We note the remarkable correspondence between the MAD and GRA density measurements, particularly when outlying low GRA density data caused by the presence of cracks and voids are ignored.

The MAD, GRA, and LWD/MWD densities show a gradual increase in the uppermost 10 m, below which the average density is approximately constant to at least 125 mbsf (Fig. F34A). This unusual density and porosity profile (Fig. F34B, F34C), which suggests underconsolidation of the sediments through most of the cored interval (see "Shear strength"), contrasts with porosity profiles observed at all other sites (see Fig. F37 in the "Site U1325" chapter).

From 170 to 190 mbsf, porosity values determined from MAD data do not decrease as smoothly as the rapidly decreasing porosity values determined for this interval from the LWD data (Fig. F34B). This anomalous behavior is likely an artifact of drilling disruption in the MAD measurements. Although the transition from APC to XCB coring occurred at Core 311-U1329C-18X (140.68 mbsf), a distinct increase in biscuiting and intrusion of drilling mud occurred at Core 22X (198.90 mbsf), as shown in Figure F34D. We speculate that a transition from ductile to brittle behavior occurred as a result of increased lithification at 170 mbsf and that Cores 311-U1329C-21X and 22X (170–189 mbsf) shattered in response to drilling.

Below 185 mbsf, density increases abruptly and LWD and MAD porosity decreases to 10% and 30%, respectively. We note that only two highly disturbed cores (Cores 311-U1329C-23P and 311-U1329E-21X) were recovered from this zone. Core 311-U1329C-23P contained numerous hard clasts that were not included in the MAD analysis; therefore, the 30% porosity obtained by analyzing the physical properties data is probably overestimated relative to the bulk formation porosity. Active migration of low-salinity fluids through this zone is suggested by IW chemistry (see "Interstitial water geochemistry"). In light of the high density and low porosity in this zone, as determined by LWD/MWD and MAD data, pervasive microcracks are unlikely here. We conclude that fluid migration occurs through this formation by macrofractures or other discrete, high-permeability structures that do not affect the index properties measured in core samples.

Magnetic susceptibility

The magnetic susceptibility at this site is relatively high in the uppermost 10 m but then decreases precipitously and remains low for the remainder of the cored interval (Fig. F30). Moreover, the pattern within the zone of high susceptibility is very consistent between holes, allowing us to determine accurate relative depths between the holes and enabling more detailed interpretation of shallow chemical and biological processes. This correlation is shown in Figure F35. We note that the relative depth shifts between holes indicated by the magnetic susceptibility data have not been applied to the tabulated data that accompany this report or to data included in the Janus database. They should, however, be taken into account for detailed comparisons between holes.

Compressional wave velocity from the multisensor track and Hamilton Frame

P-wave velocity was measured using the Hamilton frame and MST on shallow cores from Holes U1329B, U1329C, and U1329E (Table T10). MST velocity measurements, made at 2.5 cm intervals, from Cores 311-U1329B-1H, 311-U1329C-1H, 311-U1329E-1H, and 2H (Sections 1–3) are shown in Figure F36. The MST did not yield good results at greater depth because of pervasive gas expansion cracks in the sediment. *P*-wave velocity measurements were also made in all three directions using the Hamilton frame. Values were obtained for Sections 311-U1329B-1H-1 through 1H-4, Core 311-U1329C-1H through Section 2H-2, and Sections 311-U1329E-1H-1 through 1H-3. Velocities were obtained in the x-direction from slightly greater depths when compared to the y- and z-directions. *P*-wave velocity ranges from 1429 to 1550 m/s.

Velocity measurements made with the Hamilton frame have generally higher values and more scatter than those made with the MST. The velocity versus depth profiles in the y- and z-directions are approximately parallel to the MST velocity profile; both show a general increase in *P*-wave velocity with depth. There are, however, intervals where velocity decreases with depth. An example can be seen in the uppermost 1 m of Core 311-U1329E-1H (Fig. F36), where MST velocity drops linearly from 1490 to 1475 m/s. There is a fairly good correlation between the density and velocity profiles, which may explain the local decreases in velocity with depth.

Shear strength

Shear strength measurements were made routinely throughout Holes U1329B, U1329C, and U1329E us-

ing the handheld Torvane apparatus (Table T11; Fig. F37A). Measurements were made on the working half of the split core after resistivity and velocity measurements had been completed and after MAD samples had been taken. Measurements were taken in areas of the core where the sediment was undisturbed and as close as possible to where MAD samples had been extracted. At least one shear strength measurement was taken per section and often more where there were visual changes in the sediments (i.e., color and grain size). Measurements made to 155 mbsf in Hole U1329C and to 33 mbsf in Hole U1329E varied between 20 and 190 kPa. Shear strength data from Holes U1329B, U1329C, and U1329E show good agreement. Shear strength increases linearly with depth as a result of compaction and cementation of the sediment. Values are scattered at depth because of drilling disturbance, especially in XCB cores, or gas expansion cracks.

The ratio of shear strength to overburden pressure is a measure of the consolidation state of the sediments (Fig. F37B). A ratio >0.25 indicates overconsolidation (Riedel et al., 2006). No overconsolidation is apparent in these sediments. We conclude that these sediments have not been eroded, in contrast to sediments at the flanks of southern Hydrate Ridge, located in the Cascadia accretionary complex offshore Oregon (Tréhu, Bohrmann, Rack, Torres, et al., 2003; Riedel et al., 2006). The apparent underconsolidation of the sediments is consistent with rapid sedimentation and very high diatom content (see "Lithostratigraphy" and "Biostratigraphy").

Electrical resistivity

Electrical resistivity was measured on core samples by both contact and noncontact methods. Although contact resistivity measurements were a part of the standard Deep Sea Drilling Project and ODP physical property measurement suite for many years, this measurement has not been routinely made during recent years. During Expedition 311, these measurements were made using a standard Wenner-type probe array provided by Randolph Enkin (Geological Survey of Canada) (Table T12). Results for both contact and noncontact resistivity are plotted in Figure F30, where they are compared with the LWD ring resistivity. Contact resistivity and noncontact resisitivity are also plotted versus depth in Figure F38A and F38B, respectively. The contact resistivity measurements show structure that is similar to the LWD ring resistivity, except that contact resistivity is shifted to lower values in the uppermost 20 m and to higher values below ~70 mbsf. Scatter in the contact resistivity data likely arises from variations in moisture content, cracking caused by gas expansion, and drift resulting from chemical reactions of the silver or gold electrodes with the sediment. The drift issues were largely solved for contact resistivity measurements at Sites U1325, U1326, U1327, and U1328. MST noncontact resistivity exhibits extensive scatter, with anomalously high values caused largely by the presence of cracks and voids. However, the low-resistivity envelope of measured values, which might be interpreted to represent the resistivity of undisturbed sediments, does not follow the same trend as the LWD ring resistivity, particularly in the uppermost 20 m and from ~140 to 190 mbsf (TD of Hole U1329C). Overall, the noncontact resistivity values are shifted to lower values compared to the LWD/MWD and contact resistivity measurements. Contact and noncontact resisitivity values can be used to calculate the formation factor (ratio of saturated sediment resistivity to pore fluid resistivity; Fig. F38D, F38E). Using Archie's relation, it is possible to estimate porosity independently of the MAD porosity, and results are plotted in Figure F38 for m = 1.7 and a = 1. Agreement is reasonably good for contact resisitivity–derived porosity except at 50–85 and 90–145 mbsf.

Thermal conductivity

Thermal conductivity ranges from 0.8 to 1.2 W/(m·K), with most values above 1.0 W/(m·K) (Table T13; Fig. F30). Values were corrected for in situ temperature and pressure using the equation of Pribnow et al. (2000). This correction is small for the depth range and geothermal gradient at this site (Fig. F39). No significant trend with depth is observed. Values <1.0 W/(m·K) are likely caused by gas expansion cracks producing poor contact between the sediment and the thermal conductivity probe. The average value of all measurements >1.0 W/(m·K) is 1.1 ± 0.06 (1 σ). The increase in thermal conductivity with depth proposed for this region by Davis et al. (1990) (see also "Physical properties" in the "Methods" chapter) is not observed (Fig. F39).

In situ temperature profile

The APCT16 and APC3 temperature tools were deployed three and two times, respectively, in Hole U1329C. Two APCT and two DVTP deployments were conducted in Hole U1329E (Table T14; Fig. F40). With the exception of the APCT run on Core 311-U1329C-3H, which was extracted from the sediment prematurely, the measurements are of excellent quality in Hole U1329C. Ship heave during coring in Hole U1329E led to small, secondary frictional pulses at shallower depths, although the deeper DVTP data are of excellent quality.

The data for this site are relatively well calibrated because of the controlled calibration tests performed at Oregon State University (OSU) prior to the expedition (see **"Physical properties"** in the "Methods" chapter). During the OSU test, an absolute calibration shift of +0.03°C was determined for the APC3. A shift of –0.97°C was determined for the APCT16 relative to the APC3 by examining their responses in hot- and cold-water baths on the ship. A calibration shift of ~0.9°C relative to APCT16 (~0°C relative to APCT3) was determined for the DVTP by deploying it immediately after the APCT16 and comparing the apparent in situ sediment temperatures. In situ temperatures determined by extrapolating the observations using TFIT (APCT and APC3) and CONEFIT (DVTP) are shown in Table **T14.** A thermal conductivity value of 1.0 W/(m·K) was assumed for this calculation; raising the thermal conductivity to 1.1 W/(m·K) increases the estimated in situ temperature by ~0.1°C. No extrapolation was needed for the DVTP deployed at 127.1 mbsf, which showed that equilibrium had been reached on both thermistors. It is important to note that this measurement was made right at the expected BSR, within the uncertainty of depth estimates for both the tool placement and the seismic data (Fig. **F41**).

The data indicate a thermal gradient of 72 ± 4°C/km, significantly higher than the thermal gradient of 54°C/km obtained at ODP Site 889 (Westbrook, Carson, Musgrave, et al., 1994) but consistent with the regional heat flow (Hyndman and Wang, 1993). The seafloor intercept is 3.34°C ± 0.34°C, consistent with regional hydrographic data. The measurement uncertainty implied by the data misfit is 0.27°C, consistent with our estimate of the total uncertainty in the data resulting from uncertainties in measurement, calibration, and thermal conductivity. Figure **F41** shows the geothermal gradient compared to the predicted gas hydrate stability boundary for pure methane hydrate and freshwater (0%), seawater (3.5%), and saline brine (10%). The depth of the base of gas hydrate stability inferred from seismic data (~126 mbsf) corresponds very well to the depth predicted from the geothermal gradient obtained from in situ temperature measurements.

Paleomagnetism

Note: This section was contributed by Jennifer Henderson and Katerina Petronotis (Integrated Ocean Drilling Program, Texas A&M University, 1000 Discovery Drive, College Station TX 77845, USA).

Alternating-field (AF) demagnetization of the sedimentary archive-half sections was used to determine the remanent magnetization components recorded in the recovered core (Fig. **F42**). The paleomagnetic data will be used postcruise to characterize the magnetic properties of the sediments and to construct a magnetostratigraphy of the sedimentary section recovered at Site U1329. The AF demagnetization applied at 10 and 20 mT should have removed most of the drill string magnetic overprint, but postcruise demagnetization at higher fields will most likely be required.

Questionable data may be associated with remanence measurements over intervals disturbed or deformed by coring. Similarly, magnetic edge effects, which can be large when measurements are within ~5 cm of the edge of a section or edge of a void, can give biased results. To avoid interpreting results in these regions, we manually noted the disturbed intervals and voids in the cores. Data from these intervals will be removed prior to postcruise interpretation.

Pressure coring

The main objectives of pressure coring during Expedition 311 were to quantify natural gas composition and concentration in sediments and to determine the nature and distribution of gas hydrate and free gas within the sediment matrix. To achieve these objectives, we

- Measured the quantity and composition of gases released during controlled degassing experiments,
- Conducted nondestructive measurements (X-ray imaging, *P*-wave velocity, gamma ray density) at in situ pressure and during degassing, and
- Preserved gas hydrate–bearing sediments at in situ pressure for more comprehensive shore-based investigations.

The nondestructive measurements not only provide a direct indication of the existence of gas hydrate, but the resulting data (acoustic impedance) can be used to help interpret regional seismic data. Site U1329 was expected to be at the eastern limit of gas hydrate occurrence on the northern Cascadia margin, based on seismic evidence. A specific objective at this site was to confirm or disprove the presence of gas hydrate in the gas hydrate stability zone (GHSZ) and the occurrence of free gas beneath the BSR. Site U1329 had a relatively weak BSR estimated at 126 mbsf, but high resistivity values in the LWD logs from Hole U1329A (Fig. **F59**) suggested the presence of free gas at 145–165 mbsf.

Operation of pressure coring systems

Pressure coring tools were deployed eight times at Site U1329: six PCS cores for shipboard degassing ex-

periments and one HRC and one FPC core for both shipboard analyses and for archiving cores at in situ pressure (Table T15). Figure F43 shows the pressure history of the cores during deployment, coring, recovery, and chilling in the ice shuck. Pressure cores rarely retain full in situ pressure for various reasons (see "Pressure coring" in the "Methods" chapter) and can stray across the gas hydrate stability boundary when warming during tool recovery and handling (Fig. F44). The ice water–filled shuck kept this warming to a minimum, but cores recovered far below in situ pressure (e.g., Core 311-U1329C-7P) spend as much as 20 min outside the gas hydrate stability field before reentering gas hydrate stability conditions.

The PCS deployment that recovered Core 311-U1329C-23P was particularly unusual. This was the only pressure core deployment well below the depth of the BSR. The coring lasted over an hour. During the protracted coring operation, a low-pressure event was recorded that lasted >10 min (Fig. F43). When the corer was retrieved, we discovered that the bit had sheared off in the formation, damaging the aluminum outer barrel beyond repair and ending operations in Hole U1329C. In spite of this, a core was recovered, though it was at very low pressure (350 kPa).

The deployment of HRC Core 311-U1329E-9E (Fig. F44) shows the value of immediately cooling the tool in the ice shuck after recovery at the rig floor. The autoclave was not recovered under full in situ pressure. Water had filled the pressure accumulator, which is designed to buffer the pressure inside the core from changes in tool volume (see "Pressure coring" in the "Methods" chapter). As the core warmed on recovery, it approached the gas hydrate stability boundary but quickly moved away from this boundary as it chilled in the ice shuck. After shipboard analyses were complete, the HRC core was stored in seawater at 10 MPa in a pressurized storage chamber for further shore-based studies (see "Pressure coring" in the "Methods" chapter). The FPC deployment at this site recovered a good core (Core 311-U1329E-8Y), but the inner rod overretracted and the core was not recovered at pressure.

Degassing experiments

At Site U1329, the four PCS cores that were successfully recovered under pressure were investigated by controlled shipboard degassing experiments. These cores represent sediments both above (Cores 311-U1329C-7P, 311-U1329E-7P, and 10P) and below (Core 311-U1329C-23P) the BSR (Table T16). The main objectives were to

- Determine the concentration and composition of natural gases,
- Identify the presence or absence and concentration of gas hydrate within the GHSZ, and
- Constrain the presence of free gas below the BSR.

The pressure readings for the recovered PCS cores were all below predicted gas hydrate stability conditions at the temperature of the laboratory (7°C); therefore, no pressure plateaus or rebounds from dissociation of gas hydrate could be expected.

All degassing experiments included the following steps. First, the volume and density of sediment inside the inner core barrel of the PCS was monitored by X-ray analysis. Next, the PCS was slowly degassed in a temperature-controlled van (7°C), and the volume and composition of released gas and water, the pressure inside the core, and the ambient air pressure and temperature were monitored (Table T17) as described in "Pressure coring" in the "Methods" chapter. During the degassing procedure, the vertical density distribution of the PCS cores was repeatedly determined by GRA scans to examine the evolution of gas voids within the sediment. As a result of a failure of the digital pressure recorder, however, no pressure readings are available for the degassing of Core 311-U1329C-7P. After degassing was completed, PCS cores were X-rayed again. Starting with Core 311-1329C-23P, we collected the water remaining in the outer core barrel for mass balance considerations and subsampled the sediment that was extruded from the cores for IW chemistry, dissolved gases, and physical property analyses.

Degassing the four PCS cores from Site U1329 showed variable gas concentrations and compositions with depth (Table T17). Mass balance calculations indicate little, if any, gas hydrate within the GHSZ but yielded evidence of free gas beneath the depth of the BSR (Tables T18, T19; Fig. F45).

PCS Cores 311-U1329C-7P (55.6 mbsf) and 311-U1329E-7P (73.5 mbsf), taken within the predicted depth of the GHSZ, yielded 1.49 and 1.62 L of gas, respectively. The composition of the released gas did not change significantly in the course of degassing. Methane was the major component, accounting on average for 69% ± 4% of the gas emitted from Core 311-U1329C-7P and 78% ± 3% of the gas released from Core 311-U1329E-7P. In both cores, nitrogen was the second most abundant gas, contributing 19% ± 2% and 17% ± 3%, respectively. Carbon dioxide, ethane, and higher hydrocarbon gases were below the detection limit of the Agilent gas chromatograph (GC) used for continuous gas analysis during the degassing experiments. A subset of gas samples

was analyzed using methods described in **"Organic geochemistry"** in the "Methods" chapter and yielded average ethane concentrations of 34 and 32 ppmv and C_1/C_2 ratios >15,500.

Based on the methane mass balance analysis (see **"Pressure coring"** in the "Methods" chapter), the methane concentration within the pore space of the sediment is 69 mM for Core 311-U1329C-7P and 76 mM for Core 311-U1329E-7P (Table **T19**). Under in situ pressure, temperature, and salinity conditions, methane was slightly oversaturated, but the nondissolved methane would have filled <1% of the pore space as gas hydrate. Repeated density scans showed a few gas cracks developing during the degassing and an overall decrease in sediment density (Fig. **F46**). The X-ray scans did not reveal heterogeneity in the sediment except for a zone of what appeared to be disturbed core at 27–47 cm core depth in Core 311-U1329E-7P. A large gas crack developed in this zone of presumed disturbance.

PCS Core 311-U1329E-10P (125.0 mbsf), from near the base of the predicted GHSZ, yielded 1.89 L of gas. Throughout the degassing procedure, methane accounted for 91% ± 7% of the released gas and nitrogen amounted to 8% ± 5%. Carbon dioxide, ethane, and higher hydrocarbon gases were below the detection limit of the Agilent GC (Table **T17**). The released amount of methane corresponds to a pore space concentration of 92 mM, which falls near the value for a methane-saturated pore water at this depth with no gas hydrate or free gas. The uniform expansion of the core in the density scans (Fig. **F47**) supports this conclusion. The X-ray scan before degassing showed some inhomogeneity in the core, but none of the lower density regions between 5 and 25 cm developed gas cracks during degassing; therefore, we do not consider these regions to be gas hydrate related.

The deepest PCS core (Core 311-U1329C-23P; 188.5 mbsf) was taken at a considerable depth below the base of the GHSZ. The 4.19 L of gas obtained represent by far the highest gas yield at this site. At the same time, the composition of gas differs distinctly from that obtained from the three cores taken above the BSR. High methane concentrations (88% ± 5%) were accompanied by carbon dioxide (6% ± 0.3%) and ethane (0.2% ± 0.01%) (Table **T17**). The resulting C_1/C_2 ratio of 463 indicates a thermogenic origin for the gas. Assuming that all of the methane originated from the captured core, the total amount of methane inside the core corresponds to 236 mM in the pore space, which equates to a free gas concentration of 2.5% of pore volume. Unlike the other cores from this site, the core pressure did not decrease steadily in the course of the degassing experiment but stayed at a constant level of 0.22 MPa while the first 1.75 L of gas was released (Fig. **F46**). Densities did not decrease much during degassing, but some minor shifting of the rocks and clasts seen in the X-ray scan (Fig. **F47B**) is evident in the lower half of the core. It is noteworthy that the large yield of gas coincided with a very large headspace volume in the outer core barrel (1.67 L).

Measurements on HYACINTH cores

Core 311-U1329E-9E was recovered with 8 MPa pressure and was returned to 10 MPa (near in situ pressure) during the transfer into the Geotek pressure multisensor core logger (MSCL-P). Simultaneous and automated gamma ray density, *P*-wave velocity, and X-ray measurements were made in the MSCL-P system. The velocity and density profiles are shown next to the X-ray image in Figure **F48.** Two high-velocity zones can be seen at 18–28 cm (velocities up to 1630 m/s) and 73–84 cm (velocities up to 1730 m/s). These zones were associated with small density lows, deviating from the norm by <0.05 g/cm^3. These low-density layers were also clearly visible on the X-ray images but could not be distinguished by the X-rays alone from other low-density zones in the same core.

The distinctive nature of the two high-velocity zones is illustrated in a plot of gamma ray density versus *P*-wave velocity (Fig. **F49**). Gamma ray density and *P*-wave velocity in these two high-velocity zones are not correlated, whereas the other subtle variations in velocity and density throughout the core show a positive correlation of increasing velocity with increasing density. This trend is similar to that found in the measurements made on APC and XCB cores from this site (see **"Physical properties"**). The high-velocity zones fall well outside the normal trend for ocean sediments, and we interpret this anomaly as being indicative of the presence of gas hydrate. X-ray images and gamma ray density profiles show that these zones do not contain any veins, nodules, or other massive gas hydrate, so any gas hydrate in these zones is distributed at a small scale.

Core 311-U1329E-9E was transported to the Pacific Geoscience Center, Sidney, British Columbia, after Expedition 311 and was slowly depressurized under controlled conditions in a 4°C cold van. We followed the degassing procedures used during Expedition 311. Core 311-U1329E-9E released 7.9 L of gas (7.7 L of methane), equivalent to 1%–2% of gas hydrate in pore space. The gas released was ~99% methane, with a trace (~200 ppmv) of ethane.

A typical plot of gas released versus pressure shows no pressure recovery (see "Released gas" on Fig. **F50**). However, if the gas inside the storage chamber (see "Calculated gas inside SC" on Fig. **F50**) is estimated using the volume of expelled fluid and the pressure

inside the storage chamber, a pressure recovery is seen at ~3.0 MPa (see "Total gas" on Fig. **F50**). This pressure is lower than the expected pressure of methane hydrate stability at 4°C (~4.4 MPa).

Multiple gamma ray density profiles were collected during depressurization of the core while it was in the HYACINTH storage chamber (Fig. **F51**). The bulk of the core showed no expansion. Gas was released from two zones in the sediment and collected at the top of the core over time, eventually forcing sediment out of the storage chamber. The two zones that evolved gas correspond to the two higher velocity zones (Fig. **F48**), confirming that these zones contained gas hydrate. If all the excess methane contained in the core had come from within these two zones (15 and 10 cm thick, respectively) the gas hydrate concentration within the zones would have been 5%–10%, depending on the porosity. The remaining core was subsampled for further study.

The small decrease in density associated with these zones, if solely attributed to replacement of pore water by gas hydrate, would have required 40% of the pore space to be filled with gas hydrate. The gas hydrate may have inhabited layers that are intrinsically low in density, and the gas hydrate itself may have contributed little to the density anomaly. Alternatively, the formation of gas hydrate in silty clays could cause the sediment matrix to expand and hence lower the overall matrix density. Such "gas hydrate microheave" could be a precursor to the formation of massive gas hydrate veins, which have been observed elsewhere in silty clays (ODP Leg 204) and which must have forced the sediments apart. The lithology of these zones should be carefully examined in an effort to understand the nature of these gas hydrate zones in fine-grained sediments.

Gas hydrate concentration, nature, and distribution

Based on mass balance calculations from degassing experiments, Site U1329 may have contained a very small amount (<0.1%) of methane hydrate in the sediment column (Table **T19;** Fig. **F46**), with an isolated example of thin sediment layers containing 5%–10% gas hydrate by pore volume. Near the base of the GHSZ, the methane concentration drops below methane solubility and a gas hydrate phase is not present. This result agrees with the seismic evidence that this site represents the eastern extent of gas hydrate occurrence on the northern Cascadia margin. However, the methane concentration measured well below the GHSZ indicates the presence of free gas.

The low estimates of gas hydrate concentration from degassing experiments at Site U1329 are consistent with the distributed nature of gas release from the PCS, with the resistivity-derived water saturation near 100% (see **"Gas hydrate and free gas occurrence"**), and with the lack of IR anomalies (see **"Infrared images"**) or chlorinity anomalies (see **"Salinity and chlorinity"**). Gas hydrate concentrations equivalent to <0.5% of pore volume would likely be undetectable by IR imaging or IW chlorinity analyses.

Although these integrated measures of gas hydrate indicate concentrations near detection limits, Core 311-U1329E-9E (114 mbsf) contains evidence for disseminated gas hydrate at concentrations of 5%–10% within 10 cm thick, low-density, high-velocity layers. The depth of this core falls within a zone of potential gas hydrate as calculated from resistivity-derived water saturation (112–120 mbsf; see **"Gas hydrate and free gas occurrence"**). No similar layers of gas hydrate were observed in any of the IR images of APC and XCB cores.

The single PCS core from below the GHSZ (Core 311-U1329C-23P) had a distinctly complex history (see **"Operation of pressure coring systems"** and **"Measurements on HYACINTH cores"**), given the significance of the results from this core. The calculation of free gas percentage in Table **T19** assumes that during degassing all methane is released from the sediment enclosed in the PCS core. The methane contained within the outer barrel of Core 311-U1329C-23P must have come from the formation but did not necessarily all derive from the recovered sediment core. An alternate explanation for the source of this gas comes from the low-pressure event recorded during the coring operation, which indicated to the drilling crew a gas release from the formation. If a mere 15 mL of free gas had been captured in the PCS outer barrel at core depth, this could account for the 1.67 L of gas found in the outer core barrel after depressurization. Although a gas release event does not change the conclusion that free gas exists below the BSR at Site U1329, such an event would render the Core 311-U1329C-23P results qualitative rather than quantitative.

Downhole logging

Logging while drilling

Operations

LWD operations in Hole U1329A began with rigging up of the BHA at the rig floor at 1100 h on 25 September 2005. LWD tools included the GeoVISION resistivity tool, the EcoScope tool, the SonicVision tool, the TeleScope MWD tool, and the ProVISION

nuclear magnetic resonance tool. Because the EcoScope tool had been running well in the previous four holes and was collecting essentially the same data as the ADNVISION tool, we decided not to use the ADNVISION tool to save time and to spare one more manipulation of a radioactive source. For details on each tool and the measurements it collects, see **"Downhole logging"** in the "Methods" chapter. Hole U1329A was spudded at 1840 h at 970 mbrf water depth (drillers depth). Similar to the other sites, the first 6 m was drilled with a rotation rate of 10–15 rpm, a pump flow rate of 100 gallons per minute (gpm), and a rate of penetration (ROP) of 10–15 m/h. We then increased these rates to 40 rpm and 220 gpm until 30 mbsf, and then again to 60 rpm and 270 gpm (to start the MWD telemetry), keeping the instantaneous ROP below 50 m/h with depth. The deepest part of the hole proved to be surprisingly hard to drill, with a significant increase in resistivity at 1140 mbrf raising concern for the presence of free gas. Because the density was increasing as well, the annulus pressure was stable, and the sonic waveform coherence was strong, it was concluded that the change in resistivity was controlled by the lithology, and drilling proceeded, although very slowly, for the last few meters. The target depth of 220 mbsf (1190 mbrf) was reached at 0805 h on 26 September. The drill string and tools were brought back to the surface. Final rig down started at 1100 h and was completed by 1330 h. All data were downloaded and the rig floor cleared by 1430 h on 26 September.

Gas monitoring with real time logging-while-drilling/measurement-while-drilling data

The LWD logs were acquired to plan coring and pressure coring operations in subsequent holes at Site U1329. As Hole U1329A was drilled without coring, the LWD data had to be monitored for safety reasons to detect gas entering the borehole. As explained in **"Downhole logging"** in the "Methods" chapter, the primary measurement we used in gas monitoring was annular pressure while drilling measured by the EcoScope tool in the borehole annulus, the space between the drill string and the borehole wall. We looked for sudden decreases of >100 pounds psi in the annular pressure, which could be caused by low-density gas entering the borehole. We also monitored pressure increases of the same magnitude, which could be the result of fluid acceleration caused by a gas kick (Aldred et al., 1998).

Figure **F52** shows the measured borehole fluid pressure profile in Hole U1329A after subtraction of the best-fit linear trend. The borehole fluid pressure increases by a maximum of ~200 kPa (~29 psi) over the general trend at a depth of ~200 mbsf. As noted earlier, this interval was hard to drill, and the logs show sediments of high density, low porosity, and high resistivity. The observed increase in the drilling fluid pressure is probably caused by an increase in pumping rates during drilling or to the cuttings restricting flow in the annulus. The borehole fluid pressure anomalies observed in Hole U1329A were well below the 100 psi level that required preventive action. Moreover, the sonic waveform coherence image in Figure **F52** does not indicate any loss of coherence that could be attributed to free gas.

Logging quality

Figure **F52** also shows the quality control logs for Hole U1329A. Except for a short excursion to ~70 m/h at ~140 mbsf, the ROP was generally 40 m/h or less in the interval from the seafloor to TD. This is sufficient to record one measurement every 4 cm (~25 measurements per meter) in the GeoVISION resistivity, and no significant resolution loss was observed with variation in ROP. The ultrasonic caliper log, which is a direct measurement of the borehole diameter recorded by the EcoScope tool, is our best indicator of borehole size. Most of the hole had a diameter slightly larger than 10 inches (25 cm), with larger washouts up to 12 inches (30 cm) restricted to the uppermost 30 m of the hole. The density correction, calculated from the difference between the short- and long-spaced density measurements, generally varies from 0 to 0.2 g/cm^3 (Fig. **F52**), showing the good quality of the density measurements. Larger corrections (>0.25 g/cm^3) are only seen in the uppermost 30 m of the hole and between 200 mbsf and TD. Figure **F53** is a summary of the main LWD logs with density and porosity measurements from cores from Holes U1329C and U1329E superimposed (see **"Physical properties"**).

The depth relative to the seafloor was fixed for all LWD logs by identifying the step change in the gamma ray log associated with the seafloor. For Hole U1329A, the gamma ray logging pick for the seafloor was at a depth of 964 mbrf. This pick turned out to be deeper by 8 m than the wireline pick in Hole U1329D (956 mbrf). Because the wireline gamma ray log showed the seafloor more clearly, we corrected the reference seafloor depth for all LWD logs to 956 mbrf.

Wireline logging

Operations

Wireline logging was conducted in Hole U1329D, which had been drilled as a dedicated hole for logging, except for one XCB core that was taken in the lowermost 10 m to reach the target depth of 210.5

mbsf. During the previous day and night, time was spent waiting on weather, which was unsafe for any drilling or logging operations. At the start of logging operations at 1215 h on 30 September 2005, the ship's heave was still ~3 m. The hole was displaced with a barite and sepiolite mud mixture, and after the wireline was spooled, rigging of the tool string for the first run was completed by 1400 h. Wireline logging operations began with the deployment of the triple combo tool string (resistivity, density, and porosity measurements), which consists of the Hostile Environment Gamma Ray Sonde, the phasor Dual Induction Tool, the Hostile Environment Litho-Density Tool, the Accelerator Porosity Sonde, and the Lamont-Doherty Earth Observatory (LDEO) high-resolution Temperature/Acceleration/Pressure (TAP) tool. For details on the different tools, see **"Downhole logging"** in the "Methods" chapter. The tool string went down without difficulty, and TD (1166 mbrf; 210 mbsf) was reached at 1535 h. When the wireline heave compensator was activated before starting to log up, the recorded heave was still 3 m. Logging uphole occurred without problem despite two tight spots at 1144 and 1128 mbrf (188 and 172 mbsf), with caliper readings of ~6 inches (15 cm). The first pass was finished at 1635 h when we logged the seafloor at 956 mbrf. Because of the enlarged hole condition, it was agreed not to run a second pass, and the tool was brought back to the surface. Rig down was completed by 1800 h.

For the second wireline run, we deployed the FMS-sonic tool string, which consists of the FMS, the General Purpose Inclinometer Tool, the Scintillation Gamma Ray Tool, and the Dipole Sonic Imager. We reached TD (1166 mbrf; 210 mbsf) without problems, and the first pass started at 2005 h. We had difficulties passing the tight spot at 1128 mbrf, requiring us to close the FMS arms and to apply a tension of up to 5500 lb in order to proceed. It was decided not to go below this depth on our second pass, which recorded uphole from 1125 mbrf (169 mbsf). Difficulties in reentering the drill pipe and significant heave forced us to close the caliper arms and finish logging at 1036 mbrf (80 mbsf). The tool string was back on deck at 2235 h, and rig down was completed by 2330 h on 30 September.

Logging quality

Wireline logging data from the triple combo and FMS-sonic tool string runs are compromised to some extent by poor hole conditions (Fig. **F54**). The hole was enlarged between 129 and 172 mbsf, with the density tool caliper measuring a diameter >16 inches (41 cm) for most of this interval. Outside of this interval, the wireline log quality is generally very good. In the enlarged hole, however, several measurements were affected:

- Densities were too low.
- Porosities were too high.
- Spherically focused resisitivity log gave noisy readings at the shallow depth of investigation.
- Coherence of the sonic waveforms was reduced.
- Poor contact of the FMS pads with the borehole wall resulted in variable quality images.

Despite the enlarged hole conditions, the acoustic waveforms and slowness-time coherence projection (Fig. **F55**) show that the acoustic data are of good quality. Only limited reprocessing was required to extract reliable compressional (V_P) and shear (V_S) wave velocities. As expected in these shallow and poorly consolidated sediments, both velocities are very low, and V_P is only slightly higher than the borehole fluid velocity (~1500 m/s) over most of the logged interval. V_P and V_S increase sharply below ~180 mbsf, coinciding with similar increases in resistivity and density seen near the bottom of the hole. Above this depth, the dominant low frequency of the flexural dipole waveforms is typical of a large hole diameter (Harrison et al., 1990).

The depth relative to the seafloor for all wireline logs was fixed by identifying the step change in the gamma ray log associated with the seafloor. The gamma ray pick for the seafloor was identified at 956 mbrf for all wireline runs. As noted earlier, we used the same seafloor depth for the LWD data obtained in Hole U1329A because the seafloor gamma ray pick from the LWD run was less reliable than the wireline pick.

Logging-while-drilling and wireline logging comparison

Figure **F56** shows a comparison of LWD (Hole U1329A) and wireline (Hole U1329D) data, using the gamma ray, neutron porosity, density, and resistivity logs. In general, the LWD and wireline data match relatively well, exhibiting similar curve shapes and absolute logging values. The exception is the gamma ray log, where the LWD log gives higher readings (100 gAPI on average) than the wireline log (50 gAPI on average). Moreover, the LWD and wireline gamma ray curves have different shapes and there is no obvious correlation. The cause of this discrepancy is not fully understood; however, the wireline data are consistent with the values recorded during Leg 146.

The wireline neutron porosity and density contain several intervals where the neutron porosity readings are anomalously high and the density readings are

anomalously low compared to the LWD logs. Most of these anomalies are in the interval where Hole U1329D was enlarged (125–170 mbsf) and are probably caused by poor contact of the tool pad with the borehole wall. Finally, the resistivities measured by wireline and LWD tools are very similar.

Logging units

The logged section in Holes U1329A and U1329D can be divided into three logging units, based on obvious changes in the LWD and wireline gamma ray, density, electrical resistivity, and acoustic measurements (Figs. **F53, F54, F55, F56**).

Logging Unit 1 (0–130 mbsf) is characterized by a uniform low resistivity of ~1 Ωm (small fluctuations around this average are clearly visible on the resistivity images), uniform low densities of ~1.8 g/cm^3, and porosities between 50% and 60%. Logging Unit 1 corresponds to lithostratigraphic Units I and II (see **"Lithostratigraphy"**).

Logging Unit 2 (130–183 mbsf) is characterized by a small increase in resistivity and density compared to logging Unit 1. From the top to the bottom of logging Unit 2, resistivity increases from ~1.1 to 1.5 Ωm, and density increases from ~1.8 to 2 g/cm^3. In Hole U1329D, logging Unit 2 corresponds to an interval where the hole diameter is mostly >16 inches. The top of this unit corresponds to the bottom of lithostratigraphic Unit II, which is an unconformity separating Pleistocene from upper Miocene sediments (see **"Biostratigraphy"**).

Logging Unit 3 (183 mbsf to TD) is characterized by an abrupt increase in resistivity, density, and *P*-wave velocity. Resistivity and density keep increasing with depth, from ~3 Ωm and 2.3 g/cm^3 at the top of the unit to ~12 Ωm and 2.5 g/cm^3 at TD, indicating an increasingly consolidated formation with porosities possibly as low as 15% at TD. This unit was sampled only with Cores 311-U1329C-22X (178.9–188.5 mbsf), 23P (188.5–189.5 mbsf), and 311-U1329D-1X (201.0–210.5 mbsf; 1 m recovery). Logging Units 2 and 3 correspond to lithostratigraphic Unit III (see **"Lithostratigraphy"**).

Logging-while-drilling and wireline borehole images

The GeoVISION, ADNVISION, and EcoScope LWD tools generate high-resolution images of borehole log data. The ADNVISION and EcoScope tools produce images of density and hole radius computed on the basis of the density correction, which depends on the borehole standoff. The GeoVISION tool produces a gamma ray image and shallow, medium, and deep depth of investigation resistivity images. Finally, the wireline FMS tool produces an electrical resistivity image. The resolution of the resistivity images from the GeoVISION tool is considerably lower (5–10 cm) than the resolution of the images from the FMS (0.5 cm). The GeoVISION tool, however, provides 360° coverage of the borehole wall, whereas FMS images cover only ~30% of the borehole wall.

Figure **F57** shows some of the LWD images collected by the EcoScope and GeoVISION tools. It should be noted that the display in Figure **F57** is vertically compressed. The unwrapped images are ~90 cm wide (for an 11 inch diameter borehole), and the vertical scale is compressed by a factor of ~37:1. These high-resolution images can be used for detailed sedimentological and structural interpretations and to image gas hydrate distribution in sediments (e.g., in layers, nodules, or fractures). Gas hydrate–bearing sediments exhibit high resistivities. If the concentration of gas hydrate is very high, there may be a small decrease in density. On the other hand, high resistivities and high densities are likely to correspond to low-porosity, compacted, or carbonate-rich sediments. This is the case for the interval below 183 mbsf in Figure **F57** (logging Unit 3). There is also evidence of a thin layer containing high-resistivity and high-density streaks around 130 mbsf.

Logging porosities

Sediment porosities can be determined from analyses of recovered cores and from downhole measurements (see **"Physical properties"** and **"Downhole logging,"** both in the "Methods" chapter). Data from the LWD density and neutron logs were used to calculate sediment porosities from Hole U1329A. Core-derived physical property data, including porosities (see **"Physical properties"**), were used to both calibrate and evaluate the log-derived sediment porosities.

The LWD log–derived density measurements were used to calculate sediment porosities (ϕ) using the standard density-porosity relation

$$\phi = (\rho_g - \rho_b)/(\rho_g - \rho_w).$$

We used a constant water density (ρ_w) of 1.03 g/cm^3 and a grain/matrix density (ρ_g) of 2.73 g/cm^3, which is the average grain density measured in the core samples (see **"Physical properties"**). The density log–derived porosities range from ~60% at 15 mbsf to ~15% at 220 mbsf (Fig. **F58**).

The LWD neutron porosity log (Fig. **F58**) yielded sediment porosities ranging from an average value of ~60% at 15 mbsf to ~23% at 220 mbsf. Porosities measured by the neutron log are expected to be higher than those computed from the density log in sediments containing clay because the neutron log

essentially measures hydrogen abundance, and hydrogen in clay minerals is counted as porosity. The EcoScope neutron porosity shown in Figure F58 is the "best thermal neutron porosity," which has been corrected for the effect of clay so that it is only slightly higher than the density porosity.

The comparison of core- and LWD-derived porosities in Figure F58 reveals that the log-derived porosities agree with the core-derived values in logging Units 1 and 2 (0–183 mbsf), with the density porosities being slightly lower and the neutron porosities slightly higher than the core porosities. Porosities from the density and neutron logs, however, are systematically lower than the core-derived porosities below ~183 mbsf (logging Unit 3).

Gas hydrate and free gas occurrence

As previously discussed (see "Downhole logging" in the "Methods" chapter), the presence of gas hydrate is generally characterized by increases in measured electrical resistivities and acoustic velocities that are not accompanied by a corresponding decrease in porosity. A decrease in porosity alone in a water-saturated sediment can result in an increase in resistivity and acoustic velocity. Resistivities logged in Holes U1329A and U1329D do not show any obvious anomalies characteristic of gas hydrate (Figs. F53, F54). The presence of gas hydrate is known to increase sonic velocity and attenuation, and the absence of any significant velocity anomaly or energy dissipation in the waveforms (Fig. F55) is in agreement with the general inference of very low to no gas hydrate occurrence at this site.

To estimate the amount of gas hydrate that might be present at Site U1329, we used the Archie relation (e.g., Collett and Ladd, 2000)

$$S_w = [(a \times R_w)/(\phi^m \times R_t)]^{1/n},$$

where

- S_w = water saturation,
- a = tortuosity coefficient,
- R_w = formation water resistivity,
- ϕ = density porosity computed from the ADN-VISION enhanced resolution bulk density,
- m = cementation coefficient,
- R_t = GeoVISION high-resolution button deep average resistivity, and
- n = saturation coefficient.

Gas hydrate saturation (S_h) is the percentage of pore space in sediment occupied by gas hydrate, which is the complement of the water saturation S_w:

$$S_h = 1 - S_w.$$

The procedure followed to estimate S_w with Archie's relation is illustrated in Figure F59. We computed porosity from the density log as described above with a water density ρ_w of 1.03 g/cm³ and a grain/matrix density ρ_g of 2.73 g/cm³ (see "Physical properties").

To estimate the formation water resistivity (R_w), we first constructed a salinity versus depth function based on IW salinity measurements (see "Interstitial water geochemistry"). This salinity versus depth function consists of three linear segments fitted to the data (0–30, 30–177, and 177–226 mbsf). At every logging depth, we combined the salinity value with a formation temperature obtained from the geothermal gradient estimated from the downhole formation temperature measurements (see "In situ temperature profile"), and used the formulas of Fofonoff (1985) to obtain the corresponding value of the water resistivity R_w.

To estimate the water saturation S_w, we also need to choose values for the Archie coefficients a and m. One way to do this is to choose a logged interval where the sediments can be assumed to be water saturated and fit a and m to a plot of measured resistivity versus porosity, known as a "Pickett plot" (e.g., Doveton, 1994). In marine sediments, however, the range of porosity is relatively small and it is not possible to obtain a robust estimate of both a and m. We prefer to set a = 1, which is physically the most realistic value, because it gives a resistivity equal to the formation water resistivity when the porosity is 100%. We then compute a log of "estimated m" given by

$$m_{est} = -\log(F)/\log(\phi),$$

where $F = R_t/R_w$ is the formation factor. This m_{est} curve should give the appropriate value to be used in Archie's law in water saturated intervals and will give anomalously high values in intervals that contain hydrocarbons. A reasonable value of m = 2.5 can be chosen from the baseline trend of the m_{est} curve in Figure F59. A value of m = 2.0 might be more appropriate in logging Unit 3. Variations in the cementation exponent m have been related to changes in particle shape (Jackson et al., 1978), and therefore it is not necessarily expected to remain constant in a heterogeneous sequence of marine sediments.

The next step is to compute the resistivity R_0 predicted by Archie's equation for a water-saturated formation of a given porosity, which is given by

$$R_0 = (a \times R_w)/\phi^m.$$

Using Archie coefficients of a = 1 and m = 2.5, we computed an R_0 curve that closely follows the measured resistivity R_t, confirming that little or no gas hydrate is present at Site U1329 (Fig. F59). Finally, we computed the water saturation S_w using a satura-

tion exponent n = 2. Water saturation is ~1 throughout Site U1329 (Fig. F59).

There are two intervals that have a water saturation <100%, and therefore, suggests the possible presence of gas hydrate or gas between ~112 and 120 mbsf and between ~145 and 165 mbsf. The former interval is in the GHSZ, and a pressure core taken at ~115 mbsf does show a layer with a high *P*-wave velocity, which could indicate gas hydrate (see "Pressure coring"). The 145–165 mbsf interval is below the GHSZ, and it may contain a small amount of free gas, as gas hydrate and free gas are effectively electrical insulators, the resistivity analysis done here is applicable to both. A degassing experiment of pressure Core 311-U1329C-23P (~188 mbsf) suggests the presence of free gas (see "Pressure coring"). This pressure core is in logging Unit 3 (below 183 mbsf), which in Figure F59 shows water saturations >100%, because the predicted water-saturated resistivity R_0 is actually greater than the measured resistivity. As noted earlier, the sediments in logging Unit 3 are more consolidated or cemented than those of the shallower units and need a cementation exponent m of ~1.8 to get a consistent value of S_w. We repeated our water saturation analysis focusing on logging Unit 3 and using m = 1.8 but could not find convincing evidence for the presence of gas. If free gas is present in logging Unit 3, its saturation must be low.

Temperature data

The LDEO TAP tool was deployed on the wireline triple combo tool string in Hole U1329D (Fig. F60). During the process of coring and drilling, cold seawater is circulated in the hole, cooling the formation surrounding the borehole. Once drilling ceases, the temperature of the fluid in the borehole gradually rebounds to the in situ equilibrium formation temperature. Thus, the temperature data from the TAP tool cannot be immediately used to assess the formation temperatures. The temperature profile in Figure F60, however, reveals a few gradient changes that were caused by borehole temperature anomalies. Specifically, the sudden temperature increase at 187 mbsf during the downhole trip and the sudden decrease at 173 mbsf during the uphole trip correspond to two borehole restrictions clearly visible on the caliper log (Fig. F54). The smaller step decrease in temperature during the uphole trip at 131 mbsf is also likely to be related to a corresponding decrease in borehole radius as seen on the caliper log (Fig. F54).

References

Aldred, W., Cook, J., Bern, P., Carpenter, B., Hutchinson, M., Lovell, J., Rezmer-Cooper, I., and Leder, P.C., 1998. Using downhole annular pressure measurements to improve drilling performance. *Oilfield Rev.,* 10(4):40–55.

Boetius, A., Ravenschlag, K., Schubert, C.J., Rickert, D., Widdel, F., Gieseke, A., Amann, R., Jørgensen, B.B., Witte, U., and Pfannkuche, O., 2000. A marine microbial consortium apparently mediating the anaerobic oxidation of methane. *Nature (London, U. K.),* 407:623–626. doi:10.1038/35036572

Claypool, G.E., and Kaplan, I.R., 1974. The origin and distribution of methane in marine sediments. *In* Kaplan, I.R. (Ed.), *Natural Gases in Marine Sediments:* New York (Plenum), 99–139.

Collett, T.S., and Ladd, J., 2000. Detection of gas hydrate with downhole logs and assessment of gas hydrate concentrations (saturations) and gas volumes on the Blake Ridge with electrical resistivity log data. *In* Paull, C.K., Matsumoto, R., Wallace, P.J., and Dillon, W.P. (Eds.), *Proc. ODP, Sci. Results,* 164 [Online]. Available from World Wide Web: http://www-odp.tamu.edu/publications/164_SR/chap_19/chap_19.htm.

Collett, T.S., Riedel, M., Malone, M.J., and the Expedition 311 Project Team, 2005. Cascadia margin hydrates. *IODP Sci. Prosp.,* 311. doi:10.2204/iodp.sp.311.2005

Davis, E.E., Hyndman, R.D., and Villinger, H., 1990. Rates of fluid expulsion across the northern Cascadia accretionary prism: constraints from new heat flow and multichannel seismic reflection data. *J. Geophys. Res.,* 95:8869–8889.

Doveton, J.H., 1994. Geologic log interpretation. *SEPM Short Course,* 29:33–36.

Fofonoff, N.P., 1985. Physical properties of seawater: a new salinity scale and equation of state for seawater. *J. Geophys. Res.,* 90:3332–3342.

Harrison, A.R., Randall, C.J., Aron, J.B., Morris, C.F., Wignall, A.H., Dworak, R.A., Rutledge, L.L., and Perkins, J.L., 1990. Acquisition and analysis of sonic waveforms from a borehole monopole and dipole source for the determination of compressional and shear speeds and their relation to rock mechanical properties and surface seismic data. *SPE Soc. Pet. Eng. AIME,* 65:267–282.

Hyndman, R.D., and Wang, K., 1993. Thermal constraints on the zone of major thrust earthquake failure: the Cascadia subduction zone. *J. Geophys. Res.,* 98:2039–2060.

Jackson, P.D., Taylor Smith, D., and Stanford, P.N., 1978. Resistivity-porosity-particle shape relationships for marine sands. *Geophysics,* 43:1250–1268. doi:10.1190/1.1440891

Michaelis, W., Seifert, R., Nauhaus, K., Treude, T., Thiel, V., Blumenberg, M., Knittel, K., Gieseke, A., Peterknecht, K., Pape, T., Boetius, A., Amann, R., Jørgensen, B.B., Widdel, F., Peckmann, J., Pimenov, N.V., and Gulin, M.B., 2002. Microbial reefs in the Black Sea fueled by anaerobic oxidation of methane. *Science,* 297:1013–1015. doi:10.1126/science.1072502

Orphan, V., House, C.H., Hinrichs, K.-U., McKeegan, K.D., and DeLong, E.F., 2002. Multiple archaeal groups mediate methane oxidation in anoxic cold seep sediments. *Proc. Natl. Acad. Sci. U. S. A.,* 99:7663–7668.

Pimmel, A., and Claypool, G., 2001. Introduction to shipboard organic geochemistry on the *JOIDES Resolution. ODP Tech. Note,* 30 [Online]. Available from World Wide

Web: **http://www-odp.tamu.edu/publications/tnotes/tn30/INDEX.HTM.**

Pribnow, D.F.C., Kinoshita, M., and Stein, C.A., 2000. Thermal data collection and heat flow recalculations for ODP Legs 101–180. Institute for Joint Geoscientific Research, GGA, Hanover, Germany, 0120432. Available from World Wide Web: **http://www-odp.tamu.edu/publications/heatflow/ODPReprt.pdf.**

Riedel, M., Long, P., Liu, C.S., Schultheiss, P., Collett, T., and the ODP Leg 204 Shipboard Scientific Party, 2006. Physical properties of near-surface sediments at southern Hydrate Ridge: results from ODP Leg 204. *In* Tréhu, A.M., Bohrmann, G., Torres, M.E., and Colwell, F.S. (Eds.), *Proc. ODP, Sci. Results,* 204 [Online]. **http://www-odp.tamu.edu/publications/204_SR/104/104.htm**

Sloan, E.D., 1998. *Clathrate Hydrates of Natural Gases* (2nd ed.): New York (Marcel Dekker).

Tréhu, A.M, Bohrmann, G., Rack, F.R., Torres, M.E., et al., 2003. *Proc. ODP, Init. Repts.,* 204 [Online]. Available from World Wide Web: **http://www-odp.tamu.edu/publications/204_IR/204ir.htm.**

Westbrook, G.K., Carson, B., Musgrave, R.J., et al., 1994. *Proc. ODP, Init. Repts.,* 146 (Pt. 1): College Station, TX (Ocean Drilling Program).

Xu, W., 2002. Phase balance and dynamic equilibrium during formation and dissociation of methane gas hydrate. *Fourth Int. Conf. Gas Hydrates,* 19023:199–200.

Xu, W., 2004. Modeling dynamic marine gas hydrate systems. *Am. Mineral.,* 89:1271–1279.

Zhang, C.L., Li, Y., Wall, J.D., Larsen, L., Sassen, R., Huang, Y., Wang, Y., Peacock, A., White, D.C., Horita, J., and Cole, D.R., 2002. Lipid and carbon isotopic evidence of methane-oxidizing and sulfate-reducing bacteria in association with gas hydrates from the Gulf of Mexico. *Geology,* 20:239–242.

Publication: 28 October 2006
MS 311-107

Figure F1. Seismic site survey data in the vicinity of Site U1329. There are two seismic lines acquired virtually over the same location: multichannel seismic (MCS) Line 89-08 (from the presite survey for ODP Leg 146) and Line PGC9902_ODP-1 with MCS and 3.5 kHz subbottom profiler data. Shotpoints and common depth points (CDPs) are indicated in different colors. Green = Line 89-08 CDPs, red = Line PGC9902_ODP-1 MCS CDPs, blue = Line PGC9902_ODP-1 3.5 kHz data shot points. SCS = single channel seismic. Axes are universal transverse Mercator (UTM) projection easting and northing coordinates using the WGS-84 reference.

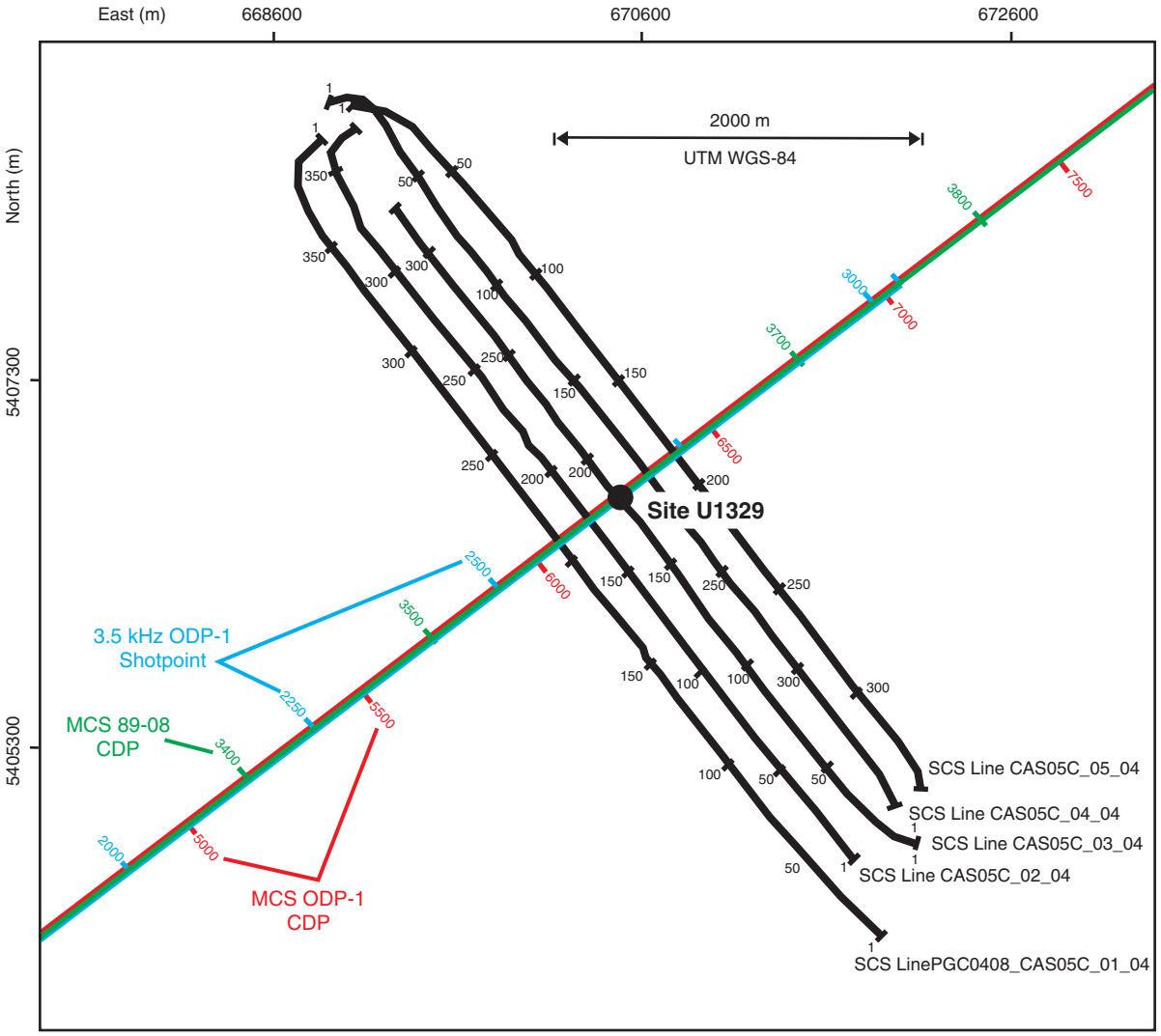

Figure F2. High-resolution 3.5 kHz data acquired along Line PGC9902_ODP-1. No evidence of the presence of the transparent Holocene sediments is apparent at Site U1329; however, the transparent layer abruptly appears near Shotpoint 2400 and covers the entire basin sediments. V.E. = vertical exaggeration.

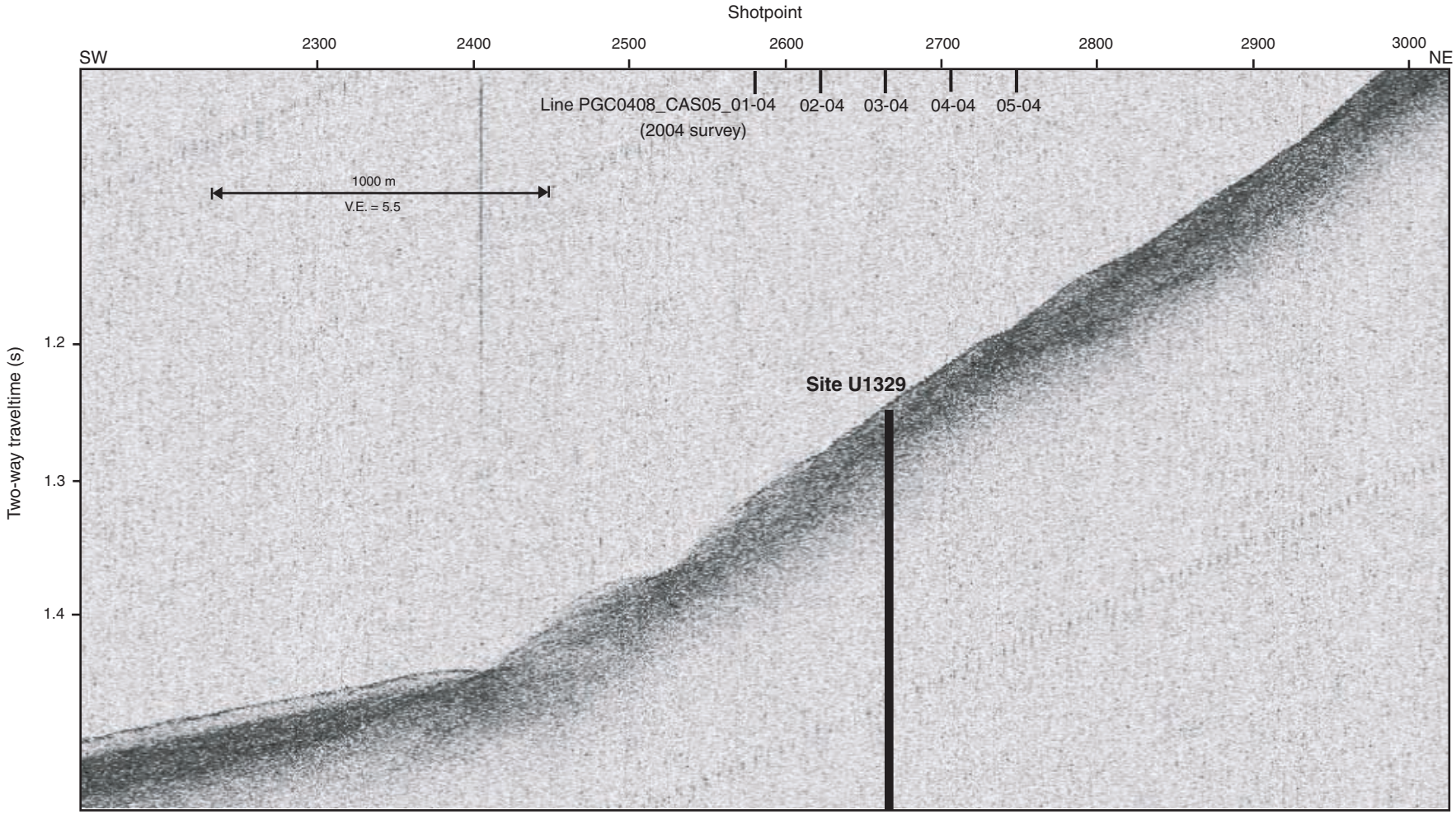

Figure F3. Portion of multichannel seismic Line 89-08 showing the location of Site U1329 to a total depth of 270 mbsf. Below the seismic unconformity, reflectors show higher amplitude and lower frequencies. BSR = bottom-simulating reflector, CDP = common depth point, V.E. = vertical exaggeration.

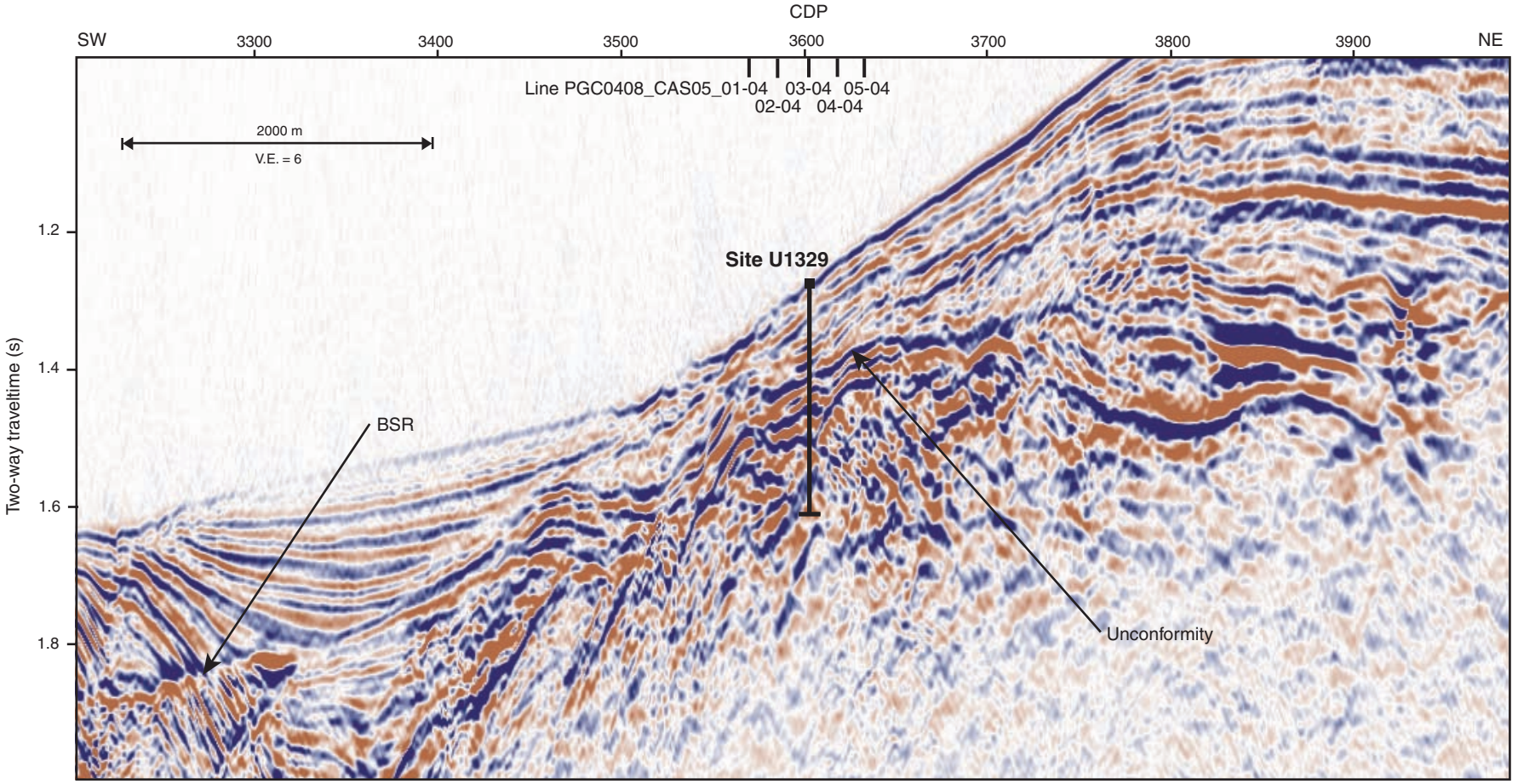

Figure F4. Portion of multichannel seismic Line PGC9902_ODP-1 showing the location of Site U1329 to a total depth of 270 mbsf. There is a faint bottom-simulating reflector (BSR)-like reflection at 126 mbsf. CDP = common depth point, V.E. = vertical exaggeration.

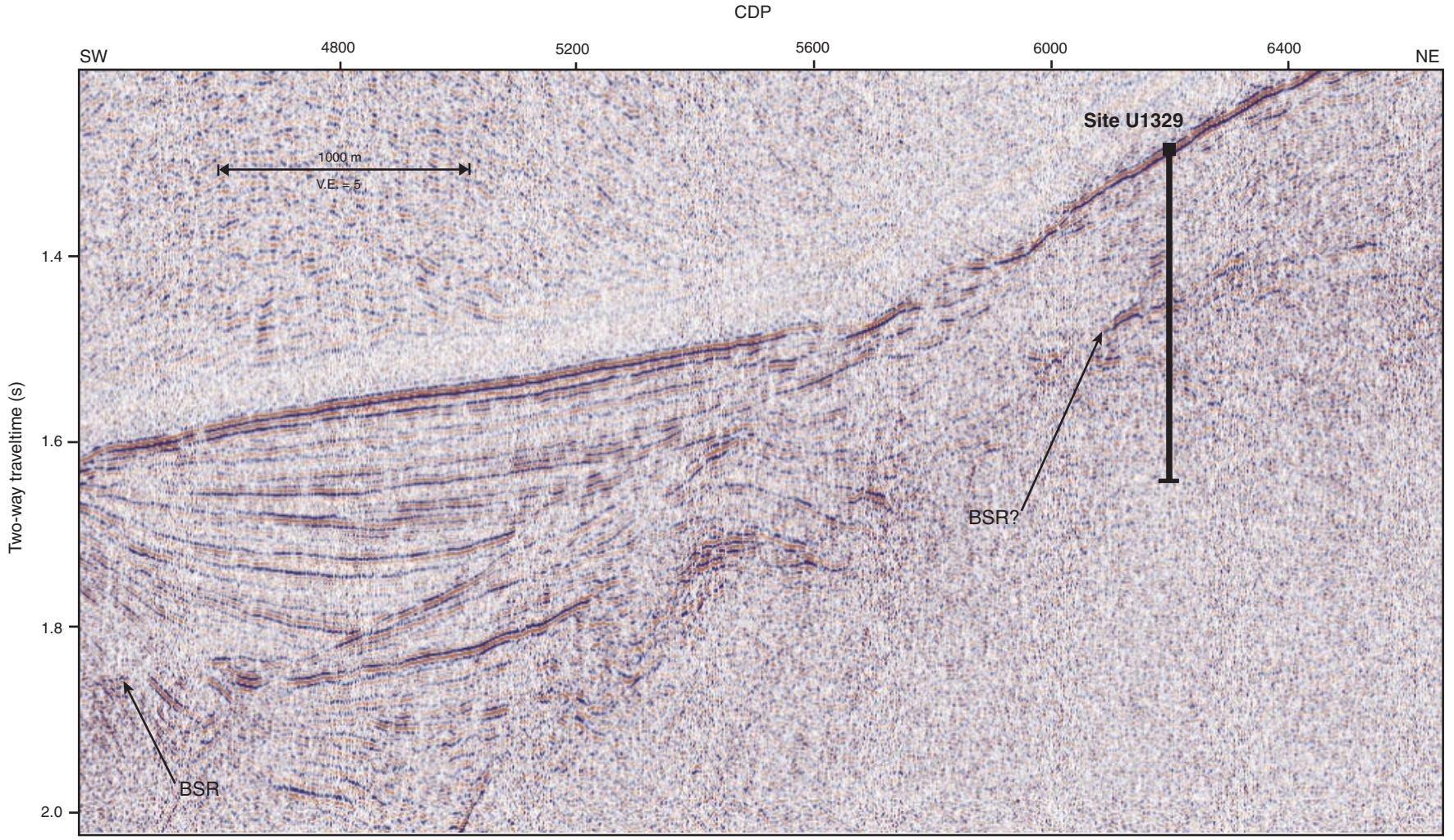

Figure F5. Single-channel seismic Line PGC0408_CAS05_line03-04 showing the best image of the bottom-simulating reflector (BSR) at this site. This line crosses Lines 89-08 and PGC9902_ODP-1 in a perpendicular direction. CDP = common depth point, V.E. = vertical exaggeration.

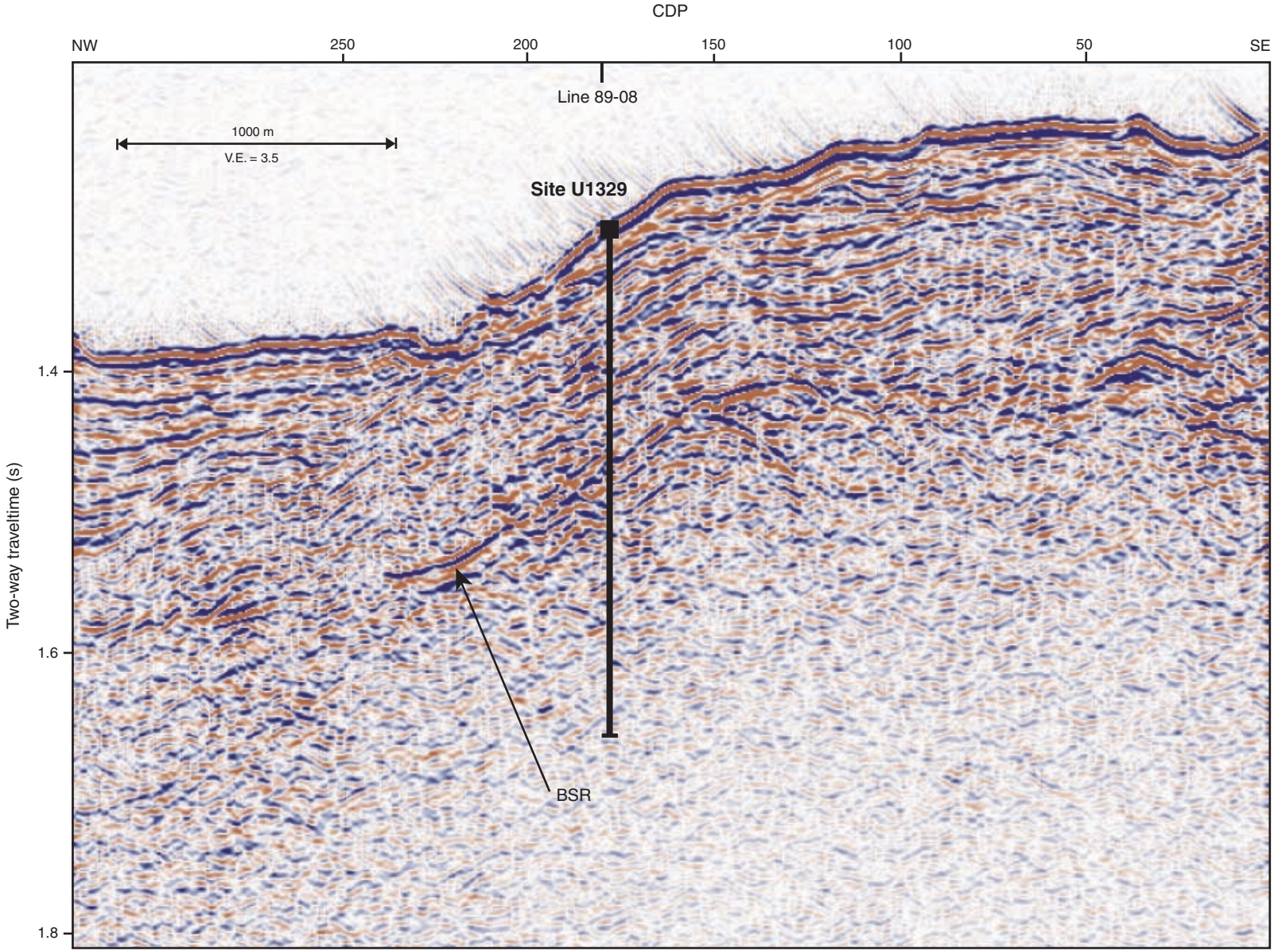

Figure F6. Location of holes drilled at Site U1329, showing track lines with seismic survey shotpoints. Axes are Universal Transverse Mercator (UTM) projection easting and northing coordinates using the WGS-84 reference.

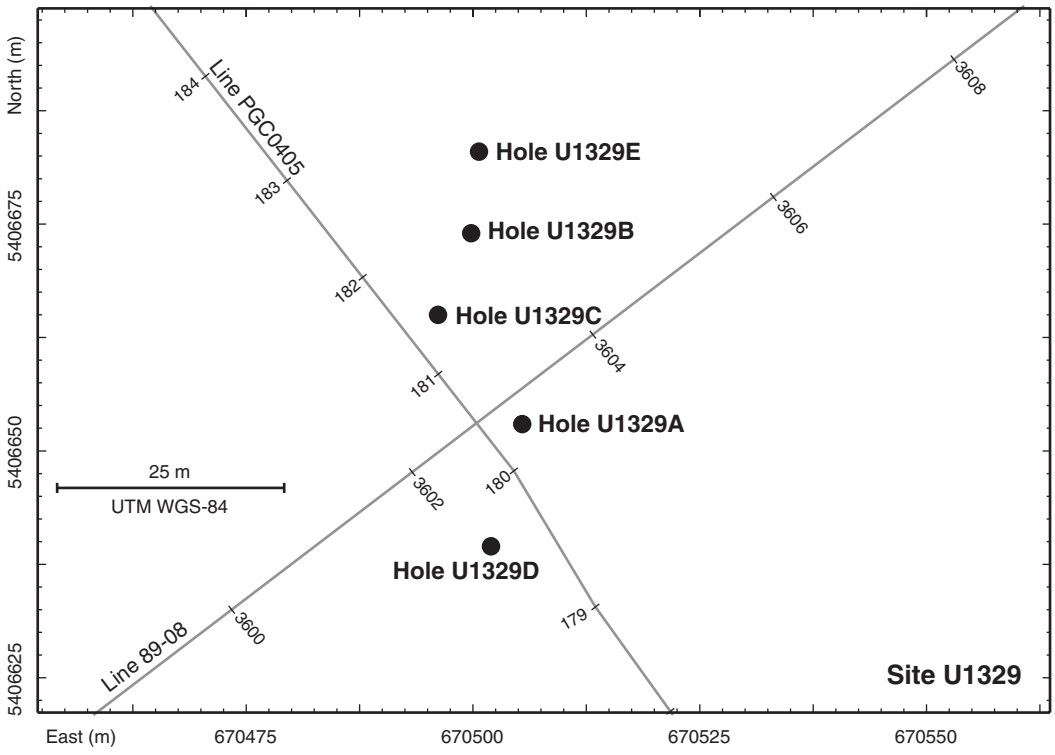

Figure F7. Lithostratigraphic summary for Hole U1329C showing the percentage of clay, silt, sand, biogenic opal (diatoms, radiolarians, siliceous spicules, and silicoflagellates), foraminifers, nannofossils, and archive multisensor track color reflectance (a*) in the major lithology.

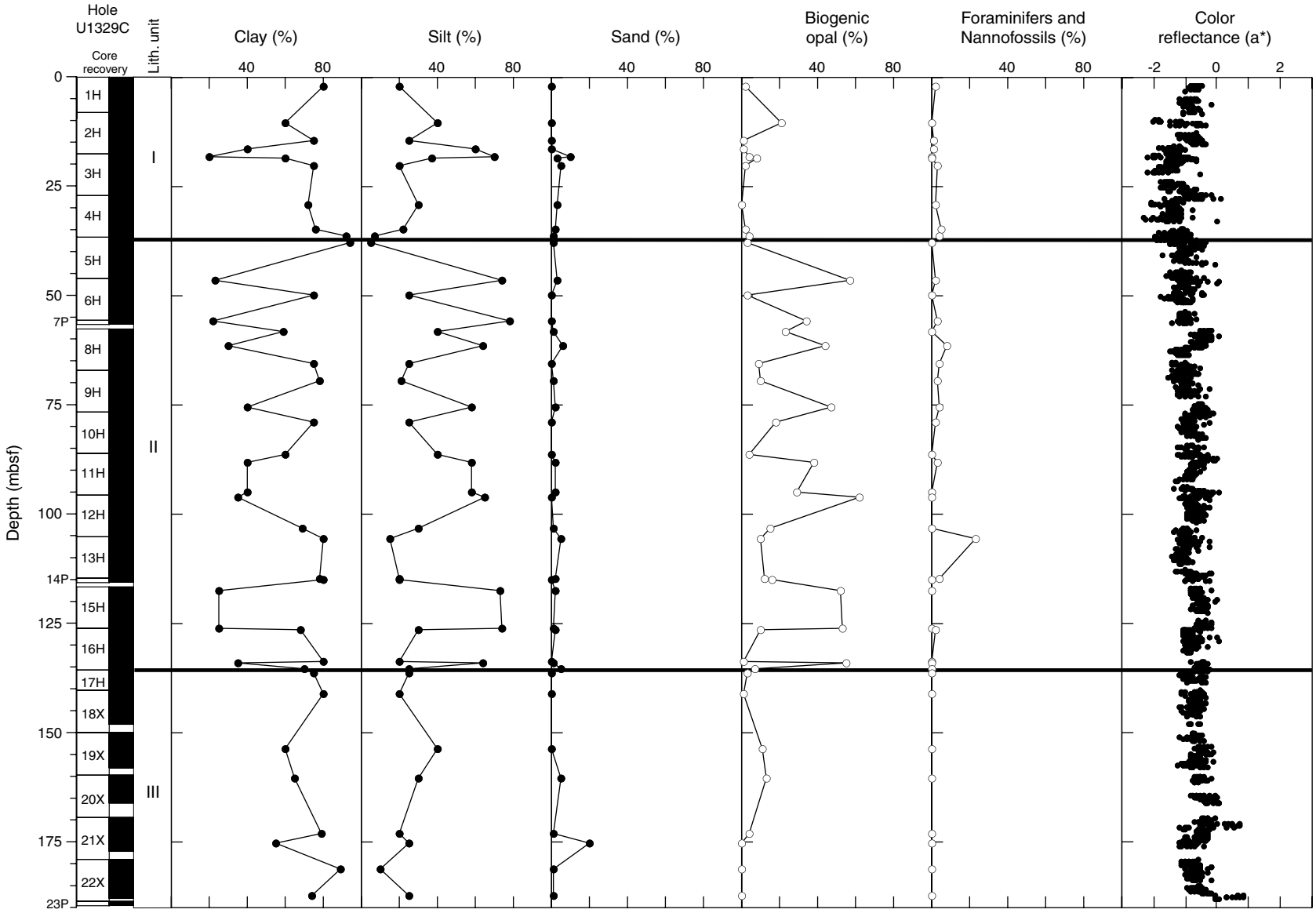

Figure F8. Dark gray clay and dark olive gray silty clay with a wood fragment in lithostratigraphic Unit I (interval 311-U1329E-1H-2, 48–78 cm).

Figure F9. (**A**) Unlithified dolomite cement (interval 311-U1329C-4H-3, 113–130 cm), (**B**) partly lithified dolomite (interval 311-U1329C-4H-3, 131–148 cm), and (**C**) lithified dolomite (interval 311-U1329E-4H-5, 92–124 cm) within clay in lithostratigraphic Unit I.

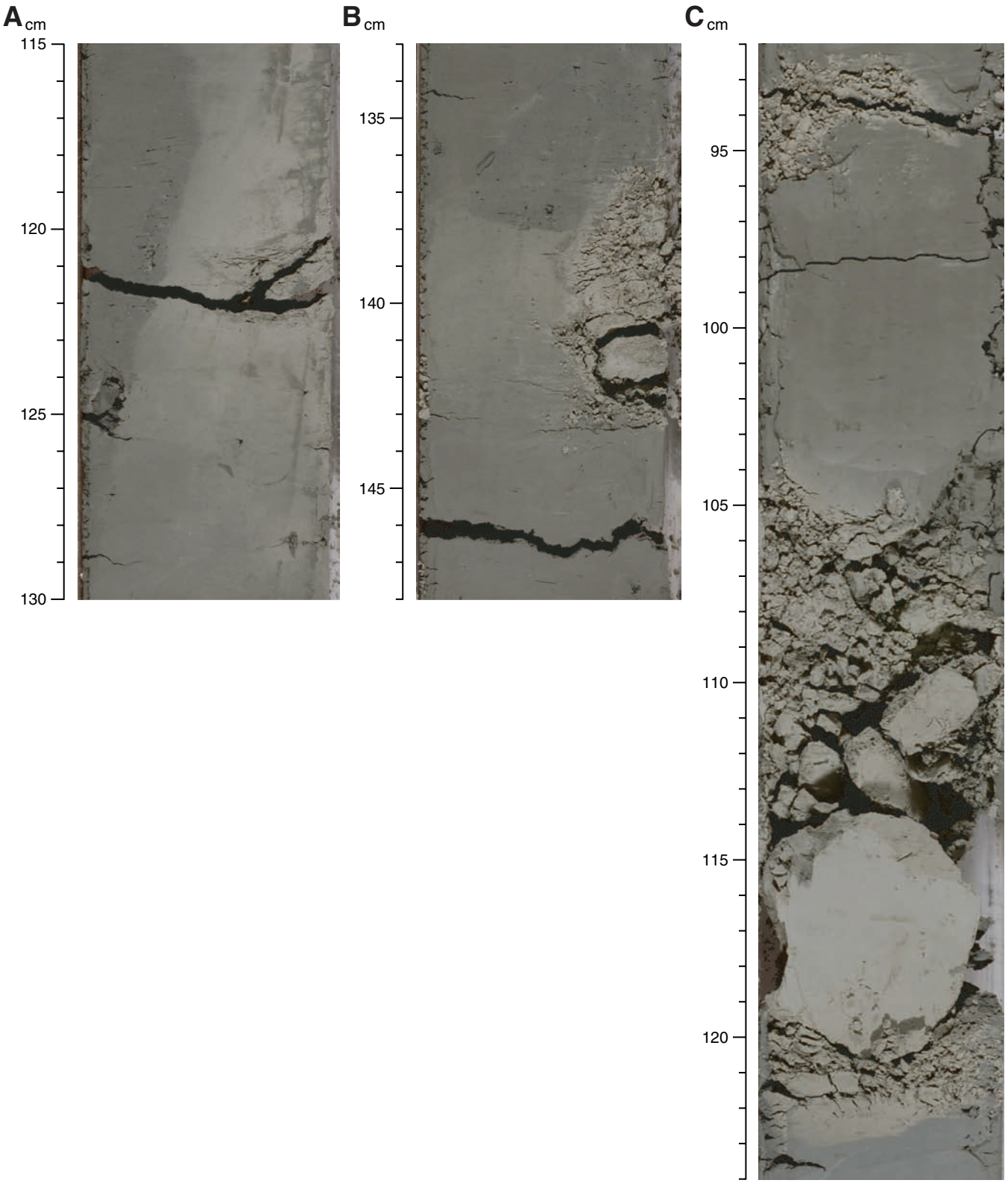

Figure F10. XRD record from a dolomite sample in lithostratigraphic Unit I (Sample 311-U1329E-4H-5, 116–117 cm).

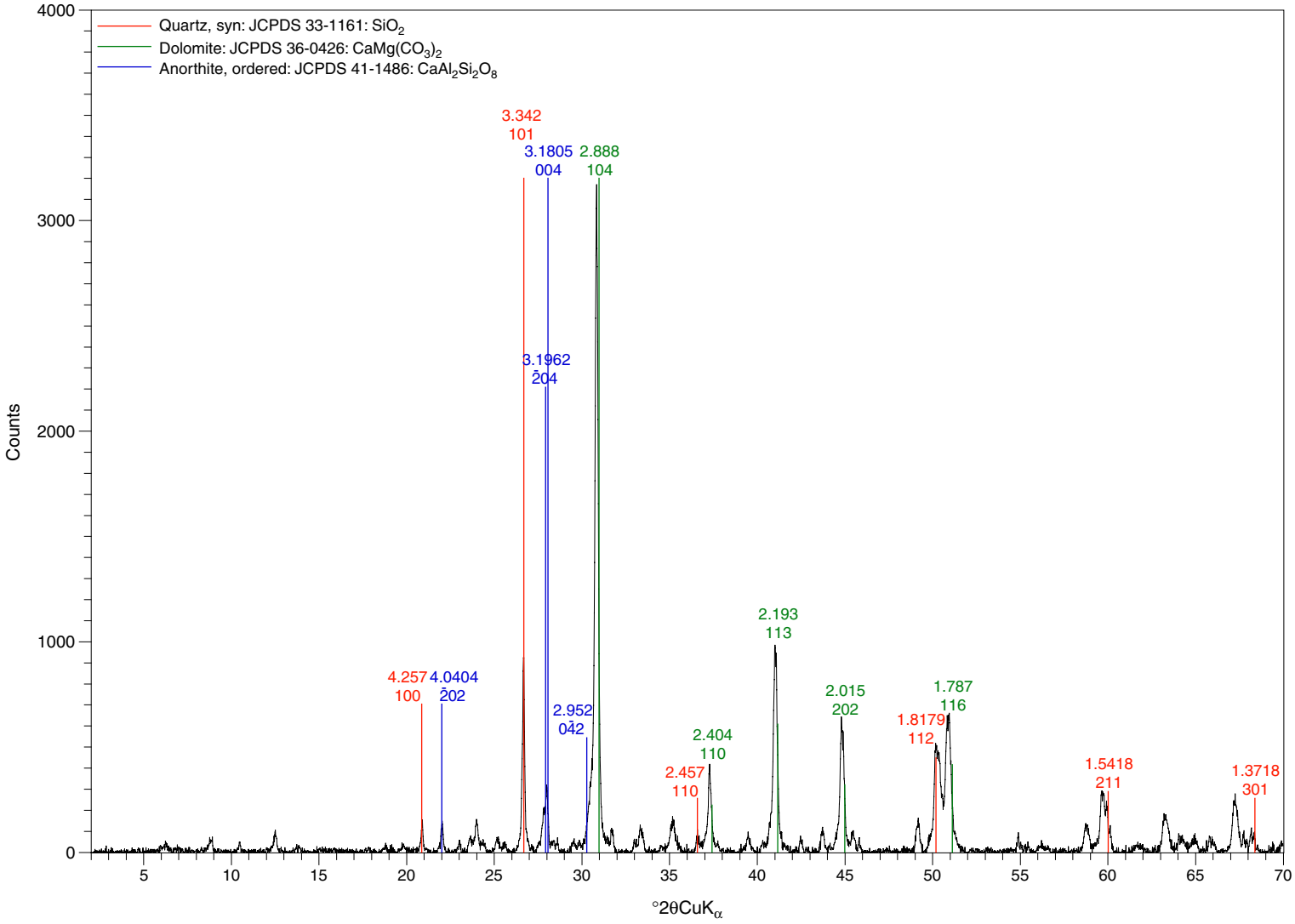

Figure F11. Irregular, sharp boundary between dark gray silty clay and dark olive gray diatom ooze in lithostratigraphic Unit II (interval 311-U1329C-16H-6, 0–15 cm).

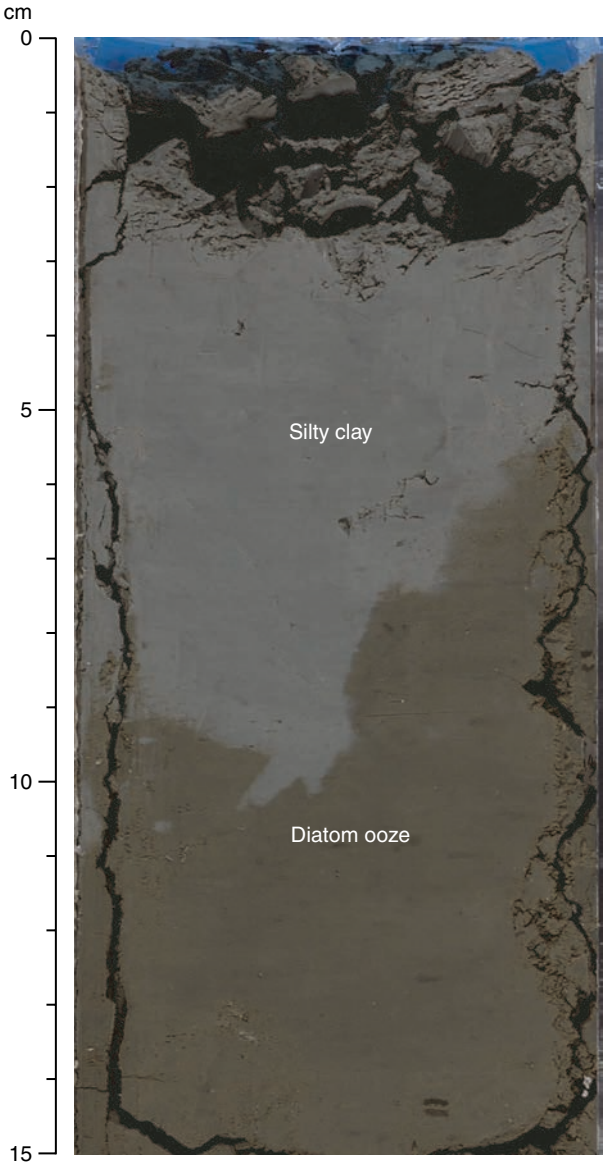

Figure F12. Dark greenish gray silty clay with diatoms and a broken bivalve shell in lithostratigraphic Unit II (interval 311-U1329C-8H-1, 126–140 cm).

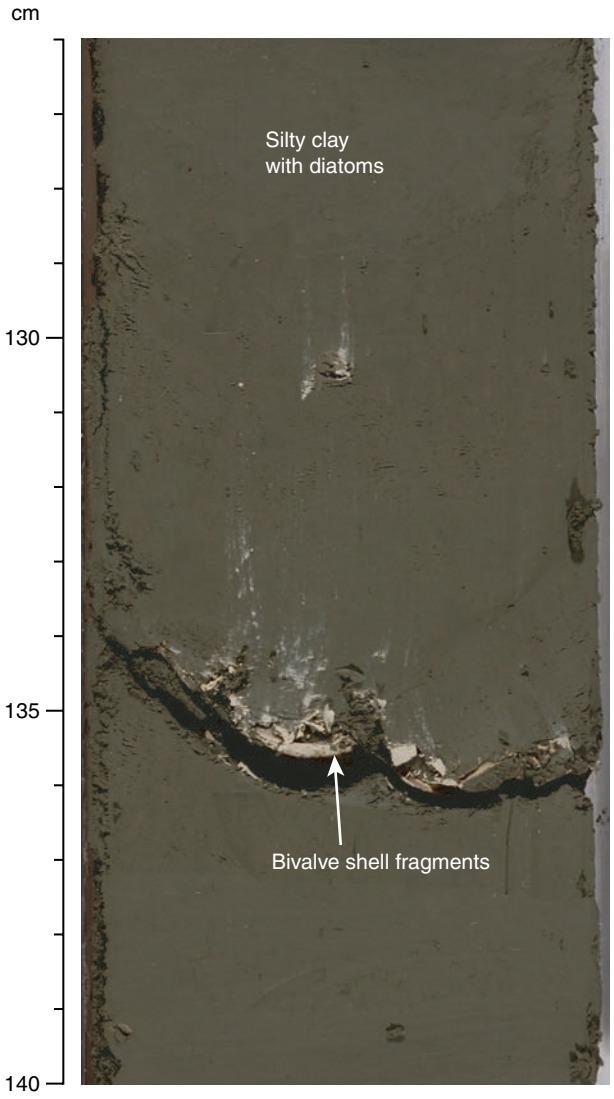

Figure F13. Diatom ooze in lithostratigraphic Unit II (Sample **311-U1329C-10H-4, 134 cm**).

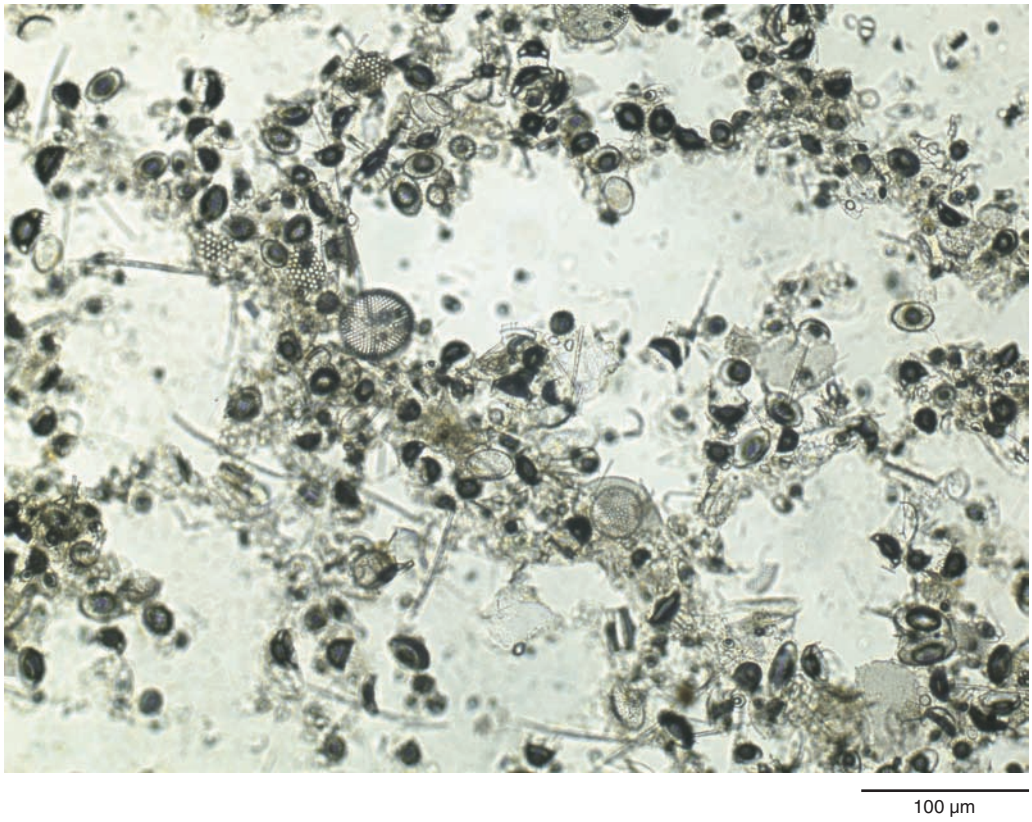

Figure F14. Conglomerate composed of different mud clasts at the base of lithostratigraphic Unit II (interval 311-U1329C-16H-7, 23–42 cm).

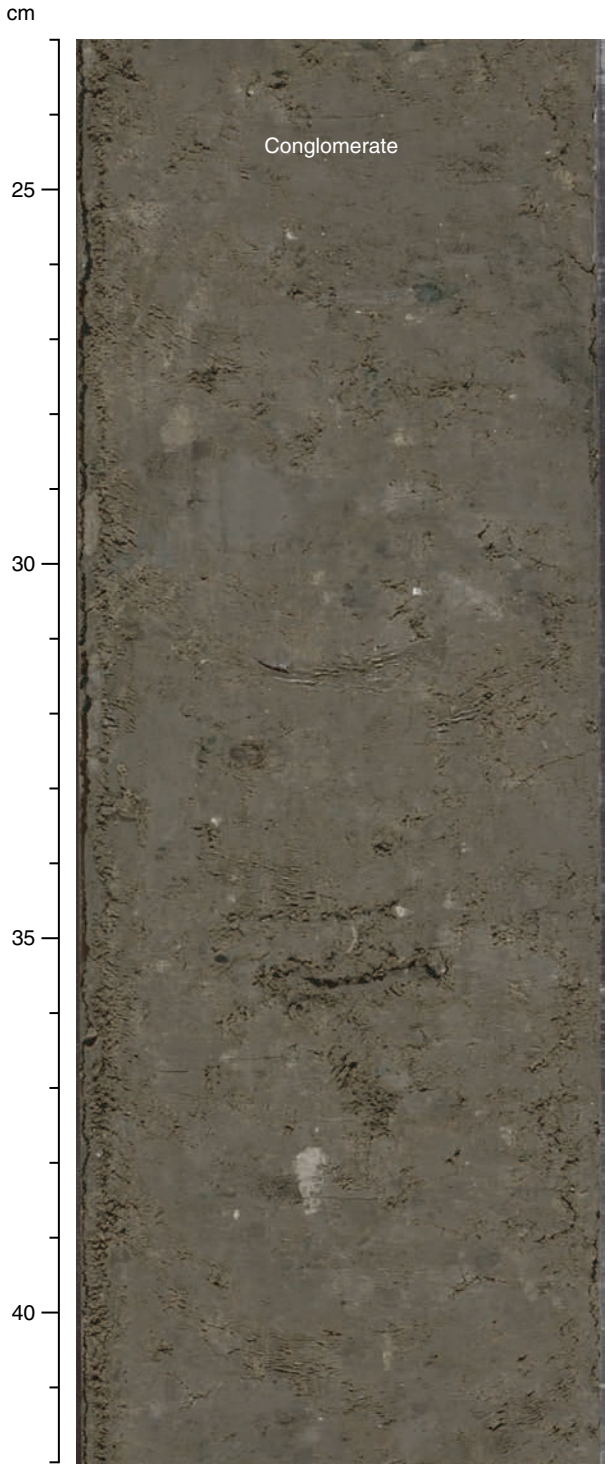

Figure F15. Dark greenish gray clay in lithostratigraphic Unit III (interval 311-U1329C-18X-2, 104–140 cm).

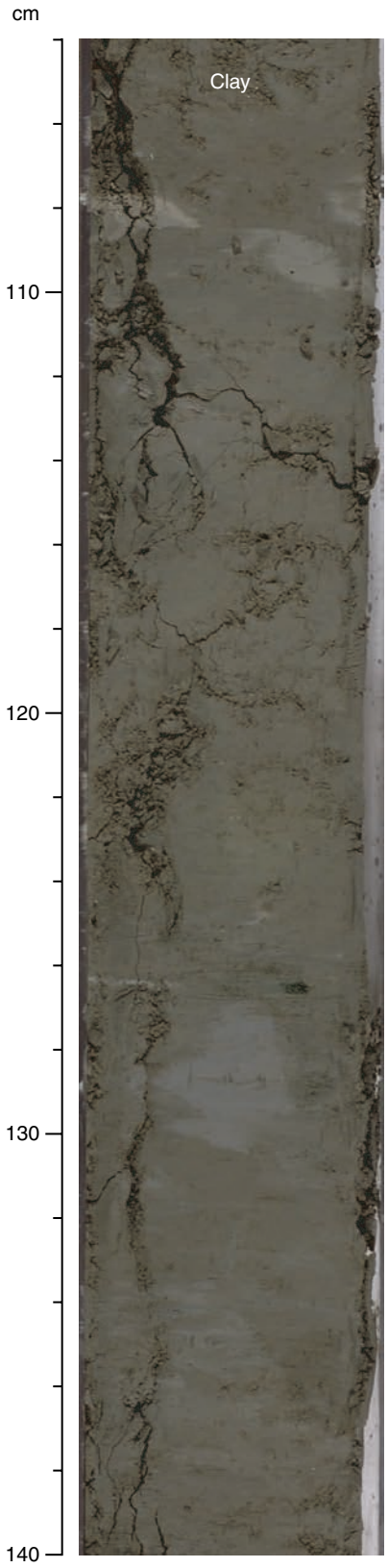

Figure F16. Silty clay with a high Mg–calcite lithified carbonate in lithostratigraphic Unit III (interval 311-U1329C-20X-3, 26–46 cm).

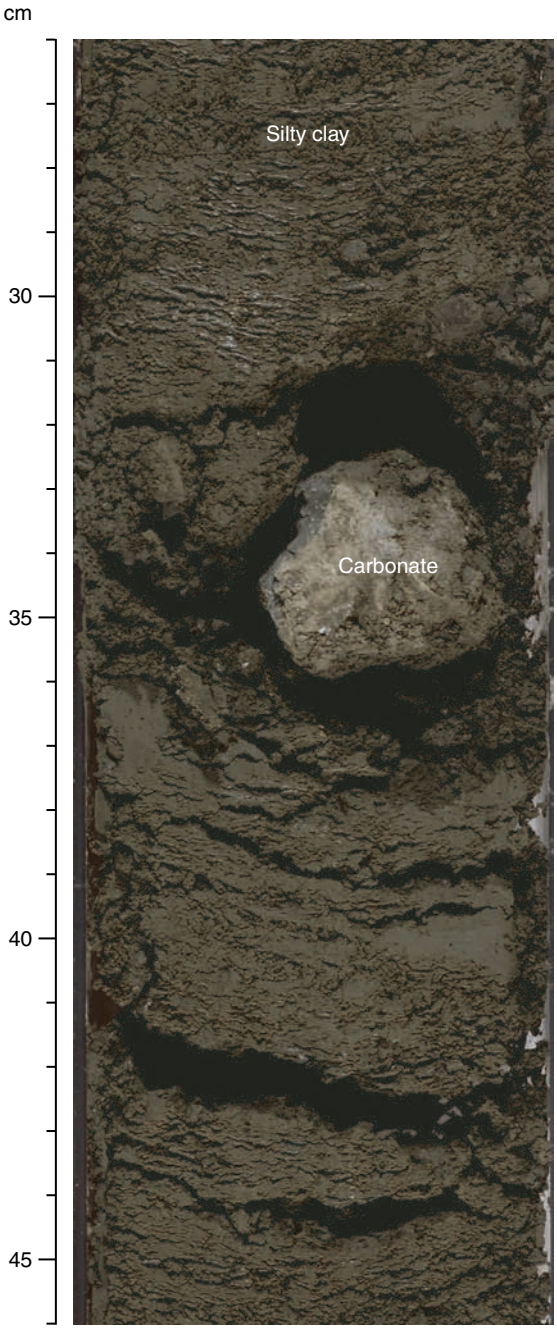

Figure F17. Siderite in lithostratigraphic Unit II (Sample **311-U1329C-19X-1, 68 cm**).

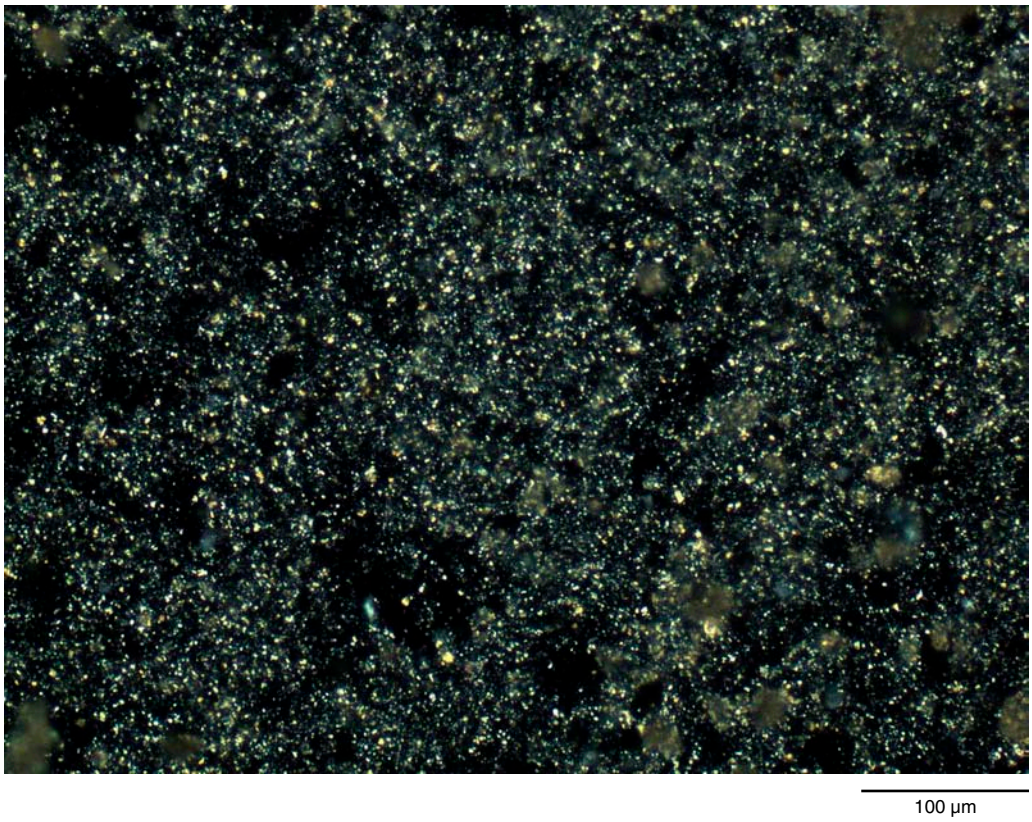

Figure F18. XRD record from a siderite sample in lithostratigraphic Unit III (Sample **311-U1329C-19X-1, 68–69 cm**).

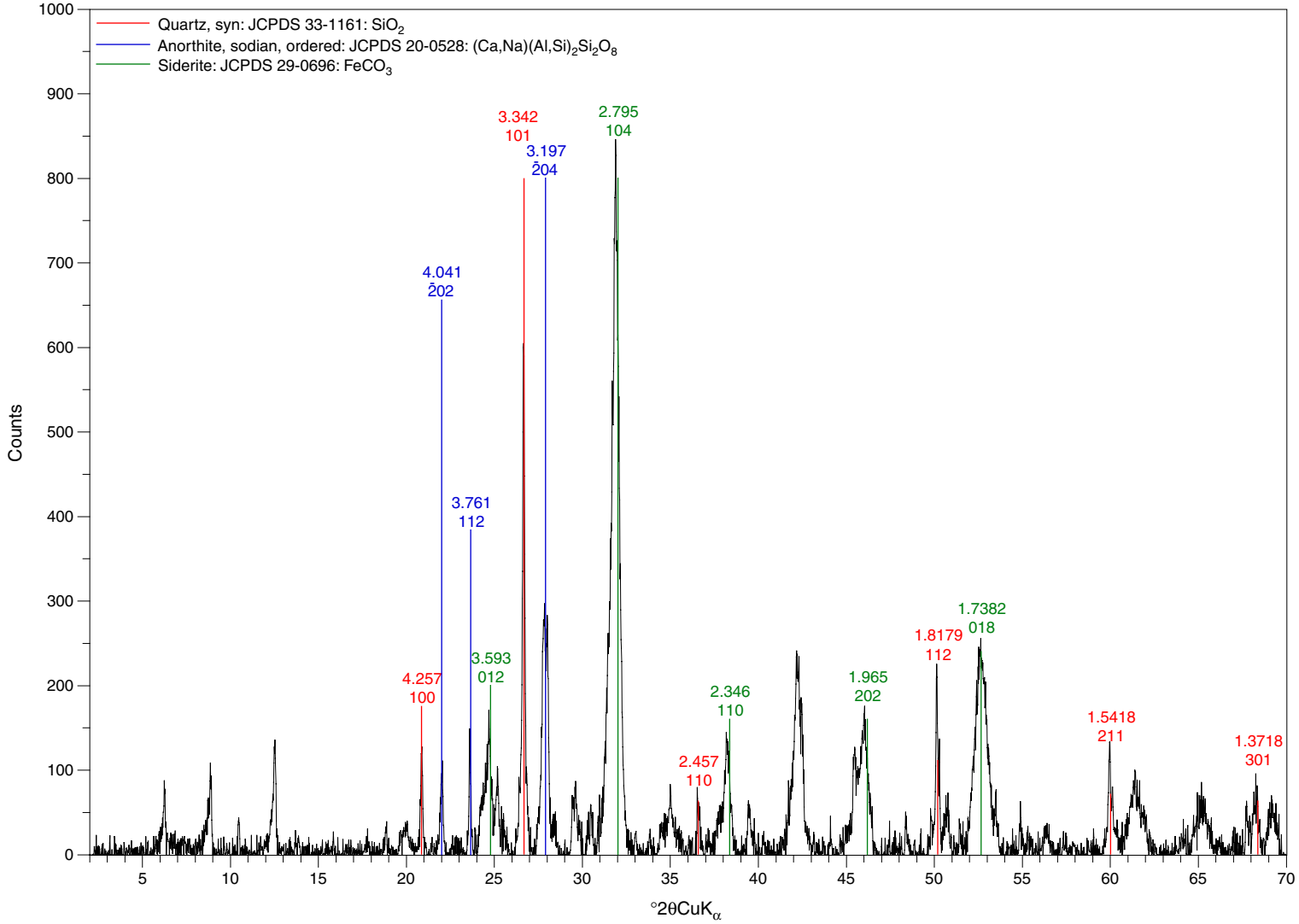

Figure F19. Glauconite grains in lithostratigraphic Unit III (Sample 311-U1329E-18X-2, 126 cm).

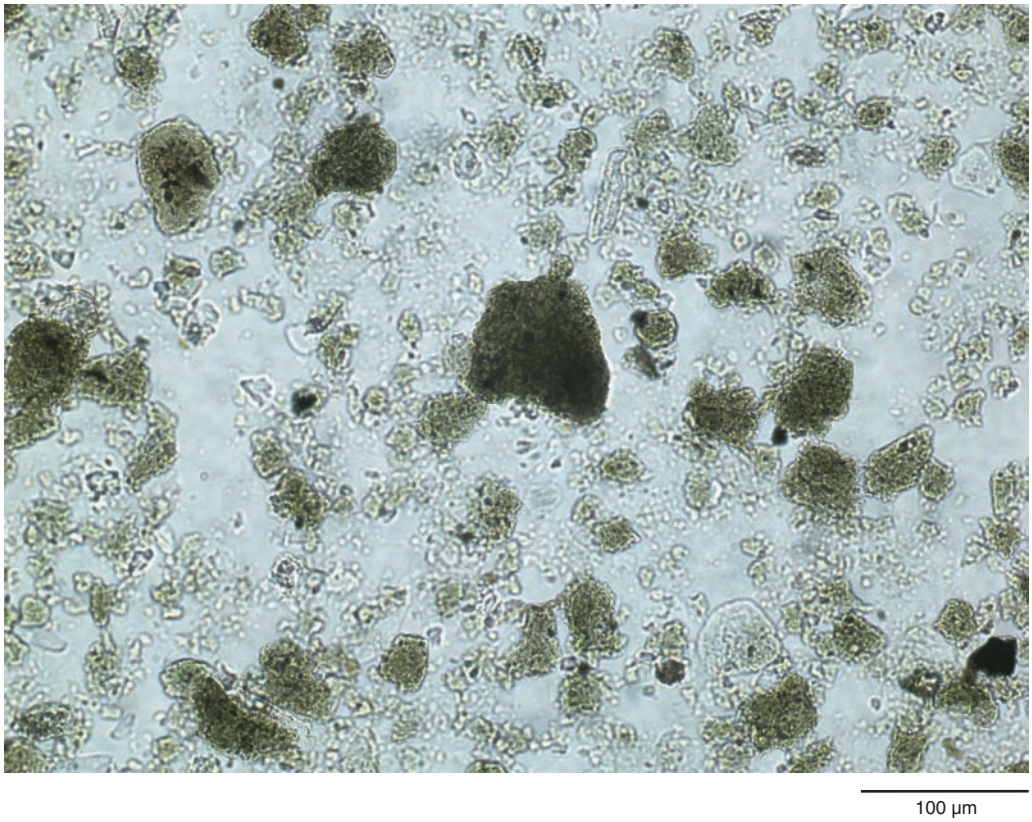

Figure F20. Concentration vs. depth profiles of salinity, chloride, sodium, and potassium in interstitial waters from Holes U1329C, U1329D, and U1329E. SW = seawater, BSR = seismically inferred bottom-simulating reflector.

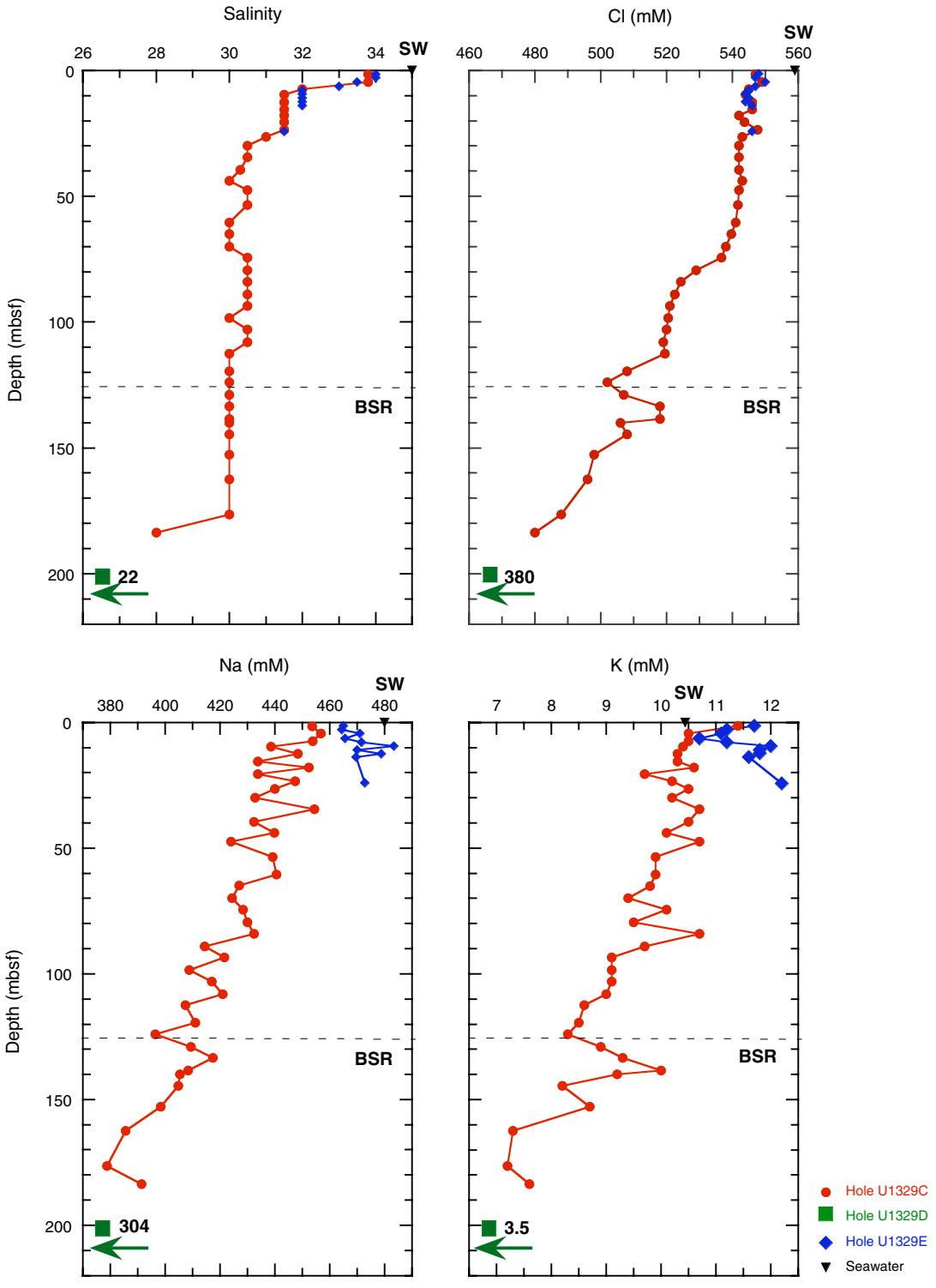

Figure F21. Concentration vs. depth profiles of alkalinity, sulfate, ammonium, and phosphate in interstitial waters from Holes U1329C, U1329D, and U1329E. SW = seawater, BSR = seismically inferred bottom-simulating reflector.

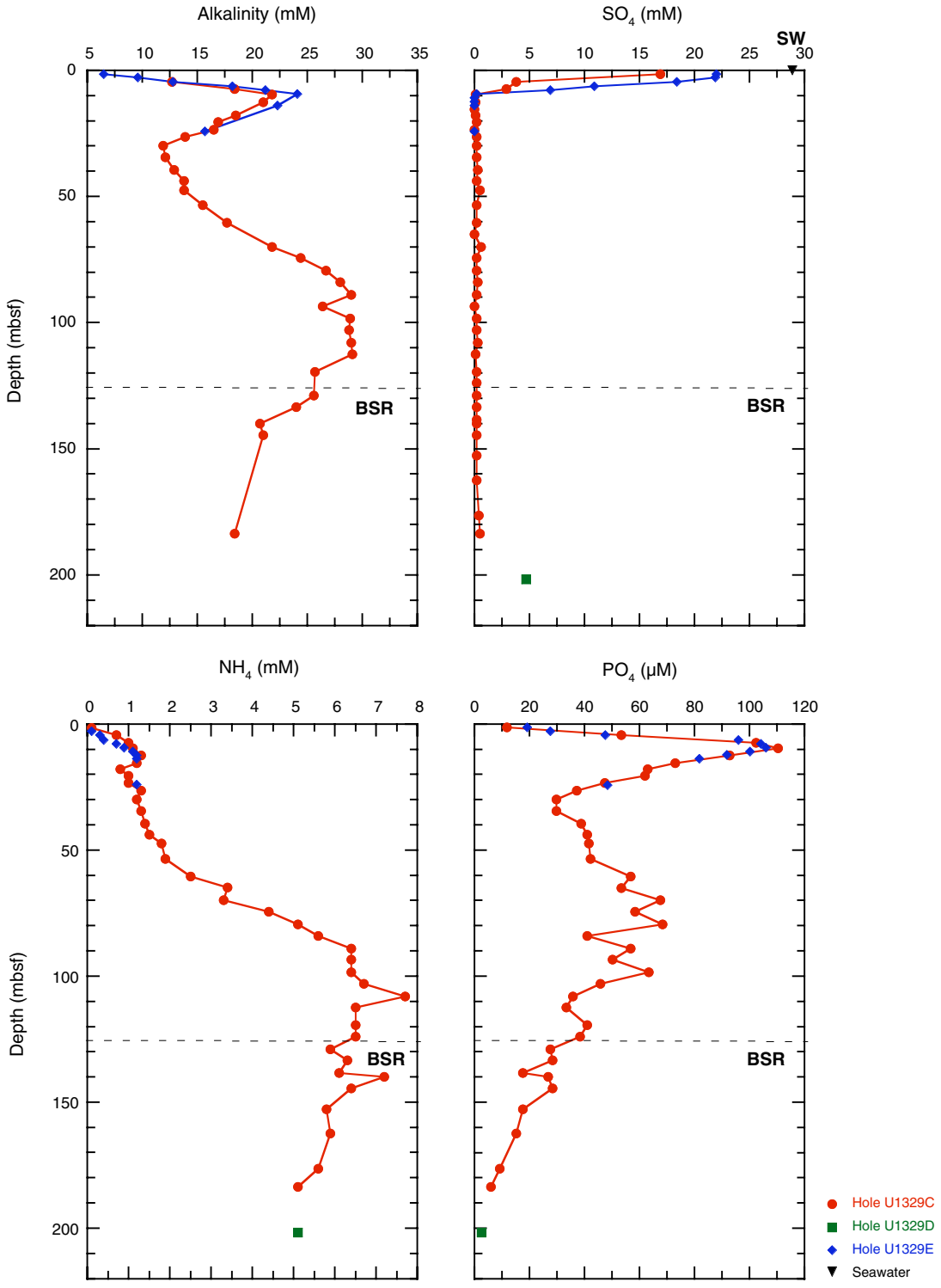

Figure F22. Concentration vs. depth profiles of calcium, magnesium, Mg/Ca ratios, and strontium in interstitial waters from Holes U1329C, U1329D, and U1329E. SW = seawater, BSR = seismically inferred bottom-simulating reflector.

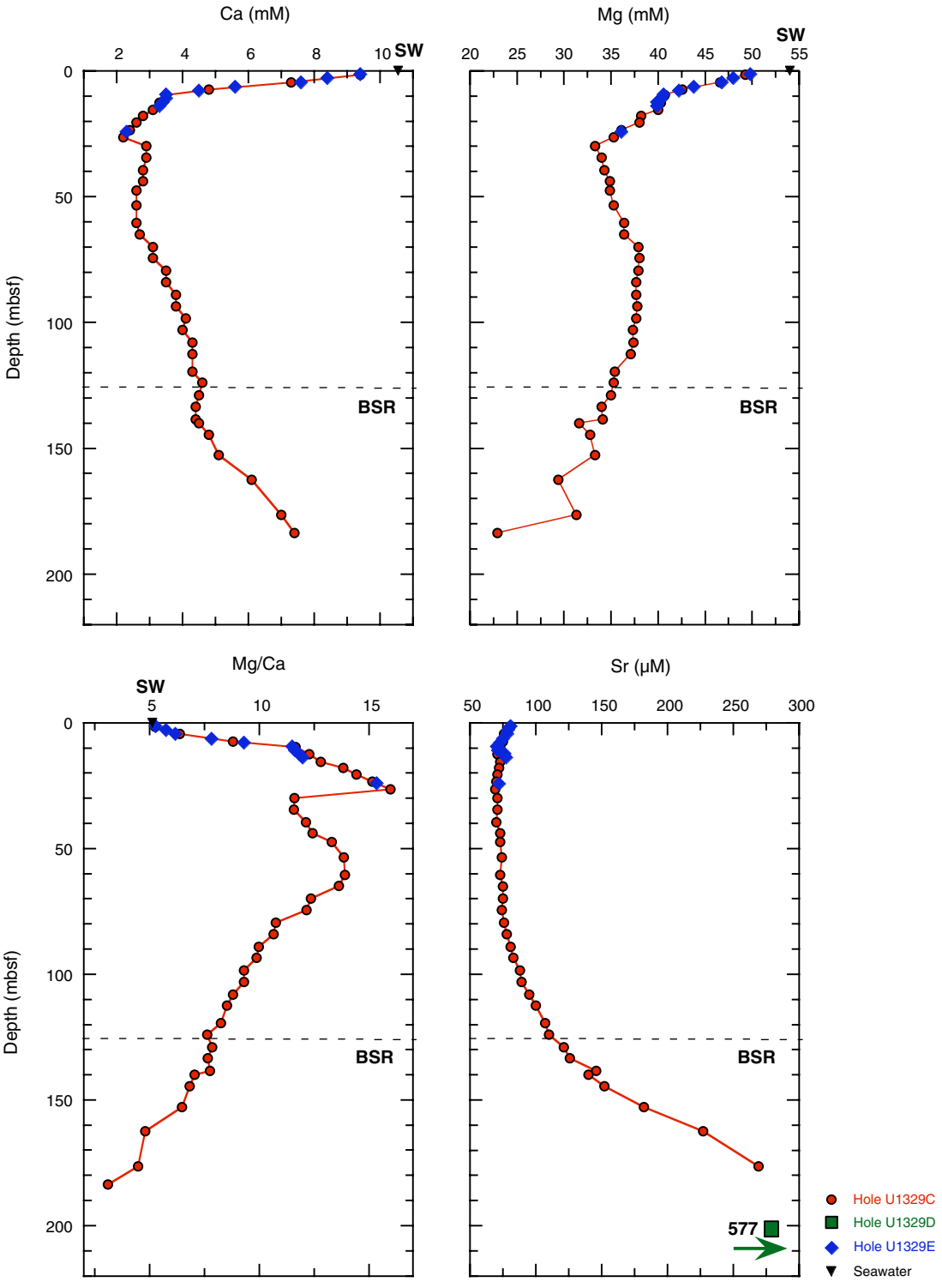

Figure F23. Dissolved sulfate vs. depth profile from the seafloor to 10 mbsf for Hole U1329E. The depth of the sulfate/methane interface is at 9.5 mbsf.

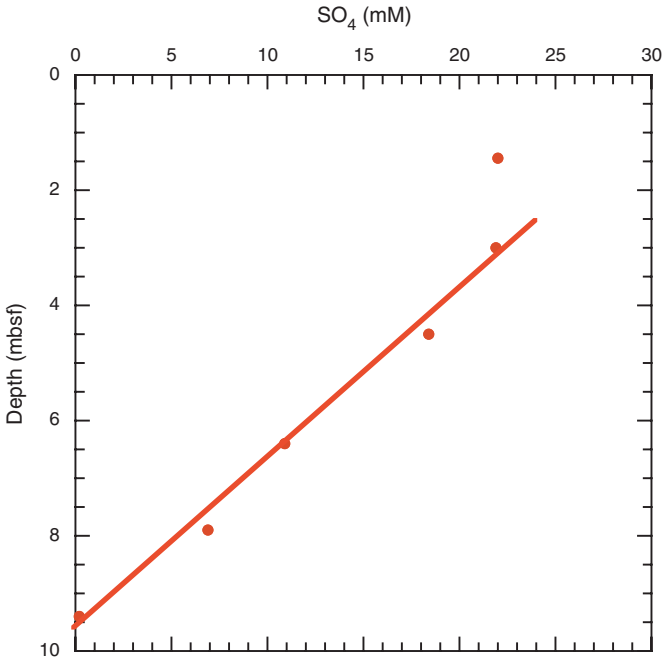

Figure F24. Concentrations of methane and ethane in headspace gas samples from Site U1329. BSR = bottom-simulating reflector.

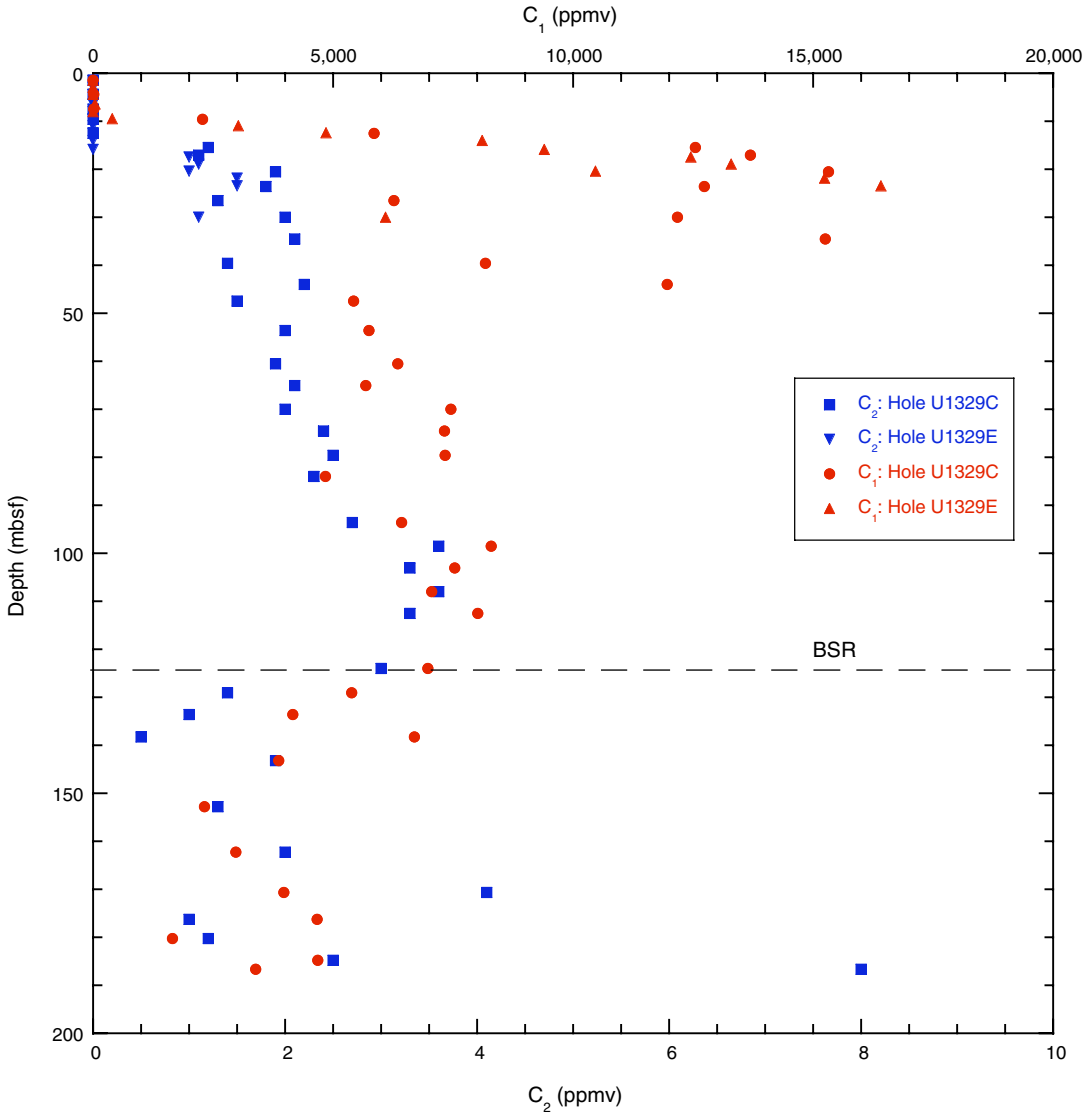

Figure F25. Concentrations of methane and ethane in void gas samples from Site U1329. BSR = bottom-simulating reflector.

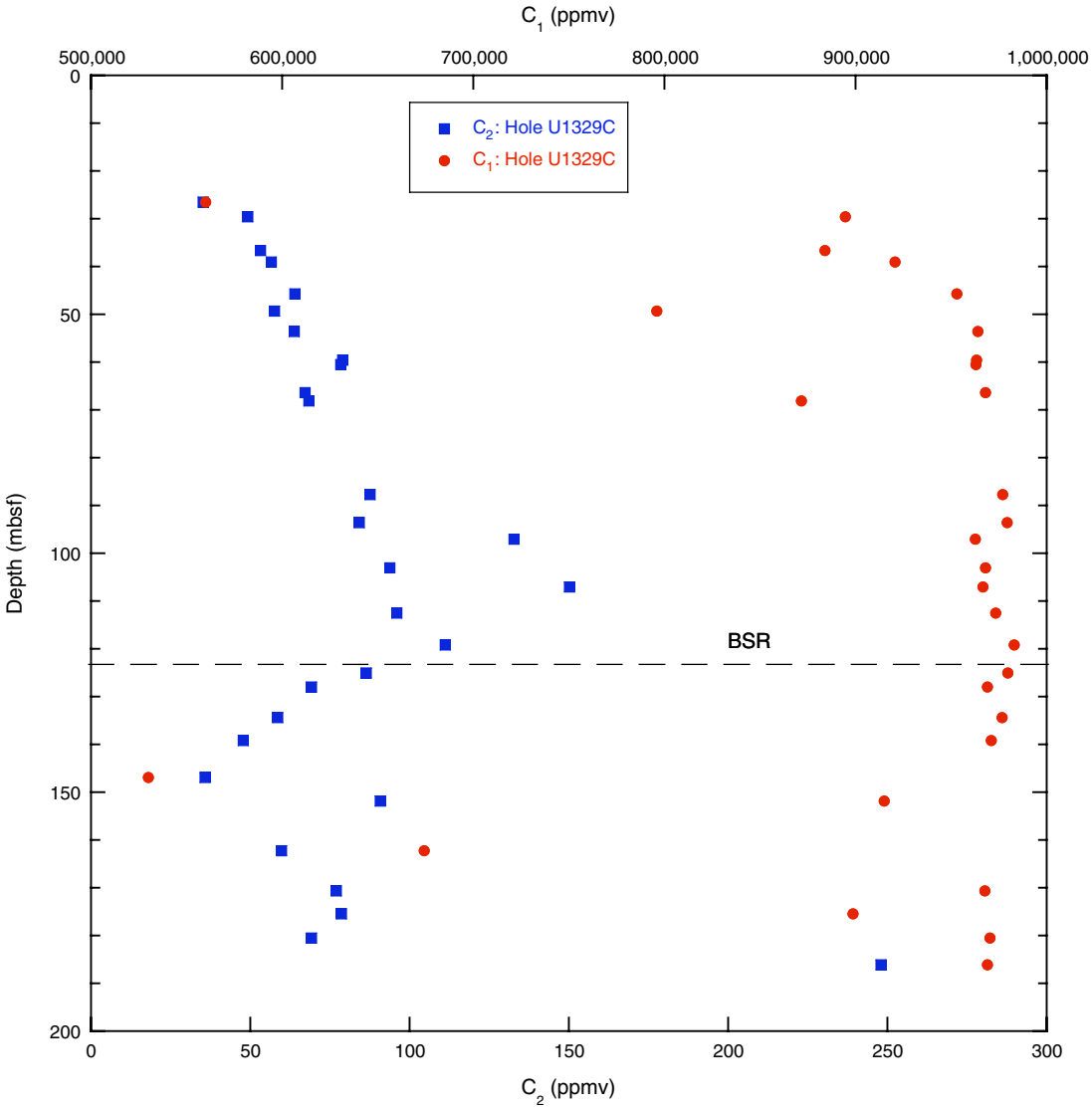

Figure F26. C_1/C_2 ratios in headspace gas (HS), void gas (VAC), and Pressure Core Sampler (PCS) gas samples from Site U1329. Lithostratigraphic Units I–III are shown on the right (see **"Lithostratigraphy"**). BSR = bottom-simulating reflector.

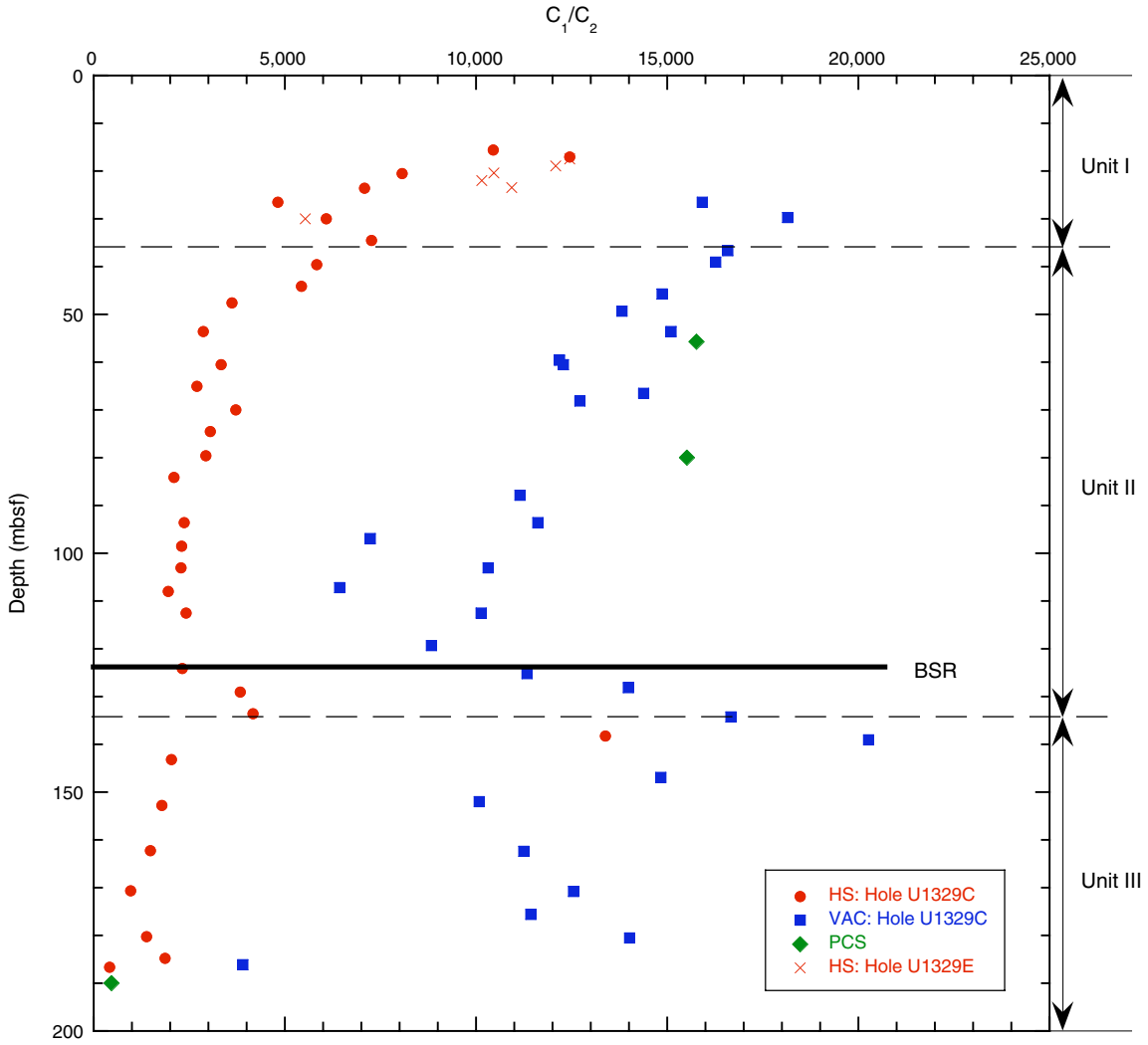

Figure F27. C_1/C_2 ratio vs. temperature at Site U1329. HS = headspace gas, VAC = void gas.

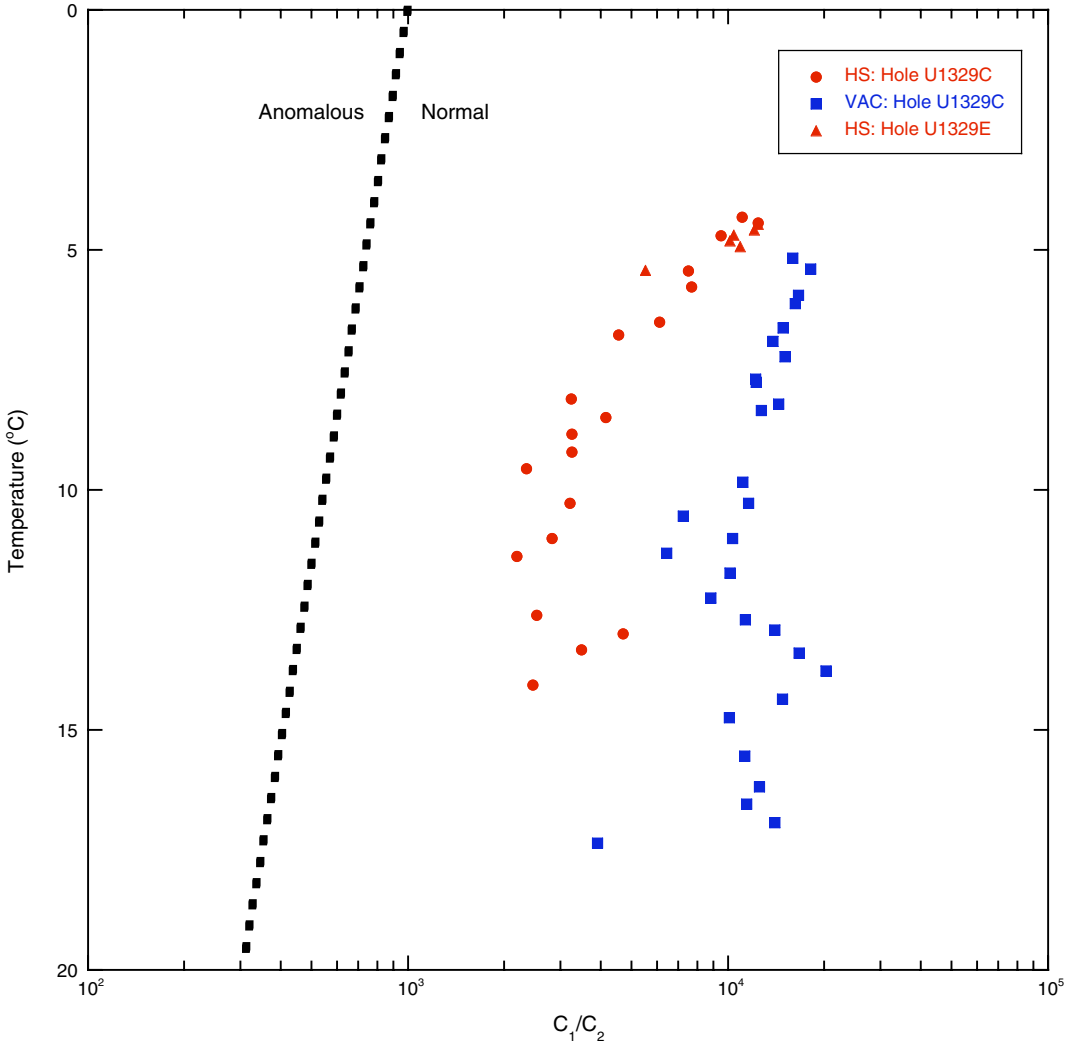

Figure F28. Dissolved sulfate and methane concentrations from Site U1329. SMI = sulfate/methane interface.

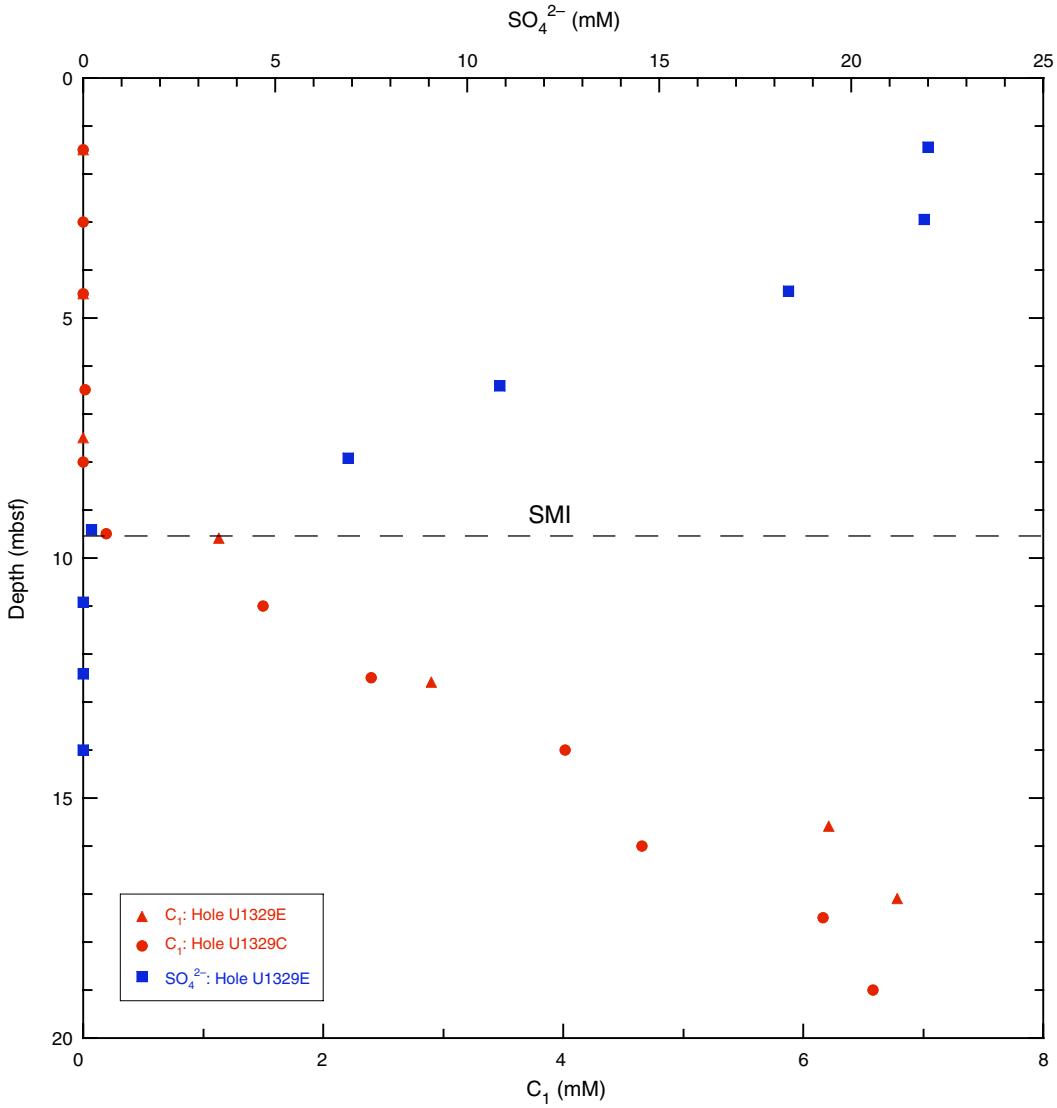

Figure F29. Concentrations of inorganic carbon (IC), calcium carbonate, total organic carbon (TOC), total nitrogen (TN), and C/N ratios in sediments from Site U1329.

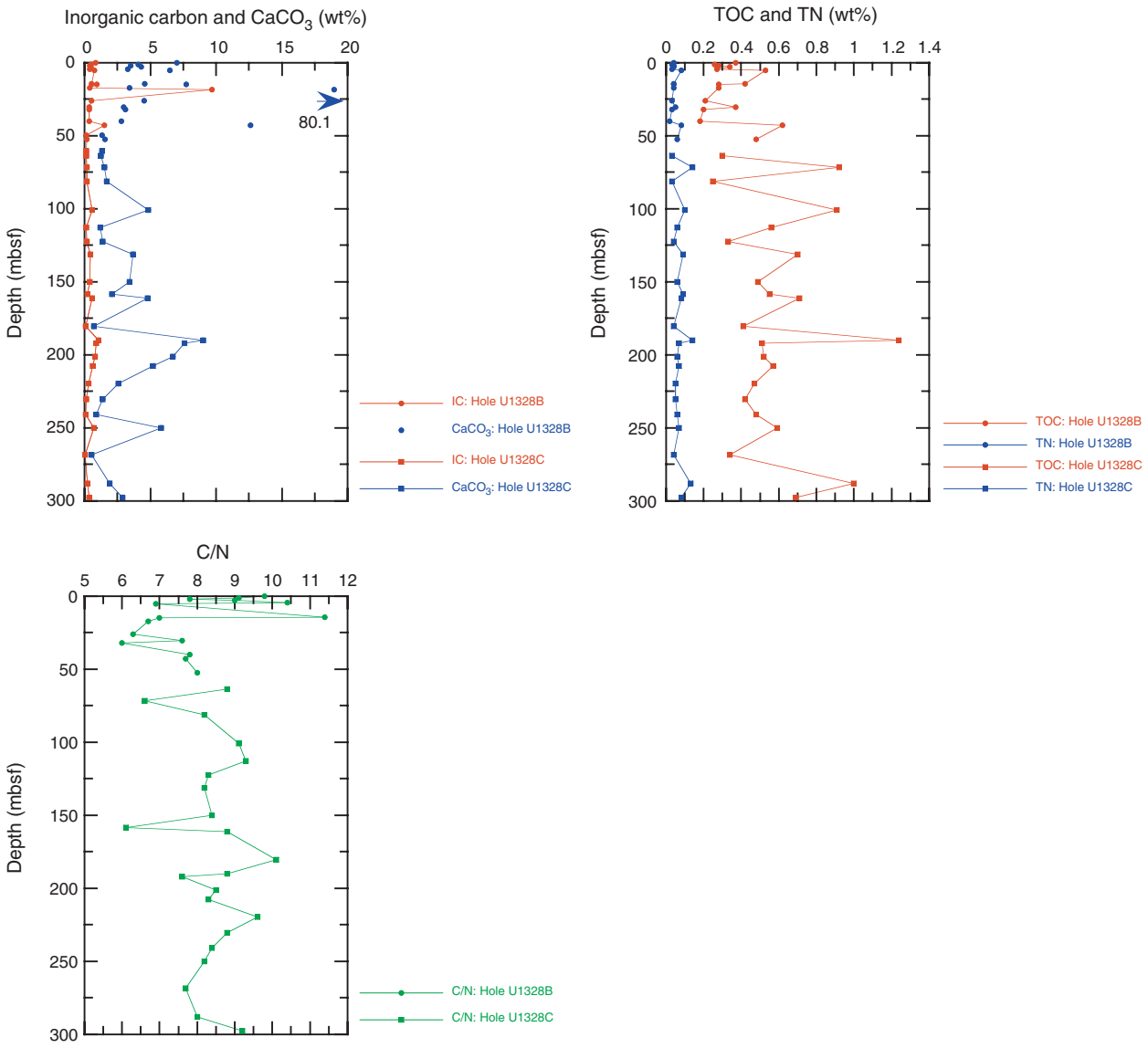

Figure F30. Overview of physical property data from Site U1329. Plotted from left to right are core recovery; logging-while-drilling (LWD) and moisture and density (MAD) porosity; LWD, multisensor track (MST), and MAD bulk density; MAD grain density; LWD, MST contact, and MST noncontact resistivity; MST magnetic susceptibility; thermal conductivity (line shows regional trend from Davis et al., 1990); Torvane shear strength; and lithostratigraphic units. APC = advanced piston corer, XCB = extended core barrel, BSR = bottom-simulating reflector.

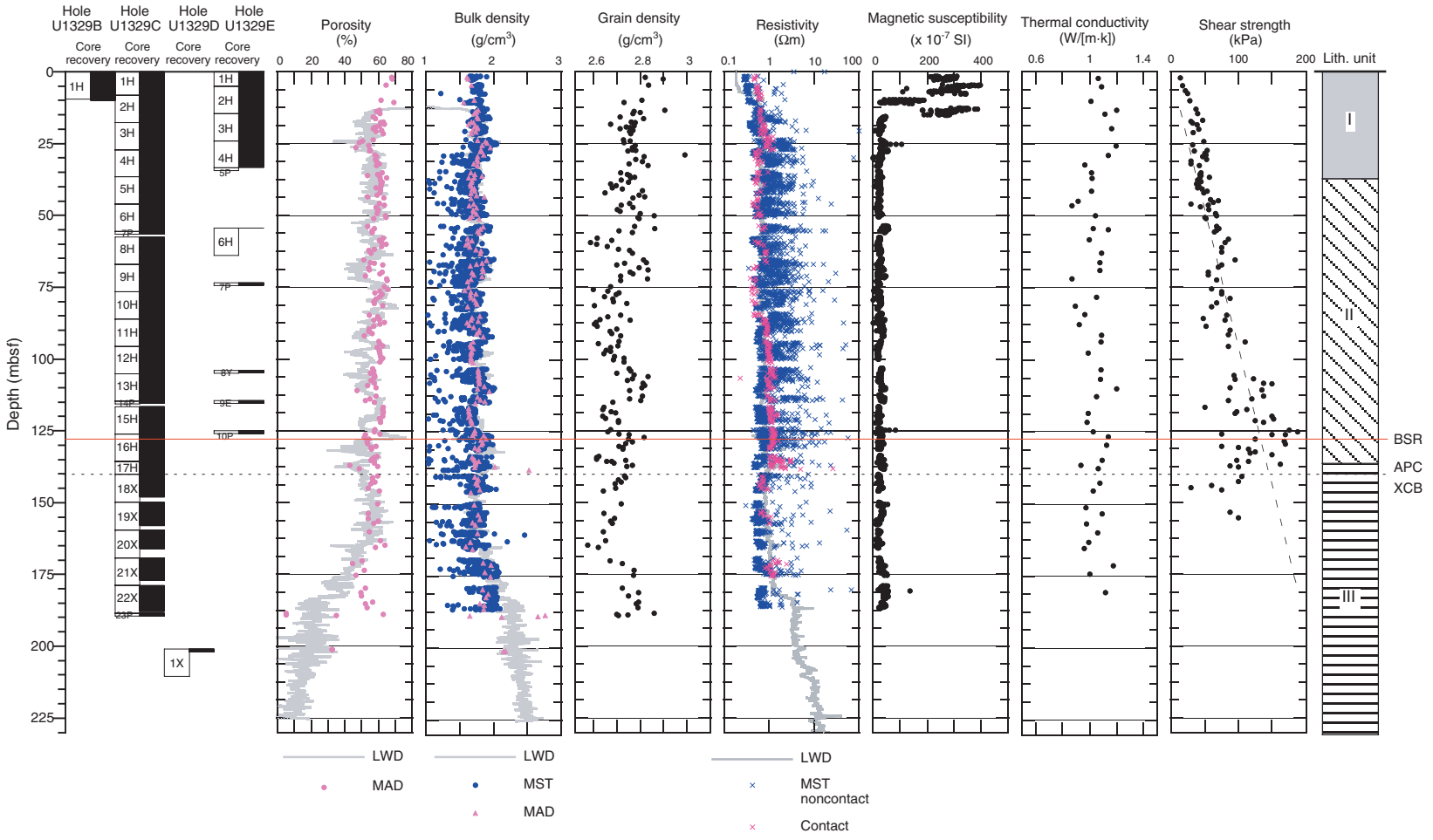

Figure F31. Combined infrared (IR) images of core liner temperature from Hole U1329C, compared to LWD resistivity and calculated pore water saturation from Hole U1329A. Core recovery and core handling time are also shown. RAB = resistivity-at-the-bit, BSR = bottom-simulating reflector. (This figure is also available in an **oversized format**).

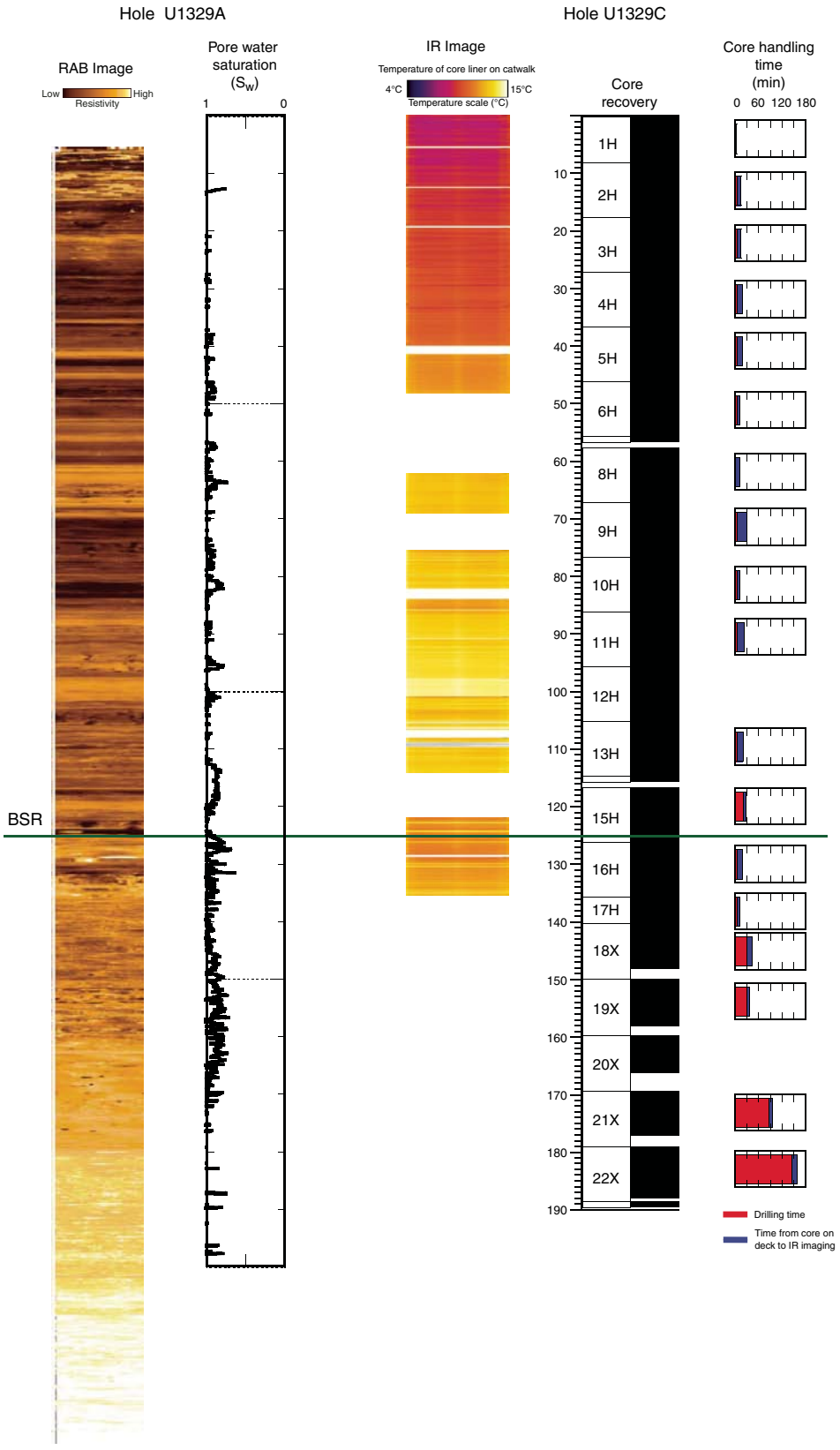

Figure F32. A. Downhole temperature based on concatenation of core liner temperatures averaged across each pixel row (see text for details), Hole U1329C. **B.** Detail of the temperature profile from 38 to 45 mbsf.

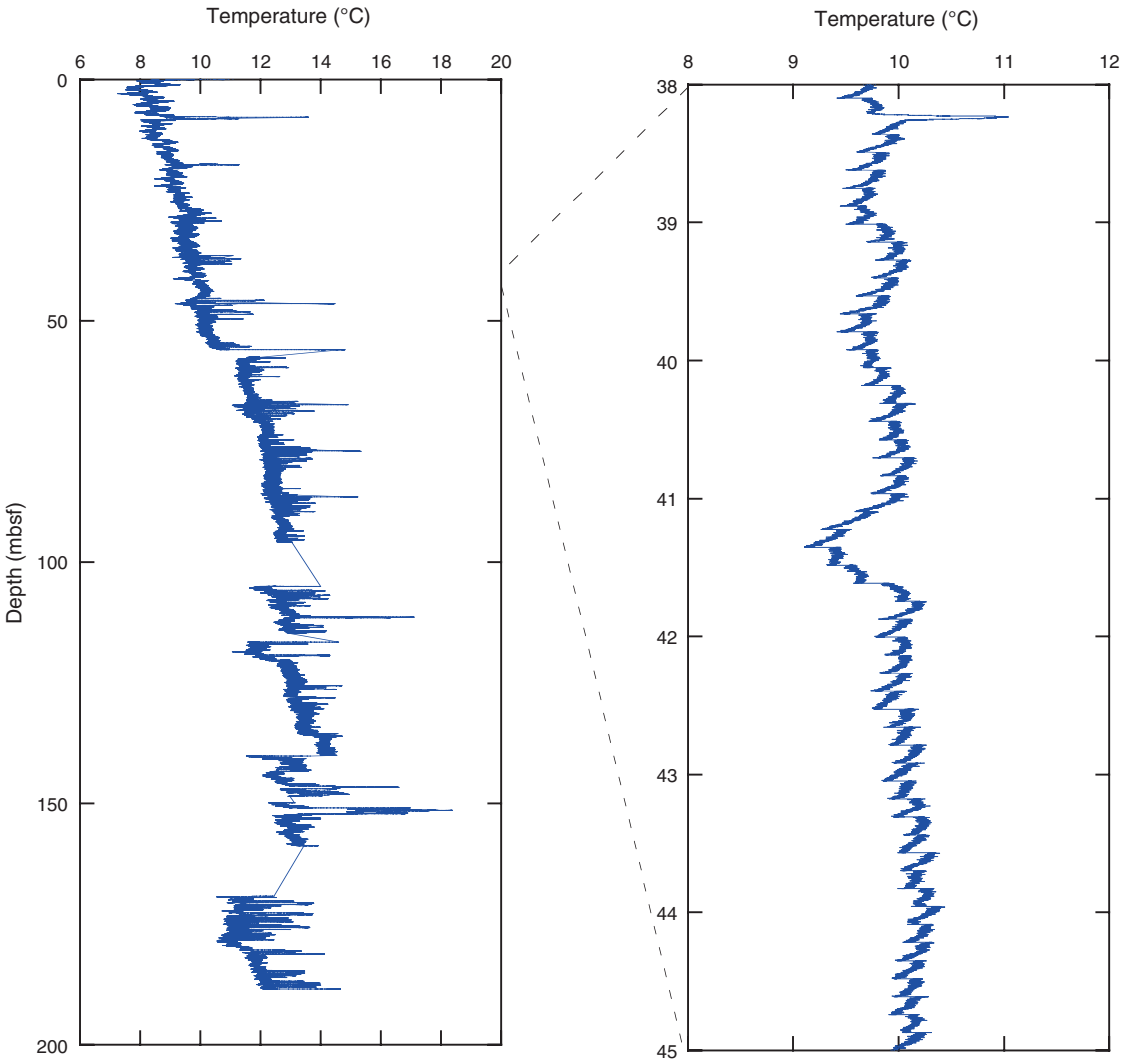

Figure F33. IR image of the bottom of a section destined for microbiological sampling and associated temperature profile.

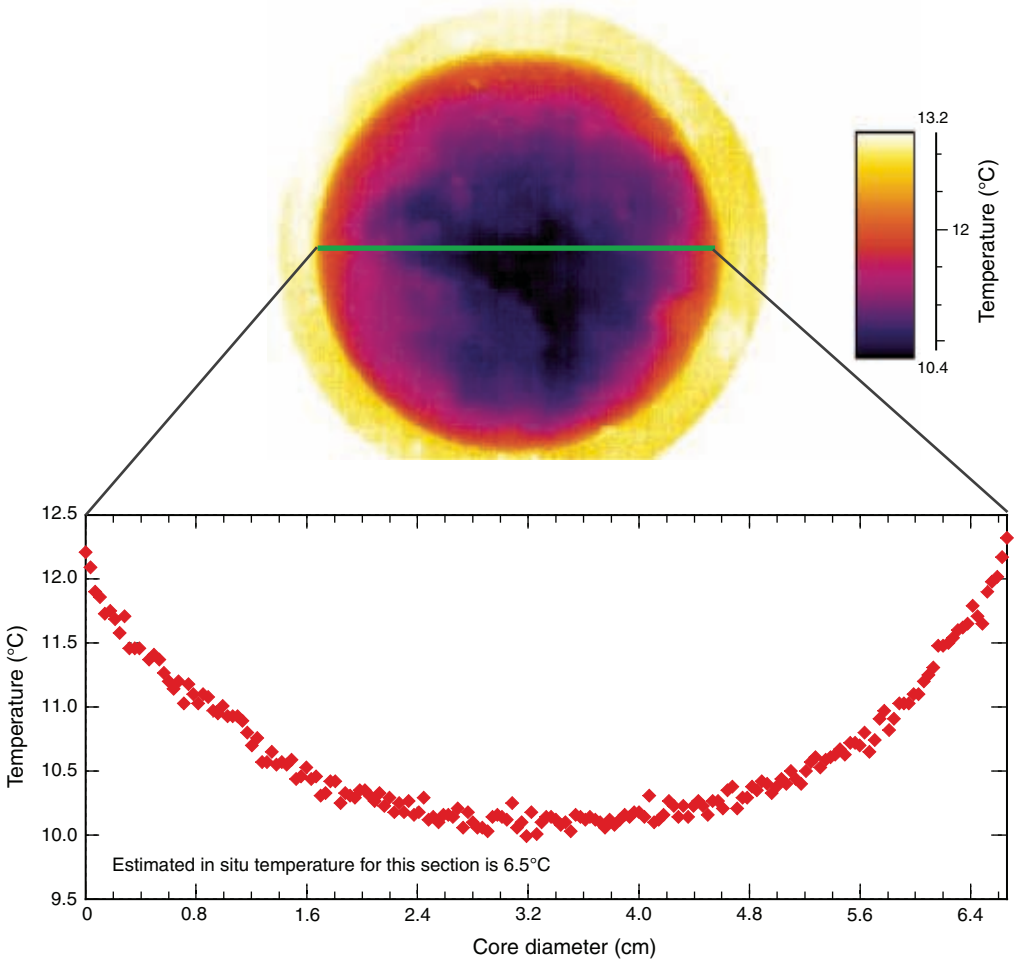

Figure F34. A. Moisture and density (MAD) bulk density from Hole U1329C compared to logging-while-drilling (LWD) density from Hole U1329A. **B.** MAD porosity from Hole U1329C compared to LWD porosity from Hole U1329A. **C.** Porosity averaged over 25 m intervals to further illustrate the anomalously low rate of porosity decrease with depth at this site. (Continued on next page.)

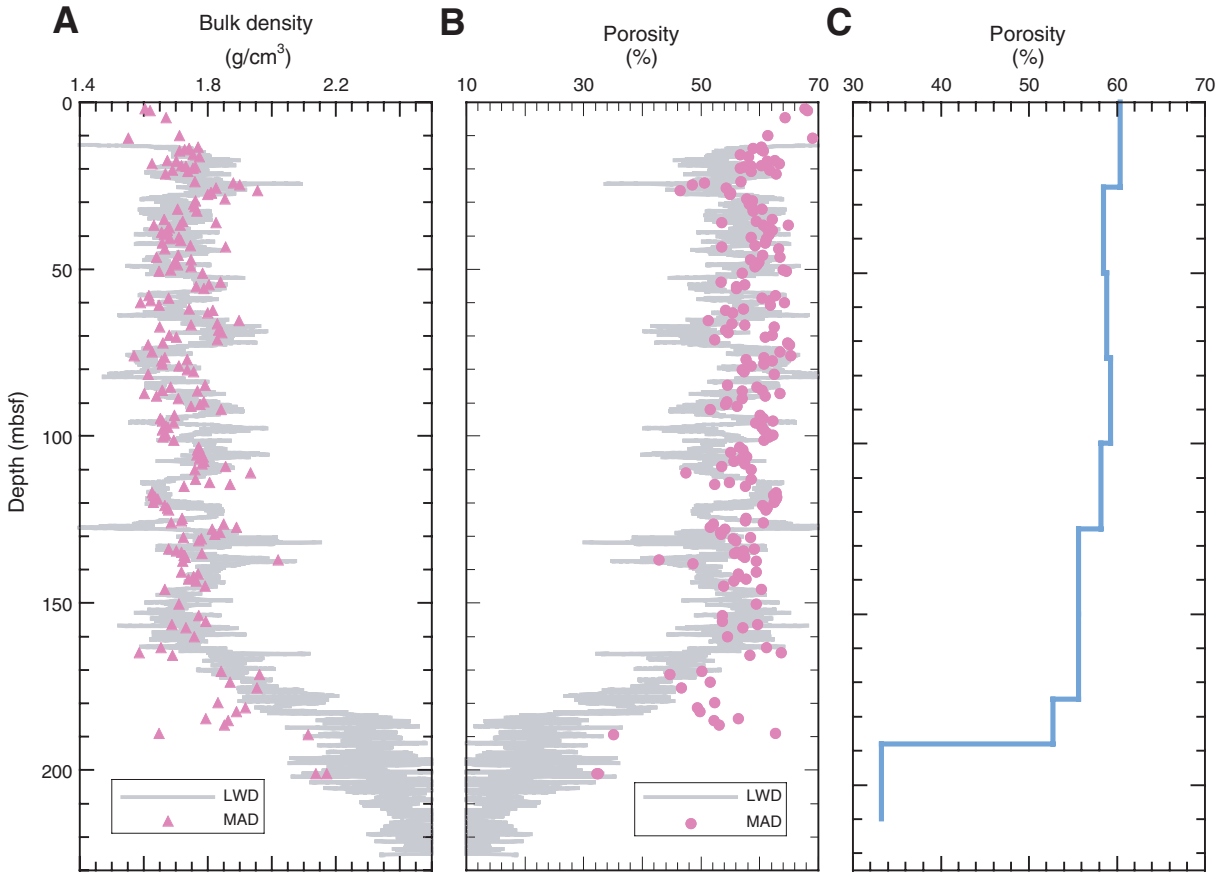

Figure F34 (continued). D. Examples of XCB cores from above and within the anomalous zone at 170–190 mbsf.

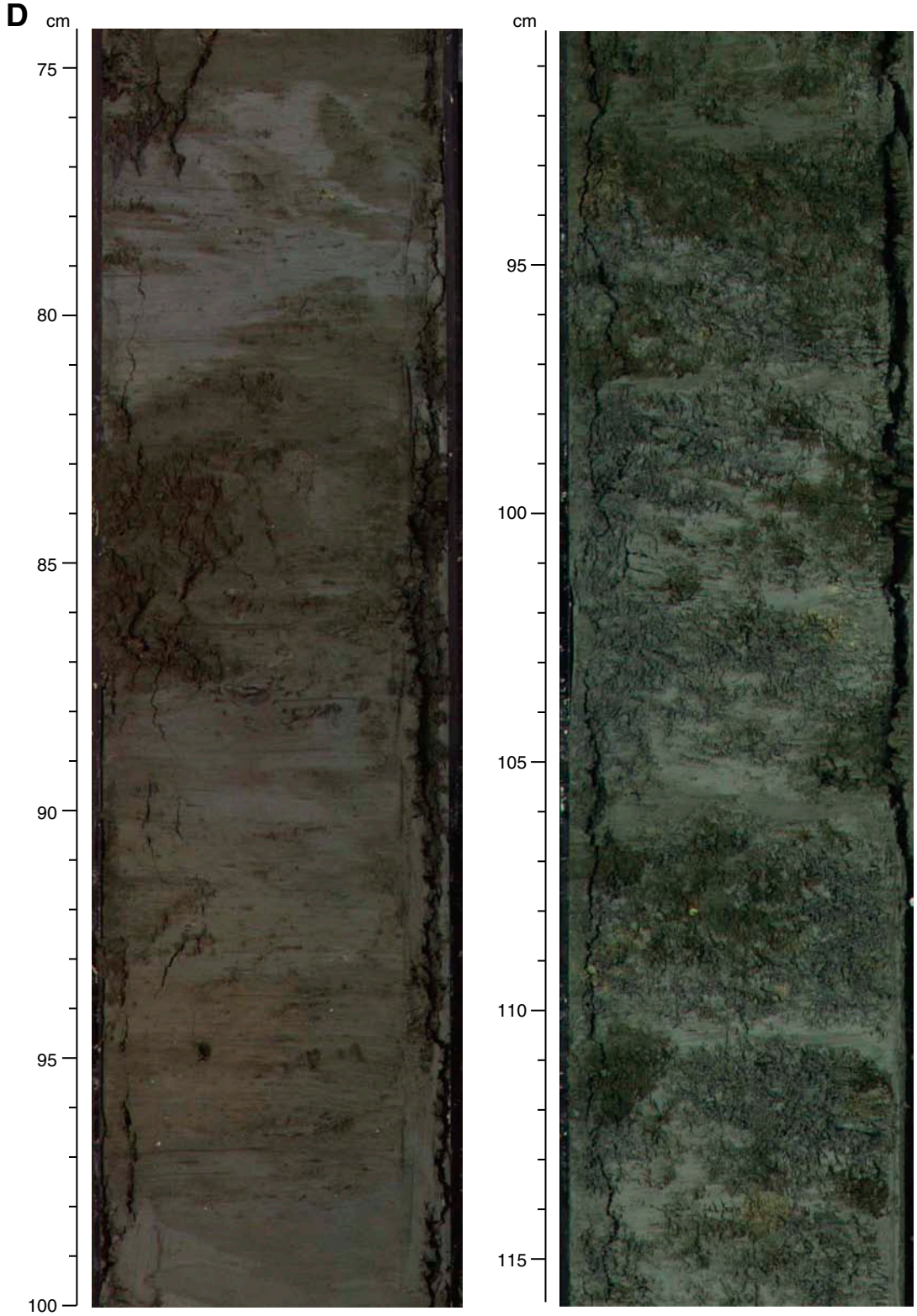

Interval 311-U1329C-18X-3, 75–100 cm

Interval 311-U1329C-22X-3, 91–115 cm

Figure F35. Magnetic susceptibility from Holes U1329B, U1329C, and U1329E. Correlation of the data between holes indicates depth shifts relative to Hole U1329C of 6.3 and –0.2 m for Holes U1329B and U1329E, respectively. These shifts in seafloor baseline have not been applied to the Expedition 311 data in the Janus database. The negative top depth for Hole U1329E results from a missed mudline core.

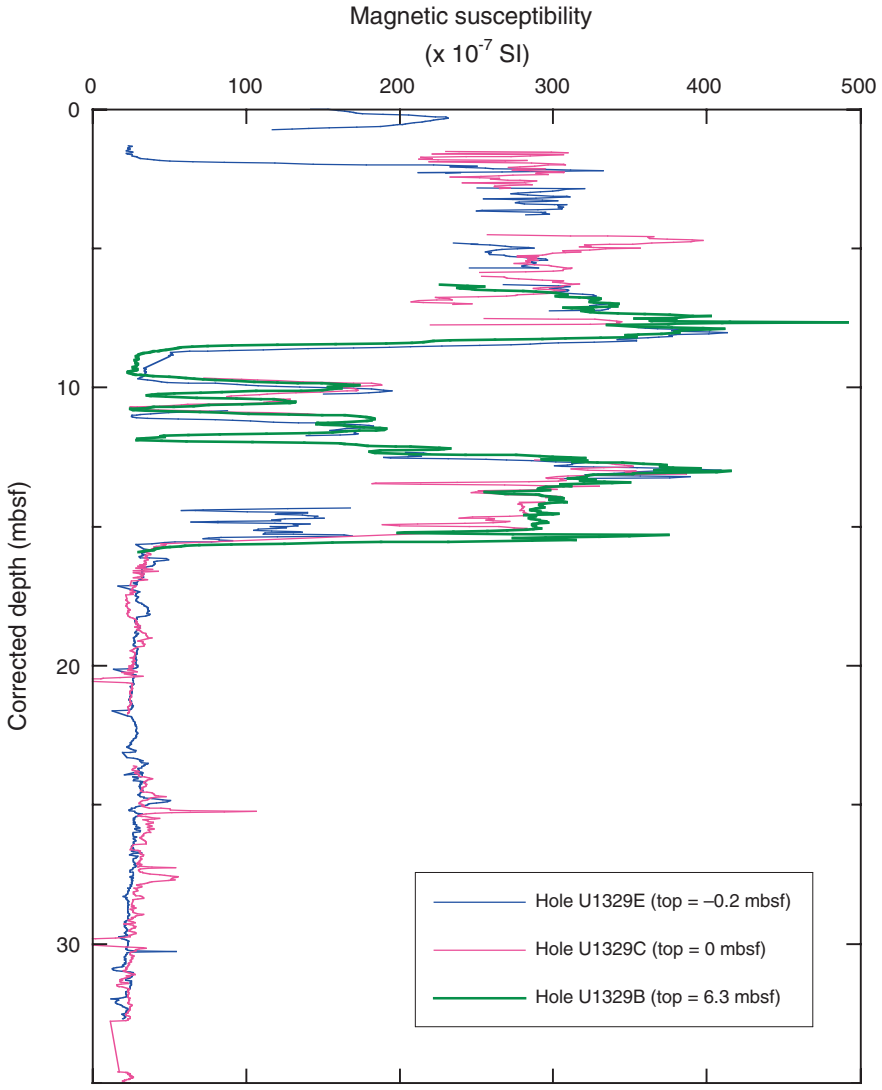

Figure F36. Comparison between multisensor track (MST) and Hamilton frame *P*-wave sensor (PWS) velocity from Holes U1329B, U1329C, and U1329E. Depths for Hole U1329B have been corrected for the 6.3 m offset documented in Figure F35.

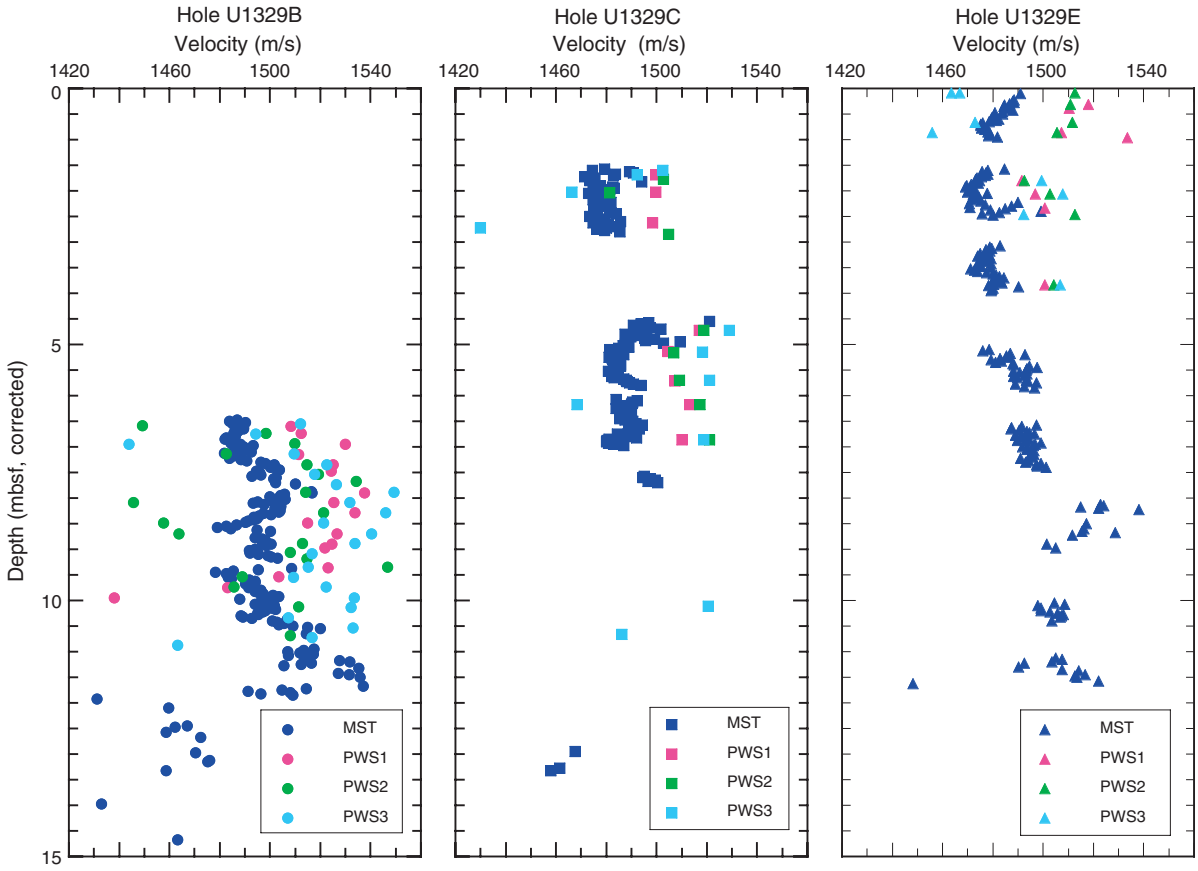

Figure F37. A. Torvane shear strength measurements from Hole U1329C. **B.** Ratio of shear strength to overburden pressure. This provides information on the degree of sediment underconsolidation or overconsolidation. **C.** Overburden pressure calculated from MAD bulk density data.

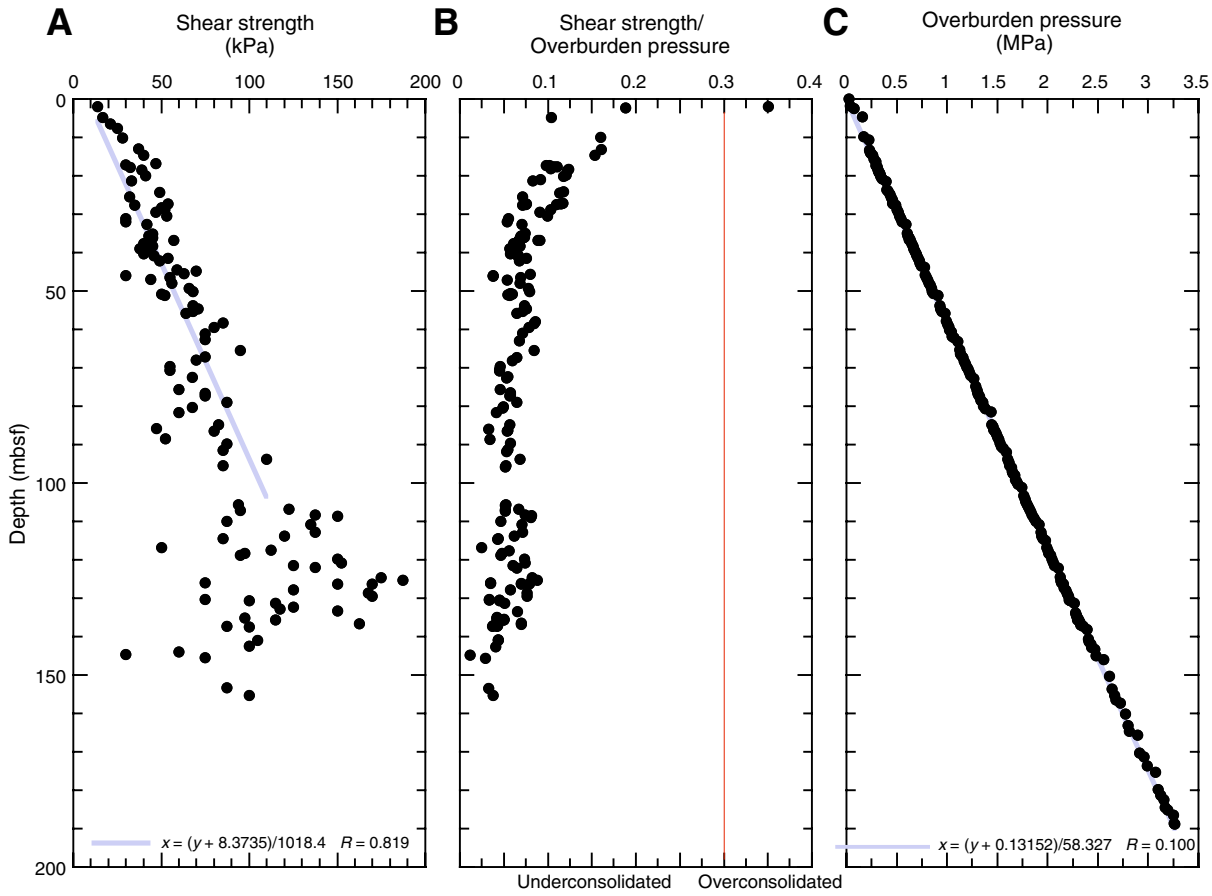

Figure F38. A. Comparison between contact resistivity from Hole U1329C and calculated pore water resistivity from pore water salinity. **B.** Formation factor (ratio of sediment resistivity to pore water resistivity) calculated from contact resistivity. **C.** Comparison of porosity derived from moisture and density (MAD) measurements and Archie's equation. (Continued on next page).

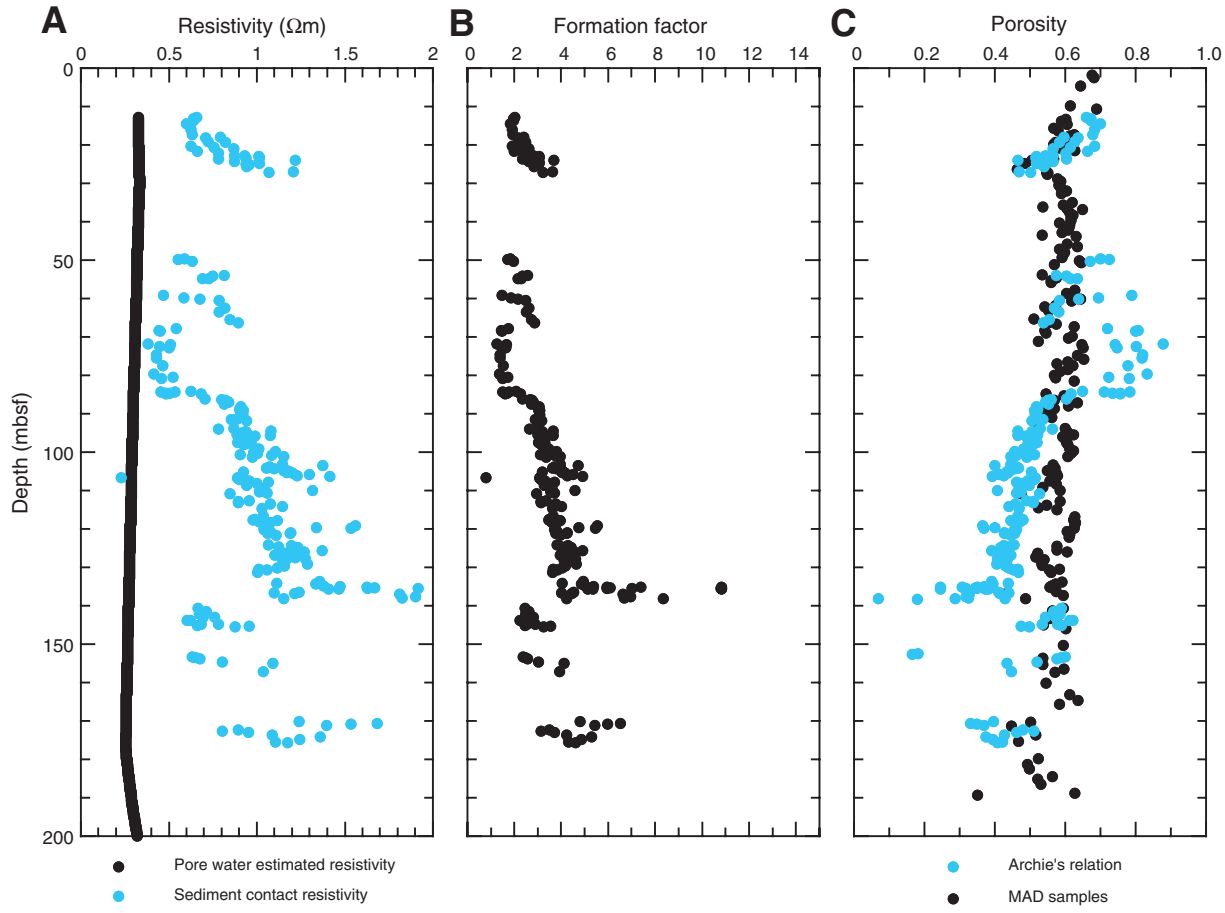

Figure F38 (continued). D. Comparison between noncontact resistivity from Hole U1329C and calculated pore water resistivity from pore water salinity. **E.** Formation factor calculated from noncontact resistivity. **F.** Comparison of porosity derived from moisture and density (MAD) measurements and Archie's equation.

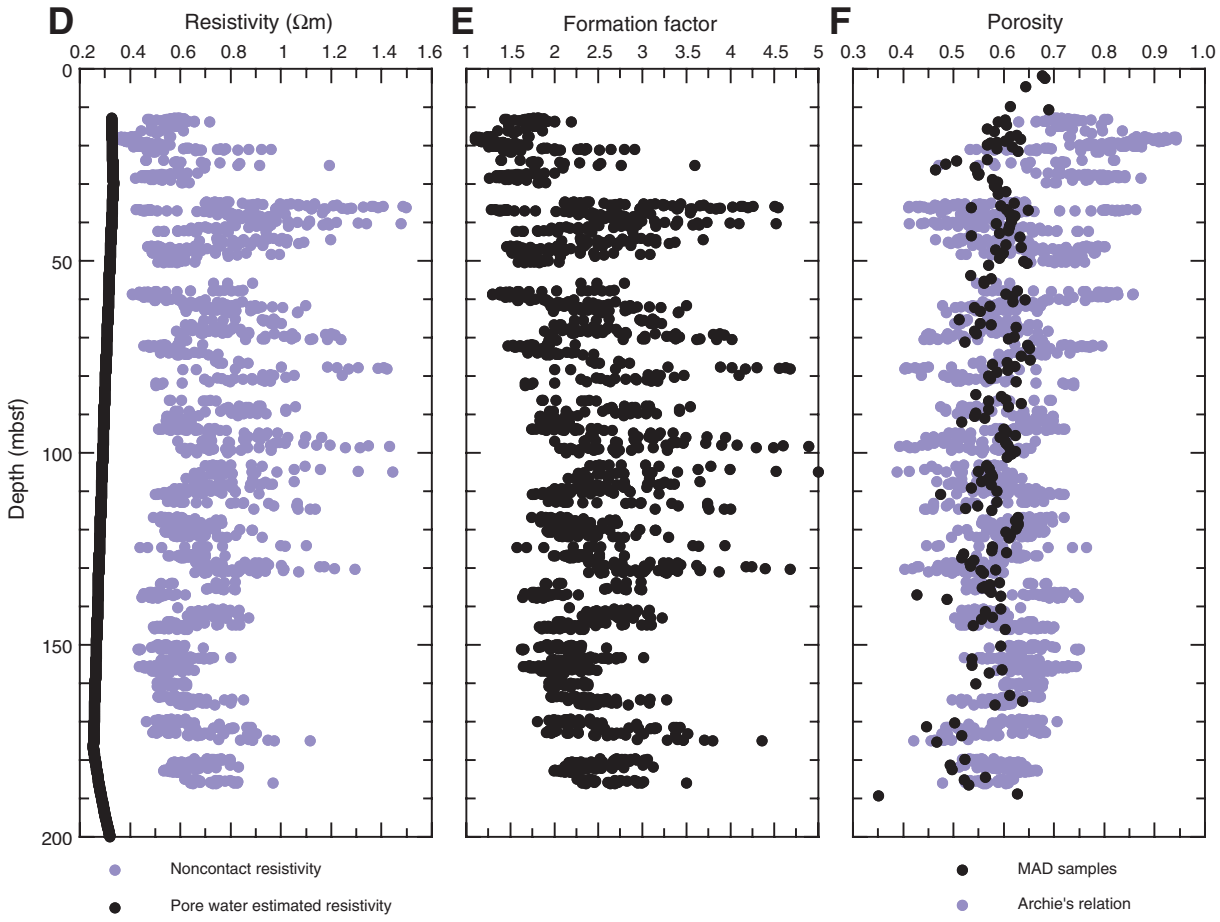

Figure F39. Thermal conductivity from Holes U1329B, U1329C, and U1329E. Values were corrected for in situ temperature and pressure using the equation of Pribnow et al. (2000). Open circles = uncorrected values, solid circles = corrected values, dashed line = correction factor, solid line = regional trend derived by Davis et al. (1990).

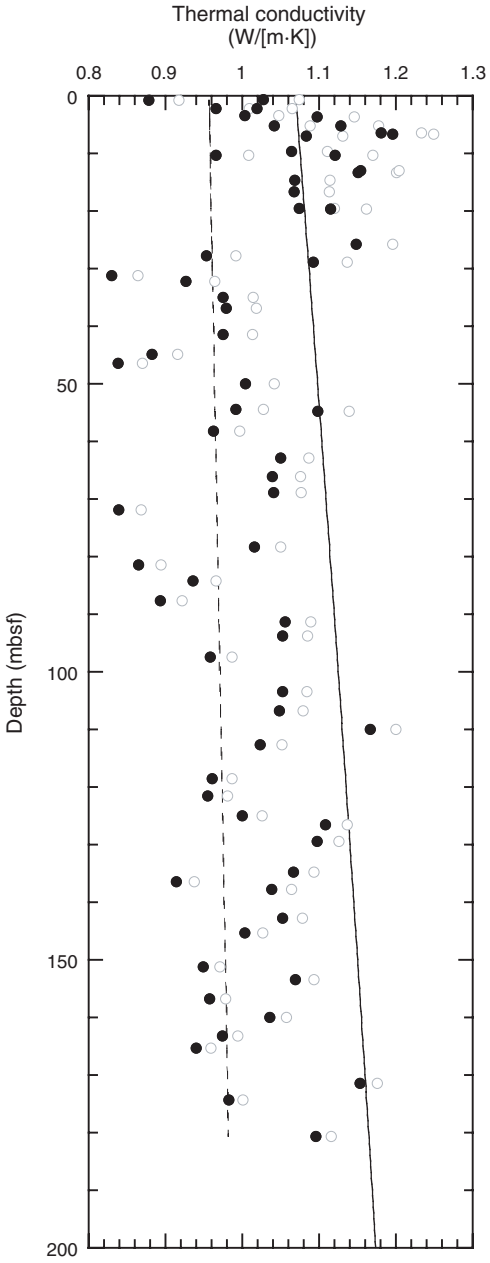

Figure F40. A. Advanced piston corer temperature (APCT) tool in situ temperature measurements from Site U1329. (Continued on next page).

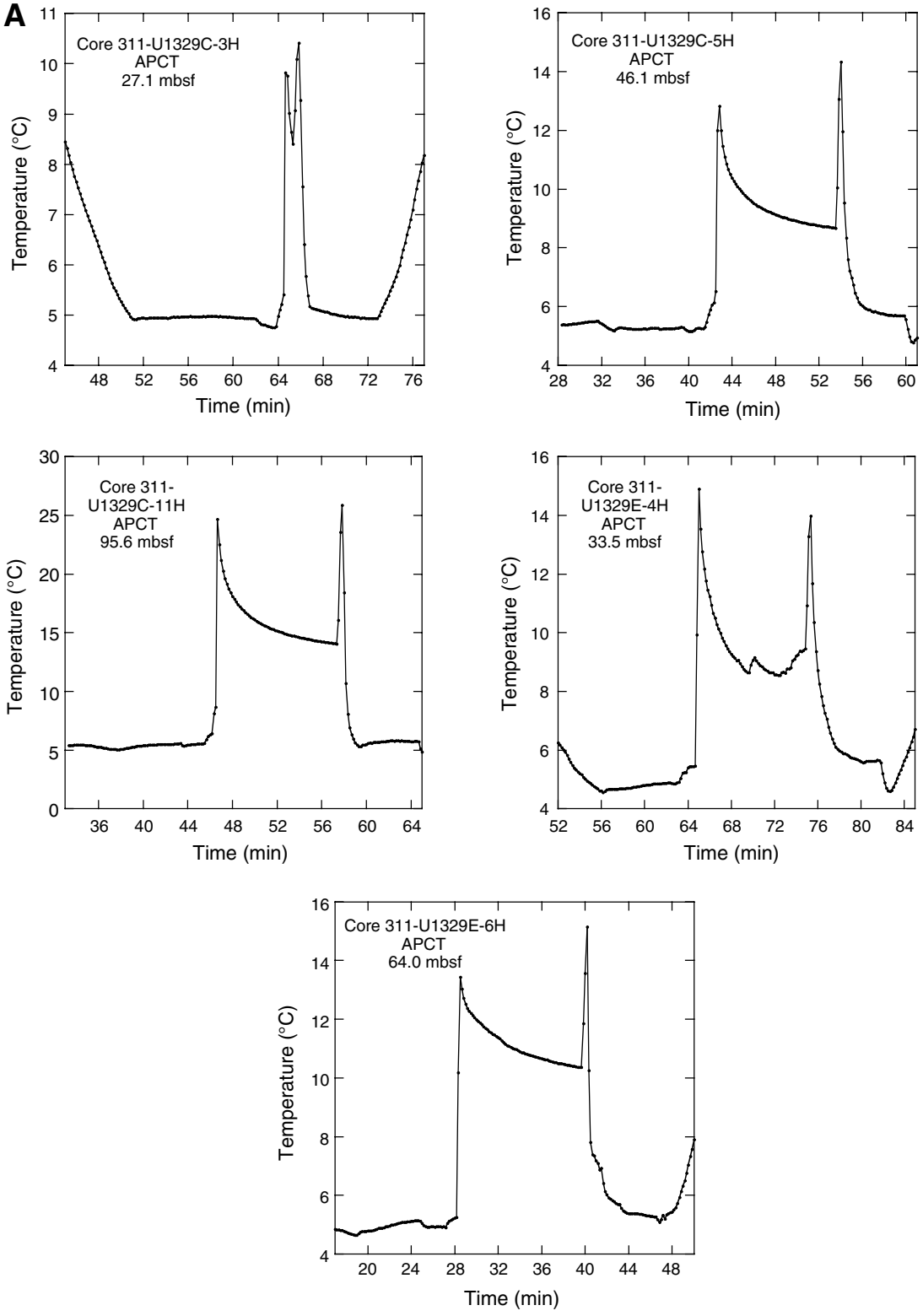

Figure F40 (continued). B. Third-generation advanced piston corer (APC3) temperature tool and Davis-Villinger Temperature Probe (DVTP) in situ temperature measurements from Site U1329. Both the upper (red) and lower (black) thermistors and the acceleration are shown for the DVTP, which provided excellent data at this first cored site. Unfortunately, it could not be used during the remainder of the expedition.

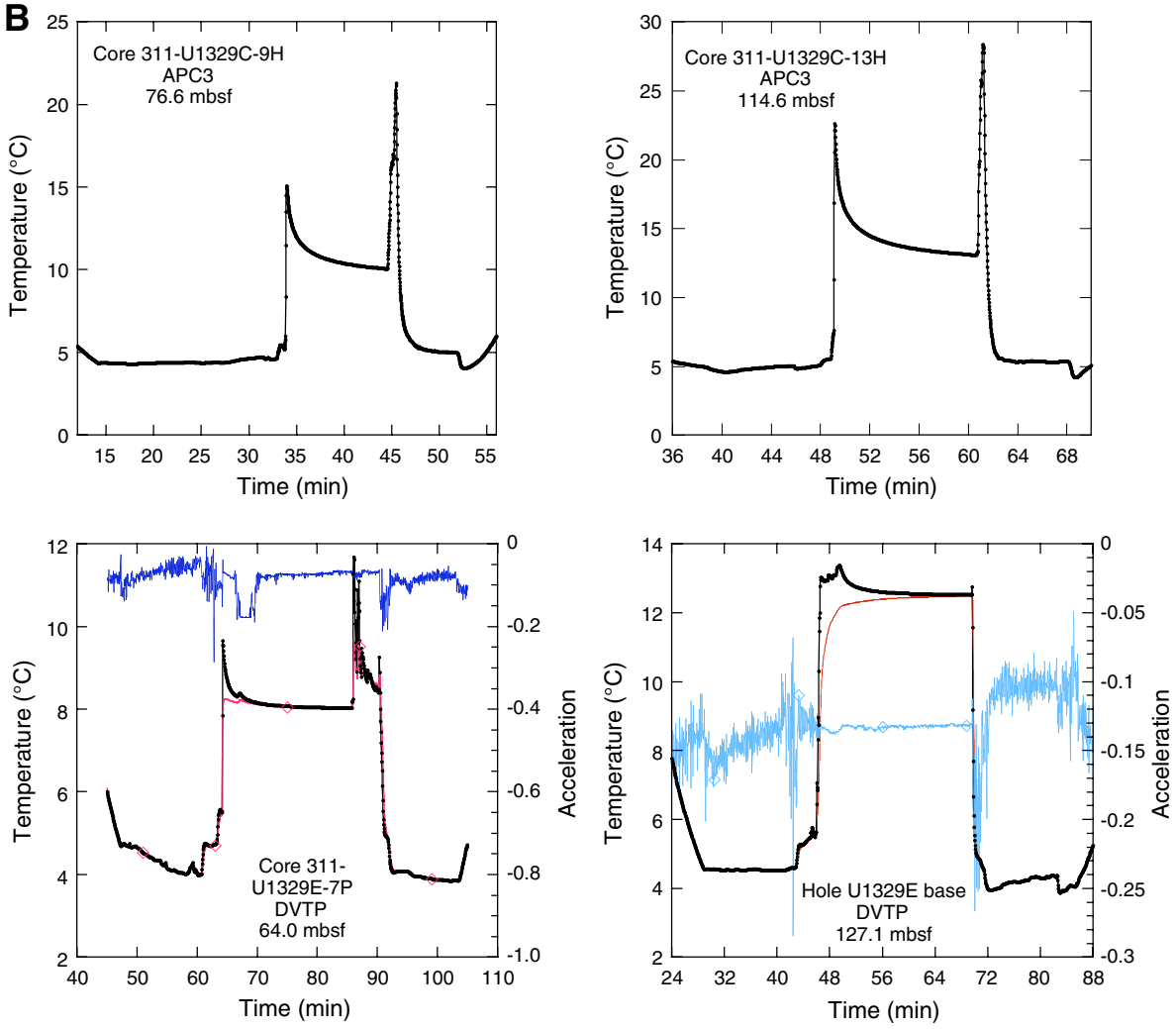

Figure F41. A. Geothermal gradient at Site U1329. Approximate uncertainty limits are shown by dashed red lines. Uncertainties on the slope and intercept of the best-fit line are given in the text. The stability boundary for methane hydrate at hydrostatic pressure is shown (calculated using CSMHY; Sloan, 1998) for water with salinities of 0%, 3.5%, and 10%. **B.** Seawater temperature from hydrographic profiles for the locations shown in C. Data were collected during Cruise PR06_18DD9309 in May 1993 and obtained from **www.ewoce.org** in September 2005. The depths of the drill sites are indicated. **C.** Location of drill sites (red squares) and hydrographic stations (black circles).

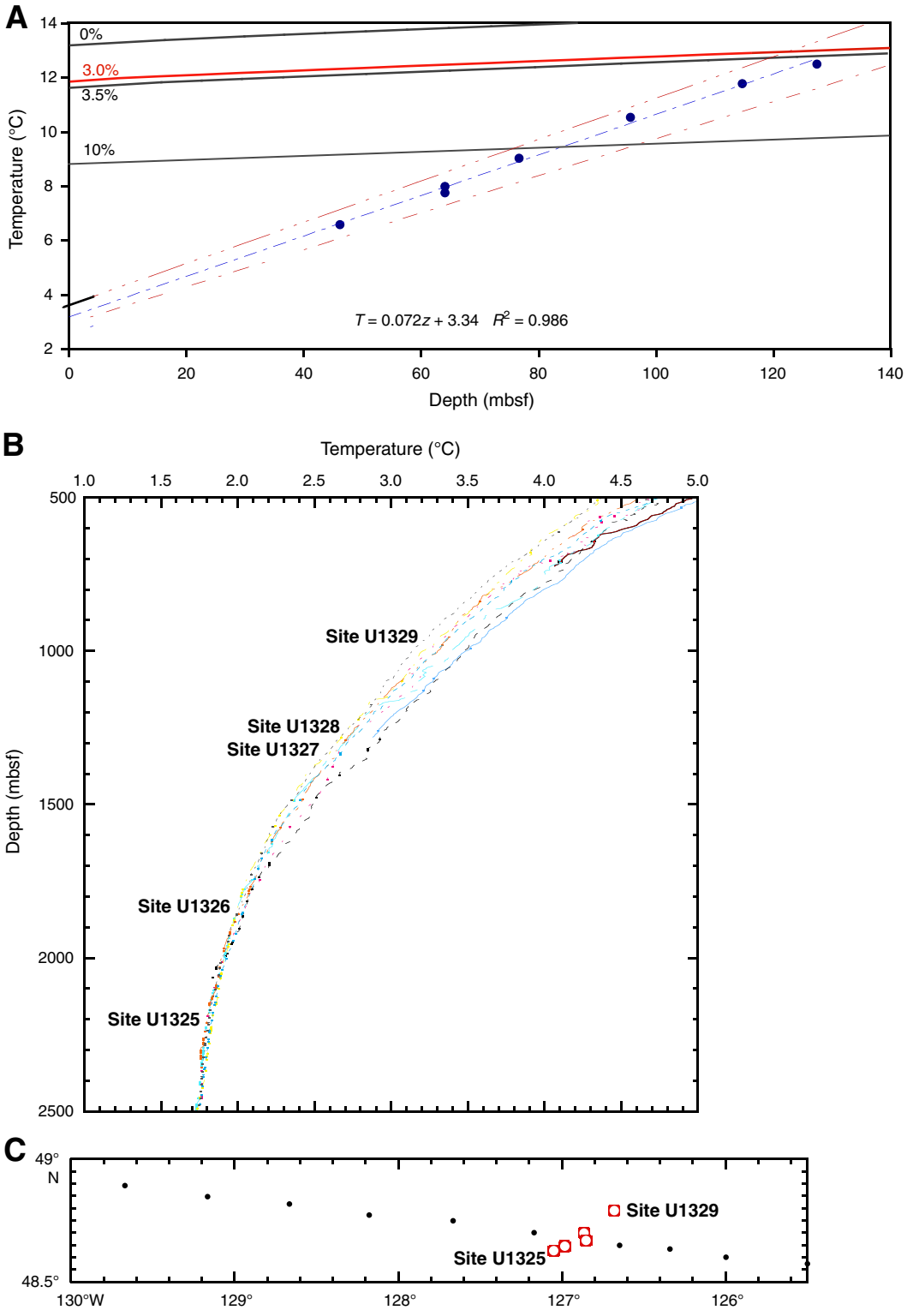

Figure F42. Paleomagnetic data after 20-mT alternating-field demagnetization from Hole U1329C.

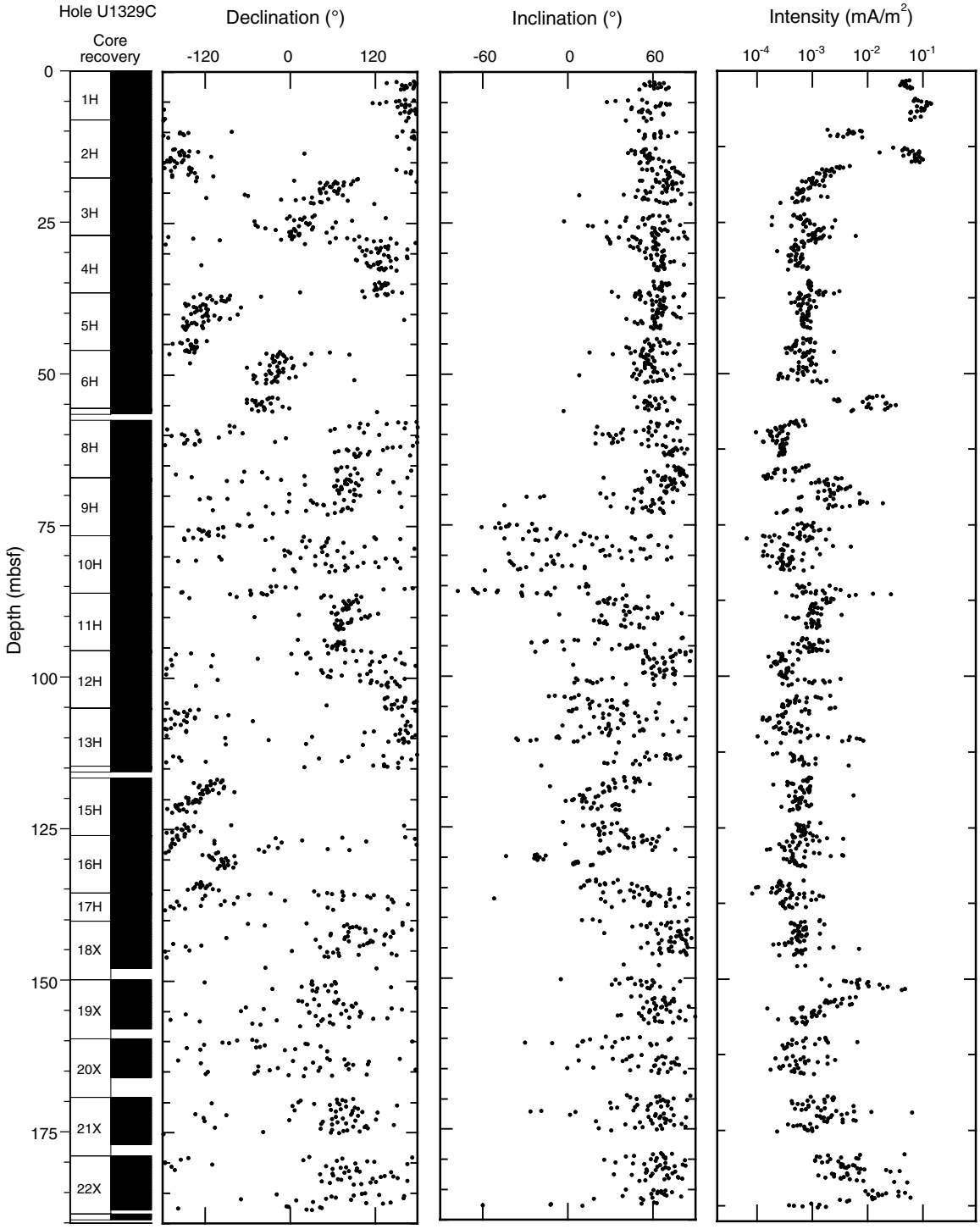

Figure F43. Temperature and pressure vs. elapsed time for each pressure core deployment as recorded by the corer's internal data logger. Deployment and recovery are shaded orange, operation at coring depth is shaded yellow, and autoclave immersion in the ice shuck is shaded blue. Arrow shows low-pressure event during coring of Core 311-U1329C-23P. No data are available for Core 311-U1329E-5P. Cores 311-U1329C-14P and 311-U1329E-8Y were not chilled after retrieval. (Continued on next page).

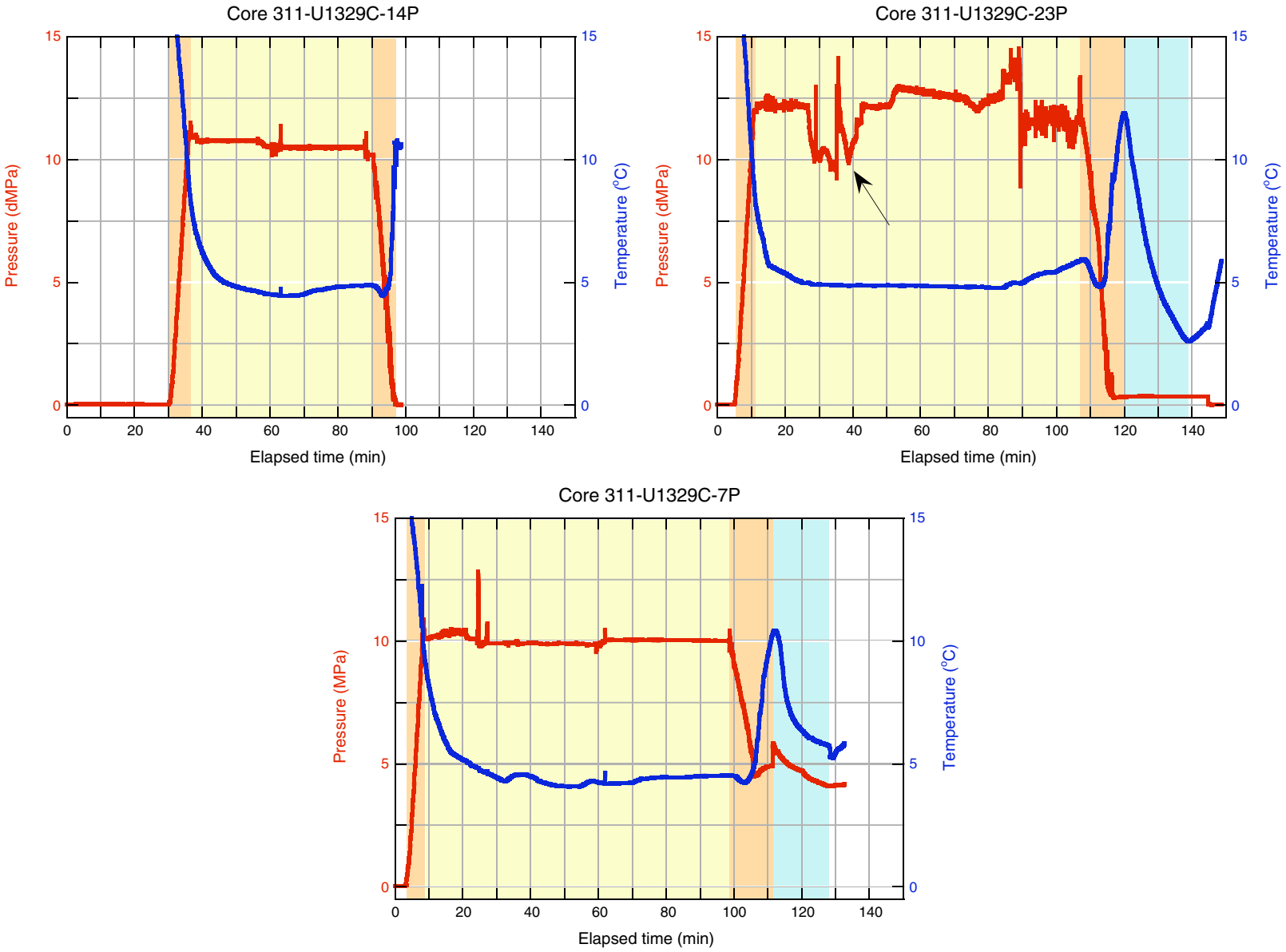

Figure F43 (continued). Temperature and pressure vs. elapsed time.

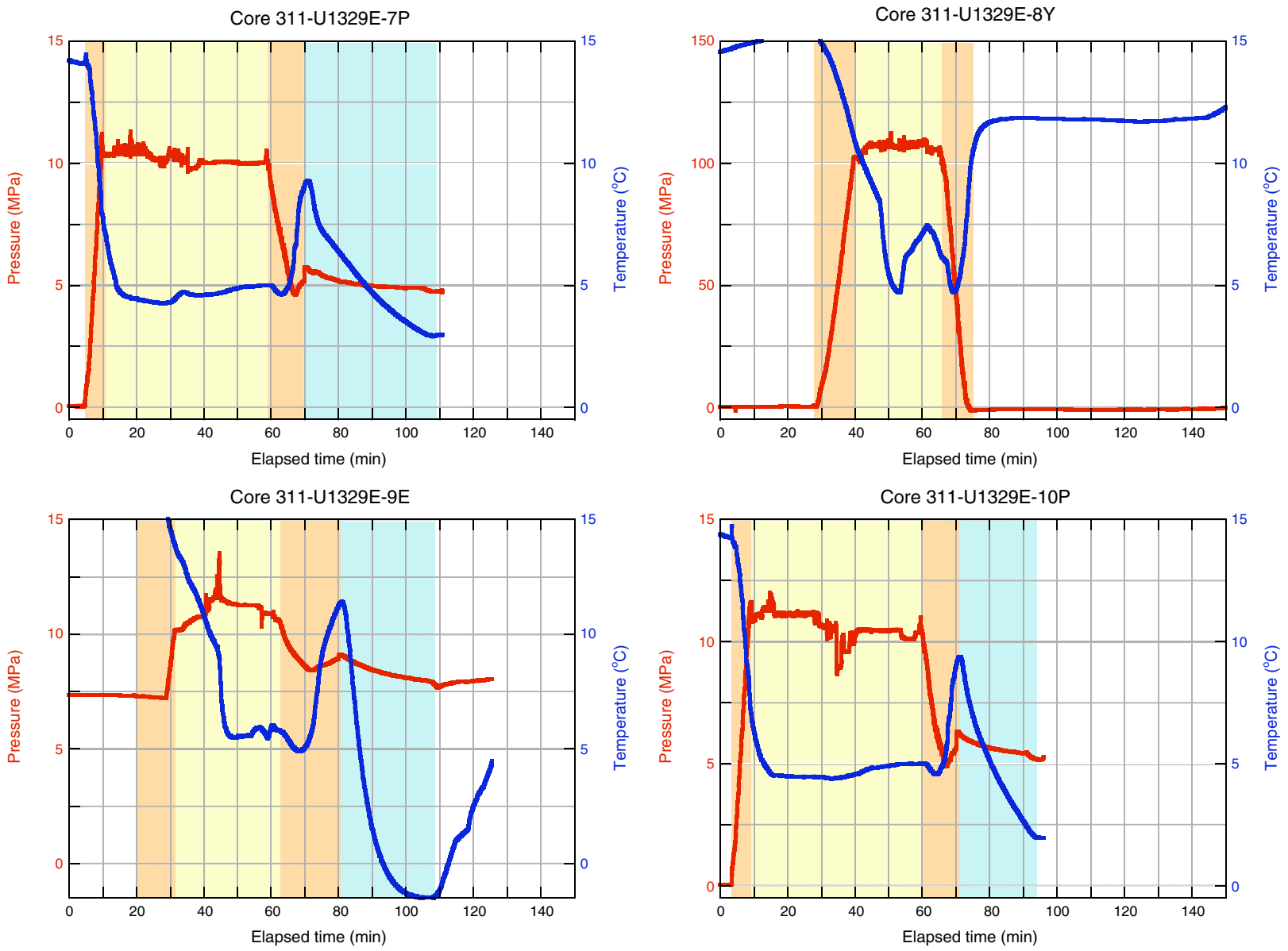

Figure F44. Temperature vs. pressure for all pressure core deployments, showing trajectories relative to gas hydrate stability at 20 and 35 ppt salinity (Xu, 2002, 2004). Circles = final temperature and pressure of autoclave prior to data logger removal, squares = pressure and temperature conditions in the cold laboratory van.

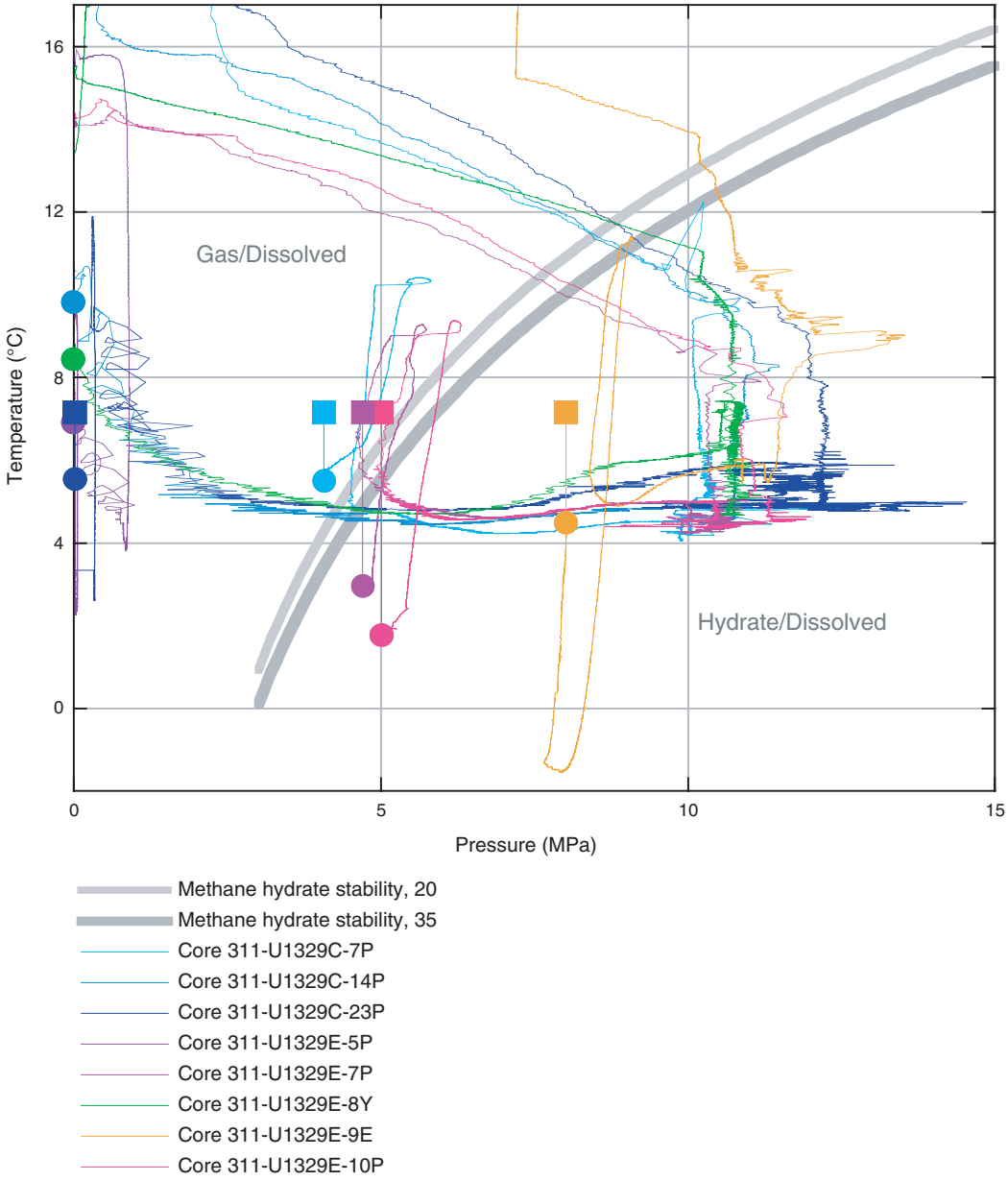

Figure F45. Methane phase diagram, with total methane concentration measured from the four degassed PCS cores and one degassed HRC core at Site U1329. Methane concentration for Core 311-U1329E-9E is shown based on the entire core pore volume (yellow) and the pore volumes of the high-velocity zones (orange). The seafloor temperature and thermal gradient were taken from **"In situ temperature profile,"** the salinity profile was taken from Table **T3,** and methane saturation was calculated according to Xu (2002, 2004). BSR = bottom-simulating reflector.

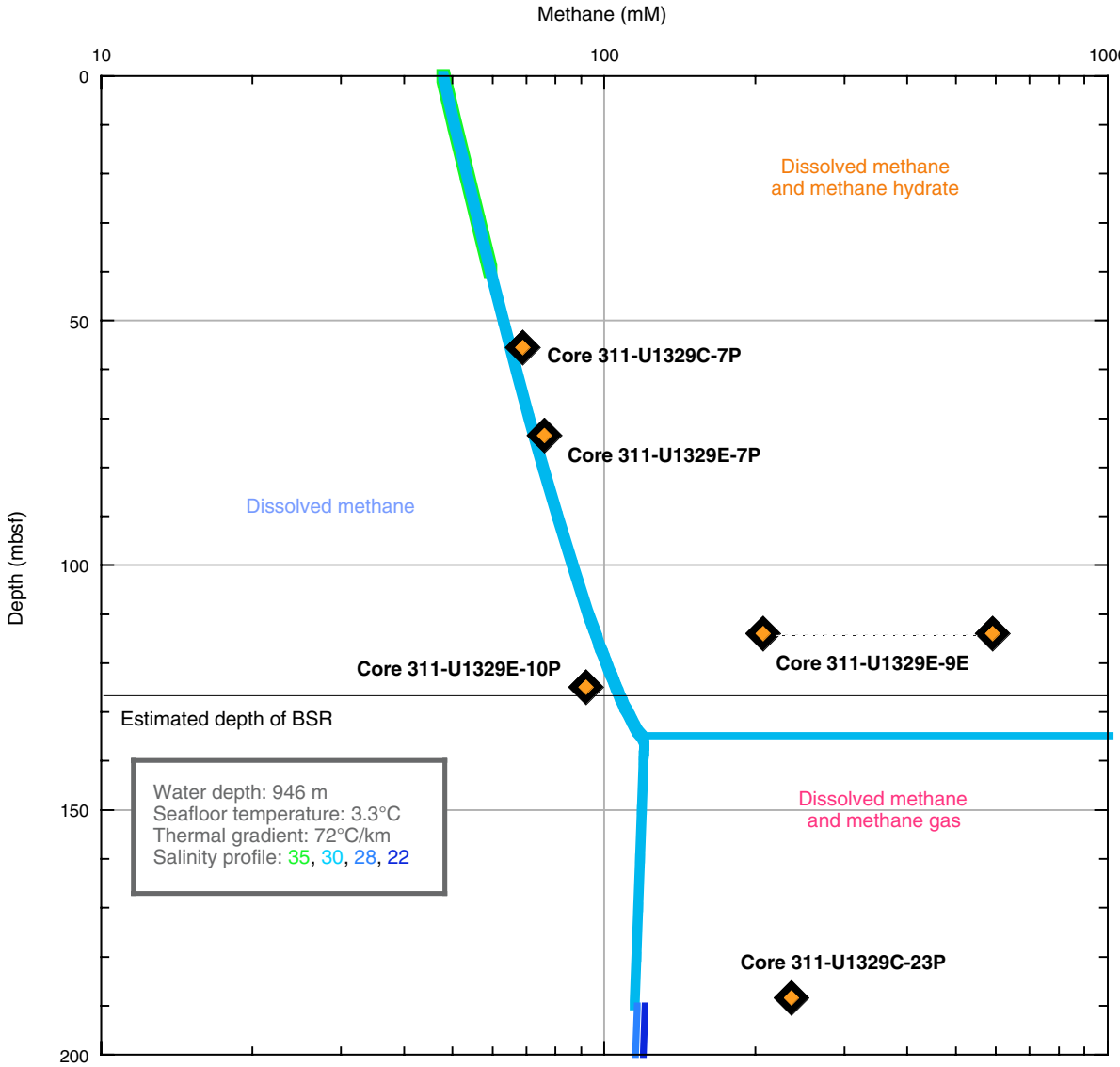

Figure F46. Pressure vs. released gas volume for PCS cores during degassing experiments at Site U1329. Pressure was not recorded for Core 311-U1329C-7P, and pressure was constant and low (<0.25 MPa) for Core 311-U1329C-23P.

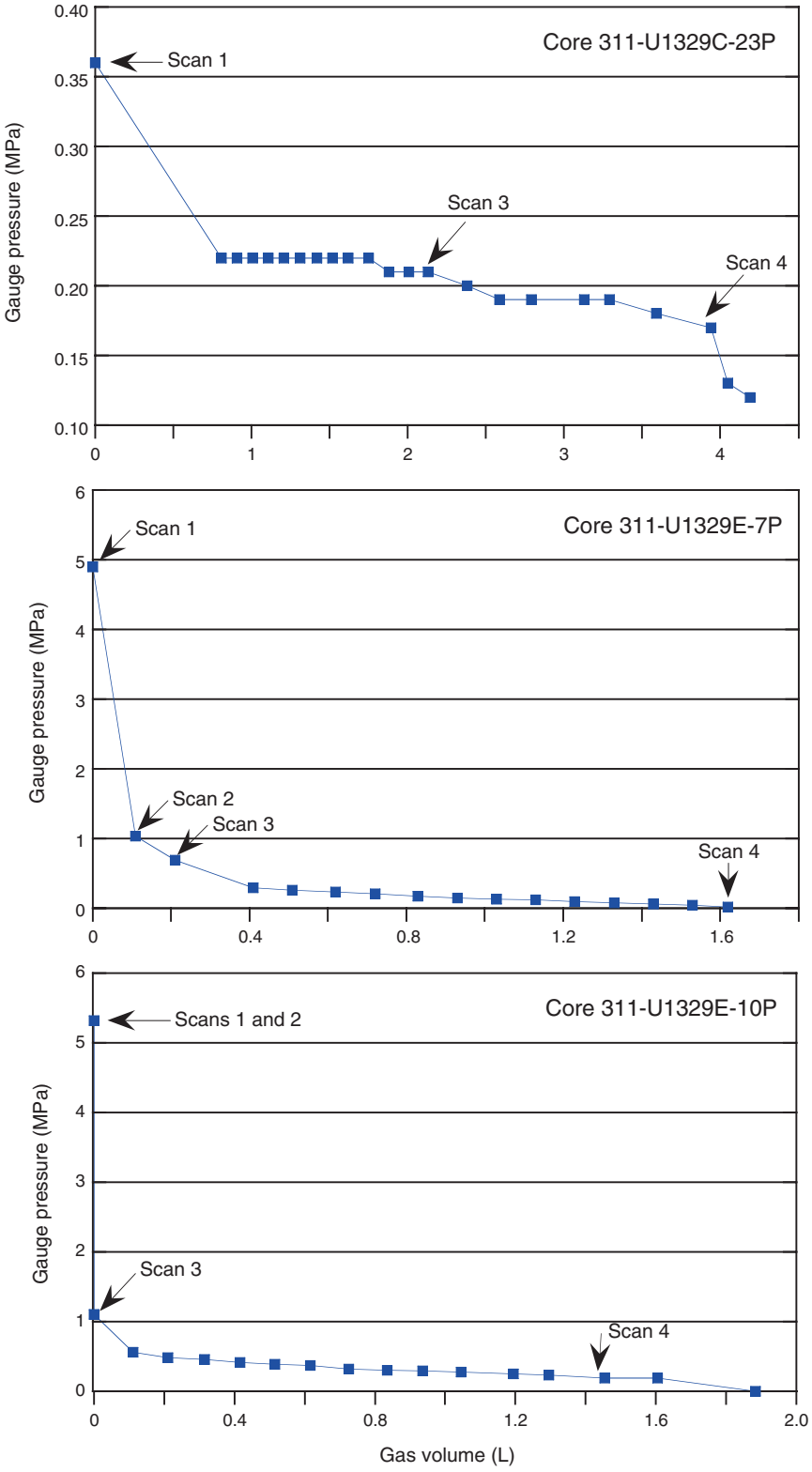

Figure F47. Summary of data collected from PCS cores at Site U1329, including gamma ray density scans collected during degassing experiments, X-ray images collected before degassing, line scan images collected after degassing, and chlorinity data collected in selected zones. Gamma ray density scans are shown as differential density plots (i.e., as profiles from which the initial profile has been subtracted). **A.** Core 311-U1329C-7P. (Continued on next three pages).

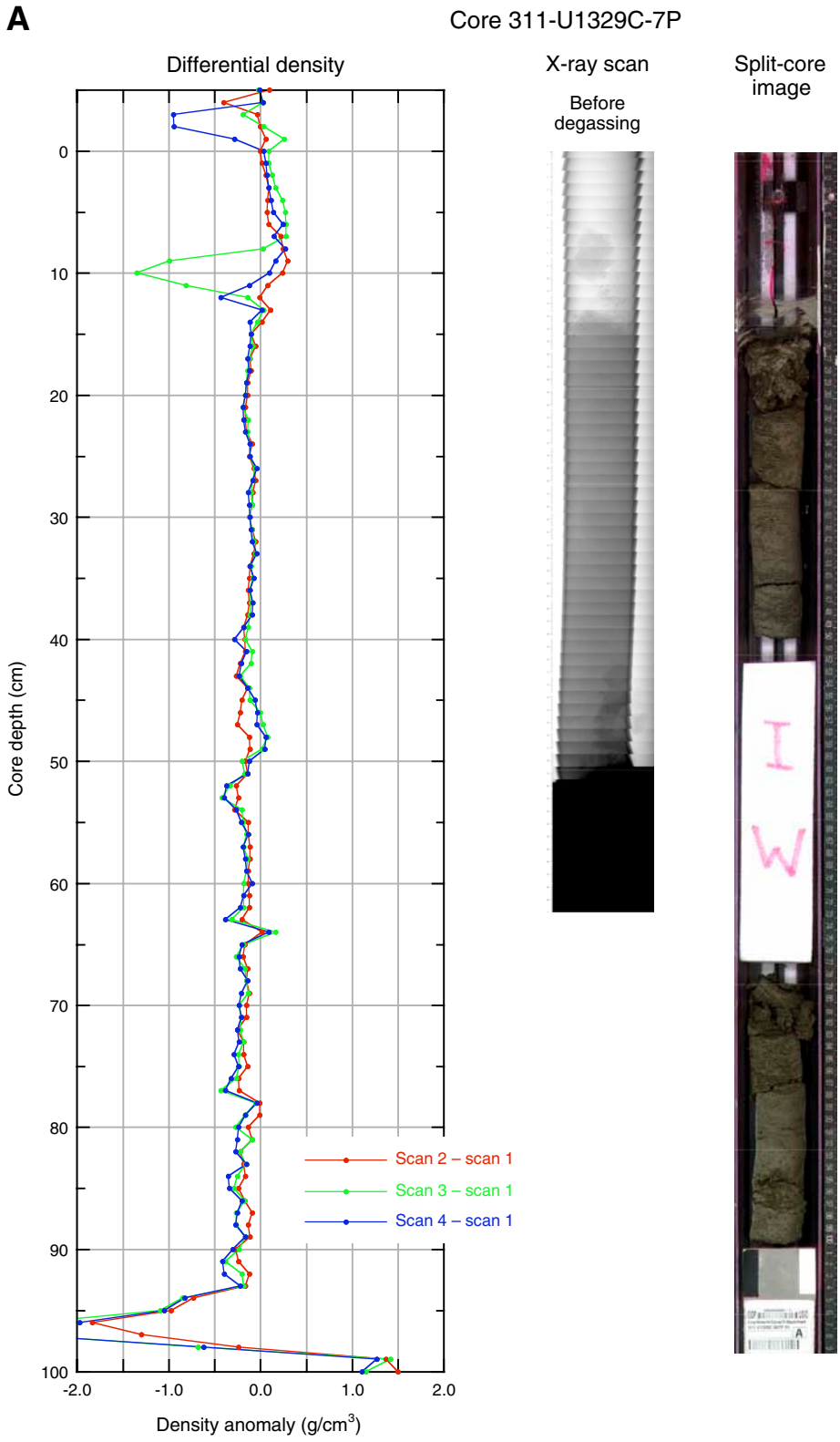

Figure F47 (continued). B. Core 311-U1329C-23P.

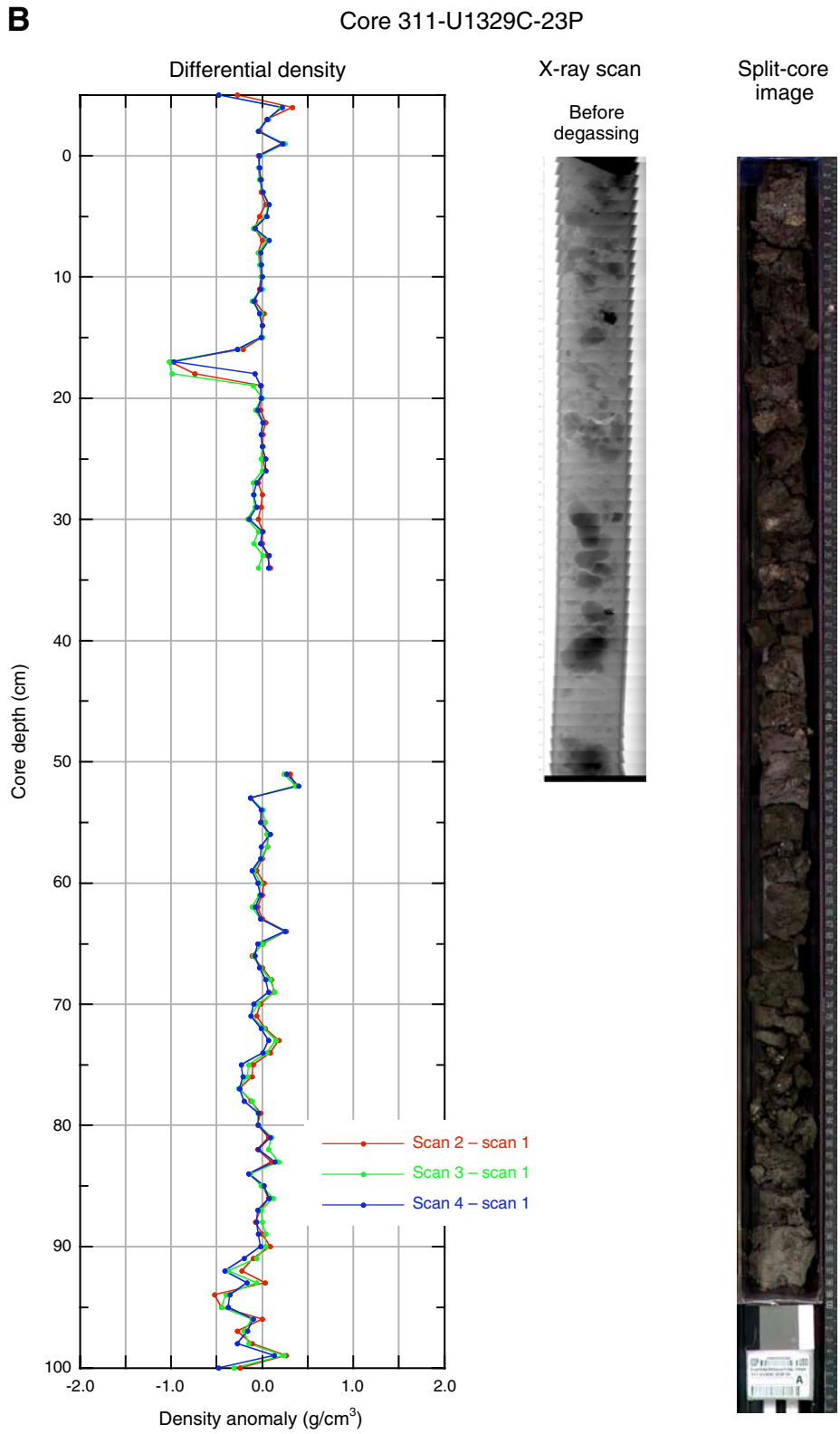

Figure F47 (continued). C. Core 311-U1329E-7P.

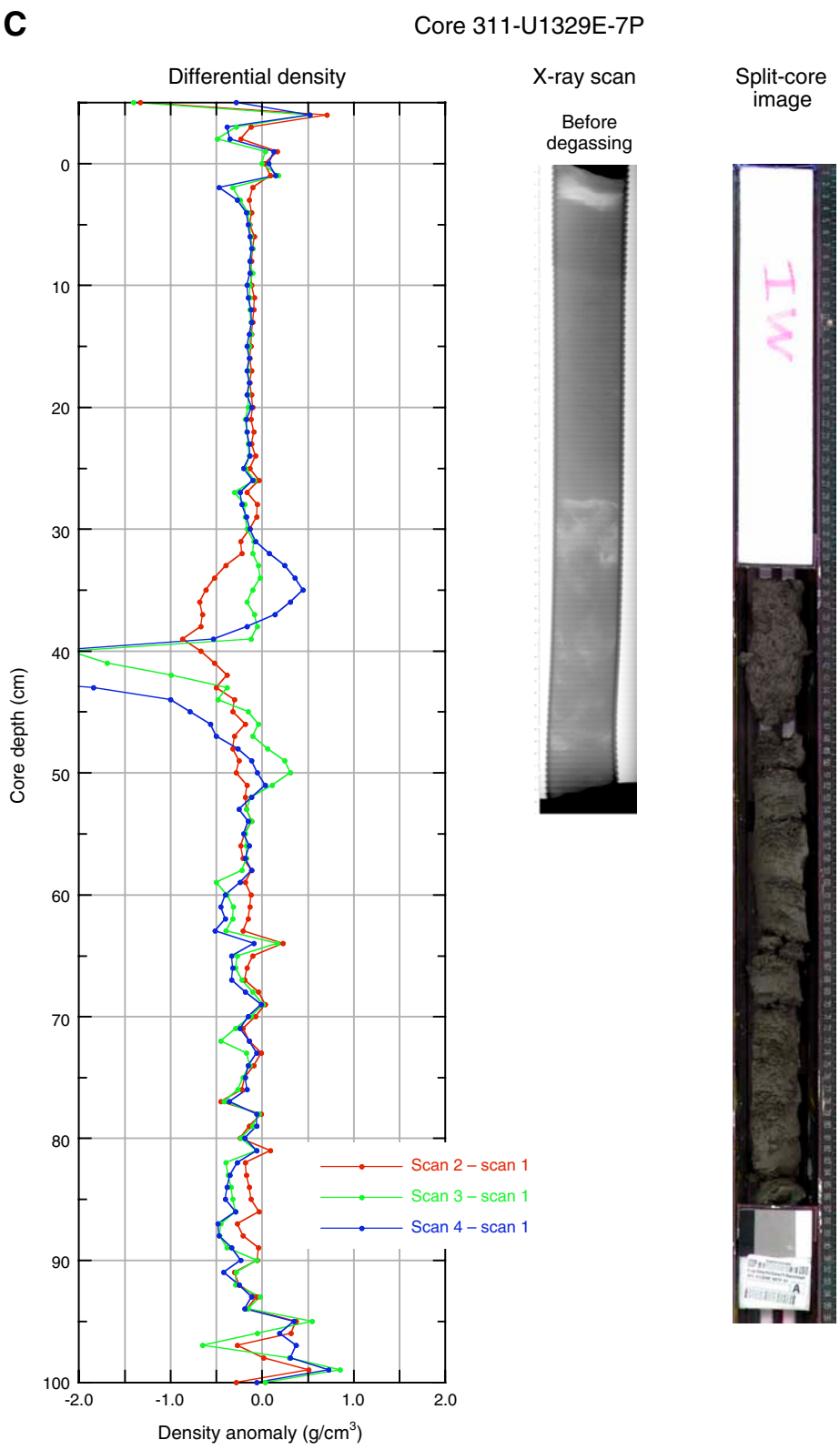

Figure F47 (continued). D. Core 311-U1329E-10P.

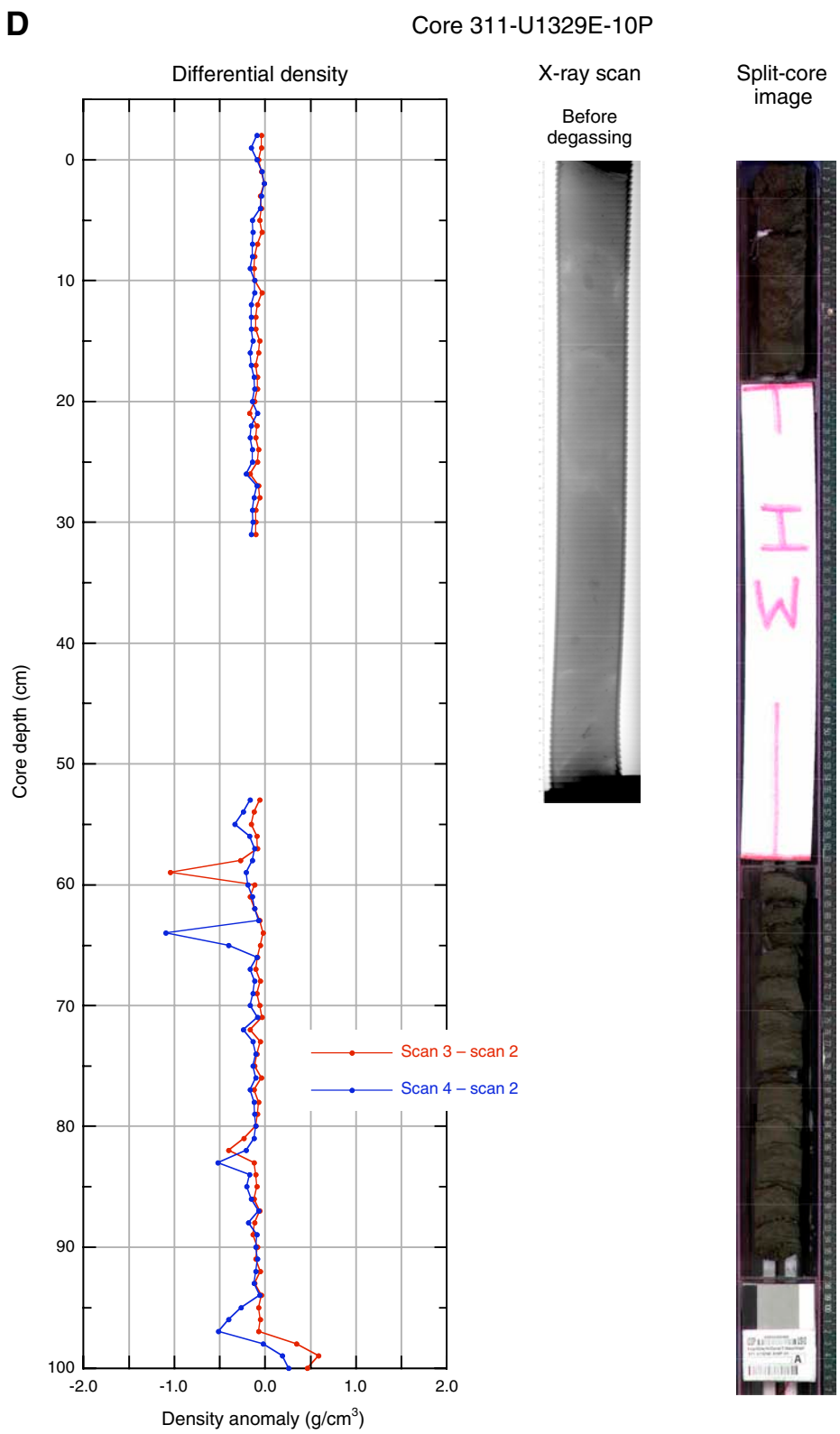

Figure F48. Data collected at in situ pressure (12 MPa) and 7°C for Core 311-U1329E-9E, including gamma ray density, *P*-wave velocity, and X-ray image. Two low-density, high-velocity zones are highlighted in color. X-ray images have been stretched 250% in the cross-core direction to show detail.

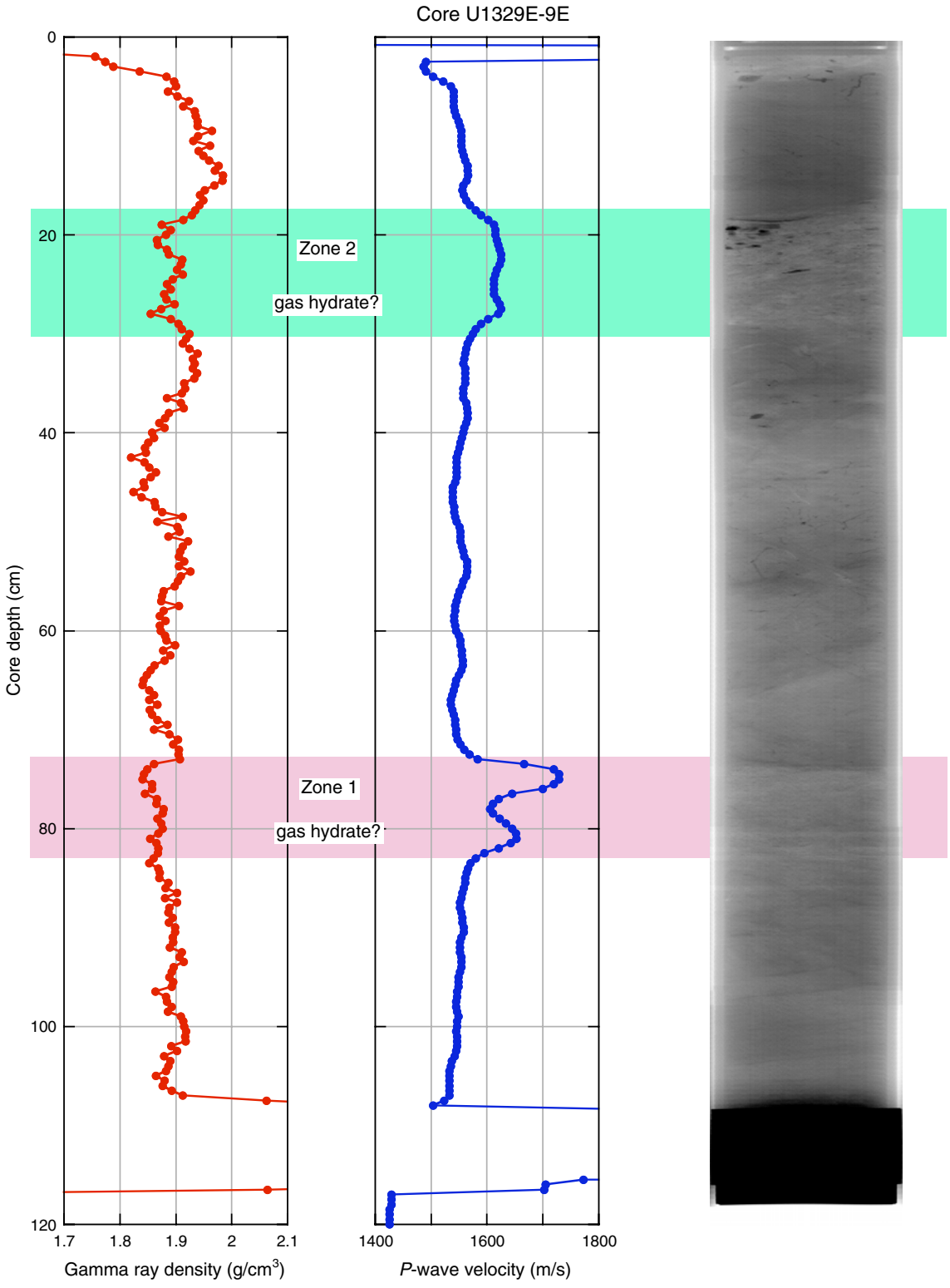

Figure F49. Gamma ray density vs. *P*-wave velocity for Core 311-U1329E-9E, showing the anomalous trend in Zones 1 and 2 (identified in Fig. F48), which evolved gas when degassed (Fig. F51) and contained gas hydrate.

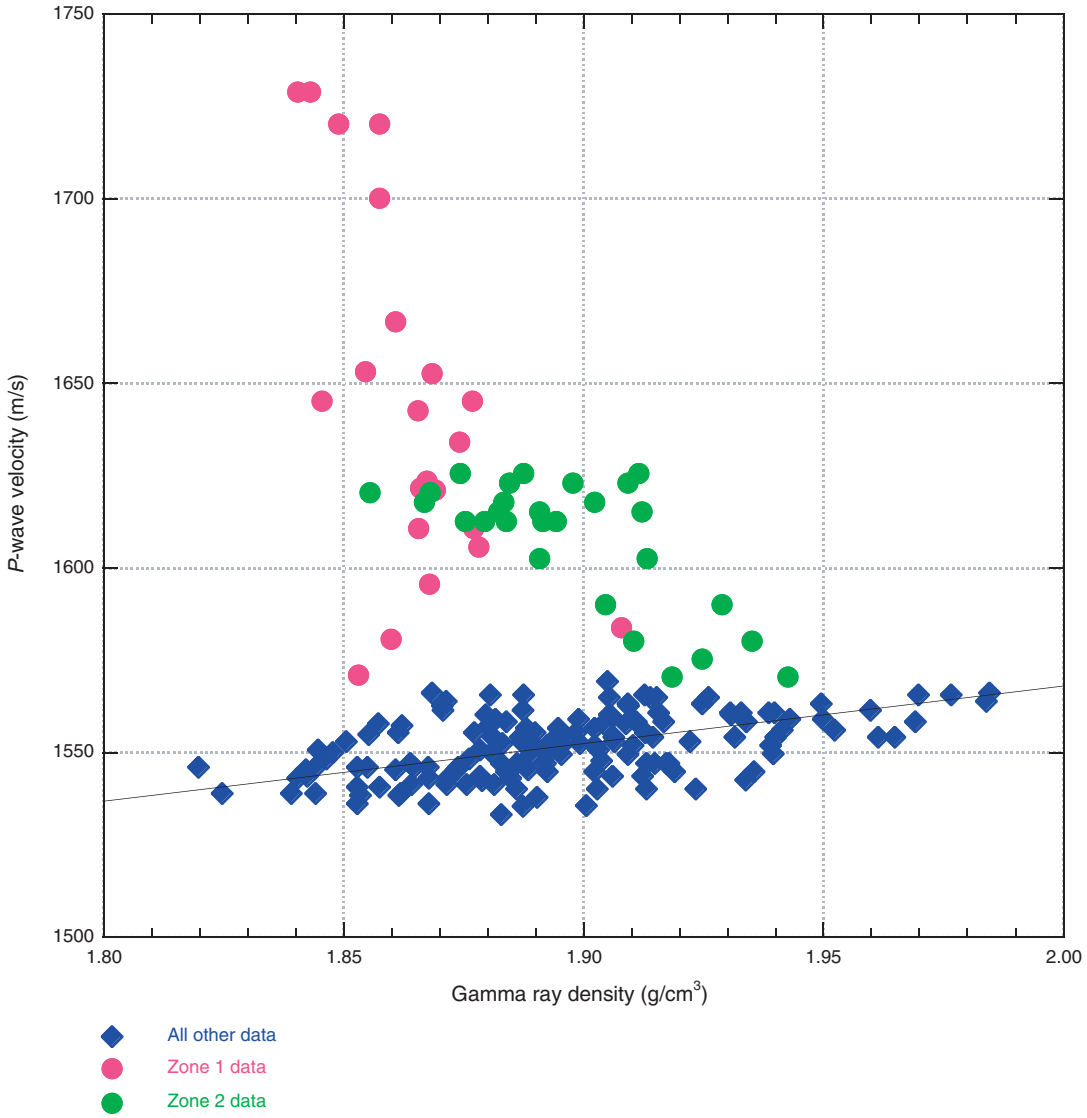

Figure F50. Pressure vs. released gas volume, released water volume, calculated volume of gas inside the HYACINTH storage chamber (SC), and total volume of gas evolved for Core 311-U1329E-9E. Arrows show placement of density scans.

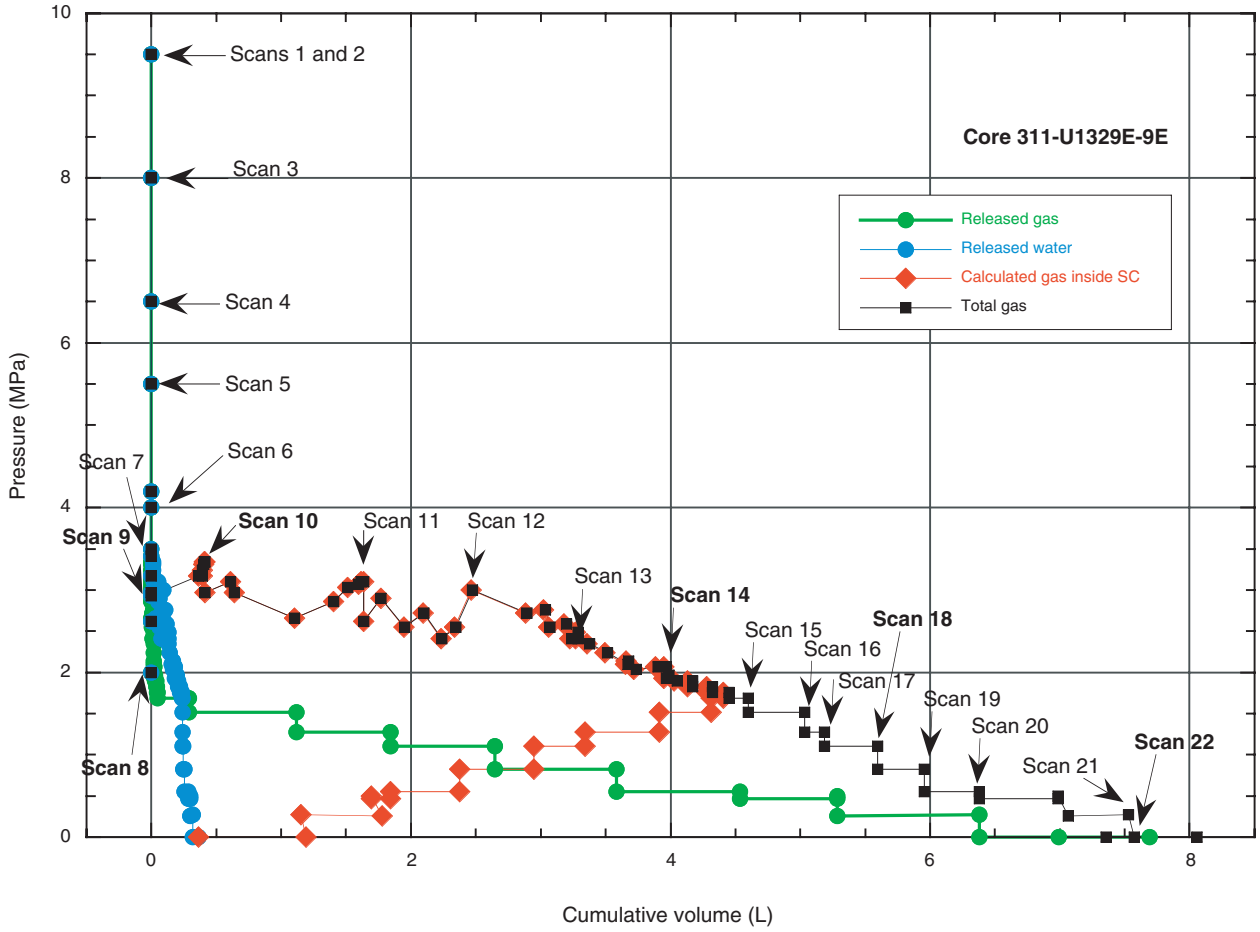

Figure F51. Gamma ray density scans collected during degassing experiments on Core 311-U1329E-9E. Gas was released in two zones corresponding to low-density, high-velocity zones seen in Geotek pressure multisensor core logger data (Fig. F48).

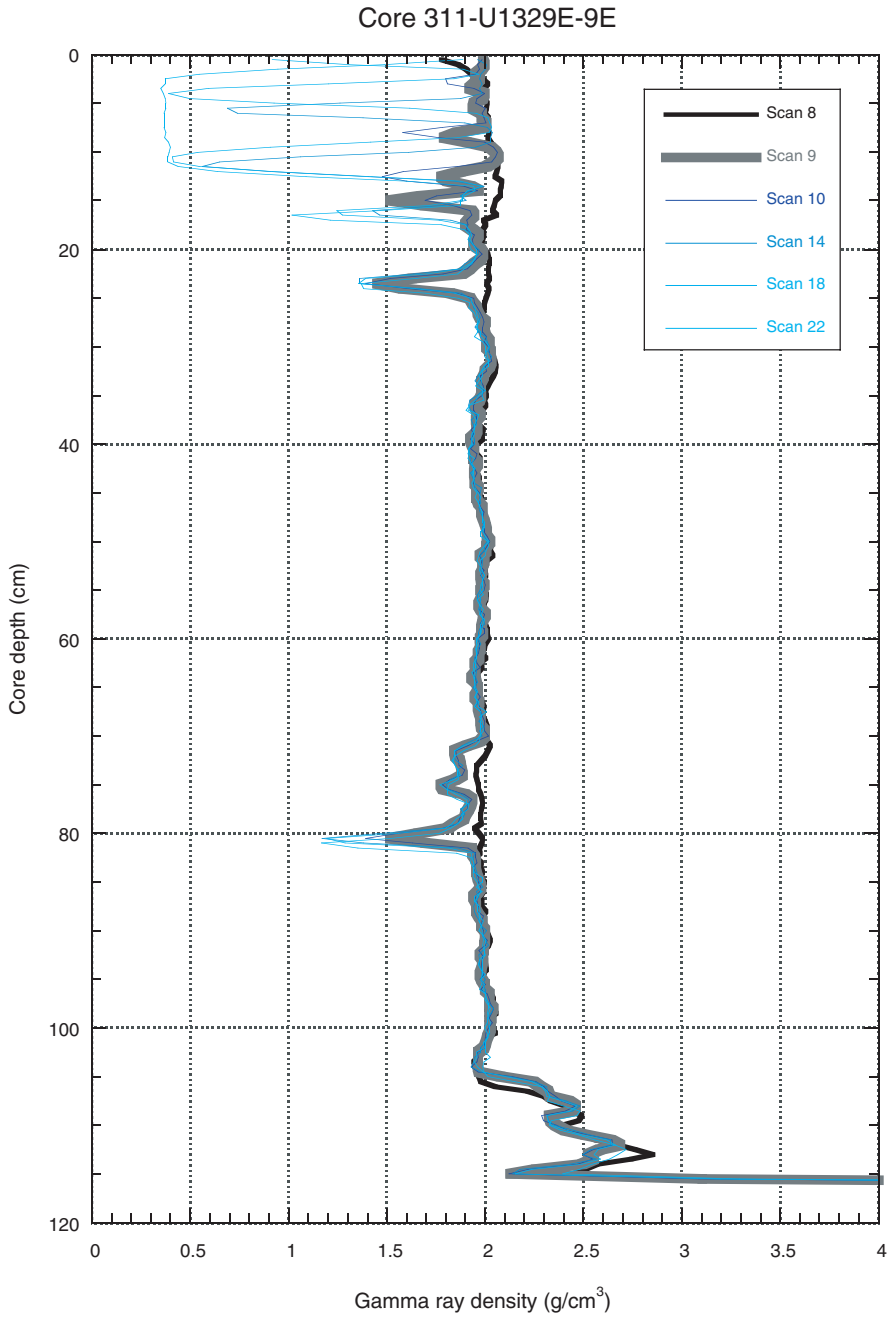

Figure F52. Monitoring and quality control LWD/MWD logs from Hole U1329A.

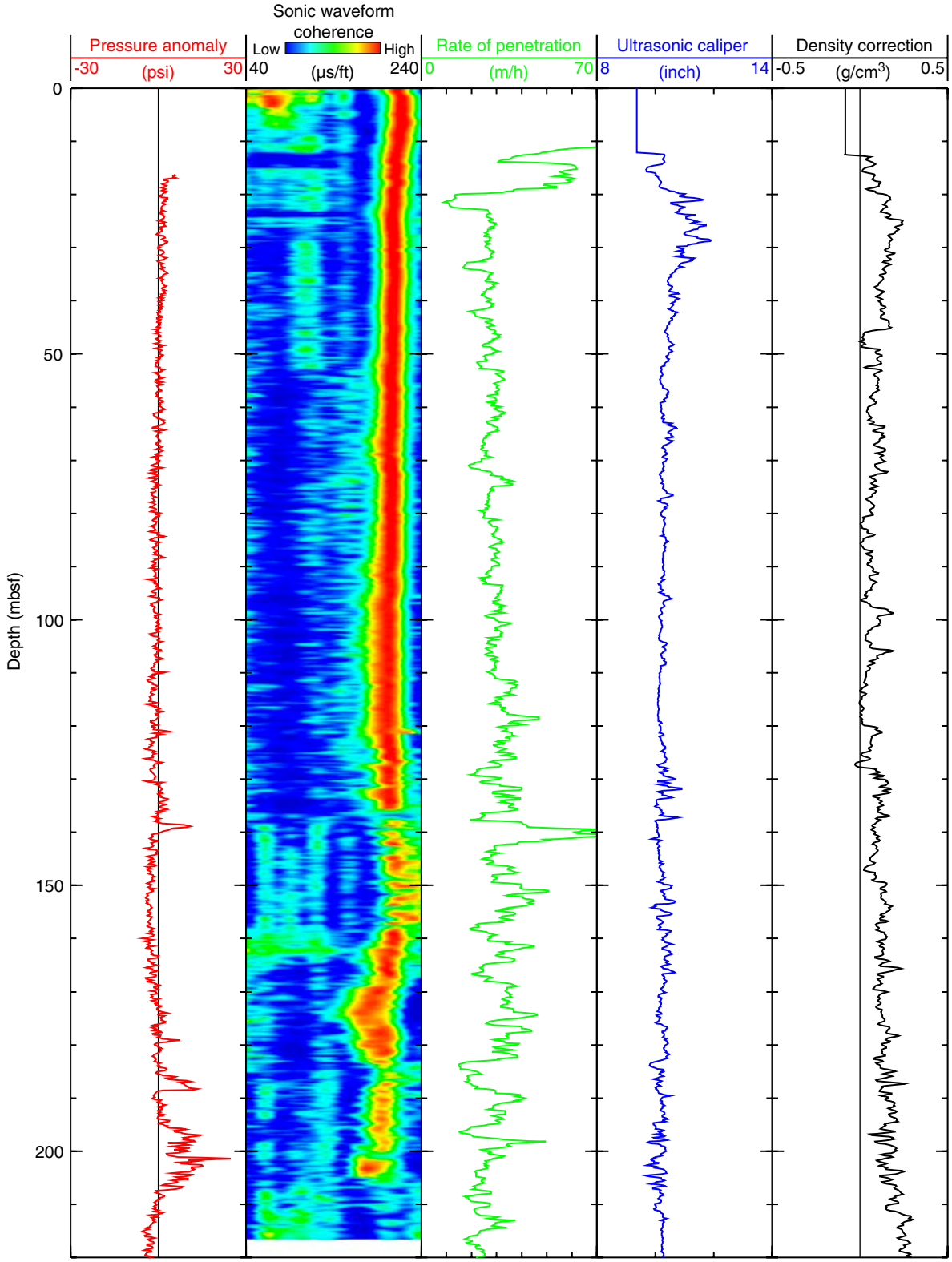

Figure F53. Summary of LWD data from Hole U1329A. avg. = average, P16B = phase-shift resistivity measured by the EcoScope tool at a source-receiver spacing of 16 in (41 cm), A40B = attenuation resistivity measured by the EcoScope tool at a source-receiver spacing of 40 in (102 cm), RAB = resistivity-at-the-bit image obtained by the GeoVISION tool.

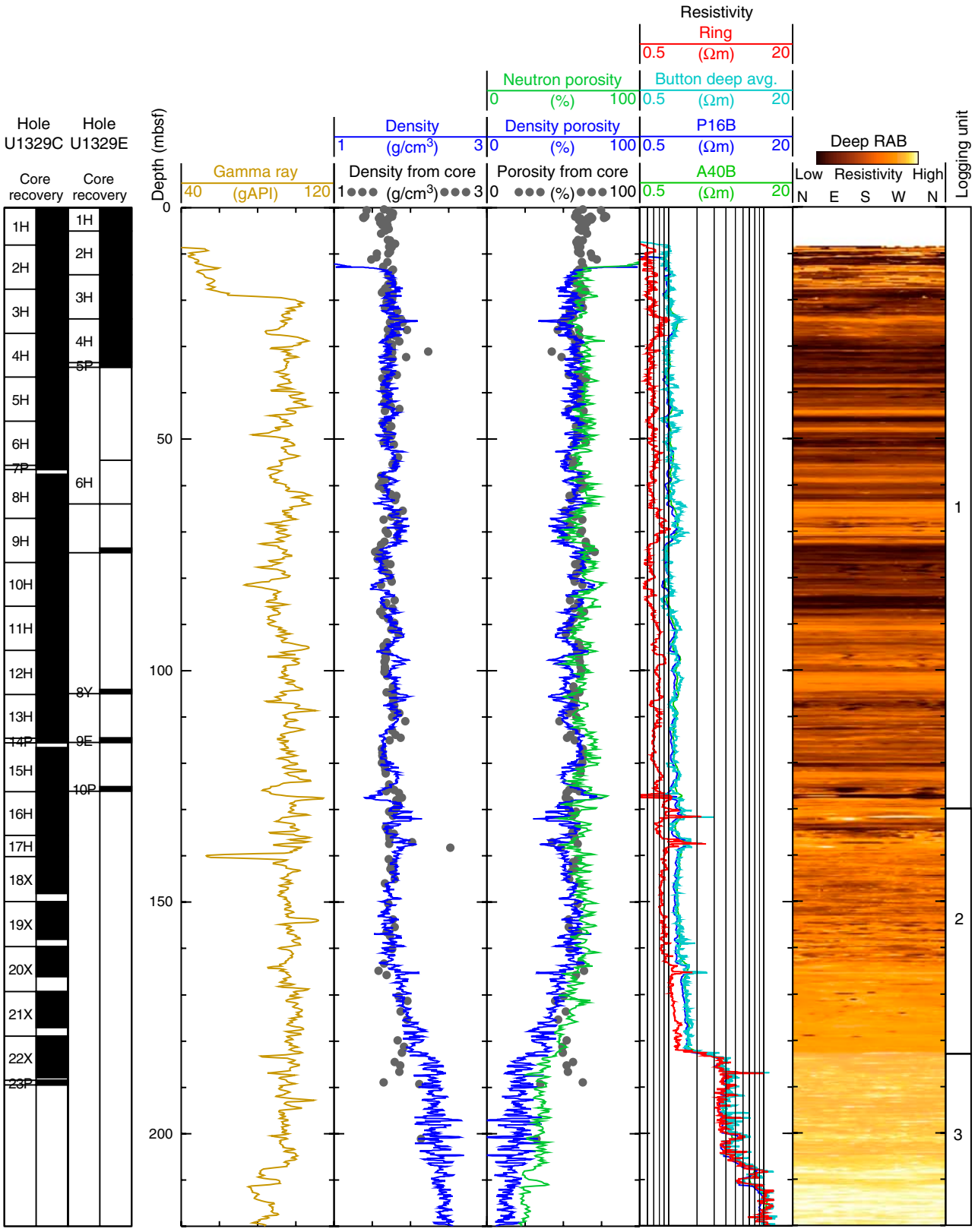

Figure F54. Summary of wireline logging data from Hole U1329D.

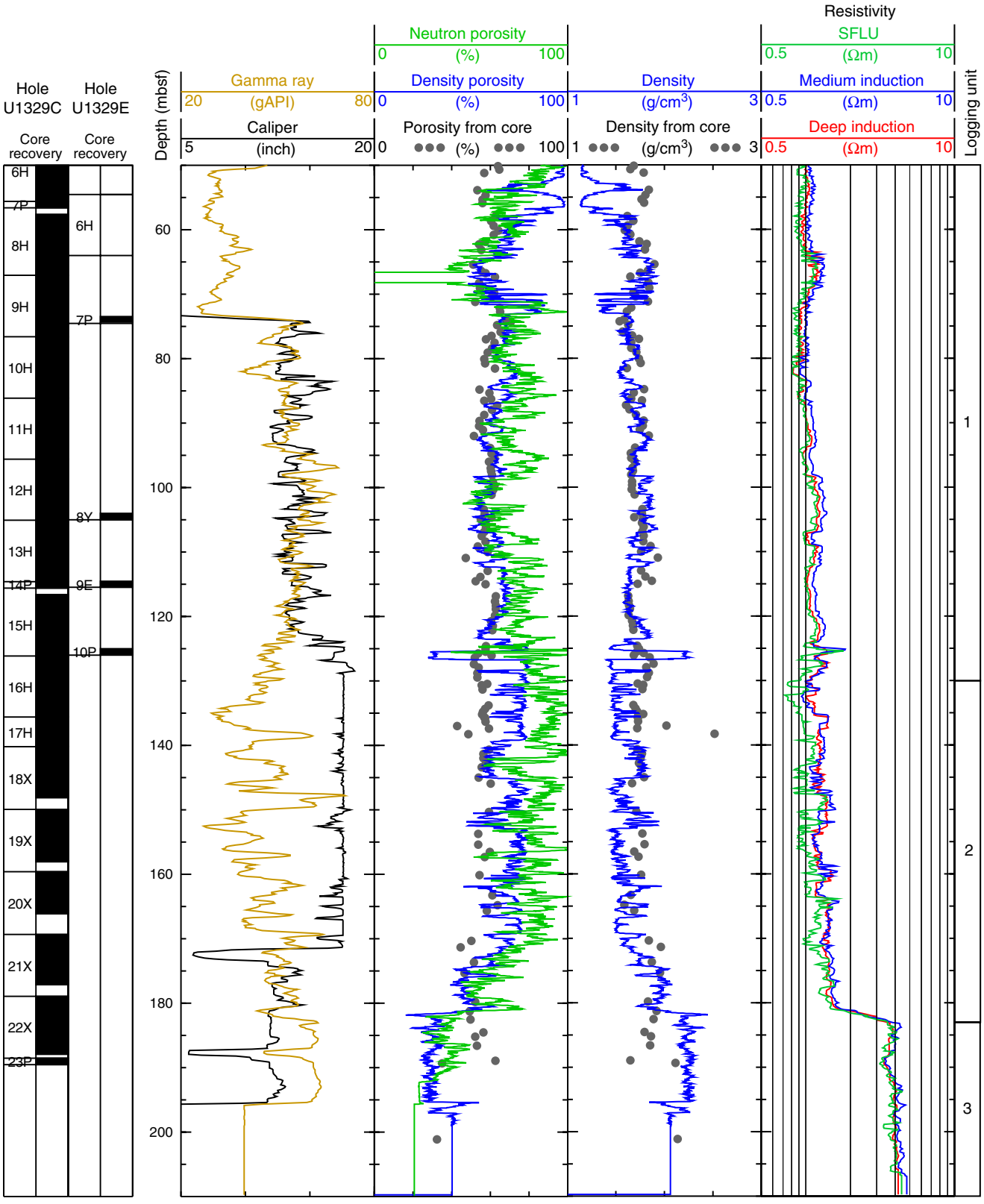

Figure F55. Sonic waveform data, *P*-wave velocity, and *S*-wave velocity obtained with the wireline Dipole Sonic Imager tool in Hole U1329D. V_P = *P*-wave velocity, Mono. = monopole, V_S = *S*-wave velocity, UD = upper dipole, LD = lower dipole.

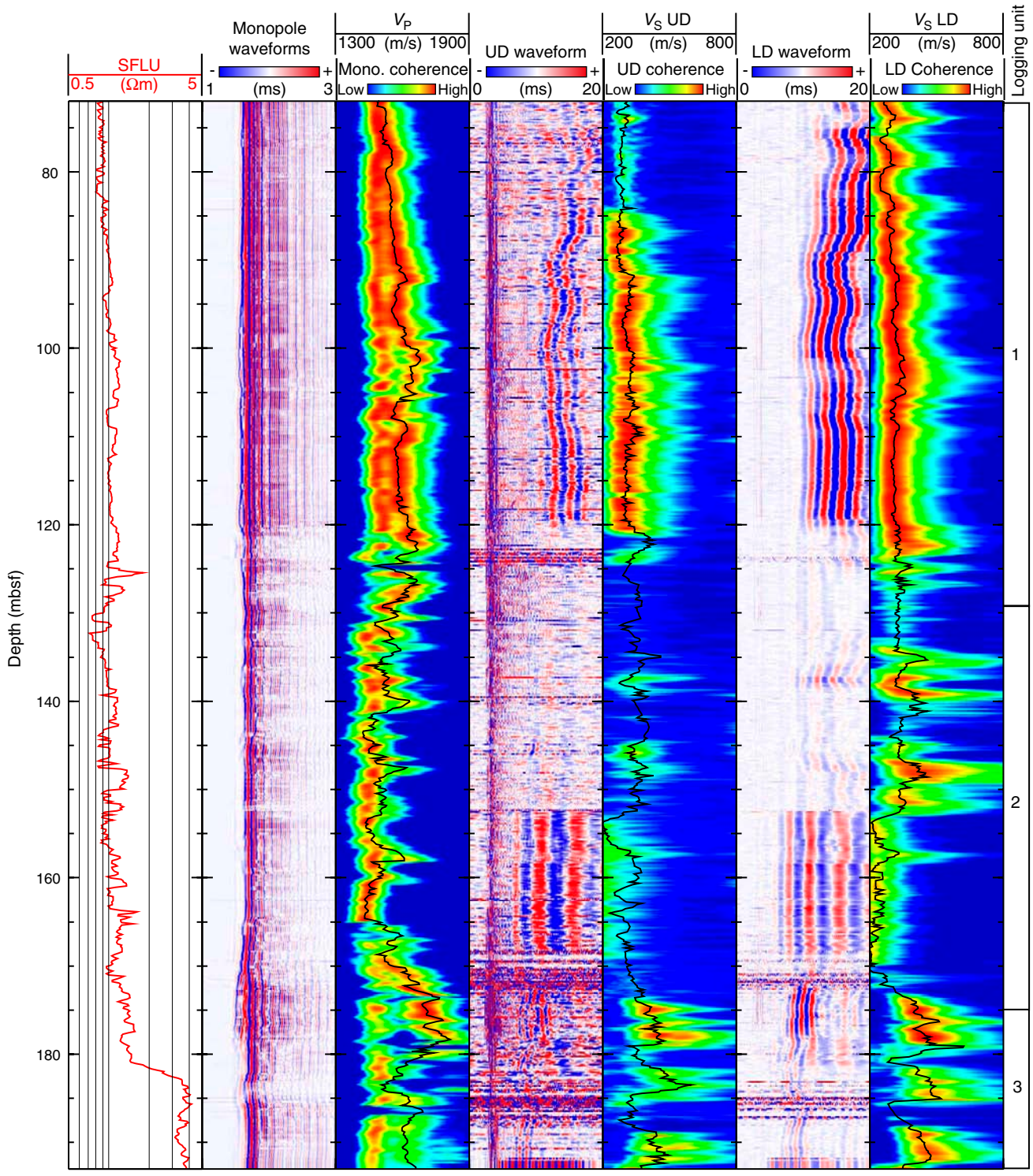

Figure F56. Comparison of logging-while-drilling (LWD; Hole U1329A) and wireline logging (WL; Hole U1329D) data. cal. = caliper, por. = porosity, P16B = phase-shift resistivity measured by the EcoScope tool at a source-receiver spacing of 16 in (41 cm), avg. = average.

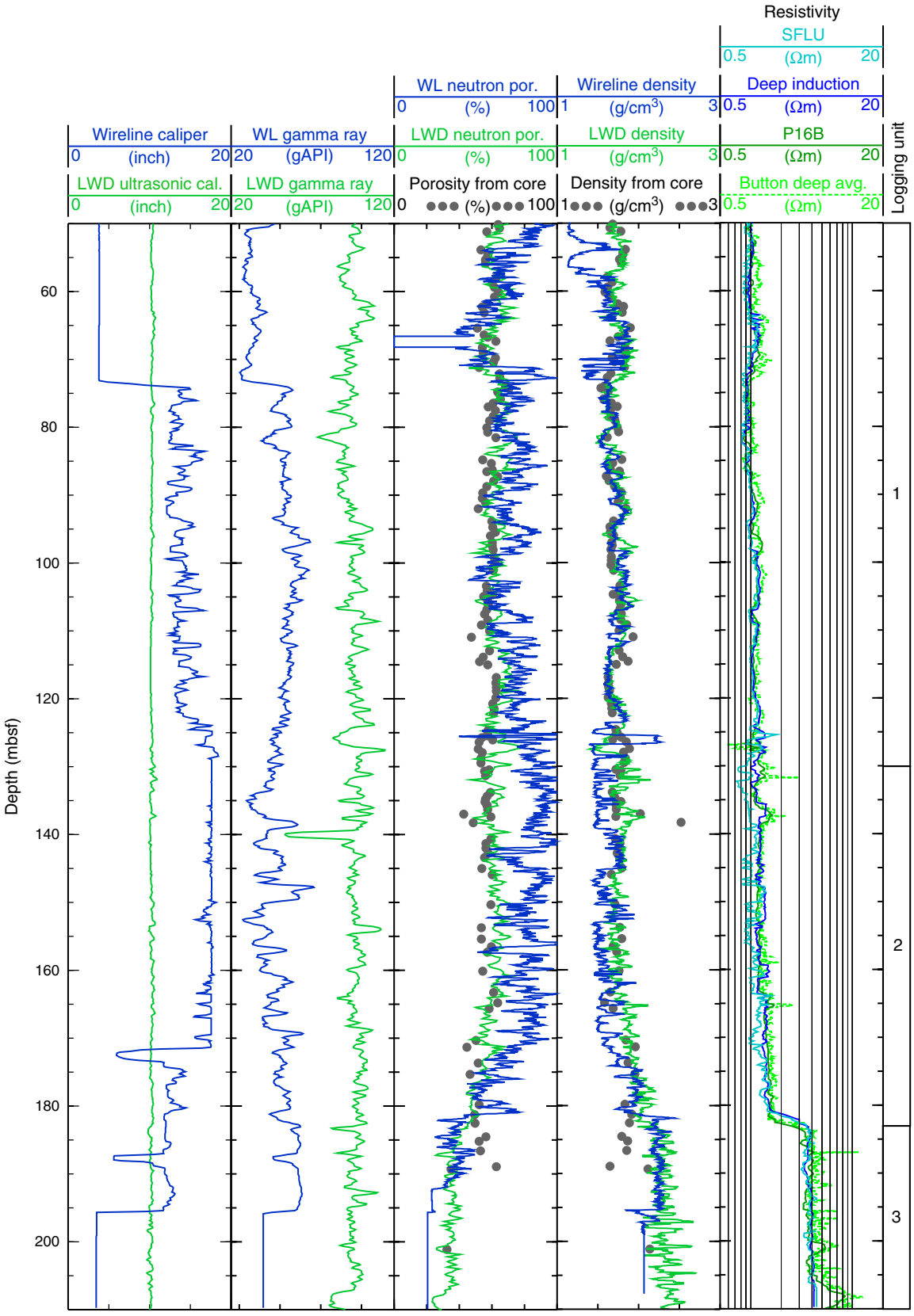

Figure F57. LWD image data from Hole U1329A. RAB = resistivity-at-the-bit image obtained by the GeoVISION tool.

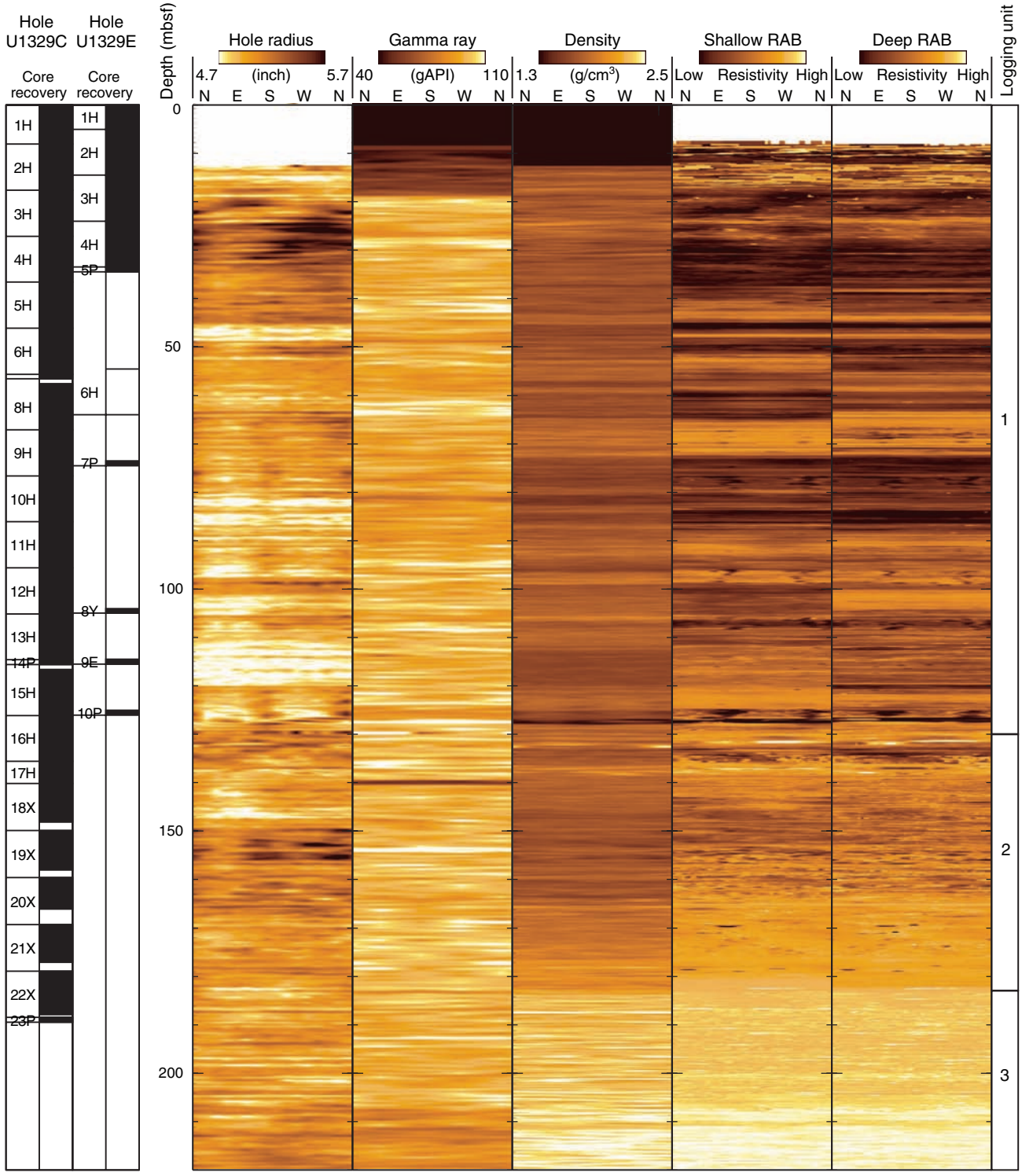

Figure F58. Comparison of LWD porosity logs with core-derived porosity data.

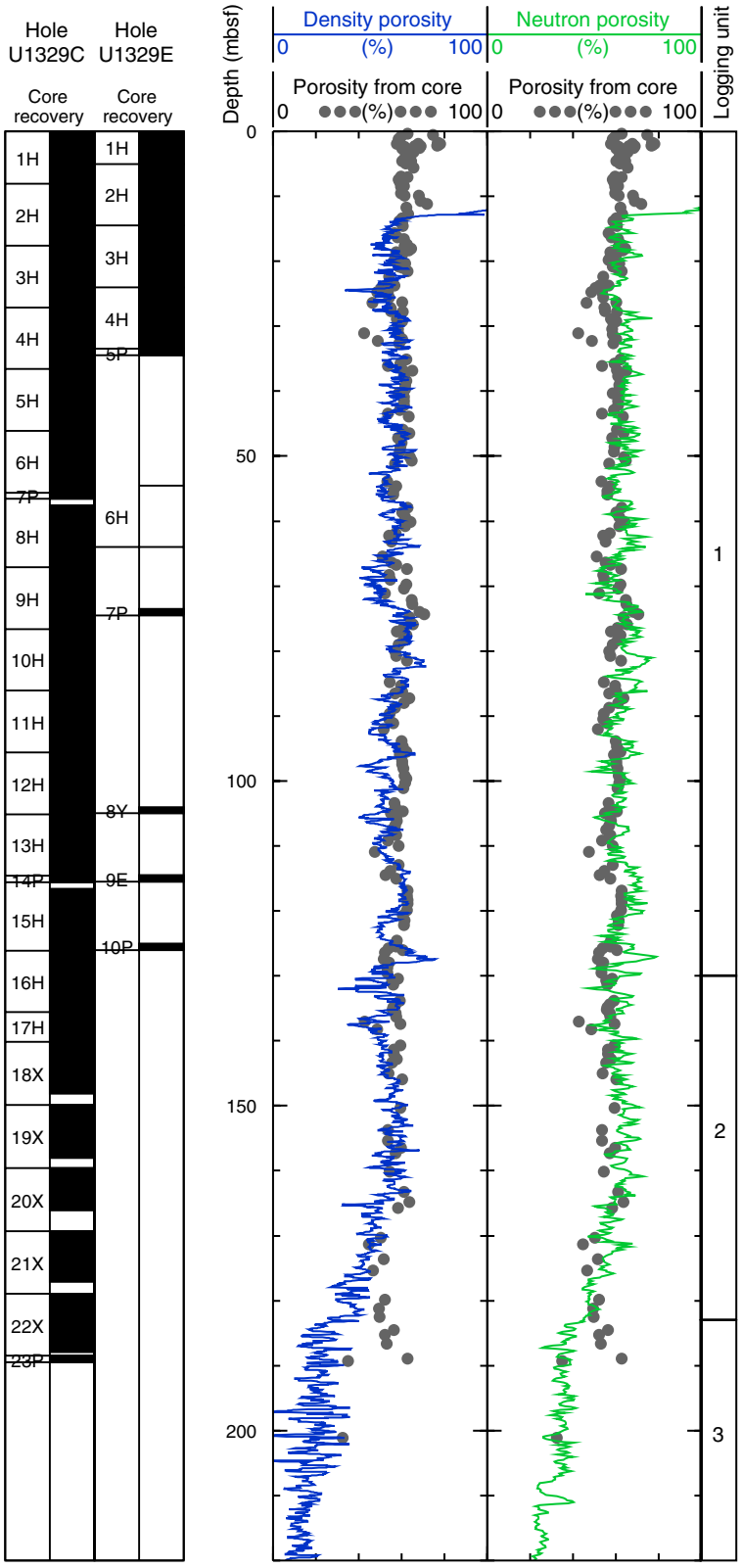

Figure F59. Water saturation from Archie's law and from LWD porosity and resistivity logs. R_w = formation water resistivity, m = cementation coefficient, R_0 = computed formation resistivity for 100% water saturation, R_t = measured resisitivity, S_w = water saturation, RAB = resistivity-at-the-bit image obtained by the GeoVISION tool.

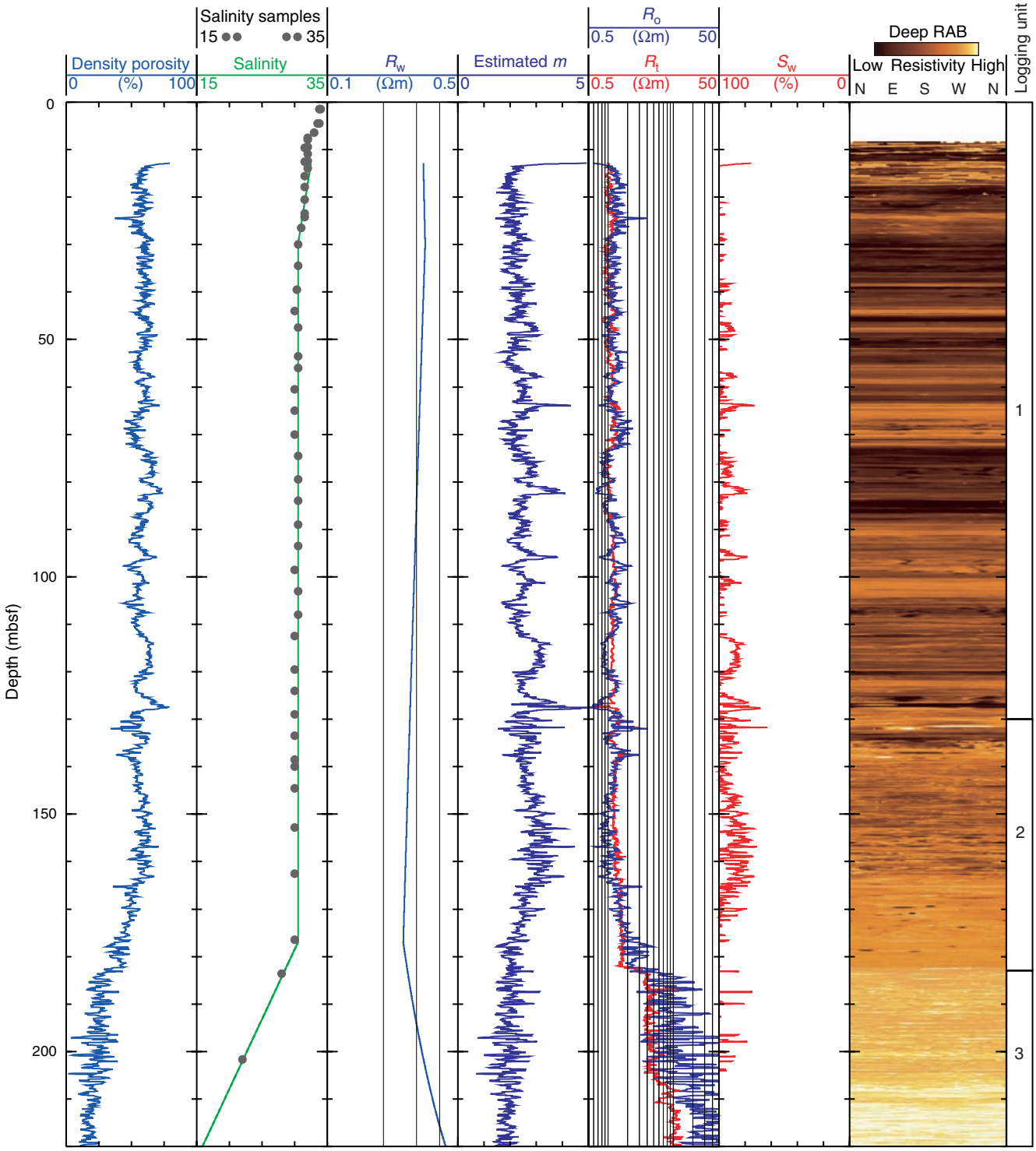

Figure F60. Borehole temperatures recorded with the Temperature/Acceleration/Pressure tool in Hole U1329D.

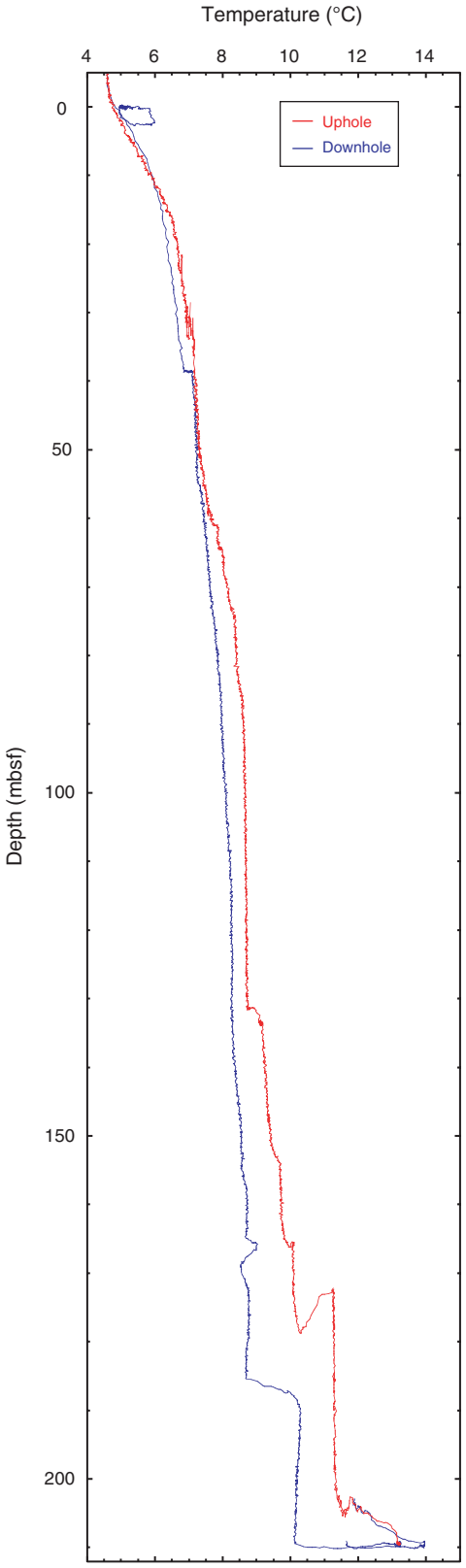

Table T1. Site U1329 coring summary. (See table note. Continued on next page.)

Hole U1329A
Latitude: 48°47.369′N
Longitude: 126°40.713′W
Seafloor (drill pipe measurement from rig floor, mbrf): 970
Distance between rig floor and sea level (m): 10.9
Water depth (drill pipe measurement from sea level. m): 959.1
Total penetration (mbsf): 220.0
Total drilled interval (mbsf): 220.0; LWD/MWD

Hole U1329B
Latitude: 48°47.375′N
Longitude: 126°40.720′W
Seafloor (drill pipe measurement from rig floor, mbrf): 964.0
Distance between rig floor and sea level (m): 11.0
Water depth (drill pipe measurement from sea level, m): 953
Total penetration (mbsf): 9.5

Hole U1329C
Latitude: 48°47.375′N
Longitude: 126°40.720′W
Seafloor (drill pipe measurement from rig floor, mbrf): 957.4
Distance between rig floor and sea level (m): 11.0
Water depth (drill pipe measurement from sea level. m): 946.4
Total penetration (mbsf): 189.5
Total drilled interval (mbsf): 2

Hole U1329D
Latitude: 48°47.361′N
Longitude: 126°40.716′W
Seafloor (drill pipe measurement from rig floor, mbrf): 957.4
Distance between rig floor and sea level (m): 11.0
Water depth (drill pipe measurement from sea level. m): 946.4
Total penetration (mbsf): 210.5
Total length of cored section (m): 9.5
Total drilled interval (m): 201.0

Hole U1329E
Latitude: 48°47.385′N
Longitude: 126°40.716′W
Seafloor (drill pipe measurement from rig floor, mbrf): 956.5
Distance between rig floor and sea level (m): 11.0
Water depth (drill pipe measurement from sea level, m): 945.5
Total penetration (mbsf): 127.1
Total length of cored section (m): 48.1
Total drilled interval (m): 79

Core, section	Date (2005)	Local time (h)	Top depth (mbsf)	Length (m) Cored	Length (m) Recovered	Recovery (%)	Comments
311-U1329A-							
		*****Drilled from 0.0 to 220.0 mbsf*****					LWD/MWD
311-U1329B-							
1H	27 Sep	2105	0.0	9.5	10.02	105.5	Missed mudline
		Core totals:		9.5	10.02	105.5	
311-U1329C-							
1H	27 Sep	2150	0.0	8.1	8.19	101.1	
2H	27 Sep	2235	8.1	9.5	10.30	108.4	APCT-3 housing test
3H	27 Sep	2320	17.6	9.5	10.19	107.3	APCT; fluorescent microspheres
4H	27 Sep	2359	27.1	9.5	10.13	106.6	
5H	28 Sep	0056	36.6	9.5	10.13	106.6	APCT
6H	28 Sep	0135	46.1	9.5	10.17	107.1	
7P	28 Sep	0255	55.6	1.0	1.00	100.0	Sheared OS pin
		*****Drilled from 55.6 to 57.6 mbsf*****					Overdrill of pressure core
8H	28 Sep	0500	57.6	9.5	10.15	106.8	
9H	28 Sep	0600	67.1	9.5	10.27	108.1	APCT-3
10H	28 Sep	0645	76.6	9.5	10.12	106.5	Fluorescent microspheres
11H	28 Sep	0740	86.1	9.5	9.97	104.9	APCT
12H	28 Sep	0825	95.6	9.5	9.77	102.8	
13H	28 Sep	0920	105.1	9.5	10.05	105.8	APCT-3
14P	28 Sep	1110	114.6	1.0	1.00	100.0	Sheared OS pin
		*****Drilled from 114.6 to 116.6 mbsf*****					Overdrill of pressure core
15H	28 Sep	1300	116.6	9.5	9.78	102.9	

Table T1 (continued).

Core, section	Date (2005)	Local time (h)	Top depth (mbsf)	Length (m) Cored	Length (m) Recovered	Recovery (%)	Comments
16H	28 Sep	1400	126.1	9.5	9.98	105.1	
17H	28 Sep	1515	135.6	4.6	4.55	98.9	
18X	28 Sep	1645	140.2	9.7	7.90	81.4	Fluorescent microspheres
19X	28 Sep	1745	149.9	9.7	8.15	84.0	
20X	28 Sep	1845	159.6	9.7	6.53	67.3	
21X	28 Sep	2035	169.3	9.6	7.83	81.6	
22X	28 Sep	2335	178.9	9.6	9.00	93.8	
23P	29 Sep	0210	188.5	1.0	1.00	100.0	PCS cutting shoe left in hole
			Core totals:	187.5	186.16	99.3	
311-U1329D-							
			*****Drilled from 0.0 to 201.0 mbsf*****				
1X	30 Sep	1015	201.0	9.50	1.03	10.80	
			Core totals:	9.50	1.03	10.80	
311-U1329E-							
1H	01 Oct	0300	0.0	5.0	5.05	101.0	Extra wireline run to unlock lockable float valve
2H	01 Oct	0340	5.0	9.5	9.46	99.6	
3H	01 Oct	0415	14.5	9.5	10.06	105.9	
4H	01 Oct	0505	24.0	9.5	9.31	98.0	APCT
5P	01 Oct	0630	33.5	1.0	0.00	0.0	
			*****Drilled from 33.5 to 54.5 mbsf*****				Overdrill of pressure core
6H	01 Oct	0835	54.5	9.5	0.05	0.5	APCT; deployed DVTP after core
			*****Drilled from 54.5 to 73.5 mbsf*****				Overdrill of pressure core
7P	01 Oct	1220	73.5	1.0	0.86	86.0	Sheared OS pin
			*****Drilled from 73.5 to 104.0 mbsf*****				Overdrill of pressure core
8Y	01 Oct	1430	104.0	1.0	1.00	100.0	
			*****Drilled from 104.0 to 114.5 mbsf*****				Overdrill of pressure core
9E	01 Oct	1625	114.5	1.0	1.00	100.0	
			*****Drilled from 114.5 to 125.0 mbsf*****				Overdrill of pressure core
10P	01 Oct	1940	125.0	1.0	0.95	95.0	Deployed DVTP after core
			*****Drilled from 125.0 to 126.0 mbsf*****				Overdrill of pressure core; deployed DVTP
			Core totals:	48.0	37.74	78.6	

Note: LWD/MWD = logging while drilling/measurement while drilling, APCT-3 = third-generation advanced piston corer temperature tool, APCT = advanced piston corer temperature tool, OS = overshot, PCS = Pressure Core Sampler, DVTP = Davis-Villinger Temperature Probe.

Table T2. Occurrence of diatoms, Hole U1329C. (**See table notes.** Continued on next page.)

Age	Diatom zone	Core, section, interval (cm)	Depth (mbsf)	Abundance	Number of diatom valves/row × 100	Preservation	Marine diatoms																													Nonmarine diatoms				Total number of valves	Resting spores of *Chaetoceros* spp.	Marine and nonmarine diatoms ratio
							Actinocyclus curvatulus Janisch	*Actinocyclus oculatus* Jousé	*Coscinodiscus marginatus* Ehrenberg	*Coscinodiscus symbolophorus* Grunow s.l.	*Coscinodiscus* spp.	*Cyclotella striata* (Kutzing) Grunow	*Fragilariopsis doliola* (Walich) Medlin and Sims	*Neodenticula kamtschatica* (Zabelina) Akiba and Yanagisawa	*Neodenticula seminae* (Simonsen and Kanaya) Akiba and Yanagisawa	*Nitzschia marina*	*Nitzschia reinholdii*	*Paralia sulcata* (Ehrenberg) Cleve	*Proboscia barboi* (Brun) Jordan and Priddle	*Proboscia curvirostris* (Jousé) Jordan and Priddle	*Rouxia californica* Peragallo	*Stephanopyxis dimorpha* Schrader	*Stephanopyxis* spp.	*Thalassionema nitzschioides* H. and M. Peragallo	*Thalassionema schraderi* Akiba	*Thalassiosira antiqua* (Grunow) Cleve-Euler	*Thalassiosira gravida*	*Thalassiosira jouseae* Akiba	*Thalassiosira trifulta* Fryxel	*Thalassiosira* spp.	Miscellaneous	*Aulacoseira granulata* (Ehrenberg) Simonsen s.l.	*Cyclotella* spp.	*Stephanodiscus* spp.	Miscellaneous				
Holocene–Pleistocene	NPD12 *N. seminae*	311-U1329C- 1H-1, 10–12	0.10	R	3.4	M	2				+				2							+	7	49						3	22	8	4		+	3	100	49	
		1H-CC	8.14	R	2.4	P	+				1				+			4				+	13	42			+			2	12	6	17		1	2	100	86	
		2H-CC	18.30	R	4.8	P					+	8	3		2								9	48							9	6	12		2	1	100	44	
		3H-CC	27.69	B																																					
	NPD11 *P. curvirostris*	4H-CC	37.18	VR	2.4	P	+				+				2				2		4	32					19		3	17	11	5			5	100	88	
		5H-CC	46.63	A	31.8	M	2				+				39						6	28	10				1	1	5	4	2			2	100	339	
		6H-CC	55.96	C	15.6	M					+				17			2	+		5	39	2				5	+	20	4	4		1	1	100	343	
		8H-CC	67.70	C	14.4	P	+				+				28			+	+		6	43	8			1	2	+	4	8	+			+	100	421	
		9H-CC	77.32	VA	144.0	M	+				+				79						+	2	11						7	1			+	+	100	942	
		10H-CC	86.67	A	96.0	G			+		+				46				+		7	22	1				1	+	17	6	+			+	100	447	
		11H-CC	95.69	C	14.4	P	2				1		1		40	3	2		+		3	12	6						6	5	14	1	+	4	100	266	
	NPD10 *A. oculatus*	12H-CC	105.32	C	6.0	M	3	+			+				7						23	43	4				1		2	7	5	3		2	100	1241	
		13H-CC	115.10	C	6.0	P	+	+	+		+				15				+		14	54	1					1	9	4	2			+	100	56	
		15H-CC	126.33	A	30.0	M					+	2			17		+	2	+		8	34	16						5	7	9	+	+	+	100	1228	
		16H-CC	135.98	VA	36.0	M	1	+	1		+				22			+		+	7	39	17				1	1	3	6	2				100	695	
late Miocene	NPD7A *R. californica*	17H-1, 10–12	135.70	VR	0.3	VP			+		+							4				2	8						+		17			1	32	7	
		17H-2, 10–12	137.20	VR	0.1	VP			1		+			1				1				1	1						+	2	4			+	11	2	
		17H-CC	140.05	VR	0.6	P					+												13	+					1	1	7			+	22	8	
		18X-CC	148.00	R	1.7	P					1			1				1					66	2					8	8	13				100	16	
		19X-CC	157.95	A	36.0	M			+	+	4	+		+				+				2	83	1					2	6	2				100	15	
		20X-1, 10–12	159.70	VA	48.0	M			+		2							1	+	2		3	68	4					10	10					100	20	
		20X-3, 10–12	161.20	A	15.6	M			+	+	2							+	+			1	65	1					7	24					100	45	
late Miocene	NPD6B *T. schraderi*	20X-5, 10–12	165.20	C	7.8	P			2		18							+	7			2	47	3					5		2			14	100	108	
		20X-CC	166.03	C	2.4	M			+	+	+								3	2		2	61	7	+				12		2			10	100	142	
		21X-CC	176.98	VR	0.3	P			1		+								+			3	1						3	5	11			+	24	2	

Table T2 (continued).

Age	Diatom zone	Core, section, interval (cm)	Depth (mbsf)	Abundance	Number of diatom valves/row × 100	Preservation	Marine diatoms: *Actinocyclus curvatulus* Janisch	*Actinocyclus oculatus* Jousé	*Coscinodiscus marginatus* Ehrenberg	*Coscinodiscus symbolophorus* Grunow s.l.	*Coscinodiscus* spp.	*Cyclotella striata* (Kutzing) Grunow	*Fragilariopsis doliola* (Walich) Medlin and Sims	*Neodenticula kamtschatica* (Zabelina) Akiba and Yanagisawa	*Neodenticula seminae* (Simonsen and Kanaya) Akiba and Yanagisawa	*Nitzschia marina*	*Nitzschia reinholdii*	*Paralia sulcata* (Ehrenberg) Cleve	*Proboscia barboi* (Brun) Jordan and Priddle	*Proboscia curvirostris* (Jousé) Jordan and Priddle	*Rouxia californica* Peragallo	*Stephanopyxis dimorpha* Schrader	*Stephanopyxis* spp.	*Thalassionema nitzschioides* H. and M. Peragallo	*Thalassionema schraderi* Akiba	*Thalassiosira antiqua* (Grunow) Cleve-Euler	*Thalassiosira gravida*	*Thalassiosira jouseae* Akiba	*Thalassiosira trifulta* Fryxel	*Thalassiosira* spp.	Miscellaneous	Nonmarine diatoms: *Aulacoseira granulata* (Ehrenberg) Simonsen s.l.	*Cyclotella* spp.	*Stephanodiscus* spp.	Miscellaneous	Total number of valves	Resting spores of *Chaetoceros* spp.	Marine and nonmarine diatoms ratio
late Miocene?	Not zoned	22X-1, 10–12	179.00	B																																		
		22X-2, 10–12	180.50	VR	3.0	P			1		3						1	3			1	12	44							2	7	25		+	1	100	17	
		22X-3, 10–12	182.00	C	12.0	M					+										+	+								95	+	5		100	+	
		22X-5, 10–12	184.97	VR	3.4	P					+										19	9						3	3	57		3	6	100	113	
		22X-6, 0–12	186.39	VR	2.2	P					+										4	+							3	86	6		1	100	9	

Notes: Abundance: VA = very abundant, A = abundant, C = common, R = rare, VR = very rare, B = barren. Preservation: G = good, M = moderate, P = poor, VP = very poor. + = <1% and/or valve fragments.

Table T3. Concentrations of solutes in interstitial waters, Site U1329. (See table note. Continued on next page.)

Core, section, interval (cm)	Depth (mbsf)	Volume (mL)	pH	Alkalinity	Salinity	Cl (mM)	SO_4 (mM)	PO_4 (µM)	NH_4 (mM)	H_4SiO_4 (µM)	Cations (mM)					Trace elements (µM)		
											Na	K	Mg	Ca	Mg/Ca	Li	B	Ba
311-U1329C-																		
1H-1, 140–150	1.5	65	7.68		33.8	547.0	16.9	11.8	0.1	675	453.6	11.4	49.3	9.4	5.2	47.8	512.0	0.5
1H-3, 140–150	4.5	13	7.84	12.7	33.8	549.0	3.8	53.4	0.7	640	456.8	10.5	46.6	7.3	6.4	42.1	469.4	0.6
1H-5, 140–150	7.5	60	7.84	18.4	32.0	545.0	2.9	102.4	1.0	633	453.9	10.5	42.6	4.8	8.8	39.9	529.5	2.9
2H-1, 140–150	9.6	64	7.79	21.8	31.5	544.0	0.1	110.3	1.1	690	438.6	10.4	40.7	3.5	11.7	37.0	543.6	20.1
2H-3, 140–150	12.6	47	7.83	21.0	31.5	546.0	0.1	92.8	1.3	689	448.5	10.3	40.3	3.3	12.3	37.5	530.6	25.6
2H-5, 140–150	15.6	65			31.5	546.0	0.0	73.1	1.2	584	433.7	10.3	40.0	3.1	12.8	37.4	529.6	26.2
2H-7, 140–150	17.9	50	7.98	18.5	31.5	542.0	0.1	63.0	0.8	686	452.4	10.6	38.2	2.8	13.8	37.5	528.3	25.9
3H-2, 135–150	20.5	58	7.82	16.9	31.5	543.7	0.2	61.9	1.0	672	433.7	9.7	38.0	2.6	14.4	37.7	523.7	22.8
3H-4, 135–150	23.5	58	7.93	16.5	31.5	547.7	0.0	47.3	1.0	741	447.4	10.2	36.1	2.4	15.1	39.7	527.1	21.2
3H-6, 135–150	26.5	52	7.93	13.9	31.0	543.0	0.2	37.1	1.3	655	440.0	10.5	35.3	2.2	16.0	41.3	505.4	21.4
4H-2, 120–150	30.0	54	7.70	11.9	30.5	542.0	0.2	29.8	1.2	786	432.7	10.2	33.3	2.9	11.6	42.6	495.8	21.6
4H-5, 120–150	34.5	64	7.73	12.1	30.5	542.0	0.2	29.8	1.3	797	454.4	10.7	34.0	2.9	11.6	43.3	476.4	23.6
5H-2, 130–150	39.5	52	7.82	12.9	30.3	542.0	0.3	38.8	1.4	790	432.4	10.5	34.3	2.8	12.1	43.8	493.4	26.6
5H-5, 130–150	44.0	50	7.80	13.8	30.0	543.0	0.2	41.1	1.5	863	439.8	10.1	34.9	2.8	12.4	44.8	474.3	27.8
6H-1, 135–150	47.5	60	7.82	13.8	30.5	542.0	0.5	41.6	1.8	867	424.0	10.7	34.9	2.6	13.3	45.5	486.6	30.8
6H-5, 135–150	53.5	66	7.97	15.5	30.5	541.7	0.2	42.2	1.9	831	439.1	9.9	35.3	2.6	13.9	46.2	452.3	32.3
7P-1, 25–50	56.0				30.5	542.0												
8H-2, 135–150	60.5	62	7.74	17.7	30.0	541.0	0.2	56.8	2.5	921	440.5	9.9	36.4	2.6	13.9	46.7	502.7	35.5
8H-5, 135–150	65.0	55			30.0	539.7	0.0	53.4	3.4	898	426.9	9.8	36.4	2.7	13.6	48.8	419.5	38.6
9H-2, 135–150	70.0	62	7.78	21.8	30.0	538.0	0.6	67.6	3.3	879	424.3	9.4	37.9	3.1	12.3	50.1	447.1	44.3
9H-5, 130–150	74.5	68	7.93	24.4	30.5	536.7	0.2	58.4	4.4	808	428.3	10.1	38.0	3.1	12.1	52.2	451.0	47.6
10H-2, 130–150	79.5	60	7.96	26.7	30.5	529.0	0.2	68.4	5.1	806	429.9	9.5	37.9	3.5	10.8	56.2	421.4	54.9
10H-5, 130–150	84.0	64		28.0	30.5	524.4	0.3	40.9	5.6	557	432.3	10.7	37.7	3.5	10.7	57.8	315.2	63.9
11H-2, 130–150	89.0	66	8.02	29.0	30.5	522.5	0.2	56.8	6.4	842	414.3	9.7	37.7	3.8	10.0	59.7	422.9	61.5
11H-5, 130–150	93.5	58	8.11	26.4	30.5	521.0	0.0	50.1	6.4	766	421.6	9.1	37.8	3.8	9.9	62.4	381.6	65.5
12H-2, 120–150	98.5	58	7.83	28.9	30.0	520.5	0.2	63.4	6.4	983	408.9	9.1	37.7	4.1	9.3	65.9	453.5	69.9
12H-5, 130–150	103.0	50	8.10	28.8	30.5	520.0	0.2	45.8	6.7	873	417.1	9.1	37.3	4.0	9.3	66.6	407.8	72.0
13H-2, 130–150	108.0	48	7.96	29.0	30.5	519.0	0.3	35.8	7.7	894	420.9	9.0	37.4	4.3	8.8	71.2	432.5	78.5
13H-5, 130–150	112.5	60		29.1	30.0	519.5	0.1	33.3	6.5	694	407.4	8.6	37.1	4.3	8.5	74.4	403.4	82.6
15H-2, 130–150	119.5	62	8.04	25.7	30.0	508.0	0.2	40.9	6.5	918	410.9	8.5	35.4	4.3	8.2	79.9	401.1	87.8
15H-5, 130–150	124.0	54			30.0	502.0	0.2	38.3	6.5	739	396.3	8.3	35.3	4.6	7.6	86.7	361.0	94.9
16H-2, 130–150	129.0	44	8.02	25.6	30.0	507.0	0.2	27.5	5.9	869	409.4	8.9	35.0	4.5	7.9	93.5	339.4	89.9
16H-5, 130–150	133.5	60	8.14	24.0	30.0	518.0	0.2	28.3	6.3	794	417.4	9.3	34.0	4.4	7.6	97.0	287.8	92.6
17H-2, 130–150	138.5	51			30.0	518.0	0.2	17.5	6.1	904	408.5	10.0	34.1	4.4	7.8	102.9	377.7	101.4
17H-3, 130–150	140.0	41	8.35	20.7	30.0	506.0	0.2	26.8	7.2	633	405.4	9.2	31.6	4.5	7.1	101.9	240.6	99.6
18X-3, 125–150	144.6	15	7.87	21.0	30.0	508.0	0.2	28.4	6.4	906	404.8	8.2	32.8	4.8	6.8	107.3	302.8	94.2
19X-2, 120–150	152.8	44			30.0	498.0	0.2	17.6	5.8	776	398.5	8.7	33.3	5.1	6.5	118.8	230.9	97.7
20X-2, 120–150	162.5	42			30.0	496.0	0.2	15.1	5.9	1033	385.7	7.3	29.4	6.1	4.8	127.3	326.2	108.7
21X-6, 0–30	176.5	27			30.0	488.0	0.4	9.3	5.6	920	378.9	7.2	31.3	7.0	4.5	130.7	239.6	114.9
22X-4, 0–35	183.6	14	7.92	18.4	28.0	480.0	0.5	5.9	5.1	40	391.4	7.6	22.9	7.4	3.1			
311-U1329D-																		
1X-1, 52–88	201.7				22.0	380.0	4.7	2.6	5.1	167	303.5	3.5				89.7	284.4	97.9
311-U1329E-																		
1H-1, 140–150	1.5	62	7.62	6.5	34.0	548.0	22.0	19.3	0.1	736	465.0	11.7	49.8	9.4	5.3	48.1	505.1	0.6
1H-2, 140–150	3.0		7.61	9.6	34.0	547.0	21.9	47.6	0.3	721	464.3	11.2	48.0	8.4	5.7	44.0	508.9	1.0
1H-3, 140–150	4.5	61	7.72	12.8	33.5	550.0	18.4	95.9	0.4	741	470.9	11.1	46.8	7.6	6.2	41.9	507.7	1.1
2H-1, 135–150	6.4	56	7.72	18.2	33.0	547.0	10.9	104.3	0.7	589	465.7	10.7	43.8	5.6	7.8	39.1	488.4	2.0
2H-2, 135–150	7.9	52	7.71	21.2	32.0	545.0	6.9	105.9	0.9	618	471.6	11.2	42.2	4.5	9.3	38.1	510.9	6.3
2H-3, 135–150	9.4	64	7.87	24.1	32.0	544.0	0.2	100.1	1.1	661	483.4	12.0	40.6	3.5	11.5	36.6	536.4	18.2

Table T3 (continued).

Core, section, interval (cm)	Depth (mbsf)	Volume (mL)	pH	Alkalinity	Salinity	Cl (mM)	SO_4 (mM)	PO_4 (µM)	NH_4 (mM)	H_4SiO_4 (µM)	Cations (mM)					Trace elements (µM)		
											Na	K	Mg	Ca	Mg/Ca	Li	B	Ba
2H-4, 135–150	10.9	60	7.79	18.2	32.0	545.0	0.0	91.8	1.2	732	470.0	11.8	40.4	3.5	11.6	36.5	545.8	22.8
2H-5, 135–150	12.4	52	7.75	21.6	32.0	544.0	0.0	81.8	1.2	754	478.7	11.8	39.9	3.4	11.8	37.6	583.2	27.3
2H-6, 135–150	13.9	55	7.83	22.3	32.0	546.0	0.0	44.3	1.2	616	469.5	11.6	39.9	3.3	12.0	37.5	544.3	27.5
*3H-1, 135–150	15.9																	
3H-7, 63–78	24.2	54	7.86	15.7	31.5	546.0	0.0	48.4	1.2	745	472.7	12.2	36.1	2.3	15.3	40.5	530.2	24.0

Note: * = no interstitial water squeezed because of poor quality of sample.

Table T4. Headspace gas concentrations of hydrocarbons, Holes U1329C and U1329E.

Core, section, interval (cm)	Depth (mbsf)	Sediment volume (mL)	C_1/C_2	C_1 (ppmv)	C_2 (ppmv)	$C_{2=}$ (ppmv)	C_3 (ppmv)	C_1 (mM)*
311-U1329C-								
1H-2, 0–5	1.5	3.0		5	0	0	0	0.00
1H-4, 0–5	4.5	3.0		7	0	0	0	0.00
1H-6, 0–5	7.5	3.0		7	0	0	0	0.00
2H-2, 0–5	9.6	3.0		2,285	0	0	0	1.13
2H-4, 0–5	12.6	3.0		5,857	0	0	0	2.90
2H-6, 0–5	15.6	3.0	10,456	12,547	1.2	0	0	6.22
2H-7, 0–5	17.1	3.0	12,449	13,694	1.1	0	0	6.78
3H-3, 0–5	20.6	3.0	8,062	15,318	1.9	0	0	7.59
3H-5, 0–5	23.6	3.0	7,078	12,740	1.8	0	0	6.31
3H-7, 0–5	26.6	3.0	4,819	6,264	1.3	0	0	3.10
4H-3, 0–5	30.1	3.0	6,088	12,177	2.0	0	0	6.03
4H-6, 0–5	34.6	3.0	7,263	15,253	2.1	0	0	7.56
5H-3, 0–5	39.6	3.0	5,842	8,178	1.4	0	0	4.05
5H-6, 0–5	44.1	3.0	5,438	11,964	2.2	0	0	5.92
6H-2, 0–5	47.6	3.0	3,621	5,431	1.5	0	0	2.69
6H-6, 0–5	53.6	3.0	2,872	5,744	2.0	0	0	2.85
8H-3, 0–5	60.6	4.0	3,344	6,353	1.9	0	0	2.28
8H-6, 0–5	65.1	4.5	2,706	5,683	2.1	0	0	1.74
9H-3, 0–5	70.1	4.9	3,724	7,447	2.0	0.5	0	2.07
9H-6, 0–5	74.6	4.2	3,051	7,323	2.4	0.6	0	2.45
10H-3, 0–5	79.6	4.8	2,934	7,336	2.5	0	0	2.07
10H-6, 0–5	84.1	4.6	2,107	4,845	2.3	0	0	1.46
11H-6, 0–5	93.6	5.5	2,380	6,427	2.7	0	0	1.53
12H-3, 0–5	98.6	5.6	2,303	8,289	3.6	0	0	1.93
12H-6, 0–5	103.1	5.1	2,283	7,534	3.3	0.8	0	1.99
13H-3, 0–5	108.1	4.9	1,958	7,048	3.6	0	0	1.95
13H-6, 0–5	112.6	5.2	2,429	8,016	3.3	0	0	2.04
15H-6, 0–5	124.1	3.0	2,326	6,979	3.0	0	0	3.46
16H-3, 0–5	129.1	3.0	3,842	5,379	1.4	0	0	2.66
16H-6, 0–5	133.6	3.0	4,164	4,164	1.0	0	0	2.06
17H-2, 120–125	138.3	3.0	13,384	6,692	0.5	0	0	3.32
18X-3, 0–5	143.2	3.0	2,031	3,859	1.9	0	0	1.91
19X-3, 0–5	152.9	3.0	1,784	2,319	1.3	0	0	1.15
20X-2, 115–120	162.3	3.0	1,485	2,969	2.0	0	0	1.83
21X-1, 145–150	170.8	3.0	968	3,971	4.1	0	0	3.45
21X-5, 95–100	176.3	3.0		4,666	1.0	0	0	5.50
22X-2, 0–5	180.4	3.0	1,379	1,655	1.2	0	0	1.80
22X-5, 0–5	184.9	3.0	1,870	4,675	2.5	0	0	5.37
22X-6, 41–46	186.7	3.0	422	3,380	8.0	0	19.9	3.98
311-U1329E-								
1H-2, 0–5	1.5	3.0		2	0	0	0	0.00
1H-3, 0–5	3.0	3.0		3	0	0	0	0.00
1H-4, 0–5	4.5	3.0		2	0	0	0	0.00
2H-2, 0–5	6.5	3.0		37	0	0	0	0.02
2H-3, 0–5	8.0	3.0		5	0	0	0	0.00
2H-4, 0–5	9.5	3.0		394	0	0	0	0.19
2H-5, 0–5	11.0	3.0		3,024	0	0	0	1.50
2H-6, 0–5	12.5	3.0		4,850	0	0	0	2.40
2H-7, 0–5	14.0	3.0		8,106	0	0	0	4.02
3H-2, 0–5	16.0	3.0		9,397	0	0	0	4.66
3H-3, 0–5	17.5	3.0	12,447	12,447	1.0	0	0	6.17
3H-4, 0–5	19.0	3.0	12,082	13,291	1.1	0	0	6.58
3H-5, 0–5	20.5	3.0	10,464	10,464	1.0	0	0	5.18
3H-6, 0–5	22.0	3.0	10,158	15,238	1.5	0	0	7.55
3H-7, 0–5	23.5	3.0	10,942	16,413	1.5	0	0	8.13
4H-5, 0–5	30.0	3.0	5,533	6,086	1.1	0	0	3.02

Note: * = dissolved residual methane obtained by the headspace equilibration method.

Table T5. Concentrations of light hydrocarbon and nonhydrocarbon gases in void gas samples, Hole U1329C.

Core, section	Depth (mbsf)	C_1/C_2	Hydrocarbons (ppmv)							Volatiles (ppmv)			
			C_1	C_2	C_3	*i*-C_4	*n*-C_4	*i*-C_5	*n*-C_5	H_2S	CO_2	O_2	N_2
311-U1329C-													
3H-7	26.6	15,915	560,208	35.2	0	0	0	0	0	0	4,171	80,278	345,529
4H-2	29.7	18,149	894,736	49.3	0	0	0	0	0	0	3,350	8,569	87,308
4H-7	36.7	16,586	884,050	53.3	0	0	0	0	0	0	4,464	17,692	87,308
5H-2	39.1	16,266	920,642	56.6	0	0	0	0	0	0	2,644	3,039	64,310
5H-7	45.8	14,866	952,909	64.1	0	0	0	0	0	0	2,460	0	85
6H-3	49.4	13,818	795,894	57.6	0	0	0	0	0	0	6,047	NA	NA
6H-6	53.6	15,113	964,211	63.8	0	0	0	0	0	0	3,002	1,840	17,089
8H-2	59.7	12,196	963,503	79.0	0	0	0.2	0	0	0	4,652	952	21,996
8H-3	60.6	12,285	963,139	78.4	0	0	0.2	0	0	0	4,626	1,273	22,495
8H-6	66.5	14,383	967,969	67.3	0	0	0	0	0	0	5,078	40,488	159,784
9H-1	68.2	12,727	871,797	68.5	0	0	0	0	0	0	4,986	33,824	132,730
11H-2	87.8	11,159	977,214	87.6	0	0	0.6	0	0	0	2,507	596	3,282
11H-6	93.6	11,615	979,490	84.3	0	0	1.0	0	0	0	558	NA	NA
12H-1	97.1	7,244	962,756	132.9	0	0	1.3	0.2	0	0	7,082	1,400	12,266
12H-6	103.1	10,320	967,982	93.8	0	0	1.5	0.3	0	0	4,537	1,207	7,746
13H-2	107.2	6,435	966,543	150.2	0	0	1.0	0	0	0	4,707	1,985	13,156
13H-6	112.6	10,140	973,432	96.0	0	0	1.3	0	0	0	3,221	1,066	10,059
15H-2	119.3	8,832	983,043	111.3	0	0	1.9	0	0	0	4,089	484	4,904
15H-6	125.2	11,327	979,771	86.5	0	0	0.3	0	0	0	4,866	1,004	7,118
16H-2	128.1	13,985	969,145	69.3	0	0	3.6	0	0	0	6,090	737	10,027
16H-6	134.4	16,678	976,817	58.6	0	0.3	0.6	0	0	0	5,079	1,170	9,177
17H-3	139.2	20,275	971,157	47.9	0	4.1	1.4	0	0	0	3,935	520	4,899
18X-5	147.0	14,830	530,173	35.8	0	0	2.0	0	0	0	7,990	87,207	354,922
19X-2	152.0	10,076	914,933	90.8	8.8	0.6	0.6	0	0	0	14,509	10,258	42,477
20X-2	162.4	11,260	674,470	59.9	0	0.5	0.3	0.3	0	0	9,774	63,433	252,453
21X-2	170.8	12,552	967,772	77.1	0	0.3	11.3	0	0	0	7,483	581	5,138
21X-5	175.6	11,435	898,762	78.6	0	0.5	13.8	0.3	0	0	9,369	14,892	58,966
22X-2	180.6	14,020	970,209	69.2	7	3.8	1.6	1.2	0	0	5,130	52,395	208,175
22X-5	186.2	3,906	969,144	248.1	131.5	51.8	21.6	17.1	0.7	0	8,270	59,208	236,783

Note: NA = not analyzed.

Table T6. Composition of gas samples from PCS degassing experiments.

Hole, core, section	Depth (mbsf)	C_1/C_2	Hydrocarbons (ppmv)							Volatiles (ppmv)			
			C_1	C_2	C_3	*i*-C_4	*n*-C_4	*i*-C_5	*n*-C_5	H_2S	O_2	N_2	CO_2
311-													
U1329C-7P	55.80												
PCSG 2		15,765	542,794	34	0	0	1	0	0	0	56,043	352,320	0
U1329E-7P	73.50												
PCSG 4		15,850	502,754	32	0	0	0	4	0	0	57,153	382,926	0
U1329E-23P	188.50												
PCSG 3		194	817,325	4,204	2,019	672	301	97	25	0	18,807	87,679	19,971
PCSG 5		475	789,720	1,662	1,994	667	316	105	30	0	22,247	107,853	24,153

Table T7. Contents of inorganic carbon, $CaCO_3$, organic carbon, total organic carbon, and total nitrogen in sediment, Holes U1329C and U1329E.

Core, section, interval (cm)	Depth (mbsf)	Carbon (wt%)				Total nitrogen (wt%)	C/N
		Inorganic	$CaCO_3$	Total	Total organic		
311-U1329C-							
1H-1, 140–150	1.4	0.16	1.33	0.56	0.40	0.04	10.5
1H-3, 140–150	4.4	0.30	2.49	0.78	0.48	0.05	10.3
1H-5, 140–150	7.4	0.71	5.91	1.43	0.72	0.07	10.4
2H-1, 140–150	9.5	0.25	2.11	1.39	1.14	0.12	9.2
2H-3, 140–150	12.5	0.52	4.29	1.05	0.53	0.06	9.0
2H-7, 74–84	17.8	1.59	13.26	2.00	0.41	0.06	7.0
3H-2, 135–150	20.5	0.70	5.86	1.16	0.46	0.05	9.1
3H-4, 135–150	23.5	0.48	3.97	0.91	0.43	0.04	10.4
3H-6, 135–150	26.5	0.18	1.51	0.54	0.36	0.03	11.9
4H-2, 120–150	29.8	0.47	3.91	1.09	0.62	0.05	11.4
4H-5, 120–150	34.3	0.88	7.30	1.56	0.68	0.07	9.5
5H-2, 130–150	39.4	0.04	0.32	1.06	1.02	0.09	11.3
5H-5, 130–150	43.9	0.58	4.79	1.06	0.49	0.05	10.3
6H-1, 135–150	47.5	0.66	5.46	1.66	1.00	0.09	11.5
6H-5, 135–150	53.5	0.07	0.60	0.49	0.42	0.04	10.7
7P-1, 25–50	55.9	0.28	2.31	1.24	0.96	0.09	10.9
8H-2, 135–150	60.5	0.31	2.57	1.75	1.44	0.12	12.4
8H-5, 135–150	65.0	0.49	4.09	0.98	0.49	0.05	9.9
9H-2, 128–150	69.9	1.11	9.28	1.76	0.65	0.07	9.6
9H-5, 130–150	74.4	1.37	11.40	2.34	0.97	0.09	10.3
10H-2, 130–150	79.4	0.60	5.02	1.36	0.76	0.07	11.4
10H-5, 130–150	83.9	0.64	5.35	1.75	1.11	0.12	9.1
11H-2, 130–150	88.9	0.65	5.41	1.64	0.99	0.12	8.3
11H-5, 130–150	93.4	0.34	2.81	0.72	0.38	0.03	12.6
12H-2, 130–150	98.4	0.64	5.31	1.89	1.25	0.14	8.7
12H-5, 130–150	102.9	0.43	3.55	1.44	1.01	0.10	9.9
13H-2, 130–150	107.9	0.51	4.22	1.34	0.83	0.09	9.6
13H-5, 130–150	112.4	0.37	3.05	1.11	0.74	0.09	8.4
15H-2, 130–150	119.4	0.06	0.52	1.70	1.64	0.17	9.9
15H-5, 130–150	123.9	0.08	0.66	1.71	1.63	0.17	9.5
16H-2, 130–150	128.9	0.42	3.52	1.07	0.65	0.07	9.4
16H-5, 130–150	133.4	0.36	2.98	0.75	0.39	0.03	11.5
17H-2, 130–150	138.4	0.06	0.48	1.40	1.34	0.12	11.0
17H-3, 130–150	139.9	0.20	1.67	1.28	1.08	0.13	8.1
18X-3, 125–150	144.5	0.27	2.24	1.13	0.86	0.10	8.5
19X-2, 120–150	152.6	0.32	2.70	1.34	1.02	0.13	7.9
20X-2, 120–150	162.3	0.05	0.39	1.60	1.55	0.16	9.4
21X-6, 0–30	176.3	0.17	1.41	0.65	0.48	0.04	12.4
22X-4, 0–35	183.4	0.40	3.31	1.19	0.79	0.10	7.8
311-U1329E-							
1H-1, 140–150	1.4	0.27	2.28	0.70	0.43	0.04	9.8
1H-2, 140–150	2.9	0.21	1.75	0.64	0.43	0.04	9.8
1H-3, 140–150	4.4	0.19	1.59	0.87	0.68	0.05	14.2
2H-1, 135–150	6.4	0.59	4.95	1.10	0.51	0.06	8.5
2H-2, 135–150	7.9	0.24	1.97	1.90	1.66	0.17	9.9
2H-3, 135–150	9.4	0.85	7.07	1.59	0.74	0.08	9.5
2H-4, 135–150	10.9	0.88	7.37	1.66	0.78	0.07	10.6
2H-5, 135–150	12.4	0.98	8.15	1.69	0.71	0.08	8.6
2H-6, 135–150	13.9	0.20	1.64	1.08	0.88	0.06	14.0
3H-7, 63–78	24.1	0.57	4.72	0.67	0.01	0.04	2.6
7P-1, 0–36	73.5	1.15	9.54	1.83	0.68	0.09	7.3
10P-1, 18–59	125.2	0.54	4.53	1.39	0.85	0.11	7.6

Table T8. Perfluorocarbon tracer and fluorescent microsphere concentrations, Site U1329.

Core, section, interval (cm)	Depth (mbsf)	Detected PFT (ng/g sediment)		Detected particles (number/g sediment)	
		Inner	Outer	Inner	Outer
311-U1329C-					
3H-4, 35–40	22.45	BDL	BDL	BDL	$>1.0 \times 10^4$
10H-4, 20–25	81.30	1.27	0.60	BDL	4.2×10^4
18X-5, 40–45	146.60	3.20	5.20	BDL	BDL

Note: PFT = perfluorocarbon tracers, BDL = below detection limit.

Table T9. Moisture and density, Holes U1329B, U1329C, U1329D, and U1329E. (Continued on next page.)

Core, section, interval (cm)	Depth (mbsf)	Density (g/cm^3)		Porosity (%)
		Bulk	Grain	
311-U1329B-				
1H-1, 38–40	0.38	1.654	2.718	62.8
1H-1, 78–80	0.78	1.729	2.776	59.7
1H-1, 118–120	1.18	1.773	2.830	58.6
1H-2, 38–40	1.88	1.760	2.769	57.8
1H-2, 79–81	2.29	1.592	2.707	66.2
1H-2, 119–121	2.69	1.700	2.723	60.2
1H-3, 39–40	3.39	1.665	2.707	61.9
1H-3, 78–80	3.78	1.701	2.808	62.1
1H-3, 118–120	4.18	1.676	2.708	61.3
1H-4, 9–11	4.59	1.717	2.766	60.2
1H-4, 46–48	4.96	1.671	2.724	61.9
1H-5, 93–95	6.93	1.708	2.724	59.8
1H-5, 146–148	7.46	1.744	2.762	58.6
1H-6, 26–28	7.76	1.799	2.922	59.2
1H-6, 97–99	8.47	1.723	2.816	61.0
1H-7, 51–53	9.51	1.733	2.789	59.8
311-U1329C-				
1H-2, 39–41	1.89	1.604	2.821	67.7
1H-2, 103–105	2.53	1.620	2.897	68.2
1H-4, 12–14	4.62	1.670	2.836	64.4
2H-2, 31–33	9.91	1.712	2.806	61.4
2H-2, 112–114	10.72	1.553	2.728	69.0
2H-4, 77–79	13.37	1.771	2.905	60.3
2H-4, 126–128	13.86	1.743	2.772	58.9
2H-5, 6–8	14.16	1.729	2.800	60.3
2H-5, 52–54	14.62	1.712	2.768	60.6
2H-6, 9–11	15.69	1.755	2.711	56.7
2H-6, 74–76	16.34	1.774	2.814	58.1
2H-7, 32–34	17.42	1.674	2.760	62.6
3H-1, 6–8	17.66	1.702	2.778	61.3
3H-1, 71–73	18.31	1.627	2.672	63.4
3H-1, 133–135	18.93	1.718	2.773	60.3
3H-2, 3–5	19.13	1.733	2.738	58.6
3H-2, 27–29	19.37	1.763	2.756	57.4
3H-2, 70–72	19.80	1.754	2.712	56.7
3H-2, 124–126	20.34	1.691	2.767	61.7
3H-3, 22–24	20.82	1.739	2.752	58.6
3H-3, 95–97	21.55	1.669	2.758	62.8
3H-5, 14–16	23.74	1.760	2.726	56.8
3H-5, 49–51	24.09	1.880	2.756	50.6
3H-5, 119–121	24.79	1.901	2.729	48.5
3H-6, 52–54	25.62	1.825	2.778	54.3
3H-6, 131–133	26.41	1.956	2.764	46.4
3H-7, 53–55	27.13	1.811	2.766	54.8
4H-1, 20–22	27.30	1.813	2.779	55.1
4H-1, 55–57	27.65	1.800	2.746	54.9
4H-2, 32–34	28.92	1.855	2.992	57.8
4H-2, 92–93	29.52	1.762	2.815	58.8
4H-3, 37–39	30.47	1.757	2.779	58.2
4H-3, 114–116	31.24	1.761	2.807	58.7
4H-4, 40–42	32.00	1.707	2.750	60.4
4H-4, 101–103	32.61	1.766	2.831	58.9
4H-6, 48–50	35.08	1.665	2.715	62.1
4H-6, 115–117	35.75	1.722	2.743	59.4
4H-7, 5.5–7.5	36.16	1.825	2.753	53.6
4H-7, 64–66	36.74	1.714	2.775	60.6
5H-1, 27–29	36.87	1.633	2.758	64.9
5H-1, 111–113	37.71	1.681	2.717	61.2
5H-2, 30–32	38.40	1.674	2.747	62.2
5H-2, 90.5–92.5	39.01	1.656	2.670	61.6
5H-3, 13–15	39.73	1.665	2.695	61.6
5H-3, 77.5–79.5	40.38	1.711	2.679	58.5
5H-3, 128–130	40.88	1.682	2.721	61.2
5H-4, 38–40	41.48	1.717	2.807	61.1
5H-4, 110–112	42.20	1.658	2.648	61.0
5H-5, 32–34	42.92	1.747	2.795	59.2
5H-5, 83–85	43.43	1.857	2.817	53.5
5H-5, 132–134	43.92	1.666	2.768	63.2
5H-7, 32–34	45.92	1.708	2.753	60.5
6H-1, 35–37	46.45	1.641	2.717	63.5
6H-1, 110–112	47.20	1.749	2.767	58.4
6H-2, 35–37	47.95	1.696	2.700	59.9
6H-2, 100–102	48.60	1.707	2.713	59.5
6H-3, 25.5–27.5	49.36	1.748	2.798	59.2
6H-3, 103.5–105.5	50.14	1.684	2.858	64.0
6H-4, 9.5–11.5	50.70	1.649	2.789	64.6
6H-4, 59–61	51.19	1.785	2.795	57.0
6H-6, 28.5–30.5	53.89	1.841	2.776	53.4
6H-6, 105.5–107.5	54.66	1.805	2.861	57.5
6H-7, 24–36	55.34	1.764	2.707	56.1
6H-7, 80–82	55.90	1.789	2.764	56.1
8H-1, 32.5–34.5	57.93	1.617	2.615	62.7
8H-1, 107–109	58.67	1.679	2.677	60.4
8H-2, 30–32	59.40	1.622	2.585	61.7
8H-2, 100–102	60.10	1.591	2.612	64.3
8H-3, 17–19	60.77	1.648	2.657	61.8
8H-3, 127–129	61.87	1.742	2.706	57.3
8H-4, 16–18	62.26	1.816	2.753	54.2
8H-4, 106–108	63.16	1.800	2.764	55.4
8H-6, 32–34	65.42	1.898	2.814	51.2
8H-6, 130–132	66.40	1.830	2.825	55.3
8H-7, 14–16	66.74	1.749	2.730	57.5
9H-1, 24–26	67.34	1.651	2.697	62.5
9H-1, 119–121	68.29	1.835	2.795	54.2
9H-2, 46–48	69.06	1.845	2.832	54.6
9H-2, 120–122	69.80	1.680	2.756	62.1
9H-3, 32–34	70.42	1.703	2.767	61.0
9H-3, 107–109	71.17	1.830	2.715	52.3
9H-4, 50–52	72.10	1.660	2.830	64.8
9H-4, 116–118	72.76	1.614	2.716	65.1
9H-6, 22–24	74.82	1.626	2.672	63.5
9H-6, 127–129	75.87	1.570	2.598	65.3
9H-7, 39–41	76.49	1.667	2.660	60.7
10H-1, 42–44	77.02	1.737	2.708	57.7
10H-1, 91–93	77.51	1.656	2.695	62.2
10H-2, 32–34	78.42	1.659	2.644	60.8
10H-2, 94–96	79.04	1.711	2.682	58.6
10H-3, 47–49	80.07	1.737	2.683	57.0
10H-3, 113–115	80.73	1.757	2.742	57.4
10H-4, 42–44	81.52	1.615	2.601	62.5
10H-6, 70–72	84.80	1.793	2.716	54.5
10H-6, 126–128	85.36	1.684	2.659	59.6
10H-7, 64–66	86.24	1.658	2.626	60.4
11H-1, 45–47	86.55	1.769	2.756	57.0
11H-1, 118–120	87.28	1.603	2.608	63.5
11H-2, 36–38	87.96	1.640	2.603	61.0
11H-2, 110–112	88.70	1.708	2.615	57.0
11H-3, 57–59	89.67	1.788	2.699	54.4
11H-3, 135–137	90.45	1.776	2.669	54.2
11H-4, 50–52	91.10	1.748	2.676	56.2
11H-4, 140–142	92.00	1.842	2.716	51.6
11H-6, 25–27	93.85	1.696	2.707	60.1
11H-6, 111–113	94.71	1.652	2.618	60.6
11H-7, 39–41	95.49	1.658	2.703	62.3
12H-1, 41–43	96.01	1.695	2.671	59.3
12H-1, 138–140	96.98	1.670	2.653	60.3
12H-2, 38–40	97.46	1.675	2.670	60.4
12H-2, 98–100	98.06	1.659	2.642	60.8
12H-3, 56–58	99.14	1.668	2.688	61.3
12H-3, 107–109	99.65	1.666	2.729	62.3
12H-4, 24–26	100.32	1.661	2.683	61.6
12H-4, 107–109	101.15	1.694	2.728	60.7
12H-6, 31–33	103.39	1.773	2.751	56.6
12H-6, 105–107	104.13	1.768	2.757	57.1
12H-7, 35–37	104.93	1.778	2.698	55.0

Table T9 (continued).

Core, section, interval (cm)	Depth (mbsf)	Density (g/cm^3)		Porosity (%)
		Bulk	Grain	
13H-1, 46–48	105.56	1.767	2.773	57.5
13H-1, 102–104	106.12	1.786	2.831	57.8
13H-2, 28–30	106.88	1.775	2.765	56.9
13H-2, 96–98	107.56	1.788	2.744	55.6
13H-3, 27–29	108.37	1.783	2.810	57.5
13H-3, 106–108	109.16	1.857	2.819	53.6
13H-4, 40–42	110.00	1.761	2.806	58.6
13H-4, 131–133	110.91	1.934	2.753	47.4
13H-6, 30–32	112.90	1.762	2.807	58.6
13H-6, 125–127	113.85	1.806	2.754	54.8
13H-7, 40–42	114.50	1.870	2.802	52.4
14P-1, 40–42	115.00	1.726	2.682	57.6
15H-1, 27–29	116.87	1.627	2.643	62.8
15H-1, 106–108	117.66	1.631	2.638	62.4
15H-2, 23–25	118.33	1.636	2.675	62.9
15H-2, 75–77	118.85	1.645	2.694	62.8
15H-3, 28–30	119.88	1.630	2.639	62.5
15H-3, 116–118	120.76	1.666	2.649	60.5
15H-4, 38–40	121.48	1.674	2.705	61.3
15H-4, 105–107	122.15	1.678	2.704	61.1
15H-6, 52–54	124.62	1.721	2.672	57.7
15H-6, 135–137	125.45	1.718	2.660	57.6
15H-7, 44–46	126.04	1.686	2.707	60.6
16H-1, 27–29	126.37	1.851	2.750	52.1
16H-1, 128–130	127.38	1.891	2.815	51.6
16H-2, 34–36	127.94	1.815	2.749	54.1
16H-2, 120–122	128.80	1.838	2.766	53.3
16H-3, 38–40	129.48	1.822	2.736	53.4
16H-3, 136–138	130.46	1.724	2.708	58.4
16H-4, 10–12	130.70	1.781	2.724	55.5
16H-4, 74–76	131.34	1.772	2.724	56.0
16H-6, 22–24	133.82	1.678	2.622	59.1
16H-6, 76–78	134.36	1.702	2.611	57.3
16H-6, 123–125	134.83	1.719	2.611	56.2
16H-7, 13–15	135.23	1.782	2.736	55.7
16H-7, 58–60	135.68	1.725	2.655	57.0
17H-1, 12–14	135.72	1.729	2.676	57.3
17H-1, 72–74	136.32	1.730	2.685	57.5
17H-1, 141–143	137.01	2.020	2.765	42.8
17H-2, 28–30	137.38	1.722	2.741	59.4
17H-2, 116–118	138.26	2.520	3.943	48.7
18X-1, 48–50	140.68	1.718	2.732	59.4
18X-1, 114–116	141.34	1.771	2.737	56.4
18X-2, 33–35	142.03	1.756	2.704	56.4
18X-2, 110–112	142.80	1.740	2.718	57.7
18X-3, 18–20	143.38	1.764	2.691	55.6
18X-4, 29–31	144.99	1.793	2.693	53.9
18X-4, 125–127	145.95	1.666	2.641	60.3
19X-1, 46–48	150.36	1.711	2.717	59.4
19X-3, 85–87	153.75	1.773	2.642	53.7
19X-4, 98–100	155.38	1.794	2.688	53.7
19X-5, 62–64	156.52	1.688	2.672	59.7
19X-6, 43–45	157.33	1.732	2.679	57.2
20X-1, 55–57	160.15	1.759	2.640	54.5
20X-3, 68–70	163.28	1.655	2.650	61.2
20X-4, 68–70	164.78	1.586	2.573	63.7
20X-5, 60–62	165.70	1.690	2.620	58.3
21X-1, 105–107	170.35	1.842	2.668	50.2
21X-2, 51–53	171.31	1.963	2.722	44.7
21X-3, 136–138	173.66	1.871	2.773	51.6
21X-5, 3–5	175.33	1.955	2.769	46.7
22X-1, 91–93	179.81	1.833	2.721	52.3
22X-2, 86–88	181.26	1.919	2.792	49.4
22X-3, 61–63	182.51	1.890	2.748	49.8
22X-4, 116–118	184.56	1.794	2.792	56.4
22X-5, 36–38	185.23	1.864	2.781	52.2
22X-6, 30–32	186.59	1.853	2.789	53.1
22P-0, 13–15	188.63	2.762	2.858	5.2
23P-1, 41–43	188.91	1.648	2.697	62.7
24P-2, 62–63	189.12	2.657	2.604	5.1
23P-1, 83–85	189.33	2.115	2.706	35.1
311-U1329D-				
1X-1, 12–14	201.12	2.173	2.721	32.3
1X-1, 14–16	201.14	2.139	2.676	32.5
311-U1329E-				
1H-1, 56–58	0.56	1.428	2.622	74.7
1H-2, 25–27	1.75	1.410	2.703	77.0
1H-2, 45–47	1.95	1.405	2.754	78.0
1H-2, 62–64	2.12	1.386	2.616	77.3
1H-2, 68–70	2.18	1.389	2.602	76.8
1H-2, 75–77	2.25	1.591	2.843	68.8
1H-2, 91–93	2.41	1.713	2.805	61.3
1H-3, 23–25	3.23	1.607	2.712	65.5
1H-3, 77–79	3.77	1.631	2.708	63.9
2H-1, 57–59	5.57	1.619	2.747	65.5
2H-2, 57–59	7.07	1.733	2.935	62.9
2H-3, 49–51	8.49	1.757	2.838	59.6
2H-4, 36–38	9.86	1.560	2.706	68.1
2H-5, 22–24	11.22	1.487	2.679	72.0
2H-5, 71–73	11.71	1.699	2.813	62.3
2H-6, 21–23	12.71	1.647	2.708	63.0
3H-2, 63–65	16.63	1.713	2.796	61.1
3H-3, 58–60	18.08	1.642	2.759	64.4
3H-3, 114–116	18.64	1.766	2.774	57.6
3H-4, 68–70	19.68	1.761	2.769	57.8
3H-5, 51–53	21.01	1.701	2.734	60.4
3H-6, 38–40	22.38	1.829	2.780	54.2
3H-7, 28–30	23.78	1.809	2.678	52.6
4H-1, 76–78	24.76	1.732	2.553	53.7
4H-2, 81–83	26.31	1.707	2.748	60.4
4H-3, 76–78	27.76	1.711	2.764	60.5
4H-4, 77–79	29.27	1.714	2.765	60.4
4H-5, 110–110	31.10	2.236	3.133	42.5
4H-6, 75–77	32.25	1.943	2.824	48.9
7P-1, 52–55	74.02	1.583	2.786	68.3
7P-1, 80–81	74.30	1.537	2.768	70.6
8Y-CC, 23–25	104.65	1.687	2.706	60.6
10P-1, 10–12	125.10	1.737	2.702	57.5
10P-1, 73–75	125.73	1.787	2.674	53.8

Table T10. Compressional wave velocity, Holes U1329B, U1329C, and U1329E.

Core, section, interval (cm)	Depth (mbsf)	Velocity (m/s)		
		PWS1	PWS2	PWS3
311-U1329B-				
1H-1, 25.7	0.26			1512.1
1H-1, 28.8	0.29		1449.3	
1H-1, 29.6	0.30	1508.4		
1H-1, 44.1	0.44		1498.5	
1H-1, 44.6	0.45	1512.6		
1H-1, 44.7	0.45			1494.3
1H-1, 64.1	0.64		1509.8	
1H-1, 64.8	0.65			1444.0
1H-1, 65.3	0.65	1529.9		
1H-1, 84.1	0.84		1482.6	
1H-1, 84.3	0.84			1509.7
1H-1, 84.8	0.85	1511.5		
1H-1, 104.8	1.05			1522.7
1H-1, 105	1.05	1525.2		
1H-1, 105	1.05		1514.8	
1H-1, 117.3	1.17	1524.5		
1H-1, 124.1	1.24			1517.7
1H-1, 124.2	1.24		1519.4	
1H-1, 138.2	1.38		1534.3	
1H-1, 143.7	1.44			1526.4
1H-2, 9.3	1.59		1514.2	
1H-2, 9.3	1.59			1549.3
1H-2, 10.1	1.60	1537.6		
1H-2, 29.2	1.79		1445.7	
1H-2, 29.3	1.79	1525.4		
1H-2, 29.5	1.80			1531.7
1H-2, 48.2	1.98		1521.4	
1H-2, 48.9	1.99			1546.1
1H-2, 49.6	2.00	1534.0		
1H-2, 68.9	2.19		1457.8	
1H-2, 69.3	2.19			1521.4
1H-2, 69.6	2.20	1514.9		
1H-2, 89.5	2.40		1463.9	
1H-2, 89.7	2.40			1540.5
1H-2, 90	2.40	1526.6		
1H-2, 108.3	2.58		1512.8	
1H-2, 109.3	2.59			1533.8
1H-2, 109.6	2.60	1524.5		
1H-2, 118.1	2.68	1521.9		
1H-2, 125.9	2.76		1508.3	
1H-2, 129.2	2.79			1516.9
1H-2, 138.3	2.88		1514.8	
1H-3, 5	3.05			1515.3
1H-3, 5.6	3.06		1546.9	
1H-3, 6.8	3.07	1523.2		
1H-3, 24.7	3.25	1503.5		
1H-3, 24.7	3.25		1488.9	
1H-3, 24.8	3.25			1509.3
1H-3, 43.4	3.43		1485.8	
1H-3, 44.1	3.44			1522.4
1H-3, 44.8	3.45	1483.2		
1H-3, 64.4	3.64			1533.5
1H-3, 65	3.65	1438.1		
1H-3, 83	3.83		1511.5	
1H-3, 83.9	3.84			1532.4
1H-3, 104.1	4.04			1507.3
1H-3, 123.3	4.23			1533.0
1H-3, 139.4	4.39		1508.3	
1H-3, 142.6	4.43			1516.7
1H-4, 8	4.58			1463.4
311-U1329C-				
1H-2, 10	1.60			1502.5
1H-2, 19	1.69	1499.9		
1H-2, 19	1.69			1492.4
1H-2, 28	1.78		1502.7	
1H-2, 52	2.02	1499.8		
1H-2, 52	2.02			1466.3
1H-2, 54	2.04		1481.3	
1H-2, 113	2.63	1498.3		
1H-2, 123	2.73			1429.9
1H-2, 135	2.85		1504.8	
1H-4, 23	4.73	1517.0		
1H-4, 23	4.73		1518.7	
1H-4, 23	4.73			1528.9
1H-4, 64	5.14	1504.5		
1H-4, 65	5.15			1518.2
1H-4, 67	5.17		1506.9	
1H-4, 120	5.70		1509.	
1H-4, 120	5.70			1521.1
1H-4, 122	5.72	1507.4		
1H-5, 17	6.17	1513.3		
1H-5, 17	6.17		1517.2	
1H-5, 17	6.17			1468.4
1H-5, 86	6.86	1510.1		
1H-5, 86	6.86			1518.8
1H-5, 87	6.87		1521.1	
2H-2, 51	10.11			1520.5
2H-2, 106	10.66			1486.3
3H-1, 26	17.86			1453.4
311-U1329E-				
1H-1, 9	0.09		1512.7	
1H-1, 9	0.09			1463.7
1H-1, 32	0.32	1518.0		
1H-1, 32	0.32		1510.9	
1H-1, 39	0.39	1510.5		
1H-1, 66	0.66		1511.6	
1H-1, 66	0.66			1472.9
1H-1, 86	0.86	1507.3		
1H-1, 86	0.86		1505.5	
1H-1, 86	0.86			1455.9
1H-1, 96	0.96	1533.6		
1H-2, 30	1.80	1491.6		
1H-2, 30	1.80		1492.6	
1H-2, 30	1.80			1499.4
1H-2, 57	2.07	1496.9		
1H-2, 57	2.07		1502.8	
1H-2, 57	2.07			1507.9
1H-2, 84	2.34	1500.6		
1H-2, 97	2.47		1512.7	
1H-2, 97	2.47			1492.4
1H-3, 84	3.84	1500.6		
1H-3, 84	3.84		1504.3	
1H-3, 84	3.84			1506.9

Table T11. Torvane shear strength, Holes U1329B, U1329C, and U1329E. (See table note. Continued on next page.)

Core, section, interval (cm)	Depth (mbsf)	Torvane shear strength (kPa)	Torvane size
311-U1329B-			
1H-1, 72–74	0.72	20	M
1H-2, 75–77	2.25	20	M
1H-3, 73–75	3.73	31	M
1H-4, 84–86	5.34	30	M
1H-5, 86–88	6.86	37	M
1H-6, 87–89	8.37	25	M
1H-7, 58–60	9.58	25	M
311-U1329C-			
1H-2, 58–60	2.08	14	M
1H-5, 62–64	6.62	21	M
1H-4, 44–46	4.94	17	M
1H-6, 16–18	7.66	25	M
2H-2, 58–60	10.18	28	M
2H-4, 46–48	13.06	37	M
2H-5, 57–59	14.67	40	M
2H-6, 126–128	16.86	47	M
2H-7, 11–13	17.21	30	M
3H-1, 31–33	17.91	32.5	M
3H-1, 89–91	18.49	39	M
3H-2, 90–92	20.00	41	M
3H-3, 69–71	21.29	33	M
3H-5, 72–74	24.32	49	M
3H-6, 43–45	25.53	32	M
4H-1, 23–25	27.33	54	M
4H-1, 52–54	27.62	35	M
4H-1, 122–124	28.32	50	M
4H-2, 27–29	28.87	52	M
4H-2, 94.5–96.5	29.55	47	M
4H-3, 40–42	30.50	53	M
4H-3, 109.5–111.5	31.19	30	M
4H-4, 36–38	31.96	30	M
4H-4, 105–107	32.65	42	M
4H-6, 51–53	35.11	45	M
4H-6, 109–111	35.69	43	M
4H-7, 7–9	36.17	45	M
4H-7, 68–70	36.78	57	M
5H-1, 24.5–26.5	36.85	43	M
5H-1, 107–109	37.67	40	M
5H-2, 26.5–28.5	38.37	45	M
5H-2, 94.5–96.5	39.04	38	M
5H-3, 17–19	39.77	41	M
5H-3, 72.5–74.5	40.33	40	M
5H-3, 123.5–125.5	40.83	46	M
5H-4, 42–44	41.52	54	M
5H-4, 107–109	42.17	49	M
5H-6, 37–39	44.47	59	M
5H-6, 77–79	44.87	70	M
5H-6, 139–141	45.49	63	M
5H-7, 38–40	45.98	30	M
6H-1, 41.5–43.5	46.51	55	M
6H-1, 97–99	47.07	44	M
6H-2, 40–42	48.00	56	M
6H-3, 109–111	50.19	68	M
6H-3, 20.5–22.5	49.31	66	M
6H-4, 20.5–22.5	50.81	50	M
6H-4, 53–55	51.13	52	M
6H-6, 32–34	53.92	68	M
6H-6, 100.5–102.5	54.60	71	M
6H-7, 19–21	55.29	68	M
6H-7, 74.5–76.5	55.85	64	M
8H-1, 70–72	58.30	85	S
8H-2, 42–44	59.52	80	S
8H-3, 58–60	61.18	75	S
8H-4, 66–68	62.76	75	S
8H-6, 42–44	65.52	95	S
8H-7, 65–67	67.25	75	S
9H-1, 87–89	67.97	70	S
9H-2, 107–109	69.67	55	S
9H-3, 58–60	70.68	55	S
9H-4, 91–93	72.51	67.5	S
9H-6, 100–102	75.60	60	S
9H-7, 58–60	76.68	75	S
10H-1, 76–78	77.36	75	S
10H-2, 88–90	78.98	87.5	S
10H-3, 80–82	80.40	67.5	S
10H-6, 74–76	84.84	82.5	S
10H-7, 32–34	85.92	47.5	S
10H-4, 64–66	81.74	60	S
11H-1, 39–41	86.49	80	S
11H-2, 100–102	88.60	52.5	S
11H-3, 81–83	89.91	87.5	S
11H-4, 96–98	91.56	85	S
11H-6, 36–38	93.96	110	S
11H-7, 46–48	95.56	85	S
13H-1, 60–62	105.70	93.75	S
13H-2, 60–62	107.20	95	S
13H-2, 31–33	106.91	122.5	S
13H-3, 60–62	108.70	150	S
13H-4, 45–47	110.05	87.5	S
13H-6, 27–29	112.87	137.5	S
13H-6, 130–132	113.90	120	S
13H-7, 45–47	114.55	85	S
13H-4, 126–128	110.86	135	S
13H-3, 32–34	108.42	137.5	S
15H-1, 20–22	116.80	50	S
15H-1, 101–103	117.61	112.5	S
15H-2, 17–19	118.27	97.5	S
15H-2, 80–82	118.90	95	S
15H-3, 22–24	119.82	150	S
15H-3, 122–124	120.82	152.5	S
15H-4, 43–45	121.53	125	S
15H-4, 101–103	122.11	137.5	S
15H-6, 56–58	124.66	175	S
15H-6, 128–130	125.38	187.5	S
15H-7, 49–51	126.09	75	S
16H-1, 31.5–33.5	126.42	150	S
16H-1, 24–26	126.34	170	S
16H-2, 30–32	127.90	125	S
16H-2, 116–118	128.76	167.5	S
16H-3, 43–45	129.53	170	S
16H-3, 132–134	130.42	75	S
16H-4, 15–17	130.75	100	S
16H-4, 79–81	131.39	115	S
16H-5, 26–28	132.36	125	S
16H-5, 70–72	132.80	117.5	S
16H-5, 128–130	133.38	150	S
16H-7, 12–14	135.22	97.5	S
16H-7, 62–64	135.72	115	S
17H-1, 105–107	136.65	162.5	S
17H-2, 40–42	137.50	100	S
17H-2, 19–21	137.29	87.5	S
18X-1, 72–74	140.92	105	S
18X-2, 86–88	142.56	100	S
18X-3, 88–90	144.08	60	S
18X-4, 5–7	144.75	30	S
18X-4, 88–90	145.58	75	S
19X-3, 43–45	153.33	87.5	S
19X-4, 93–95	155.33	100	S
311-U1329E-			
1H-1, 73–75	0.73	4	M
1H-2, 42–44	1.92	8	M
1H-2, 82–84	2.32	8	M
2H-1, 62–64	5.62	15	M

Table T11 (continued).

Core, section, interval (cm)	Depth (mbsf)	Torvane shear strength (kPa)	Torvane size
2H-2, 62–64	7.12	21	M
2H-3, 54–56	8.54	33	M
2H-4, 41–43	9.91	29	M
2H-5, 62–64	11.62	34	M
2H-6, 82–84	13.32	34	M
3H-2, 77–79	16.77	14	M
3H-3, 65–67	18.15	19	M
3H-4, 126–128	20.26	24	M
3H-5, 124–126	21.74	22.5	M
3H-6, 129–131	23.29	45	M
3H-7, 24–26	23.74	25	M
4H-1, 81–83	24.81	51	M
4H-2, 76.5–78.5	26.26	35	M
4H-3, 82.5–84.5	27.83	36	M
4H-4, 81–83	29.31	35	M
4H-5, 71–73	30.71	46	M
4H-6, 70–72	32.20	34	M
8-CC, 4–6	104.46	80	M
8-CC, 9–11	104.51	65	M
8-CC, 33–35	104.75	79	M

Note: M = medium (2.5 cm diameter), S = small (1.9 cm diameter).

Table T12. Contact resistivity, Holes U1329C and U1329E. (Continued on next two pages.)

Core, section, interval (cm)	Depth (mbsf)	Resistivity (Ωm)
Parallel		
311-U1329C-		
1H-2, 4	1.54	0.517
1H-2, 46	1.96	0.483
1H-2, 80	2.30	0.470
1H-2, 98	2.48	0.475
1H-2, 129	2.79	0.473
1H-4, 30	4.80	0.554
1H-4, 79	5.29	0.539
1H-4, 89	5.39	0.529
1H-4, 124	5.74	0.549
1H-4, 134	5.84	0.560
1H-5, 30	6.30	0.541
1H-5, 50	6.50	0.564
1H-5, 70	6.70	0.581
1H-5, 90	6.90	0.529
1H-5, 100	7.00	0.551
1H-6, 6	7.56	0.669
2H-1, 31	8.41	0.623
2H-1, 5	8.15	0.598
2H-1, 35	8.45	0.604
2H-1, 62	8.72	0.561
2H-1, 84	8.94	0.666
2H-1, 134	9.44	0.621
2H-1, 135	9.45	0.627
2H-1, 135	9.45	0.639
2H-1, 135	9.45	0.624
2H-4, 30	12.90	0.660
2H-4, 63	13.23	0.641
2H-4, 115	13.75	0.641
2H-5, 35	14.45	0.600
2H-5, 61	14.71	0.638
2H-6, 41	16.01	0.626
2H-6, 61	16.21	0.708
2H-6, 112	16.72	0.638
2H-7, 30	17.40	0.635
3H-1, 46	18.06	0.793
3H-1, 66	18.26	0.709
3H-1, 120	18.80	0.739
3H-2, 7	19.17	0.726
3H-2, 33	19.43	0.823
3H-2, 58	19.68	0.788
3H-2, 85	19.95	0.812
3H-2, 110	20.20	0.664
3H-2, 135	20.45	0.628
3H-3, 5	20.65	0.756
3H-3, 37	20.97	0.870
3H-3, 67	21.27	0.773
3H-3, 94	21.54	0.633
3H-3, 119	21.79	0.663
3H-4, 12	22.22	0.781
3H-4, 42	22.52	1.217
3H-4, 67	22.77	0.872
3H-4, 80	22.90	0.933
3H-4, 101	23.11	1.011
3H-4, 125	23.35	1.015
3H-4, 143	23.53	0.939
3H-5, 12	23.72	0.781
3H-5, 42	24.02	1.217
3H-5, 67	24.27	0.872
3H-5, 80	24.40	0.933
3H-5, 101	24.61	1.011
3H-5, 125	24.85	1.015
3H-5, 143	25.03	0.939
3H-6, 5	25.15	0.957
3H-6, 34	25.44	0.850
3H-6, 59	25.69	0.900
3H-6, 69	25.79	0.943
3H-6, 95	26.05	0.858
3H-6, 123	26.33	0.866
3H-7, 30	26.90	1.267
3H-7, 47	27.07	1.207
3H-7, 65	27.25	1.071
4H-1, 7	27.17	0.577
4H-1, 34	27.44	0.665
4H-1, 67	27.77	0.491
4H-1, 92	28.02	0.493
4H-1, 135	28.45	0.609
4H-2, 5	28.65	0.503
4H-2, 45	29.05	0.516
4H-2, 46	29.06	0.512
4H-2, 91	29.51	0.588
4H-3, 26	30.36	0.494
4H-3, 75	30.85	0.565
4H-3, 110	31.20	0.661
4H-4, 7	31.67	0.711
4H-4, 33	31.93	0.564
4H-4, 84	32.44	0.546
4H-6, 35	34.95	0.593
4H-6, 36	34.96	0.941
4H-6, 37	34.97	0.532
4H-6, 83	35.43	0.605
4H-6, 122	35.82	0.547
5H-1, 35	36.95	0.570
5H-1, 63	37.23	0.466
5H-1, 64	37.24	0.548
5H-1, 130	37.90	0.537
5H-2, 36	38.46	0.485
5H-2, 39	38.49	0.508
5H-2, 100	39.10	0.521
5H-2, 120	39.30	0.769
5H-4, 31	41.41	0.626
5H-4, 86	41.96	0.659
5H-4, 120	42.30	0.536
5H-6, 6	44.16	0.530
5H-6, 44	44.54	0.555
5H-6, 69	44.79	0.564
5H-6, 96	45.06	0.551
5H-6, 126	45.36	0.438
6H-1, 28	46.38	0.433
6H-1, 62	46.72	0.476
6H-1, 91	47.01	0.541
6H-1, 131	47.41	0.570
6H-3, 5	49.15	0.643
6H-3, 36	49.46	0.597
6H-3, 62	49.72	0.589
6H-3, 80	49.90	0.553
6H-3, 94	50.04	0.695
6H-3, 123	50.33	0.633
6H-3, 137	50.47	0.488
6H-3, 140	50.50	0.487
6H-6, 7	53.67	0.588
6H-6, 38	53.98	0.817
6H-6, 63	54.23	0.749
6H-6, 120	54.80	0.690
6H-6, 136	54.96	0.728
8H-2, 4	59.14	0.471
8H-2, 36	59.46	0.552
8H-2, 39	59.49	0.592
8H-2, 68	59.78	0.584
8H-2, 113	60.23	0.676
8H-2, 132	60.42	0.785
8H-4, 34	62.44	0.888
8H-4, 46	62.56	0.819
8H-4, 86	62.96	0.840
8H-4, 95	63.05	0.851
8H-4, 117	63.27	0.827
8H-4, 145	63.55	0.787
8H-6, 38	65.48	0.847
8H-6, 70	65.80	0.812
8H-6, 135	66.45	0.894
9H-1, 80	67.90	0.526
9H-1, 81	67.91	0.541
9H-1, 125	68.35	0.446
9H-1, 143	68.53	0.453
9H-4, 34	71.94	0.383
9H-4, 37	71.97	0.511
9H-4, 85	72.45	0.447
9H-4, 123	72.83	0.504
9H-6, 5	74.65	0.429
9H-6, 62	75.22	0.499
9H-6, 96	75.56	0.429
9H-6, 123	75.83	0.409
10H-1, 5	76.65	0.540
10H-1, 60	77.20	0.419
10H-1, 95	77.55	0.467
10H-3, 6	79.66	0.414
10H-3, 40	80.00	0.485
10H-3, 100	80.60	0.524
10H-3, 129	80.89	0.459
10H-6, 15	84.25	0.627
10H-6, 24	84.34	0.454
10H-6, 34	84.44	0.537
10H-6, 57	84.67	0.483
10H-6, 67	84.77	0.508
10H-6, 79	84.89	0.682
10H-6, 79	84.89	0.483
11H-1, 5	86.15	0.706
11H-1, 28	86.38	0.800
11H-1, 40	86.50	0.824
11H-1, 64	86.74	0.899
11H-1, 96	87.06	0.840
11H-1, 138	87.48	0.817
11H-2, 2	87.62	0.743
11H-2, 30	87.90	0.800
11H-2, 55	88.15	0.911
11H-2, 97	88.57	0.895
11H-2, 125	88.85	0.909
11H-2, 125	88.85	0.901
11H-3, 5	89.15	0.924
11H-3, 5	89.15	0.919
11H-3, 30	89.40	0.907
11H-3, 59	89.69	0.956
11H-3, 84	89.94	0.895
11H-3, 125	90.35	0.921
11H-4, 25	90.85	0.807
11H-4, 50	91.10	0.862
11H-4, 75	91.35	0.890
11H-4, 100	91.60	0.856
11H-4, 125	91.85	0.943
11H-6, 25	93.85	0.869
11H-6, 50	94.10	0.781
11H-6, 99	94.59	1.081
11H-6, 70	94.30	0.879
11H-6, 111	94.71	0.940
11H-6, 132	94.92	0.924
11H-7, 11	95.21	0.981
11H-7, 40	95.50	0.887
12H-1, 5	95.65	1.075
12H-1, 24	95.84	0.991
12H-1, 44	96.04	0.964
12H-1, 111	96.71	0.969
12H-1, 140	97.00	0.947
12H-2, 8	97.16	0.930
12H-2, 21	97.29	0.939
12H-2, 40	97.48	0.891
12H-2, 61	97.69	0.969

Table T12 (continued).

Core, section, interval (cm)	Depth (mbsf)	Resistivity (Ωm)
12H-2, 79	97.87	0.938
12H-2, 104	98.12	0.922
12H-2, 127	98.35	0.992
12H-3, 7	98.65	1.090
12H-3, 32	98.90	1.034
12H-3, 57	99.15	1.012
12H-3, 82	99.40	1.008
12H-3, 107	99.65	0.994
12H-3, 134	99.92	1.108
12H-3, 146	100.04	0.983
12H-4, 7	100.15	1.002
12H-4, 29	100.37	1.003
12H-4, 54	100.62	0.905
12H-4, 79	100.87	1.084
12H-4, 111	101.19	1.152
12H-4, 136	101.44	0.975
12H-6, 8	103.16	1.146
12H-6, 33	103.41	1.059
12H-6, 55	103.63	1.373
12H-6, 80	103.88	1.074
12H-6, 105	104.13	1.055
12H-6, 133	104.41	1.099
12H-7, 5	104.63	1.070
12H-7, 22	104.80	1.154
12H-7, 36	104.94	1.171
12H-7, 56	105.14	1.188
13H-1, 6	105.16	0.926
13H-1, 24	105.34	1.171
13H-1, 49	105.59	1.206
13H-1, 74	105.84	1.299
13H-1, 104	106.14	1.229
13H-1, 129	106.39	1.416
13H-1, 145	106.55	1.279
13H-2, 5	106.65	0.230
13H-2, 5	106.65	0.892
13H-2, 30	106.90	0.892
13H-2, 55	107.15	0.902
13H-2, 97	107.57	0.955
13H-2, 128	107.88	1.066
13H-3, 8	108.18	1.001
13H-3, 28	108.38	0.954
13H-3, 57	108.67	0.941
13H-3, 79	108.89	0.982
13H-3, 107	109.17	0.949
13H-3, 145	109.55	1.036
13H-4, 15	109.75	1.103
13H-4, 40	110.00	1.316
13H-4, 71	110.31	1.015
13H-4, 104	110.64	1.059
13H-4, 132	110.92	0.847
13H-6, 6	112.66	0.959
13H-6, 31	112.91	0.895
13H-6, 57	113.17	0.897
13H-6, 94	113.54	1.076
13H-6, 126	113.86	1.072
13H-7, 5	114.15	1.146
13H-7, 40	114.50	1.376
13H-7, 61	114.71	1.029
14P-1, 9	114.69	1.069
15H-1, 9	116.69	1.038
15H-1, 28	116.88	0.986
15H-1, 43	117.03	1.129
15H-1, 65	117.25	1.167
15H-1, 90	117.50	0.989
15H-1, 106	117.66	0.980
15H-1, 125	117.85	1.117
15H-1, 150	118.10	1.182
15H-2, 4	118.14	1.014
15H-2, 23	118.33	1.077
15H-2, 35	118.45	1.045
15H-2, 60	118.70	1.039
15H-2, 85	118.95	1.066
15H-2, 94	119.04	1.142
15H-2, 106	119.16	1.559
15H-2, 113	119.23	1.375
15H-3, 13	119.73	1.339
15H-3, 28	119.88	1.535
15H-3, 53	120.13	1.041
15H-3, 69	120.29	1.081
15H-3, 82	120.42	1.095
15H-3, 107	120.67	1.077
15H-3, 117	120.77	1.076
15H-3, 142	121.02	1.194
15H-4, 4	121.14	1.062
15H-4, 16	121.26	1.190
15H-4, 41	121.51	1.229
15H-4, 62	121.72	1.111
15H-4, 87	121.97	1.055
15H-4, 106	122.16	1.153
15H-6, 6	124.16	1.067
15H-6, 33	124.43	1.196
15H-6, 53	124.63	1.124
15H-6, 78	124.88	1.232
15H-6, 90	125.00	1.222
15H-6, 112	125.22	1.206
15H-6, 135	125.45	1.303
15H-7, 8	125.68	1.372
15H-7, 33	125.93	1.243
15H-7, 45	126.05	1.270
15H-7, 69	126.29	1.157
16H-1, 5	126.15	1.387
16H-1, 28	126.38	1.200
16H-1, 45	126.55	1.197
16H-1, 63	126.73	1.300
16H-1, 80	126.90	1.101
16H-1, 97	127.07	1.263
16H-1, 112	127.22	1.218
16H-1, 140	127.50	1.217
16H-2, 4	127.64	1.192
16H-2, 18	127.78	1.277
16H-2, 36	127.96	1.167
16H-2, 61	128.21	1.145
16H-2, 89	128.49	1.646
16H-2, 105	128.65	1.242
16H-2, 123	128.83	1.196
16H-3, 8	129.18	1.286
16H-3, 25	129.35	1.292
16H-3, 38	129.48	1.157
16H-3, 63	129.73	1.157
16H-3, 92	130.02	1.209
16H-3, 118	130.28	1.116
16H-3, 143	130.53	1.012
16H-4, 5	130.65	1.060
16H-4, 24	130.84	1.121
16H-4, 46	131.06	1.045
16H-4, 75	131.35	1.003
16H-6, 7	133.67	1.356
16H-6, 32	133.92	1.125
16H-6, 41	134.01	1.012
16H-6, 61	134.21	1.112
16H-6, 77	134.37	1.334
16H-6, 111	134.71	1.777
16H-6, 124	134.84	1.378
16H-6, 144	135.04	1.475
16H-7, 5	135.15	2.968
16H-7, 13	135.23	2.965
16H-7, 39	135.49	2.964
16H-7, 51	135.61	2.962
16H-7, 67	135.77	2.964
16H-7, 36	135.46	1.630
16H-7, 5	135.15	1.627
16H-7, 11	135.21	2.028
16H-7, 26	135.36	1.670
16H-7, 37	135.47	1.560
16H-7, 51	135.61	1.917
16H-7, 63	135.73	1.464
16H-7, 74	135.84	1.985
16H-7, 83	135.93	1.730
17H-1, 13	135.73	1.407
17H-1, 33	135.93	1.082
17H-1, 54	136.14	1.100
17H-1, 86	136.46	1.239
17H-1, 111	136.71	1.100
17H-1, 133	136.93	1.216
17H-1, 140	137.00	1.134
17H-1, 147	137.07	1.811
17H-2, 5	137.15	1.082
17H-2, 30	137.40	2.222
17H-2, 52	137.62	1.901
17H-2, 95	138.05	1.825
17H-2, 87	137.97	2.281
17H-2, 101	138.11	1.152
17H-2, 107	138.17	2.278
17H-2, 114	138.24	26.068
17H-2, 122	138.32	5.031
18X-1, 53	140.73	0.667
18X-1, 85	141.05	0.761
18X-1, 85	141.05	0.747
18X-1, 136	141.56	0.711
18X-2, 137	143.07	0.696
18X-2, 44	142.14	0.672
18X-2, 81	142.51	0.761
18X-2, 128	142.98	0.760
18X-3, 26	143.46	0.622
18X-3, 74	143.94	0.621
18X-3, 74	143.94	0.604
18X-4, 75	145.45	0.957
18X-4, 76	145.46	0.877
18X-4, 14	144.84	0.783
18X-4, 15	144.85	0.682
18X-4, 48	145.18	0.662
19X-3, 10	153.00	0.739
19X-3, 46	153.36	0.632
19X-3, 70	153.60	0.651
19X-3, 100	153.90	0.677
19X-3, 132	154.22	0.748
19X-4, 23	154.63	0.804
19X-4, 59	154.99	1.090
19X-4, 95	155.35	0.984
19X-6, 26	157.16	1.036
19X-6, 46	157.36	0.990
21X-1, 80	170.10	1.527
21X-1, 81	170.11	1.240
21X-1, 146	170.76	1.683
21X-2, 4	170.84	1.536
21X-2, 35	171.15	1.398
21X-2, 55	171.35	2.408
21X-2, 91	171.71	1.083
21X-2, 113	171.93	1.040
21X-3, 4	172.34	0.895
21X-3, 44	172.74	0.805
21X-3, 81	173.11	0.954
21X-3, 138	173.68	1.089
21X-4, 32	174.12	1.018
21X-4, 33	174.13	1.359
21X-4, 100	174.80	1.243
21X-4, 124	175.04	1.268
21X-4, 145	175.25	1.174
21X-5, 10	175.40	1.309
21X-5, 28	175.58	1.104

Table T12 (continued).

Core, section, interval (cm)	Depth (mbsf)	Resistivity (Ωm)
21X-5, 43	175.73	1.176
311-U1329E-		
1H-1, 5	0.05	0.348
1H-1, 15	0.15	0.422
1H-1, 25	0.25	0.307
1H-1, 35	0.35	0.314
1H-1, 35	0.35	0.361
1H-1, 45	0.45	0.390
1H-1, 55	0.55	0.466
1H-1, 55	0.55	0.380
1H-1, 65	0.65	0.428
1H-1, 75	0.75	0.411
1H-1, 90	0.90	0.398
1H-1, 100	1.00	0.357
1H-2, 5	1.55	0.369
1H-2, 15	1.65	0.345
1H-2, 25	1.75	0.382
1H-2, 35	1.85	0.379
1H-2, 45	1.95	0.400
1H-2, 55	2.05	0.386
1H-2, 65	2.15	0.354
1H-2, 70	2.20	0.375
1H-2, 72	2.22	0.438
1H-2, 75	2.25	0.481
1H-2, 80	2.30	0.447
1H-2, 90	2.40	0.470
1H-2, 100	2.50	0.444
1H-3, 10	3.10	0.501
1H-3, 20	3.20	0.460
1H-3, 30	3.30	0.434
1H-3, 40	3.40	0.424
1H-3, 50	3.50	0.458
1H-3, 60	3.60	0.490
1H-3, 70	3.70	0.527
1H-3, 80	3.80	0.497
1H-3, 90	3.90	0.501
2H-1, 15	5.15	0.450
2H-1, 25	5.25	0.459
2H-1, 35	5.35	0.463
2H-1, 45	5.45	0.505
2H-1, 55	5.55	0.489
2H-1, 65	5.65	0.513
2H-1, 75	5.75	0.479
2H-1, 85	5.85	0.497
2H-1, 95	5.95	0.510
2H-2, 10	6.60	0.558
2H-2, 35	6.85	0.529
2H-2, 60	7.10	0.553
2H-2, 85	7.35	0.601
2H-2, 110	7.60	0.563
2H-3, 10	8.10	0.562
2H-3, 35	8.35	0.552
2H-3, 60	8.60	0.582
2H-3, 85	8.85	0.554
2H-4, 10	9.60	0.556
2H-4, 35	9.85	0.480
2H-4, 60	10.10	0.529
2H-4, 57	10.07	0.579
2H-4, 70	10.20	0.517
2H-4, 90	10.40	0.546
2H-5, 5	11.05	0.595
2H-5, 25	11.25	0.421
2H-5, 50	11.50	0.554
2H-5, 75	11.75	0.579
2H-5, 90	11.90	0.606
2H-6, 10	12.60	0.634
2H-6, 35	12.85	0.647
2H-6, 60	13.10	0.730
2H-6, 85	13.35	0.659
3H-1, 8	14.58	0.580
3H-2, 10	16.10	0.576
3H-2, 53	16.53	0.549
3H-2, 126	17.26	0.695
3H-3, 7	17.57	0.580
3H-3, 42	17.92	0.581
3H-3, 50	18.00	0.708
3H-3, 57	18.07	0.725
3H-3, 74	18.24	0.694
3H-3, 99	18.49	0.715
3H-3, 119	18.69	0.623
3H-4, 18	19.18	0.687
3H-4, 50	19.50	0.702
3H-4, 72	19.72	0.773
3H-4, 118	20.18	0.576
3H-5, 6	20.56	0.845
3H-5, 45	20.95	0.665
3H-5, 110	21.60	0.683
3H-6, 4	22.04	0.692
3H-6, 68	22.68	0.798
3H-6, 127	23.27	0.676
3H-7, 5	23.55	0.693
3H-7, 23	23.73	0.767
3H-7, 25	23.75	0.691
3H-7, 57	24.07	0.759
4H-1, 5	24.05	0.675
4H-1, 15	24.15	0.775
4H-1, 24	24.24	1.047
4H-1, 33	24.33	0.777
4H-1, 38	24.38	0.752
4H-1, 45	24.45	0.774
4H-1, 55	24.55	0.821
4H-1, 66	24.66	0.790
4H-1, 77	24.77	0.729
4H-1, 88	24.88	0.846
4H-1, 95	24.95	0.871
4H-1, 101	25.01	0.815
4H-1, 107	25.07	0.820
4H-1, 116	25.16	0.602
4H-1, 121	25.21	0.886
4H-1, 126	25.26	0.675
4H-1, 132	25.32	0.615
4H-1, 138	25.38	0.620
4H-1, 145	25.45	0.664
4H-2, 5	25.55	0.560
4H-2, 11	25.61	0.463
4H-2, 16	25.66	0.557
4H-2, 25	25.75	0.660
4H-2, 35	25.85	0.626
4H-2, 44	25.94	0.550
4H-2, 53	26.03	0.548
4H-2, 62	26.12	0.536
4H-2, 70	26.20	0.509
4H-2, 83	26.33	0.494
4H-2, 97	26.47	0.759
4H-2, 113	26.63	0.789
4H-2, 123	26.73	0.734
4H-2, 133	26.83	0.770
4H-2, 147	26.97	0.848
4H-3, 5	27.05	0.706
4H-3, 10	27.10	0.777
4H-3, 15	27.15	0.717
4H-3, 20	27.20	0.789
4H-3, 25	27.25	0.875
4H-3, 30	27.30	0.852
4H-3, 35	27.35	0.848
4H-3, 40	27.40	0.784
4H-3, 45	27.45	0.872
4H-3, 51	27.51	0.721
4H-3, 56	27.56	1.075
4H-3, 61	27.61	0.882
4H-3, 66	27.66	0.863
4H-3, 70	27.70	0.725
4H-3, 75	27.75	0.769
4H-3, 83	27.83	0.716
4H-3, 95	27.95	0.784
4H-3, 102	28.02	0.945
4H-3, 107	28.07	0.797
4H-3, 113	28.13	0.825
4H-3, 123	28.23	0.900
4H-3, 127	28.27	1.184
4H-3, 130	28.30	0.967
4H-3, 138	28.38	0.811
4H-3, 145	28.45	0.791
4H-3, 149	28.49	0.717
4H-4, 7	28.57	0.662
4H-4, 20	28.70	0.835
4H-4, 33	28.83	0.949
4H-4, 46	28.96	0.791
4H-4, 61	29.11	0.702
4H-4, 78	29.28	0.683
4H-4, 95	29.45	0.674
4H-4, 113	29.63	0.715
4H-4, 131	29.81	0.840
4H-4, 145	29.95	0.921
4H-5, 10	30.10	0.598
4H-5, 24	30.24	0.568
4H-5, 36	30.36	0.538
4H-5, 56	30.56	0.647
4H-5, 74	30.74	0.567
4H-5, 89	30.89	0.724
4H-5, 102	31.02	0.757
4H-5, 130	31.30	0.700
4H-5, 141	31.41	0.790
4H-6, 7	31.57	0.887
4H-6, 23	31.73	0.816
4H-6, 45	31.95	0.876
4H-6, 67	32.17	0.787
4H-6, 94	32.44	0.754
4H-6, 112	32.62	0.831
4H-6, 136	32.86	0.697
Perpendicular		
311-U1329E-		
1H-2, 5	1.55	0.411
1H-2, 10	1.65	0.332
1H-2, 15	1.65	0.361
1H-2, 20	1.70	0.352
1H-2, 25	1.75	0.377
1H-2, 30	1.80	0.314
1H-2, 35	1.85	0.385
1H-2, 40	1.90	0.392
1H-2, 45	1.95	0.330
1H-2, 49	1.99	0.377
1H-2, 55	2.05	0.359
1H-2, 60	2.10	0.381
1H-2, 65	2.15	0.400
1H-2, 70	2.20	0.361
1H-2, 75	2.25	0.447
1H-2, 80	2.30	0.479
1H-2, 85	2.35	0.467
1H-2, 90	2.40	0.476
1H-2, 95	2.45	0.435
1H-2, 100	2.50	0.443
3H-6, 4	22.04	0.558
3H-6, 68	22.68	0.730
3H-6, 127	23.27	0.618

Table T13. Thermal conductivity, Holes U1329B, U1329C, and U1329E.

Core, section, interval (cm)	Depth (mbsf)	Thermal conductivity (W/[m·K])			
		Average	1	2	3
311-U1329B-					
1H-1, 75	0.75	1.074	1.070	1.053	1.099
1H-2, 75	2.25	1.009	1.016	1.002	1.008
1H-3, 75	3.75	1.146	1.148	1.141	1.149
1H-4, 75	5.25	1.178	1.185	1.190	1.158
1H-5, 45	6.45	1.233	1.240	1.217	1.241
1H-5, 70	6.70	1.249	1.257	1.235	1.254
311-U1329C-					
1H-2, 75	2.25	1.065	1.081	1.049	1.064
1H-4, 75	5.25	1.088	1.098	1.080	1.087
2H-2, 75	10.35	1.008	1.011	1.008	1.005
2H-4, 75	13.35	1.201	1.178	1.214	1.210
2H-5, 58	14.68	1.114	1.112	1.115	1.114
3H-2, 65	19.75	1.162	1.160	1.152	1.173
3H-6, 72	25.82	1.196	1.210	1.202	1.177
4H-2, 36	28.96	1.137	1.151	1.127	1.133
4H-4, 63	32.23	0.964	0.972	0.962	0.959
4H-6, 45	35.05	1.014	1.013	1.010	1.018
5H-1, 34	36.94	1.018	1.013	1.023	1.017
5H-4, 38	41.48	1.013	1.004	1.015	1.019
5H-6, 80	44.90	0.916	0.920	0.912	0.915
6H-1, 31	46.41	0.870	0.866	0.873	0.870
6H-3, 91	50.01	1.042	1.043	1.042	1.041
6H-6, 90	54.50	1.028	1.020	1.031	1.032
6H-6, 119	54.79	1.139	1.146	1.141	1.131
8H-1, 66	58.26	0.997	0.996	0.999	0.997
8H-4, 86	62.96	1.087	1.086	1.083	1.093
8H-6, 103	66.13	1.076	1.075	1.075	1.077
9H-2, 30	68.90	1.077	1.081	1.078	1.072
9H-4, 34	71.94	0.868	0.870	0.866	0.869
10H-2, 21	78.31	1.050	1.049	1.053	1.047
10H-4, 34	81.44	0.894	0.892	0.893	0.898
10H-6, 12	84.22	0.966	0.967	0.965	0.966
11H-2, 15	87.75	0.922	0.922	0.921	0.923
11H-4, 75	91.35	1.089	1.088	1.082	1.098
11H-6, 26	93.86	1.085	1.089	1.087	1.079
12H-2, 45	97.53	0.987	0.988	0.986	0.986
12H-6, 36	103.44	1.084	1.090	1.082	1.081
13H-2, 15	106.75	1.079	1.084	1.077	1.075
13H-4, 40	110.00	1.200	1.187	1.207	1.206
13H-6, 15	112.75	1.052	1.055	1.049	1.052
15H-2, 45	118.55	0.987	1.003	0.984	0.974
15H-4, 55	121.65	0.981	0.990	0.977	0.977
15H-6, 86	124.96	1.026	1.041	1.020	1.018
16H-1, 54	126.64	1.137	1.140	1.134	1.138
16H-3, 42	129.52	1.126	1.132	1.124	1.123
16H-6, 122	134.82	1.093	1.104	1.082	1.094
17H-1, 88	136.48	0.937	0.933	0.929	0.950
17H-2, 70	137.80	1.064	1.069	1.069	1.055
18X-2, 105	142.75	1.078	1.074	1.079	1.082
18X-4, 70	145.40	1.027	1.032	1.030	1.020
19X-1, 134	151.24	0.971	0.976	0.973	0.964
19X-3, 52	153.42	1.093	1.101	1.088	1.091
19X-5, 91	156.81	0.978	0.981	0.983	0.970
20X-1, 39	159.99	1.058	1.054	1.067	1.052
20X-3, 63	163.23	0.994	1.000	0.999	0.983
20X-5, 33	165.43	0.959	0.959	0.961	0.957
21X-2, 65	171.45	1.176	1.179	1.175	1.173
21X-4, 60	174.40	1.001	1.008	0.991	1.004
22X-2, 27	180.67	1.116	1.120	1.115	1.114
311-U1329E-					
1H-1, 80	0.80	0.918	0.921	0.918	0.916
1H-3, 50	3.50	1.048	1.055	1.040	1.050
2H-2, 55	7.05	1.131	1.148	1.120	1.126
2H-4, 12	9.62	1.111	1.113	1.108	1.111
2H-4, 82	10.32	1.170	1.170	1.161	1.178
2H-6, 55	13.05	1.204	1.222	1.200	1.191
3H-2, 65	16.65	1.113	1.089	1.116	1.135
3H-4, 60	19.60	1.120	1.077	1.141	1.143
4H-3, 88	27.88	0.992	0.993	0.992	0.992

Table T14. In situ temperature, Holes U1329C and U1329E.

Core	Depth (mbsf)	Temperature (°C)		Thermal conductivity (W/[m·K])	Calibration correction (°)	Temperature tool	Solution reliability
		Corrected	Uncorrected				
311-U1329C-							
3H	27.1	NA	NA	NA	–0.97	APCT16	Poor
5H	46.1	6.6	7.6	1	–0.97	APCT16	Excellent
9H	76.6	9.04	9.005	1	0.03	APCT-3	Excellent
11H	95.6	10.544	11.514	1	–0.97	APCT16	Excellent
13H	114.6	11.79	11.759	1	0.03	APCT-3	Excellent
311-U1329E-							
4H	33.5	5.1	5.86/6.13	1	–0.97	APCT16	Fair
6H	64	7.76	8.69	1	–0.97	APCT16	Good
6H–7P	64	7.84	7.84	1	0	DVTP	Good
Base of hole	127.1	12.1	12.1	NA	0	DVTP	Excellent

Notes: NA = not available. Two uncorrected values are given for the measurement at 33.5 mbsf, corresponding to extrapolations using only data prior to the postinsertion disturbance and using the entire decay curve (except for the first few points). This illustrates the impact of disturbance during measurement. For the slope and intercept reported in the text and on Figure **F41,** only "good" and "excellent" data were used. The total uncertainty caused by uncertainties in calibration, extrapolation, and in the thermal conductivity value used for extrapolating to in situ conditions is estimated to be ±0.15°C for "excellent" data and ±0.25°C for "good" data. APCT = advanced piston corer temperature tool, APCT-3 = third-generation advanced piston corer temperature tool, DVTP = Davis-Villinger Temperature Probe.

Table T15. Summary of pressure coring operations at Site U1329.

Core	Core-top depth (mbsf)	Length recovered* (cm)	Length curated (cm)	Pressure at core depth (MPa)	Pressure recovered (MPa)		Comments
					Logged†	Gauge‡	
311-U1329C-							
7P	55.6	86	75	10.1	42	—	Normal operation
14P	114.6	—	90	11.4	0	—	Vent valve left open
23P	188.5	90	100	11.7	0.35	0.36	Sheared off bit during coring
311-U1329E-							
5P	33.5	—	60	10.1	0	—	Ball valve did not close
7P	73.5	95	86	10.2	48	49	Normal operation
8Y	104.0	—	79	10.8	0	—	Inner core barrel over-retracted
9E	114.5	—	100	10.9	85	85	Water in accumulator
10P	125.0	98	95	10.8	54	5.3	Normal operation

Notes: Water depth at Site U1329 is 946 mbsl. P = Pressure Core Sampler (PCS), Y = Fugro Percussion Corer (FPC), E = HYACE Rotary Corer (HRC). * = based on x-ray imagery and gamma ray density profiling prior to degassing. † = last pressure recorded before data logger disconnected from corer autoclave. Temperature 2°–4°C unless otherwise noted. ‡ = pressure measured when autoclave pressure transducer connected to computer (PCS cores) or external gauge (PCS, FPC, HRC cores). Pressure measured at 7°C unless otherwise noted. — = no data.

Table T16. In situ conditions of PCS cores recovered from Site U1329.

Core	Depth (mbsf) Top	Depth (mbsf) Bottom	Temperature (°C)	Pressure (MPa)	Salinity	Methane saturation (mM)
311-U1329C-						
7P	55.6	56.6	7.3	10.1	30.5	65.4
23P	188.5	189.5	16.9	11.4	25.1	118.5
311-U1329E-						
7P	73.5	74.5	8.7	10.2	30.5	73.2
10P	125.0	126.0	12.3	10.8	30.0	106.3

Notes: Salinity was analyzed in one interstitial water sample from Core 311-1329C-7P (Table T3) and extrapolated from adjacent cores in all other cases (Table T3). Temperature was calculated from sediment depth assuming a seafloor temperature of 3.3°C and a thermal gradient of 72°C/km (see "In situ temperature profile"). Pressure was calculated from sediment and water depth (946 mbsl). Methane saturation was calculated from temperature, pressure, and salinity according to Xu (2002, 2004).

Table T17. Results from degassing experiments at Site U1329.

Core	Total volume of gas released (mL)	Total volume of methane released (mL)	Average concentration of released gas components (%)* C_1	C_2†	CO_2	N_2	C_1/C_2†	Total volume of water released (mL)	Salinity of released water	Temperature during degassing (°C)	Air pressure during degassing (MPa)
311-U1329C-											
7P	1,494	718	69.3	0.0034	BD	19.3	15,765	302	—	7.7 ± 0.6	0.1021
23P	4,190	3,421	87.6	0.1927	5.9	4.4	453	0	—	7.2 ± 0.5	0.1009
311-U1329E-											
7P	1,620	1,047	78.3	0.0032	BD	17.0	15,850	204	—	7.3 ± 0.4	0.1007
10P	1,885	1,268	91.8	—	BD	8.0	—	234	—	6.8 ± 0.3	0.1005

Notes: * = excludes initially released gas increments that are diluted by dead volume of manifold system. BD = below detection. † = obtained for selected samples from each core using methods described in "Organic geochemistry" in the "Methods" chapters (Table T6) except for Core 311-U1329C-2P (continuous analysis during degassing experiment).

Table T18. Characteristics of PCS cores used for mass balance calculations, Site U1329.

Core	Core length recovered (m)	Sediment volume in inner core barrel (mL)	Porosity (%)	Pore water volume in inner core barrel (mL)	Volume of water in outer core barrel (mL)	Sediment extruded with outer core barrel water, dry weight (g)	Headspace volume in outer core barrel (mL)	Salinity of water in outer core barrel
311-U1329C-								
7P	0.86	1261	59	742	—	—	—	—
23P	0.90	1319	50	655	1295	—	1670	—
311-U1329E-								
7P	0.95	1394	58	811	2793	40	170	—
10P	0.98	1436	56	802	0	77	2934	—

Notes: Porosity taken from measurements of nearby cores (see "Physical properties"). — = no data.

Table T19. Mass balance calculations based on degassing experiments, Site U1329.

Core	Depth (mbsf) Top	Depth (mbsf) Bottom	Total C_1 released (10^{-3} mole)	C_1 concentration (mM) Total	At laboratory conditions Dissolved*	At laboratory conditions Free†	In situ Dissolved‡	In situ Nondissolved	In situ nondissolved C_1 as percentage of pore volume if present as Free gas	In situ nondissolved C_1 as percentage of pore volume if present as Gas hydrate
311-U1329C-										
7P	55.6	56.6	50	69	2.4	67	65.4	4	<0.1	0.1
23P	188.5	189.5	152	236	3.7	232	118.5	117	2.5	1.6
311-U1329E-										
7P	73.5	74.5	60	76	2.2	74	73.2	3	<0.1	<0.1
10P	125.0	126.0	71	92	2.7	89	92	0	0	0

Notes: * = extrapolated from HS analysis of adjacent APC and XCB cores (Table **T15**). † = calculated based on the total amount of C_1 released during the degassing experiment and the pore water volume recovered by the PCS. ‡ = methane saturation of pore water (Table **T16**) except for Core 311-U1329E-10P where pore water is under saturated (in situ methane saturation is 106.3 mM).